The Hall B 12 GeV Upgrade
Preconceptual Design Report

D. Abbott, H. Avakian, F. Barbosa, S. Boyarinov, V.D. Burkert, W.K. Brooks, J. Domingo, H. Egiyan, L. Elouadrhiri, R. Ent, A. Freyberger, V. Gyurjyan, M. Ito, D. Kashy, S. Lassiter, B. Mecking, M. Mestayer, B. Niczyporuk, V. Sapunenko, Yu. Sharabian, E. Smith, C. Timmer, A. Yegneswaran, D. Weygand, E. Wolin
Jefferson Lab, Newport News, VA 23606, USA

K. Hafidi, B. Mustapha
Argonne National Laboratory, Argonne, Illinois, USA

M. Dugger, E. Pasyuk, B.G. Ritchie
Arizona State University, Department of Physics and Astronomy, Tempe, AZ 85287, USA

B.M.K. Nefkens, J.W. Price
University of California at Los Angeles, Department of Physics and Astronomy, Los Angeles, CA 90095-1547, USA

R. Schumacher
Carnegie Mellon University, Department of Physics, Pittsburgh, PA 15213, USA

D. Doughty
Christopher Newport University, Newport News, VA 23606, USA

H. Crannell, F. Klein, D. Sober
Catholic University of America, Department of Physics, Washington D.C., 20064, USA

J. Ball, D. Doré, M. Garçon, F. Sabatié
CEA Saclay, DAPNIA-SPhN, F91191 Gif-sur-Yvette Cedex, France

R.T. Jones, K. Joo
University of Connecticut, Physics Department, Storrs, CT 06269, USA

J. Kellie, K. Livingston, G. Rosner
University of Glasgow, Glasgow, United Kingdom

D. Branford
Department of Physics and Astronomy, Edinburgh University, Edinburgh EH9 3JZ, United Kingdom

L. Kramer, B. Raue
Florida International University, Miami, FL 33199, USA

C. Keppel
Hampton University, Hampton, Virginia, USA

E. De Sanctis, M. Mirazita, F. Ronchetti, P. Rossi
Istituto Nazionale di Fisica Nucleare, Laboratori Nazionali di Frascati, P.O. 13, 00044 Frascati, Italy

M. Anghinolfi, M. Battaglieri, R. De Vita, M. Ripani, G. Ricco, M. Taiuti
Istituto Nazionale di Fisica Nucleare, Sezione di Genova e Dipartimento di Fisica dell'Universita, 16146 Genova, Italy

I. Bedlinsky, M. Kossov, S. Kuleshov, N. Pivnyuk, K. Mikhailov, O. Pogorelko, S. Pozdnyakov, A. Stavinsky, A. Vlassov
Institute of Theoretical and Experimental Physics, 25 B. Cheremushkinskaya, Moscow, 117259, Russia

K. Giovanetti, I. Niculescu
James Madison University, Department of Physics, Harrisonburg, VA 22807, USA

W. Kim, K. Park, R. Yarulin, B. Shin
Kyungpook National University, Department of Physics, Taegu 702-701, South Korea

P. Bosted, R. Hicks, R. Miskimen, D. Lawrence
University of Massachusetts, Department of Physics, Amherst, MA 01003, USA

A. Boluchevskii, E.N. Golovach, G.V. Fedotov, B.S. Ishkhanov, V.I. Mokeev, N. Markov, M.V. Osipenko, N. Shvedunov
Moscow State University, 11989 Moscow, Russia

G. Gavalian, B. Hersman, M. Holtrop
University of New Hampshire, Department of Physics, Durham, NH 03824, USA

M. Khandaker, C. Salgado
Norfolk State University, Norfolk VA 23504, USA

A.N. Skrinsky
Budker Institute for Nuclear Physics, Novosibirsk, Russia

D.S. Carman, K. Hicks
Ohio University, Department of Physics, Athens, OH 45701, USA

G.E. Dodge, C. Hyde-Wright, S. Kuhn, S. Stepanyan, L. Weinstein
Old Dominion University, Department of Physics, Norfolk VA 23529, USA

J.-P. Didelez, M. Guidal, E. Hourany
Institut de Physique Nucleaire d'Orsay, IN2P3, BP 1, 91406 Orsay, France

V. Koubarovski, P. Stoler
Rensselaer Polytechnic Institute, Department of Physics, Troy, NY 12181, USA

G.S. Mutchler
Rice University, Bonner Lab, Box 1892, Houston, TX 77251, USA

G. Gilfoyle
University of Richmond, Department of Physics, Richmond, VA 23173, USA

C. Djalali, R. Gothe, D. Tedeschi
University of South Carolina, Department of Physics, Columbia, SC 29208, USA

P. Cole
University of Texas at El Paso, Department of Physics, El Paso, Texas 79968, USA

D. Crabb, R. Minehart, L.C. Smith, K. Wang
University of Virginia, Department of Physics, Charlottesville, VA 22903, USA

K. Griffioen
College of William and Mary, Williamsburg, VA 23187, USA

G. Asryan, N. Dashyan, N. Gevorgyan, K.S. Egiyan
Yerevan Physics Institute, 375036 Yerevan, Armenia

M.F. Vineyard
Department of Physics, Union College, Schenectady, NY 12308, USA

Theory

A. Afanasev, W. Melnitchouk, A.V. Radyushkin
Jefferson Lab, Newport News, VA 23606, USA

M. Anselmino
Turin University & INFN, Turin, Italy

R.A. Arndt, W.J. Briscoe, I.I. Strakovsky, R.L. Workman
Data Analysis Center, Center for Nuclear Studies, The George Washington University, Washington, D.C., 20052

A. Belitsky, X. Ji
University of Maryland, College Park, Maryland, USA

S. Brodsky
Stanford University, Stanford, California, USA

C. Carlson
College of William and Mary, Williamsburg, VA 23187, USA

A. Efremov, O. Teryaev
Joint Institute for Nuclear Research, 141980 Dubna, Russia

A. Freund
Universität Regensburg, D-93040 Regensburg, Germany

M. Gyulassy
Columbia University, New York, USA

B. Kopeliovich
Max Planck Institut für Kernphysik, Heidelberg, Germany

B. Kotzinian
CERN, CH-1211, Geneva 23, Switzerland

J.M. Laget
CEA Saclay, DAPNIA-SPhN, F91191 Gif-sur-Yvette Cedex, France

L. McLerran
Brookhaven National Laboratory, Long Island, New York, USA

P.J. Mulders
Department of Physics and Astronomy, Vrije Universiteit, Amsterdam, Netherland

J. Nemchik
Institute of Experimental Physics SAV, Slovakia

J. Qiu
Iowa State University, USA

M. Sargsian
Florida International University, Miami, FL 33199, USA

S. Simula
INFN, Rome3, Rome, Italy

M. Strikman
Pennsylvania State University, University Park, Pennsylvania, USA

M. Vanderhaeghen
Johannes Gutenberg Universität Mainz, Mainz, Germany

X.N. Wang
Lawrence Berkeley National Laboratory, Berkeley, California, USA

Contents

1 The New Frontier in Electron Scattering 11

2 Executive Summary 17
- 2.1 Quark-Gluon Dynamics and Nucleon Tomography 17
- 2.2 Valence Quark Distribution and Hadronization 22
  - 2.2.1 The Proton and Neutron Spin Structure 22
  - 2.2.2 Tagged Quark Distribution Function 23
  - 2.2.3 Novel Quark Distributions 24
  - 2.2.4 The Neutron Structure Function $F_{2n}(x, Q^2)$ 25
  - 2.2.5 Space-Time Characteristics of Hadronization 26
- 2.3 Form Factors and Resonance Excitations 27
  - 2.3.1 The Magnetic Structure of the Neutron 27
  - 2.3.2 Resonance Excitation Dynamics 28
- 2.4 The Detector 29

3 The Physics Program at 12 GeV 35
- 3.1 Deeply Exclusive Scattering and Generalized Parton Distributions . . 35
  - 3.1.1 Phenomenology of the GPDs 36
  - 3.1.2 Revealing GPDs 39
  - 3.1.3 Deeply Virtual Compton Scattering 40
  - 3.1.4 Deeply Virtual Meson Production 53
  - 3.1.5 Large Momentum Transfer Meson Electroproduction 59
- 3.2 Inclusive Nucleon Structure Functions 63
  - 3.2.1 Overview 63
  - 3.2.2 Neutron structure function at large x 65
  - 3.2.3 Spin Structure Functions 73
- 3.3 Semi-Inclusive DIS 80
  - 3.3.1 Single-Spin Asymmetries 83
  - 3.3.2 Flavor Decomposition 88
  - 3.3.3 Semi-Exclusive Meson Production 89
  - 3.3.4 Conclusions 91
- 3.4 Properties of QCD from the Nuclear Medium 93

3.4.1 Introduction . . . 93
3.4.2 Quark Propagation . . . 94
3.4.3 Color transparency in coherent vector meson production . . . 110
3.4.4 Q^2 Dependence of Nuclear Transparency for Incoherent ρ^0 Electroproduction . . . 113
3.4.5 Transparency Studies via Quasielastic Scattering . . . 121
3.4.6 Nucleon structure modification in tightly bound nucleon pairs 121
3.5 Baryon Form Factors . . . 124
3.5.1 Introduction . . . 124
3.5.2 Context and Motivation . . . 124
3.5.3 Form Factor Measurements . . . 127
3.6 Exclusive Strangeness Production . . . 134
3.7 Electroproduction at very small Q^2 . . . 138
3.7.1 Introduction . . . 138
3.7.2 Meson Spectroscopy on LH_2 Targets . . . 141
3.7.3 Meson Spectroscopy Using Coherent Production on ^{4}He. . . . 147
3.7.4 Summary . . . 151

4 Upgrade Strategy and CLAS^{++} Detector Components **153**
4.1 CLAS Upgrade Strategy . . . 153
4.2 CLAS Torus Magnet . . . 154
4.3 Central Detector . . . 156
4.3.1 Introduction . . . 156
4.3.2 Superconducting Solenoid Magnet . . . 159
4.3.3 Central Electromagnetic Calorimeter . . . 162
4.3.4 Central Time-of-Flight System . . . 168
4.3.5 Central Tracker . . . 171
4.3.6 Silicon Strip Detector . . . 175
4.4 The Forward Detector Concept . . . 180
4.4.1 Forward Detector - Overview . . . 180
4.4.2 High Threshold Cerenkov Counter (HTCC) . . . 182
4.4.3 Forward Tracking Chambers . . . 183
4.4.4 Low Threshold Cerenkov Counter . . . 185
4.4.5 Outer TOF System . . . 185
4.4.6 Inner Calorimeter . . . 189
4.4.7 Forward Angle Calorimeter . . . 190
4.4.8 Pre-shower calorimeter . . . 190

5 Other Equipment Components in Hall B **195**
5.1 Polarized Target Operation in CLAS^{++} . . . 195
5.1.1 Polarized Target in Solenoid Magnet . . . 195
5.1.2 Polarized Target with Helmholtz Coil Arrangement. . . . 196

5.1.3 Transversely Polarized Target. 196
5.2 Beam Line 196
5.2.1 Introduction 196
5.2.2 Faraday Cup 197
5.2.3 Møller Polarimeter 197
5.2.4 Magnetic Chicane 197
5.2.5 Beam raster magnets 198
5.3 Radial TPC Low Energy Particle Tracking Detector 198
5.4 Small Angle Electron Detection 200
5.4.1 Beampipe 200
5.4.2 The θ and ϕ Detector 201
5.4.3 Energy Measurement 201

6 Computing 203
6.1 Data Acquisition System and Trigger 203
6.1.1 DAQ and trigger upgrade motivation 203
6.1.2 Design criteria for the system 204
6.1.3 System upgrade 204
6.1.4 Overview of the proposal 205
6.1.5 Level1 triggering and timing system 207
6.1.6 Higher level triggering systems 208
6.1.7 Control and monitoring 208
6.2 Event Reconstruction and Offline Computing 209
6.2.1 Data Reduction and On-line Event Reconstruction 209
6.2.2 Offline Data Analysis 210
6.2.3 Event Simulation 210
6.2.4 Software Development 211

7 CLAS^{++} - Expected Performance 213
7.1 Missing mass resolution for exclusive processes 213
7.2 Effect of the solenoid field on the Moller electrons 214
7.3 Identification of Single Photon Production from $ep \rightarrow ep\gamma X$ Final State 217

Chapter 1

The New Frontier in Electron Scattering

In the past 50 years many important discoveries have been made in electron-proton scattering experiments. The finite size of the proton was measured in Hofstadter's pioneering experiment in which electrons of 188 MeV energy were elastically scattered off a hydrogen target[1]. It demonstrated conclusively that the proton is not a Dirac particle but has a finite size. This had been suspected earlier because of the proton's anomalous magnetic moment. Hofstadter was awarded the Nobel prize in 1961 for this discovery. The energy of Hofstadter's accelerator was not high enough to resolve the internal structure of the proton but it laid the groundwork for a vigorous research program of inclusive electron scattering. It took another decade, and the construction of the powerful electron accelerator and the large magnetic spectrometers at the Stanford Linear Accelerator Center (SLAC), to "see" deep into the proton's interior. At energies of 20 GeV, experimental groups led by Jerome Friedman, Henry Kendall, and Richard Taylor discovered "scaling", i.e. the independence of deeply inelastic scattering cross sections on the virtuality of the electromagnetic probe[2, 3]. These results could only be interpreted in terms of electron scattering off point-like "partons" inside the proton. They were also a triumph for the quarks postulated earlier by theorists Murray Gell-Mann[4] and George Zweig[5] as the fundamental building blocks for hadrons. Gell-Mann received the Nobel prize in 1969. For the experimental discovery of the proton's quark structure Friedman, Kendall, and Taylor shared the Nobel prize in 1990. The small but significant deviations from scaling that were observed in the SLAC experiments also had significant impact on the development of the theory of Quantum-Chromo-Dynamics (QCD), and are fully explained by the emission of gluons from the struck quarks.

Deeply Inelastic Scattering (DIS) experiments, where only the scattered electron is detected, have been carried out up to the highest energies at CERN and at DESY. The quark's longitudinal momentum and spin densities have been mapped out in

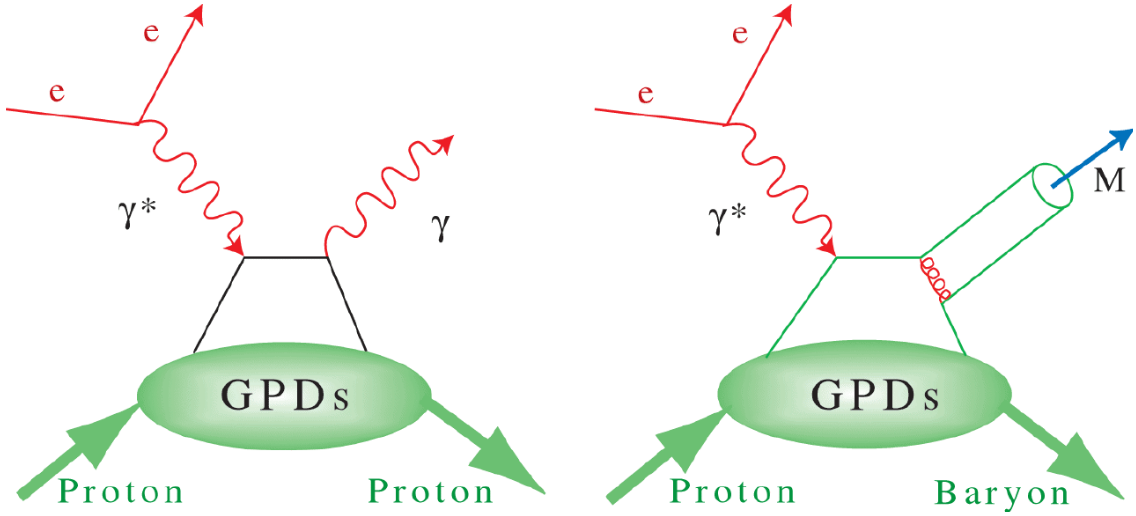

Figure 1.1: The "handbag" diagrams for deeply virtual Compton scattering (a), and for deeply virtual meson production (b). Four GPDs describe the "soft" proton structure part. They depend not only on x, but on two more variables: the momentum imbalance of the quark before and after the interaction, ξ, and the momentum transfer to the proton, t.

detail. We have also learned that the quarks are not the only tenants of the proton but that more than 50% of the proton's momentum is carried by the glue needed to bind the quarks together. More recently, inclusive polarized electron scattering off polarized protons led to the "spin puzzle", the finding that the quark spin contributes less than 25% of the total spin of the proton, leaving much to be understood about the origin of spin[6]. DIS experiments will continue to play an important role in further unraveling the valence quark structure, especially under extreme conditions, e.g. when one quark carries nearly the full proton momentum.

A glorious past and present is a good basis but not a guarantee for a successful future. So, what is the new physics that we are confident will shape the future of nuclear physics with electromagnetic probes for the coming decades? While the major discoveries in electromagnetic physics have so far come from inclusive electron scattering experiments, in particular measurement of elastic form factors and longitudinal parton densities, they are not sufficient to unravel the full structure and internal dynamics of the proton. Semi-exclusive measurements, in which one hadron is observed in addition to the scattered electron, are needed to study its flavor structure, and only fully exclusive processes in which all final products are reconstructed can unravel the complete internal dynamics of the proton. The experimental and theoretical tools for such an endeavor are now on the horizon: electron machines such as CEBAF at 12 GeV, with its CW beams and large acceptance detectors operating at

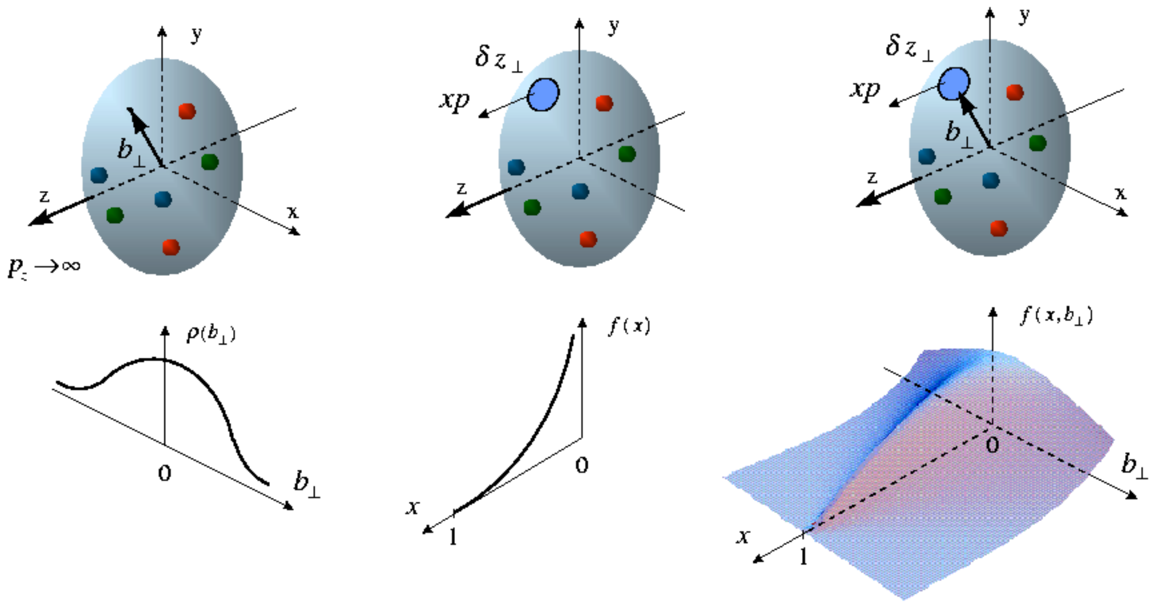

Figure 1.2: Representations of the proton properties probed in elastic scattering (left), deeply inelastic scattering (center), and deeply exclusive scattering processes (right). Elastic scattering measures the charge density $\rho(b_\perp)$ as a function of the impact parameter $b_\perp$. DIS measures the longitudinal parton momentum fraction density $f(x)$. GPDs measure the full correlation function $f(x, b_\perp, \xi)$ where ξ represents the momentum imbalance of the quark before and after the interaction. The graph shows the correlation function at $\xi = 0$.

high luminosities, are needed for the experimental part of such a program, while the new formalism of Generalized Parton Distributions (GPDs) provides the theoretical framework for the interpretation of the new experiments[7, 8, 9, 10]. The basis for this approach are the "handbag" diagrams shown in Fig. 1.1. Here the electron knocks a quark out of the proton by exchanging a deeply virtual (massive) photon. The quark then emits a high energy photon (a) and is put back into the proton. Alternatively, a $q\bar{q}$ pair (meson) is created, and one of the quarks is returned into the proton (b). At sufficiently high energies and high virtuality of the exchanged photon ("Bjorken regime") these processes are controlled by perturbative QCD, and the results can be interpreted in terms of "soft" correlation functions, the GPDs. They describe the full complexity of the proton's structure and dynamics.

What can these experiments tell us about the proton beyond what previous experiments have? Elastic scattering and deeply inelastic scattering give us two orthogonal one-dimensional projections of the proton: The quarks in the proton are subject to quantum fluctuations, resulting in variations of the proton size at a time scale of $< 10^{-23}$ seconds. Elastic scattering measures the probability of finding a proton with a transverse size $b_\perp$ matching the resolution of the probe given by the momentum

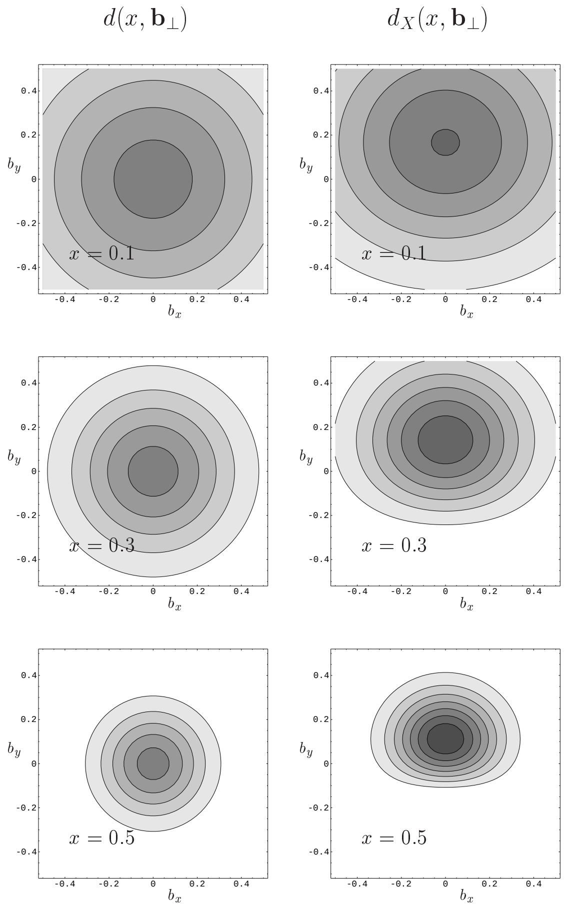

Figure 1.3: Simulated proton tomography images for the d-quarks $d(x, b_\perp)$, showing the strong correlation between the transverse size and the longitudinal momentum[11]. For small quark momentum x, the proton has a large transverse size, and it becomes very dense at large x. Left column: unpolarized, right column: $d(x, b_\perp)$ for a transversely polarized proton.

transfer t: $b_\perp \approx 1/\sqrt{|t|}$. The expression relates the momentum transfer to the transverse size of the proton probed in the interaction. Deeply inelastic scattering probes the quark's longitudinal momentum distribution, but has no sensitivity to the transverse dimension. These two aspects are illustrated in the first two panels of Fig. 1.2[12]. The information resulting from these two types of experiments is disconnected, and does not allow us to construct the image of a real 3-dimensional proton.

Deeply exclusive scattering processes connect both transverse and longitudinal information including their correlations as described by GPDs. This is shown in the third panel of Fig. 1.2. The GPDs now depend on 3 dimensions (x, ξ, t). Once the GPDs are measured they allow the construction of a spatial representation of the proton in what has been called "nucleon-tomography"[11].

On very general grounds we expect a correlation between the transverse and longitudinal variables that, for example, could be of the form[11]:

$$H_f(x,0,t) \approx q_f(x)\exp^{-a|t|(1-x)ln\frac{1}{x}} \ , \qquad (1)$$

where $q_f(x)$ is the forward parton distribution of flavor f and a is a scale parameter characterizing the transverse size. While the exact shape of this function needs to be determined experimentally, it must qualitatively contain the correlation between these parameters. Figure 1.3 illustrates the physical significance of Eqn.(1) [11]. The graphs show the strong correlation between the t-dependence (transverse size $b_\perp$) and the x-dependence (longitudinal momentum). For the spin-independent GPD $H(x,\xi,t)$ the left panels show the dramatic change in transverse profile as a function of longitudinal momentum x, while the image remains isotropic. A spatial anisotropy in the proton is observed for the spin-dependent GPD $E(x,\xi,t)$ shown in the right panels.

Electron scattering is the fundamental tool to determine the structure of atoms, nuclei, protons, and hadrons. This program must remain the flagship of an electromagnetic laboratory aimed at making fundamental contributions at the frontier of hadronic physics. This continues to be true for measurements of form factors and inclusive processes at high x. The new physics contained in the GPDs will be the climax of electron scattering and revolutionize nucleon structure physics. With the 12 GeV upgrade, JLab will be in the unique position to carry out a major part of the program using its powerful electron accelerator and its versatile instrumentation. The upgraded CLAS detector (CLAS^{++}) will make major contributions in all areas of nucleon structure physics sketched in the Introduction. In particular, CLAS^{++} will have design features that are essential for probing the new physics of the GPDs.

This document is organized as follows. Chapter 2 gives an Executive Summary outlining the main aspects of the physics program, and highlights the modifications or additions to the existing CLAS detector system that are necessary to carry out the core program described in this document. Chapter 3 outlines details of the physics program. Chapter 4 describes the requirements for the detector, and the currently envisoned realization of the CLAS^{++} detector and its new or modified components, respectively. Other Hall B equipment is briefly discussed in Chapter 5. Computing needs and the expected performance of the detector are discussed in Chapter 6 and 7.

Chapter 2

Executive Summary

The thrust of experiments proposed for the CLAS^{++} detector in conjunction with the 12 GeV CEBAF accelerator is the study of the nucleon through exclusive and semi-exclusive processes. This will provide new insights into the nucleon dynamics at the elementary quark and gluon level. The internal structure of the nucleon has been studied primarily during the past three decades through the *inclusive* scattering of high-energy leptons off the nucleon in the regime of "Deeply Inelastic Scattering" (DIS). When one sums over all possible hadronic final states, simple theoretical interpretations can be obtained in the framework of the parton model.

Inclusive measurements are largely insensitive to the internal quark-gluon dynamics, i.e. the nucleon wave function. They essentially reveal a one-dimensional image of the quark longitudinal momentum distribution. Now with the prospects of a new high-energy, high-luminosity, and continuous electron beam provided by the 12 GeV upgrade of CEBAF, a wide variety of *exclusive* processes in the Bjorken regime will become accessible experimentally when employing the large acceptance CLAS^{++} detector system in Hall B. Measurement of these processes will allow us to access the full internal dynamics of the nucleon through correlations of their elementary constituents, quarks and gluons.

The tables at the end of this chapter provide an overview of the physics topics and reactions that can be studied with CLAS^{++}. In the following sections we briefly address some of the major physics topics.

2.1 Quark-Gluon Dynamics and Nucleon Tomography

Until recently, very few exclusive processes could be treated in the framework of perturbative QCD and compared to experimental data. The recently developed formalism of Generalized Parton Distributions (GPDs) now holds promise to extend theoretical interpretations exclusive processes of the electroproduction of photons,

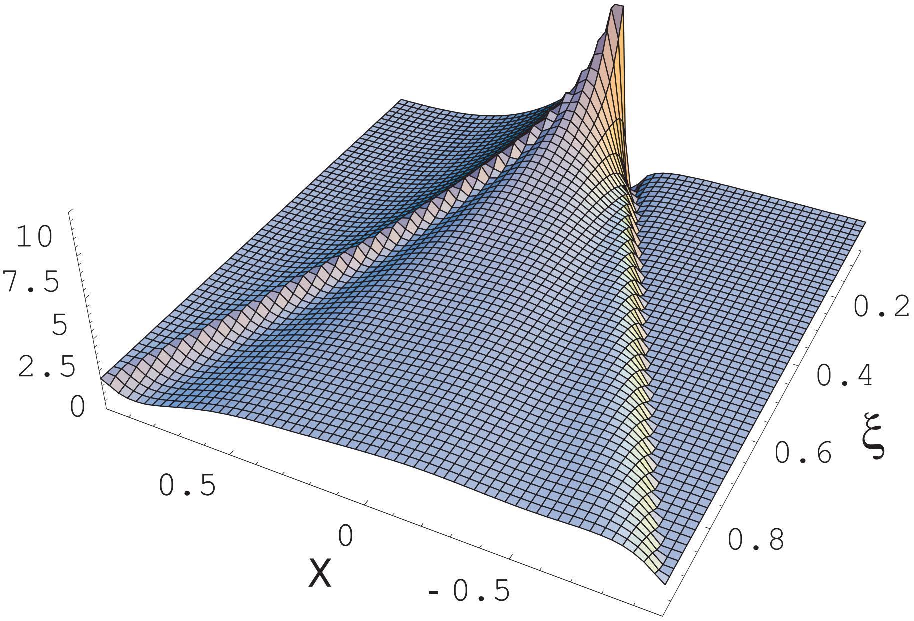

Figure 2.1: Model representation of the GPD $H(x, \xi, t = 0)$ in two dimensions. The known parton momentum densities constrain the distribution at $\xi = 0$. The new physics is contained in the ξ dependence and the t-dependence of this surface, which can currently only be modeled. The dramatic change in the shape of the surface reflects the change in the underlying physics. As ξ increases the correlations between the quarks and anti-quarks increase leading to meson-like distributions at large ξ.

vector mesons, and pseudoscalar mesons off the nucleon. GPDs encompass the standard forward-parton distribution functions, measured for instance in deeply inelastic scattering, elastic and resonance transition form factors, and the full complexity of two-parton correlations. Figure 2.1 shows a model representation of the GPD $H(x, \xi, t)$. Currently, only the distribution at the edge $H(x, 0, 0)$ is known from DIS experiments. A first foray into the realm of the new physics has been made. Measurements with CLAS at 4.3 GeV have demonstrated that the physics of GPDs can be accessed in the case of Deeply Virtual Compton Scattering (DVCS) already at lower energies[13]. Figure 2.2 shows projected data of a measurement of the DVCS process via the beam spin asymmetry using CLAS^{++}. The entire set corresponds to about 1000 data points that are measured simultaneously, and cover the entire kinematic range accessible with an 11 GeV polarized electron beam. Figure 2.3 illustrates the broad kinematic coverage of the proposed DVCS measurements. It shows the DVCS beam spin asymmetry for some bins in ξ (or Bjorken x_B) and Q^2 versus the momentum transfer t to the proton that are measured simultaneously. The graphs also show the sensitivity to different parameterizations of the GPDs.

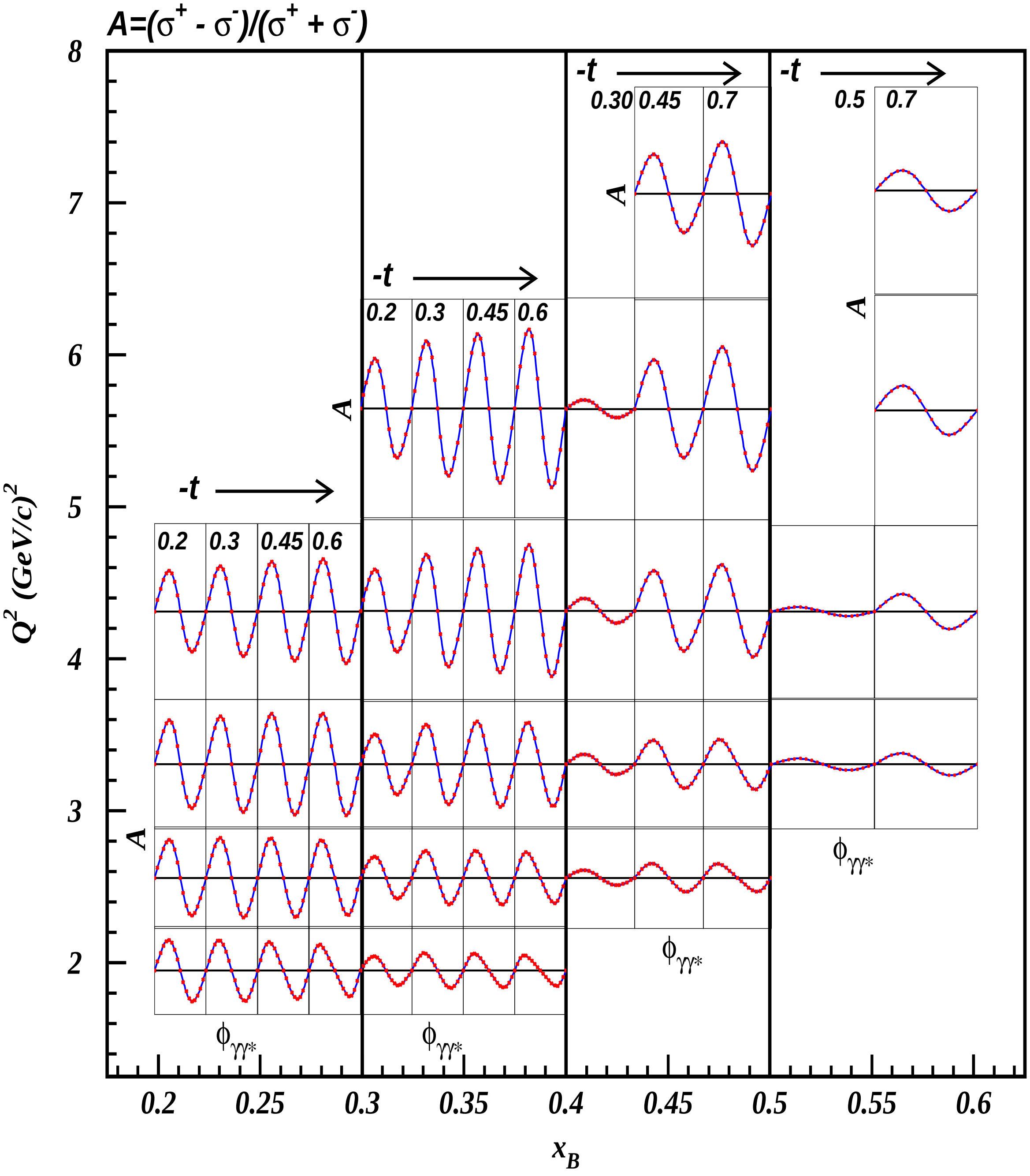

Figure 2.2: Beam spin asymmetry for $\vec{e}p \rightarrow ep\gamma$. Projected data with an upgraded CLAS and an 11 GeV electron beam for kinematic bins that are measured simultaneously. Complete azimuthal distributions in over 50 bins in Q^2, ξ, t will be collected simultaneously in 2000 hours of beam time. The curves represent a specific model for the GPDs. At the same time the DVCS cross section differences will be measured as well. In kinematics where the DVCS cross section is large, absolute cross section measurements will be possible.

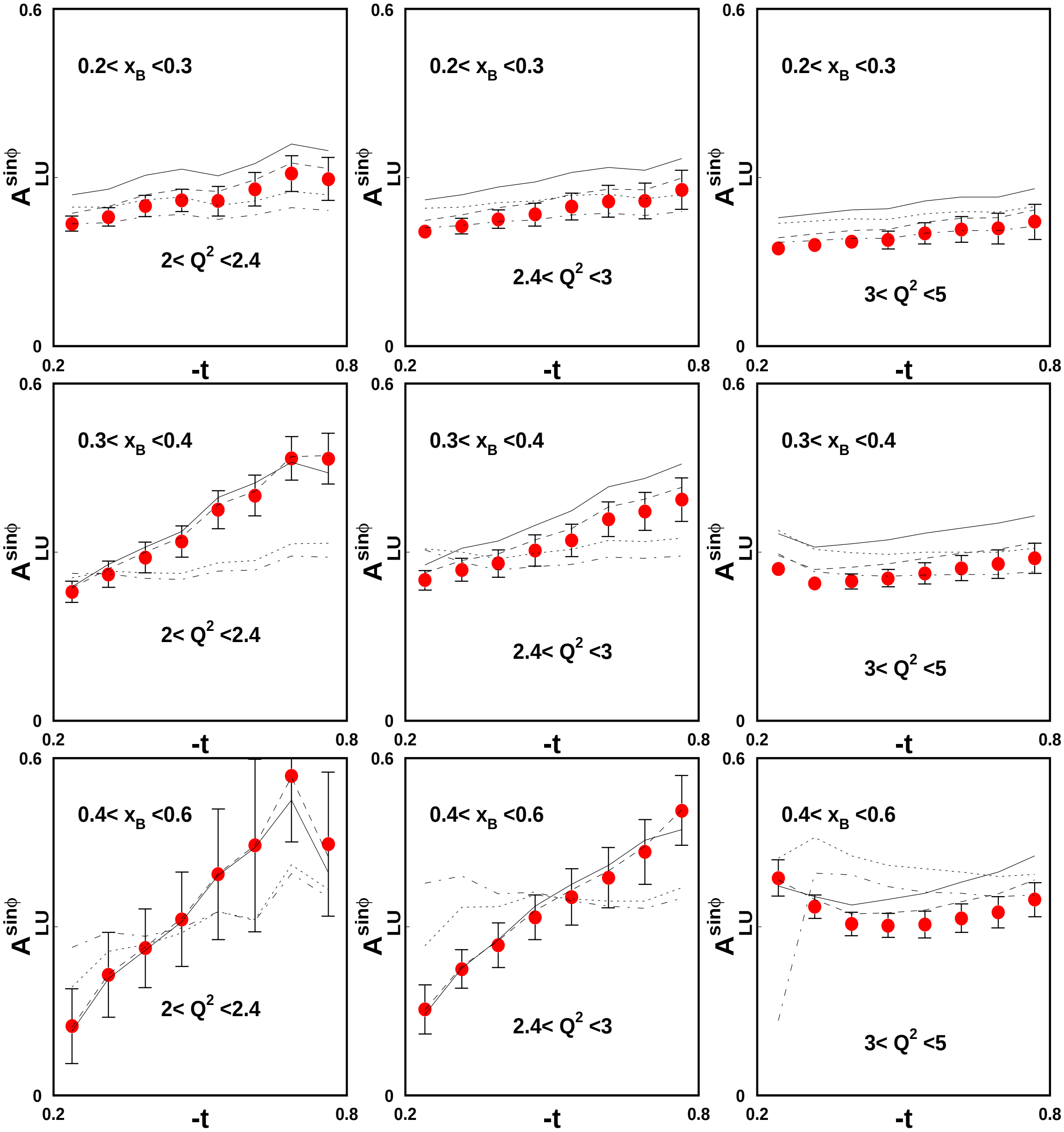

Figure 2.3: Momentum transfer-dependence of the beam spin asymmetry for $\vec{e}p \rightarrow ep\gamma$. Projected data with an upgraded CLAS and an 11 GeV electron beam for kinematic bins that are measured simultaneously. The curves represent different model parameterizations for the GPDs.

Complementary information with different sensitivities to GPD parameterizations can be obtained in measurements using polarized hydrogen (NH_3) targets. In order to separate all 4 leading twist GPDs in DVCS measurements with polarized targets are needed as well. At somewhat higher Q^2, other final states including ρ and ω vector mesons, and π^0 and η (Deeply Virtual Meson Production, DVMP) will provide information that is complementary to DVCS, allowing for an unraveling of the flavor and spin composition of the GPDs. These processes will be measured simultaneously with the DVCS beam spin asymmetry, the differential cross sections, and helicity-dependent cross section differences. Kinematic coverage will also be similar.

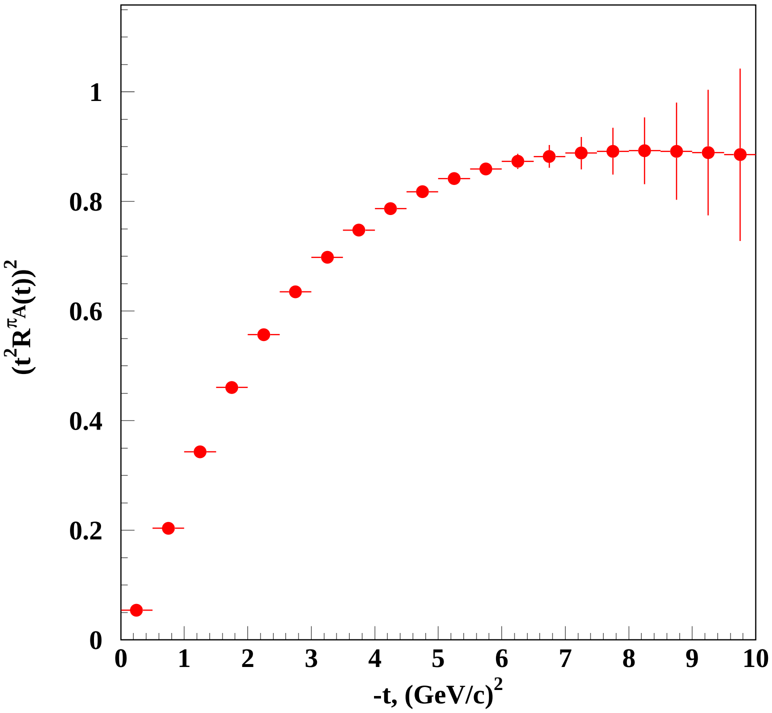

Figure 2.4: Simulated extraction of the form factor $(t^2 R_A^{\pi^0})^2$ from Eq. 3.24 compared with theory[14, 15].

Another important component of our GPD program will be to measure exclusive deeply virtual meson and photon production in the *high* t - *low* Q^2 regime, simultaneously with our measurements at *low* t - *high* Q^2. These reactions will provide x^{-1} moments for the small $b_\perp$ components of the correlations function, and combined with the $m = 0$ moments obtained in the high Q^2 form factor measurements will give powerful constraints on the nucleon's short distance parton wave functions. $R_A^{\pi^0}(t)$ is the axial form factor which is composed of the spin dependent GPDs as follows:

$$R_A^{\pi^0}(t) \sim (e_u R_A^u - e_d R_A^d)$$

$$R_A^q(t) = \int_{-1}^{1} \frac{dx}{x} \tilde{H}^q(x, 0, t)$$

$\tilde{H}^q(x, \xi, t)$ is the GPD function for quark of flavor q.
Thus, the key ingredients of the reaction which are probed are the GPDs $\tilde{H}^q(x, 0, t)$, with $H^q(x, 0, 0) = \Delta q(x)$, the pion distribution function $\phi_M(\tau)$, and the single quark hard scattering amplitude $f_0^{(q)}(\tau, s, Q^2, t)$. Figure 2.4 shows projected data for a measurement of the formfactor $R_A^{\pi^0}$ in exclusive π^0 production at high t.

In conclusion, the complete extraction of the GPDs represents an extensive program, rather than a single experiment, involving the measurement of a variety of channels and observables over a broad kinematic range.

The necessity to measure exclusive reactions at high photon virtualities and low momentum transfer to the target nucleon, as well as at low photon virtualities and high momentum transfer, is driving the CLAS upgrade.

While the GPD program is the flagship program for CLAS^{++}, there are several other programs and measurements of great importance for our understanding of the nucleon's valence quark structure that can be done best utilizing the large acceptance of CLAS^{++}. Several of them are briefly described in the following sections, others are described in the physics sections.

2.2 Valence Quark Distribution and Hadronization

2.2.1 The Proton and Neutron Spin Structure

CLAS has been used to measure the spin structure function $A_1(x, Q^2)$ for protons and deuterons through and beyond the nucleon resonance region, in the Q^2 range from 0.15 - 2 GeV^2. From these data the structure function $g_1(x, Q^2)$ and its first moment $\Gamma_1(Q^2) = \int g_1(x, Q^2)dx$ have been extracted using parameterizations of the unmeasured deeply inelastic part at small x. The upgrade will allow a large extension in the x and Q^2 range. The large x regime is crucial for determining higher moments such as $\int x^2 g_1(x, Q^2)dx$. Moments are needed for a QCD analysis using the operator product expansion of QCD, which will elucidate the importance of "higher twist" effects (strong quark-gluon correlations) in the nucleon. It will also expose the dynamics underlying the quark-hadron duality and the nature of the resonance-scaling transition. Figure 2.5 shows projected data for $A_{1p}(x)$ in the deeply inelastic regime. Data with similar coverage in x will be obtained for the deuteron (neutron). If "duality" arguments apply namely if data in the resonance region approximately average to the DIS data, the x range can be extended to $x = 0.95$.

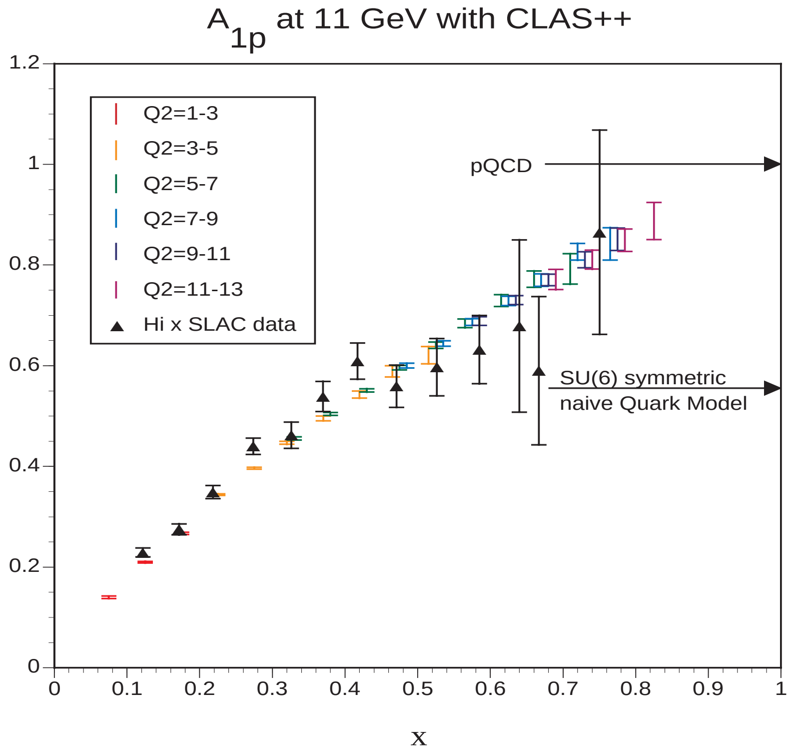

Figure 2.5: Projected CLAS^{++} data at 11 GeV for the helicity asymmetry $A_{1p}(x)$ of the proton. The x range may be extended to 0.95 if duality arguments hold. The arrows at $x \rightarrow 1$ indicate the pQCD limit of $A_{1p} = 1$, and the $SU(6)$ limit of $A_{1p} = 5/9$, respectively. The color code shows that measurements at fixed x are done at different Q^2 allowing to test for a possible Q^2 evolution.
.

2.2.2 Tagged Quark Distribution Function

Semi-inclusive processes such as $eA \rightarrow eMX$, where $A = p,\ d,\ ^3$He,..., and $M = \pi,\ \eta,\ K,\ \rho,\ \omega$ are powerful tools to tag the flavor of the struck quark, and in conjunction with polarized beams and polarized targets, to probe the quark spin distributions in nucleons and nuclei. Recent CLAS data[16] on the beam spin asymmetry in $\vec{e}p \rightarrow e\pi^+X$ indicate that factorization of the parton distribution functions and the quark fragmentation functions may already be valid at present JLab energies, provided the pion carries most of the energy of the virtual photon. Given approximate factorization, measurements of beam and target spin asymmetries in the 12 GeV energy range will probe the quark transverse spin distribution, and will also be sensitive to the quark-gluon final state interaction.

The semi-inclusive double polarization asymmetries with a longitudinally polarized target (σ_{LL}) have been the subject of considerable interest recently, both theoretically and experimentally. While the polarized u-quark distribution is reasonably well established experimentally, the polarized d-quark distribution is poorly known,

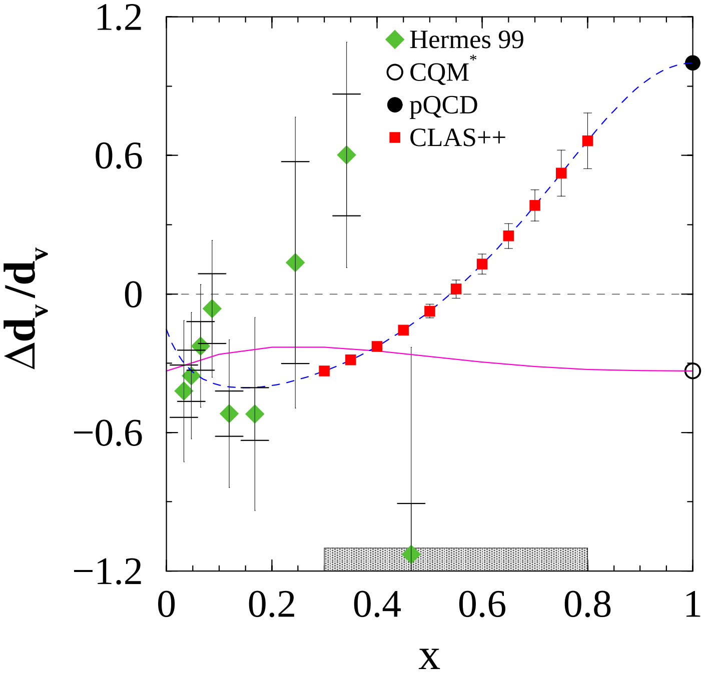

Figure 2.6: Projected data for the valence d-quark helicity distribution with CLAS^{++} from semi-exclusive pion production using a polarized beam and a longitudinally polarized target. Higher x values can be reached if duality arguments apply. In this figure, 1000 hrs of data taking with a NH_3 target and 1000 hrs with a ND_3 have been assumed. The double error bars on the existing data points represent the statistical (inner) and the total (statistics and systematics) errors. The curves represent two models of the x dependence. The shaded area at the bottom shows the expected systematic error of the measurement.

especially at large x, where there are significant differences between model predictions. The data shown in Fig. 2.6 represent the present knowledge of Δd at large x. CLAS^{++} will allow measurements in the x region above 0.5. Good particle identification is needed for a successful program to study semi-inclusive reactions.

2.2.3 Novel Quark Distributions

Apart from GPDs, there is another class of nonperturbative functions that carry information not only on longitudinal but also on transverse hadron structure. These are the transverse momentum dependent (TMD) parton distributions [17, 18, 19, 20, 21, 22, 23, 24] containing direct information about the quark orbital motion [25, 26, 24]. TMD distributions in impact parameter space are correlation functions for the transverse distance of a single parton with respect to all other partons in the wave function [27]. This is in contrast to GPDs (integrated over the transverse momentum) where the relative distance of partons to each other in a hadron stays the same. The TMDs appear in azimuthal moments of double-polarized cross sections in single-hadron production in DIS [20, 21]. As shown recently in Ref.[23], the interaction of active partons

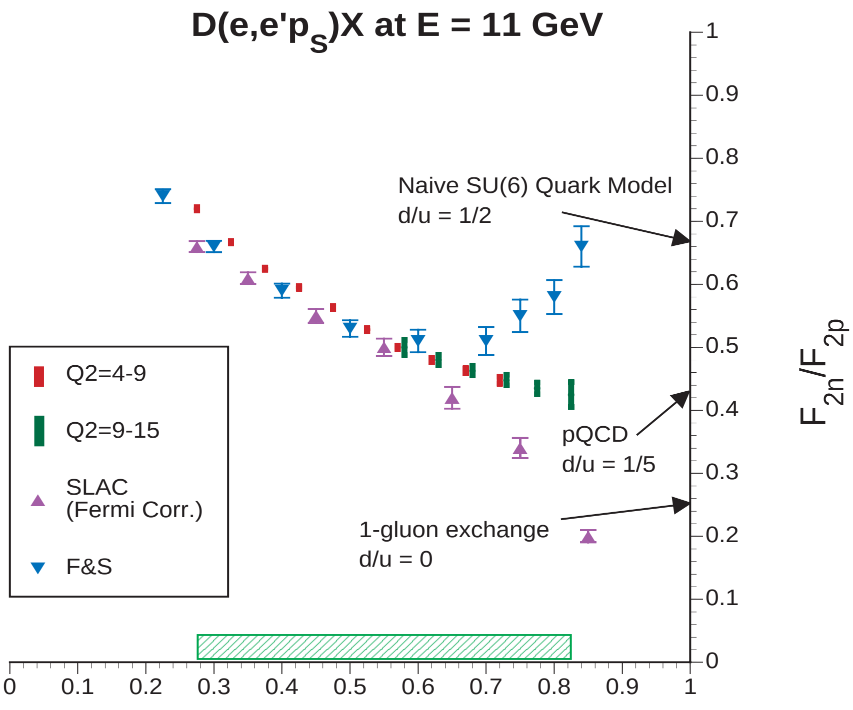

Figure 2.7: Projected CLAS^{++} data at 11 GeV for the ratio of the neutron to proton structure functions F_{2n}/F_{2p}. The read and green symbols are measurements at fixed x but different Q^2 taken simultaneously. This allows checking for a possible Q^2 evolution. The other symbols are from previous SLAC measurements interpreted with different nuclear models, indicating strong model-dependence at large x. The x range may be extended to 0.95 if duality arguments can be used.

in the hadron with the target spectators [25, 28] leads to gauge-invariant TMD parton distributions. A non trivial phase structure of QCD amplitudes due to rescattering results in *time-reversal odd* (T-odd) effects and the appearance of single-spin asymmetries at leading twist[25, 26]. The list of novel physics observables accessible in SSAs includes the chiral-odd distribution functions, such as the transversity [29, 30], the *time-reversal odd* fragmentation functions, in particular the Collins function [19], and the recently introduced [18, 22, 25, 26, 28] *time-reversal odd* distribution functions (Sivers function). Measurements of single-spin asymmetries in semi-inclusive DIS at CLAS^{++} with longitudinally and transversely polarized targets will accomplish separation of contributions from all these functions.

2.2.4 The Neutron Structure Function $F_{2n}(x, Q^2)$

New opportunities arise with the upgrade to directly determine the $F_{2n}(x, Q^2)$ structure function of the neutron for the first time in the large x region. Using a deuteron gas target, the recoil spectator proton (p_s) in the reaction $ed \rightarrow ep_sX$ can be mea-

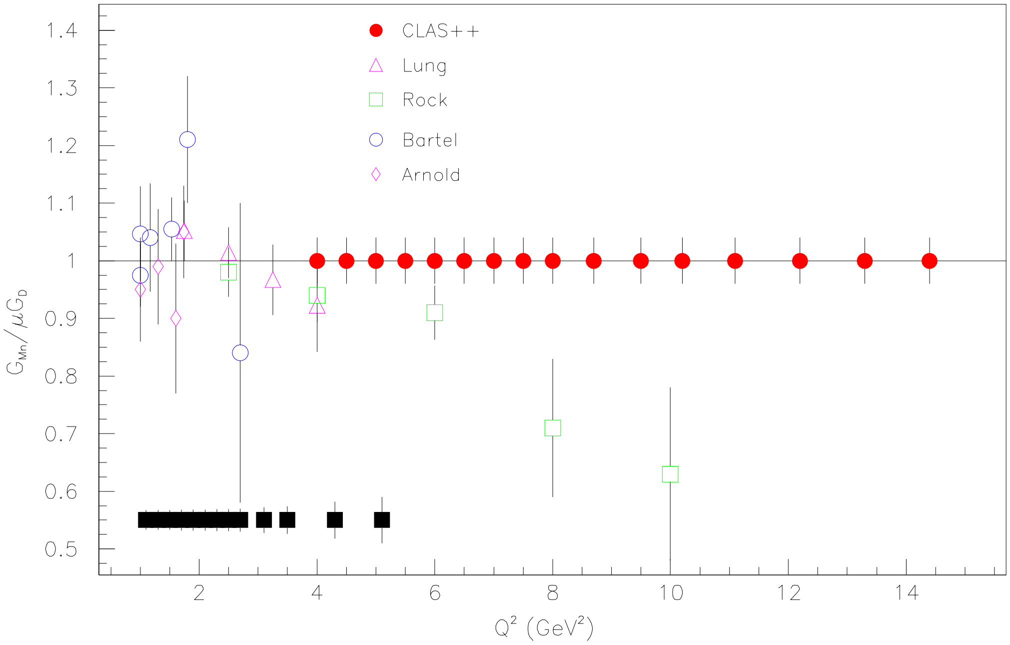

Figure 2.8: Projected CLAS^{++} data at 11 GeV for the neutron magnetic formfactor. The points at the lower left of the panel are projected errors of the existing CLAS data which are currently being analyzed. The open symbols are data from measurements at SLAC and at DESY

sured using a low-density gas detector. Recoil proton momenta as low as 80 MeV/c can be detected, allowing direct verification that the process has taken place on an almost-free neutron of known momentum. Low luminosity operation and the large acceptance of CLAS are crucial to reduce accidentals from quasi-real photoproduction events. Expected results are shown in Fig. 2.7.

2.2.5 Space-Time Characteristics of Hadronization

The hadronization process, which is the primary manifestation of confinement in QCD, has been studied at length for decades. While many features of this fundamental process are well-reproduced using phenomenological modeling, little direct experimental information is available on its space-time characteristics. Information of this type can be obtained by studying the modification of quark fragmentation functions within the nuclear medium. Recent exploratory measurements have offered tantalizing hints as to how the hadronic formation time varies with the size or mass of the quark system being formed, finding, for example, that the proton formation time is more than twice as long as that for charged pions[31][32]. However, these pioneering studies are limited to $Q^2 \approx 1-2$ GeV^2, and to just a few hadron types, by the available luminosity. With the advent of CLAS^{++}, a ground-breaking advance in such studies will become possible. A broad program of measurements using a score

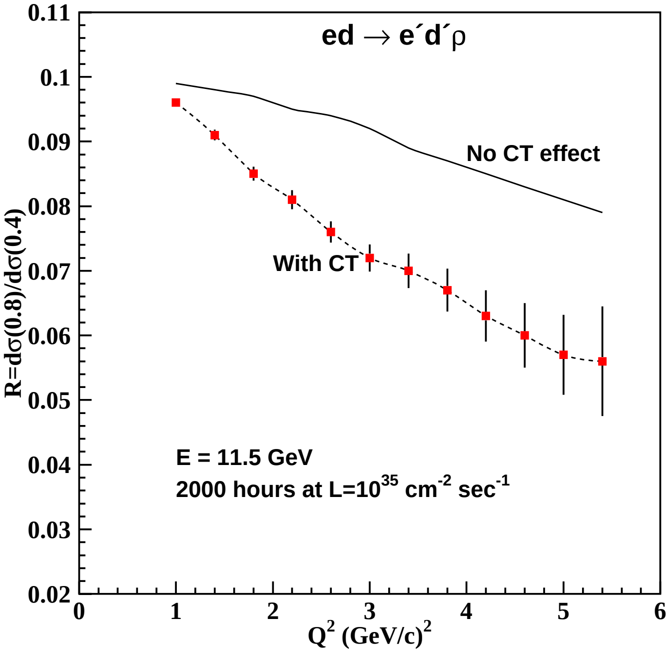

Figure 2.9: Expected errors on the cross section ratio for coherent ρ° production off deuterium at $-t = 0.4$ and 0.8 $(\mathrm{GeV/c})^2$ for 2000 hours of running at a luminosity of $10^{35}\mathrm{cm}^{-2}\mathrm{sec}^{-1}$.

of mesons and baryons (see the table in Section 3.4.2) will systematically map out the dependence of the hadron formation time as a function of Q^2, ν, p_T, z, helicity, hadron mass and size, and quark flavor. A program of this breadth can only be carried out with a large acceptance spectrometer at high luminosity. Accompanying the hadronization analysis will be an investigation of quark energy loss, and a comprehensive array of color transparency studies via vector meson production and quasielastic scattering. The analysis of such a data set will yield a wealth of new insights into the nature of the hadronization process, which is a direct manifestation of confinement in QCD. Figure 2.9 shows an example of the expected effect for coherent ρ° production off deuterium with and without the inclusion of color coherent effects.

2.3 Form Factors and Resonance Excitations

2.3.1 The Magnetic Structure of the Neutron

The electric and magnetic form factors of the neutron are the major missing pieces in the elastic form factor analysis of the nucleon charge and magnetization distributions. An experiment with CLAS at 4 GeV is using the cross section ratio of the processes $ed \rightarrow enX$ and $ed \rightarrow epX$ to precisely measure the magnetic form factor $G_{Mn}(Q^2)$ up to Q^2 =5 GeV^2[33]. With the upgrade this quantity can be measured up to Q^2=14 GeV^2 in CLAS^{++}. Projected data are shown in Fig. 2.8.

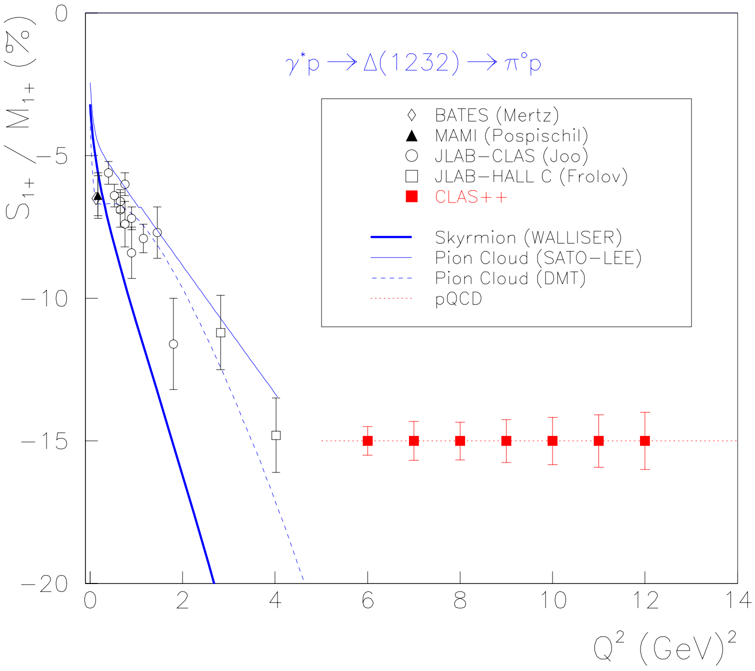

Figure 2.10: Ratio R_{SM} for the $N - \Delta$ transition. The data points at lower Q^2 are from CLAS and Hall C. The high Q^2 points correspond to projected error bars for a measurement with CLAS^{++}.

2.3.2 Resonance Excitation Dynamics

The current CLAS program is providing accurate information on resonance transition form factors for Q^2 up to 4 - 6 GeV^2. Much effort has gone into the measurement of the multipole ratio $R_{EM} = E_{1+}/M_{1+}$ for the $N - \Delta(1232)$ transition[34, 35]. R_{EM} is predicted to approach +1 asymptotically, while the ratio is nearly flat at -0.02 for $Q^2 < 4$ GeV^2 with no clear trend towards the asymptotic value. In addition we measure the longitudinal ratio $R_{SM} = S_{1+}/M_{1+}$ that exhibits an approximately linear dependence with Q^2. R_{SM} is easier to measure than R_{EM} as $|R_{SM}|$ rises with Q^2. As pQCD predicts a constant value for R_{SM} at large Q^2, a change towards a flatter Q^2 dependence may indicate the onset of significant leading-order pQCD contributions. With CLAS^{++} this measurement can be extended to $Q^2 = 12$ GeV^2 where indication of a transition to pQCD behavior may set in. Figure 2.10 shows the projected data.

Some of the higher-mass states are expected to become more prominent with increasing Q^2, opening up the possibility for a "hard" N^* spectroscopy, where connections to pQCD may be possible. At 4 GeV, measurements in the $p\pi^+\pi^-$ channel show a dramatic rise of the $P_{13}(1720)$ resonance strength with Q^2 in comparison with non-resonant contributions. With CLAS^{++} these measurements may be extended from $Q^2 = 1.5$ GeV^2 to $Q^2 > 4$ GeV^2. The program on hard N^* spectroscopy requires the full acceptance of CLAS^{++} for both the detection of photons and of charged particles.

2.4 The Detector

The CLAS^{++} detector is shown in Fig. 2.11. It meets the basic requirements of the physics program currently anticipated for the 12 GeV upgrade.

The main features of CLAS^{++} are:

- High operating luminosity of $10^{35}\text{cm}^{-2}\text{s}^{-1}$ for hydrogen targets, a ten-fold increase over current CLAS operating conditions.
- Improved detection capabilities for forward-going high momentum particles. Charged particles that bend outwards in the torus field can be reconstructed for angles as low as 5 degrees. Photon detection will be possible for angles as low as 3 degrees. Acceptances for electrons are momentum-dependent, and range from about 8 degrees to 40 degrees.
- Capability to detect the recoil baryons at large angles.
- Larger momentum range for the separation of electrons, pions, kaons, and protons. This is achieved with better resolution time-of-flight counters, and with the installation of a new gas Cerenkov detector.
- Improved hermeticity for the detection of charged particles and photons in regions where CLAS currently has no detection capabilities, achieved by instrumenting the coil regions and by extending the polar angle range for photon detection to 135 degrees.

CLAS^{++} makes use of many of the components of the current CLAS detector.

- The torus magnet will be re-used in a slightly modified form.
- All large forward calorimeters will be used for electron, photon, and neutron detection.
- All gas Cerenkov counters will be used with adjustments in the optics and replacement of 1/3 of the mirrors.
- The time-of-flight scintillator material will be used to make smaller scintillator slabs for better timing.
- Part of the CLAS drift chamber electronics will be re-used.

A major new component in CLAS^{++} is the Central Detector. Its main component is a superconducting solenoid magnet, which has a dual function: It replaces the existing mini-torus for shielding of the Møller electrons, and it provides the magnetic field for the momentum analysis of charged particles at large angles. Time-of-flight scintillators are used to provide particle identification at scattering angles greater than 40 degrees. Due to the limited space available excellent timing resolution is essential. Tracking at large angles is provided by a combination of drift chambers with cathode strip readout and a microstrip detector near the vertex. Since most charged tracks will have momenta of 1 GeV/c or less sufficient momentum resolution can be achieved even in the limited space available for tracking. A compact electromagnetic calorimeter based on tungsten powder and scintillating fiber technology provides photon detection capability for the angle range from 40-135 degree.

Much of the instrumentation of CLAS will be re-used in the CLAS^{++} Forward Detector (FD). However, some modifications and additional detectors are needed in the Forward Detector as well. The main new component is a threshold gas Cerenkov counter for pion detection. CO_2 is considered as radiator gas. The light collection is accomplished using a mirror system that focuses the Cerenkov light onto photomultipliers located sideways of the torus magnet. This area will be accessible after the removal of the CLAS drift chambers. The Cerenkov counter will allow electron and pion identification up to nearly 5 GeV/c. Beyond 5 GeV/c electrons are identified in the forward electromagnetic calorimeter. There is also additional electromagnetic calorimetry placed in the area of the torus coils for improved hermiticity. Lead-tungstate crystals have emerged as a good choice for this detector.

A pre-shower detector will be inserted in front of the existing CLAS electromagnetic calorimeters. This detector will allow separation of single photons from $\pi^0 \to \gamma\gamma$ events especially needed for deeply virtual Compton scattering.

All drift chambers in CLAS will be replaced by new ones that will cover a smaller angle range with a factor of two smaller cell sizes to reduce the accidental hit occupancy due to photon interactions allowing for a corresponding gain in luminosity.

The existing forward detection system will be modified to extend particle identification and reconstruction to higher momenta. This will be accomplished by several means: The timing resolution of the scintillation counters will be improved by using smaller scintillator slabs, and by adding an additional layer of scintillators, and by replacing the PMTs by new ones with better timing characteristics. This is expected to improve the timing resolution to about 60 psec. The existing gas Cerenkov counter will be modified for improved pion detection capabilities for momenta greater than 2.7 GeV/c. .

With these modifications and additions to the existing CLAS components, CLAS^{++} will be able to carry out the core program for the study of the internal nucleon dynamics and hadronization processes by measuring exclusive, semi-inclusive, and inclusive processes.

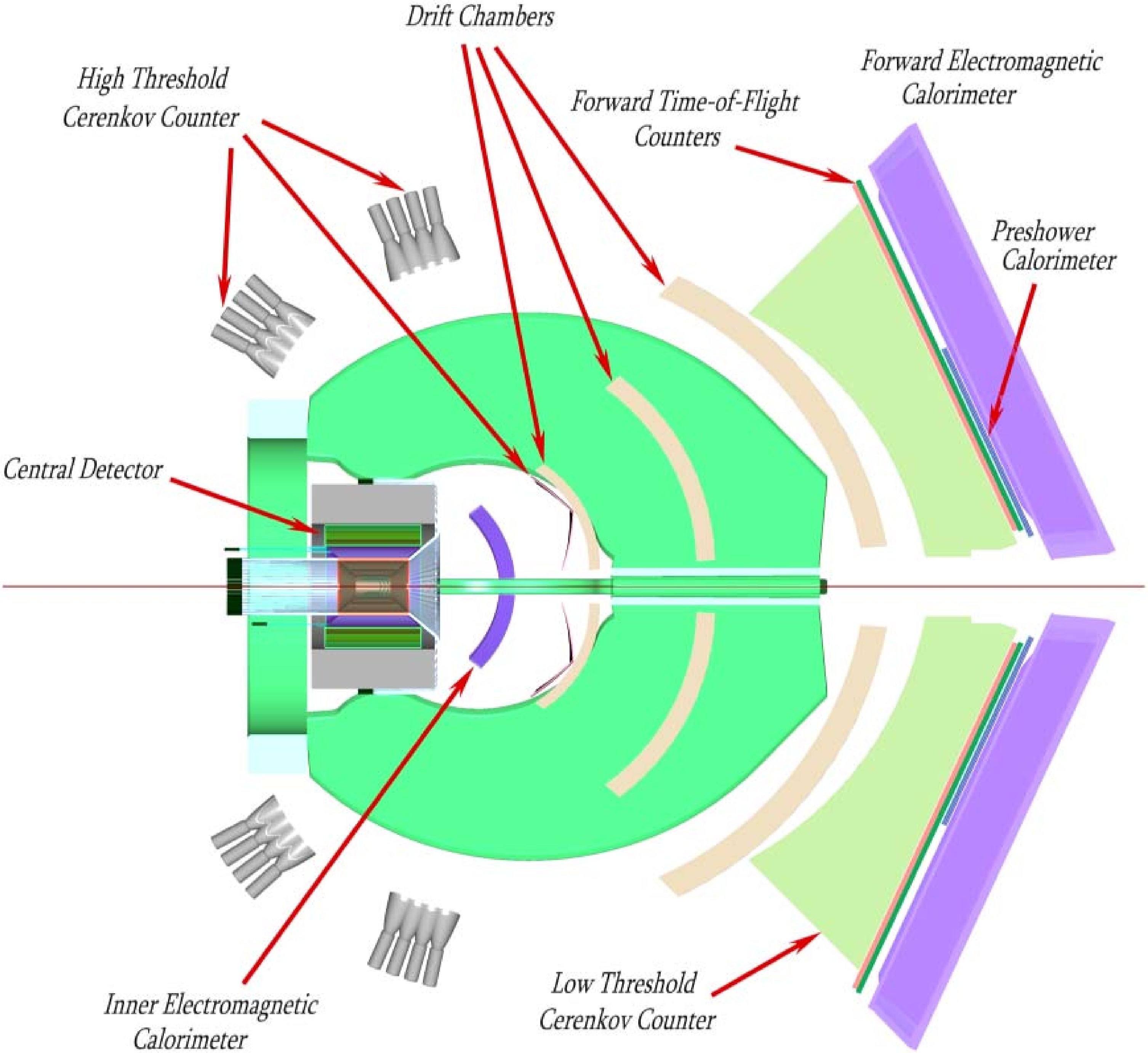

Figure 2.11: The upgraded CLAS^{++} detector.

Table 2.1: **CLAS^{++} PROGRAM SUMMARY - NUCLEON QUARK-GLUON DYNAMICS**
The color code indicates reactions that will be measured simultaneously in CLAS^{++}.

PHYSICS PROGRAM	**REACTION(s)**	**OBSERVABLES**	**REQUIREMENTS**
EXCLUSIVE REACTIONS AND GPDs			**Large Q^2, X_B, t, ϕ**
Deeply Virtual Compton Scattering(DVCS) Proton dynamics and tomography	$\vec{e}p \rightarrow ep\gamma$ $\vec{e}\vec{p} \rightarrow ep\gamma$ $\vec{e}p^T \rightarrow ep\gamma$	GPDs(H), $\xi = x$ GPDs($\tilde{H}$), $\xi = x$ GPDs($\tilde{E}$), $\xi = x$	Pol. Beam Long pol. target Trans. pol. target
Hard vector meson production Spin Filtering and flavor decomposition	$\vec{e}p \rightarrow ep(\rho, \omega, \phi)$ $\vec{e}\vec{p} \rightarrow ep(\rho, \omega, \phi)$ $\vec{e}p^T \rightarrow ep(\rho, \omega, \phi)$	GPDs and angular momentum	Multi-particle detection
Hard pseudoscalar meson production Structure of the proton at small distances	$\vec{e}p \rightarrow eN(\pi^0, \eta, \pi^+)$ $\vec{e}\vec{p} \rightarrow eN(\pi^0, \eta, \pi^+)$ $\vec{e}p^T \rightarrow eN(\pi^0, \eta, \pi^+)$	GPDs at low and high t	Multi-photon detection Large angular coverage Large t
Double DVCS (DDVCS) Δ and N^* DVCS	$\vec{e}p \rightarrow epe^+e^-$ $\vec{e}p \rightarrow ep(\Delta, N^*)\gamma$	GPDs at $-\xi < x < \xi$	Multi-particle detection
INCLUSIVE VALENCE QUARK STRUCTURE FUNCTION			**Low luminosity program**
Neutron structure function Novel method to study neutron dynamics	$\vec{e}D \rightarrow ep_sX$ $\vec{e}D \rightarrow ep_s(\pi^-p), \Delta^+\pi^-$	d/u ratio	Neutron tagging Low $L \rightarrow$ large acc.
Nucleon spin structure function	$\vec{e}\vec{p} \rightarrow eX$, $\vec{e}p^T \rightarrow eX$ $\vec{e}\vec{D} \rightarrow eX$ $\vec{e}D^T \rightarrow eX$	A_1^P, g_2^p, moments A_1^n , g_2^n, moments	Low $L \rightarrow$ large acc. Pol. targets
SEMI-INCLUSIVE DIS New quark distribution function	$\vec{e}p(D) \rightarrow e(M, \gamma)X$ $\vec{e}\vec{p}(\vec{D}) \rightarrow e(M, \gamma)X$ $\vec{e}p^T \rightarrow e(M, \gamma)X$	PDF, TMD, $\bar{d}$, $\bar{u}$ Frag. distribution fun. Transversity	Large t coverage Low $L \rightarrow$ large acc. pol. targets
FORM FACTOR AND GPDs, and BARYONS SPECTROSCOPY	$\vec{e}D \rightarrow e(n, p)$ $\vec{e}p \rightarrow eN(\pi^0, \pi^+)$ $\vec{e}p \rightarrow eN(\eta, \pi^+\pi^-, etc)$	Neutron magnetic FF $E_{1+}/M_1+, S_{1+}/M_{1+}$ $N\Delta, NN^*$, FF	Detection of n and p Full coverage Multiparticle detection

Table 2.2: **HALL B 12 GEV PHYSICS PROGRAM SUMMARY - QCD PROPERTIES**
The color code indicates reactions that will be measured simultaneously in CLAS^{++}

PHYSICS PROGRAM	**REACTION(s)**	**PHYSICS QUANTITY**	**REQUIREMENTS**
QCD PROPERTIES			
Space-time characteristics of hadronization (DIS kinematics)	$\vec{e}\,{}^{2}H \rightarrow e\ hadron\ X$ $\vec{e}\,{}^{14}N \rightarrow e\ hadron\ X$ $\vec{e}\,{}^{56}Fe \rightarrow e\ hadron\ X$ $\vec{e}\,{}^{84}Kr \rightarrow e\ hadron\ X$ $\vec{e}\,{}^{197}Au \rightarrow e\ hadron\ X$ $hadron = \pi^0, \pi^+, \pi^-, \eta, \omega, \eta', \phi, K^+, K^-, K^0, p, \bar{p}, \Lambda, \Lambda(1520), \Sigma^+, \Sigma^0, \Xi^0, \Xi^-$	Hadronization length vs. Q^2, ν, p_T, z, hadron mass and size, and quark flavor; quark energy loss, gluon emission properties, quark-gluon correlations.	Direct hadron ID for neutral and charged hadrons; Multi-particle detection Central detector
Color transparency in coherent vector meson production	$\vec{e}\,{}^{2}H \rightarrow e\ {}^{2}H\rho$ $\vec{e}\,{}^{2}H \rightarrow e\ {}^{2}H\omega$ $\vec{e}\,{}^{2}H \rightarrow e\ {}^{2}H\phi$	Onset of color transparency	Multi-particle detection charged hadron ID
Color transparency in ρ production from complex nuclei	$\vec{e}\,{}^{2}H \rightarrow e\ \rho\ X$ $\vec{e}\,{}^{14}N \rightarrow e\ \rho\ X$ $\vec{e}\,{}^{56}Fe \rightarrow e\ \rho\ X$	Color transparency at fixed coherence length	Multi-particle detection charged hadron ID
Color transparency in quasielastic scattering	quasielastic e,e'p on ${}^{2}H, {}^{14}N, {}^{56}Fe, {}^{84}Kr, {}^{197}Au$	Color transparency	Multi-particle detection
Structural modifications of bound nucleons	$\vec{e}\,{}^{2}H \rightarrow e\ p\ X$	Structure function of bound neutrons	Multi-particle detection Central detector

Table 2.3: **CLAS^{++} PROGRAM SUMMARY - PHYSICS NEAR REAL PHOTON LIMIT**
The color code indicates reactions that will be measured simultaneously.

PHYSICS PROGRAM	**REACTION(s)**	**OBSERVABLES**	**REQUIREMENTS**
MESON SPECTROSCOPY	$``\vec{\gamma}''^4He \rightarrow^4 He\pi^0\eta(\eta\prime)$ $''\vec{\gamma}''p \rightarrow p(n\pi)$ $''\vec{\gamma}''p \rightarrow p(n\pi k)$	Search for $J^{pc} = 1^{-+}$ exotics	-Forward angle electron detector -Large acceptance for photons -Thin target for low energy recoils -Lage acceptance for multi-pions and kaons
LARGE ANGLE COMPTON SCATTERING	$''\vec{\gamma}''p \rightarrow p\pi^0$	Pion GPDs	-Forward angle electron detector -Large acceptance for photons

Chapter 3

The Physics Program at 12 GeV

3.1 Deeply Exclusive Scattering and Generalized Parton Distributions

Hard scattering processes play an important role in the understanding of the quark and gluon structure of hadrons. The important feature of hard reactions is the possibility to separate the perturbative (short distance) and non-perturbative (long distance) stages of the interaction. Simply, a hard probe creates a small-size quark, antiquark, and gluon configuration that weakly interacts (the asymptotic freedom of QCD), and whose interactions can be described by means of perturbation theory. The non-perturbative stage of such a reaction describes the response of the remaining system to this configuration, or how the small size configuration evolves into hadrons.

This so-called factorization property has been successfully used (*e.g.* in Deep Inelastic Scattering (DIS) of leptons) for studying the internal structure of the nucleon. The *inclusive* scattering of high-energy leptons off the nucleon in the Bjorken regime ($Q^2, \nu \to \infty$ and $x_B = \frac{Q^2}{2M\nu}$ finite) led to the discovery of the quark and gluon substructure of the nucleon, with the quarks and gluons each carrying about half of the nucleon's momentum. Furthermore, *polarized* DIS revealed that about 25% of the spin of the nucleon is carried by the quarks. Now, with the advent of the new generation of high-energy, high-luminosity lepton accelerators, combined with large-acceptance spectrometers, a wide variety of *exclusive* processes in the Bjorken regime will become accessible experimentally. Until recently, very few exclusive processes could be treated in the framework of pQCD and compared to experimental data (typical examples are the $\pi^0\gamma\gamma^*$ transition form factor and the elastic form factors of the pion and the nucleon). Fundamental information on the structure of the nucleon has been obtained from such analyses, from the shape of light-cone meson wave functions (or distribution amplitudes) to the scale of the intrinsic transverse momentum of the partons in the nucleon (or Fermi motion), Sudakov effects, etc.

The recently developed formalism of a QCD description of Deeply Virtual Compton Scattering (DVCS) [8, 10] and Deeply Exclusive Meson Production [36], provides a framework that allows one to enlarge these type of exclusive processes. Here, the non-perturbative nucleon structure part is parameterized at the amplitude level via Generalized Parton Distributions (GPDs). The GPDs contain information on quark/antiquark correlations, and on their transverse and angular momentum distributions. GPDs provide a unifying picture for an entire set of fundamental quantities parameterizing information on hadronic structure, such as nucleon form factors (which are related to matrix elements of vector and axial vector currents), polarized and unpolarized parton distributions, and the contributions to the spin of the nucleon due to orbital excitations of quarks and gluons.

The complete extraction of the GPDs requires an extensive program rather than a single experiment, involving the measurement of a variety of channels and observables over a broad kinematic range. A global analysis will be required to extract the GPDs from a large set of measurements.

The field is currently expanding rapidly on the theoretical side (for recent reviews see [37, 38]). Experimental facilities such as COMPASS, HERMES, and JLAB at 6 GeV are conducting exploratory studies of GPDs. However, due to either luminosity (HERMES, COMPASS) or beam energy (JLab at 6 GeV) limitations, a full program with, ultimately, a complete de-convolution of the GPDs, cannot be carried out at these existing facilities.

The goal is to simultaneously measure the Q^2, x_B, and t dependencies of cross sections and beam/target spin asymmetries for a wide variety of exclusive channels. These observables involve the leading-order pQCD amplitudes which can be analyzed directly in the GPD formalism. This program requires:

- high energy to reach high enough Q^2 and a large x_B range,
- high luminosity to compensate for the fast drop of exclusive cross sections with increasing Q^2 and hadronic center-of-mass energy,
- good detector resolution to identify exclusive channels,
- large acceptances for charged and neutral particle detection to measure various channels over a large kinematical range.

JLab at 12 GeV with the proposed CLAS^{++} detector will meet these basic requirements. The program presented here is the first to explore this new GPD domain of hadronic physics in a systematic fashion.

3.1.1 Phenomenology of the GPDs

It has been shown [8, 10] that in leading-order pQCD, the Deeply Virtual Compton Scattering amplitude in the forward direction can be factorized into a hard-scattering part (exactly calculable in pQCD), and a non-perturbative nucleon structure part as illustrated in Fig. 3.1a. A QCD factorization proof has also been given for hard exclusive meson production with longitudinally polarized photons [36], Fig. 3.1b. In these so-called "handbag" diagrams, the lower blob represents the structure of the nucleon which can be parameterized at leading twist in terms of four structure functions, i.e. GPDs.

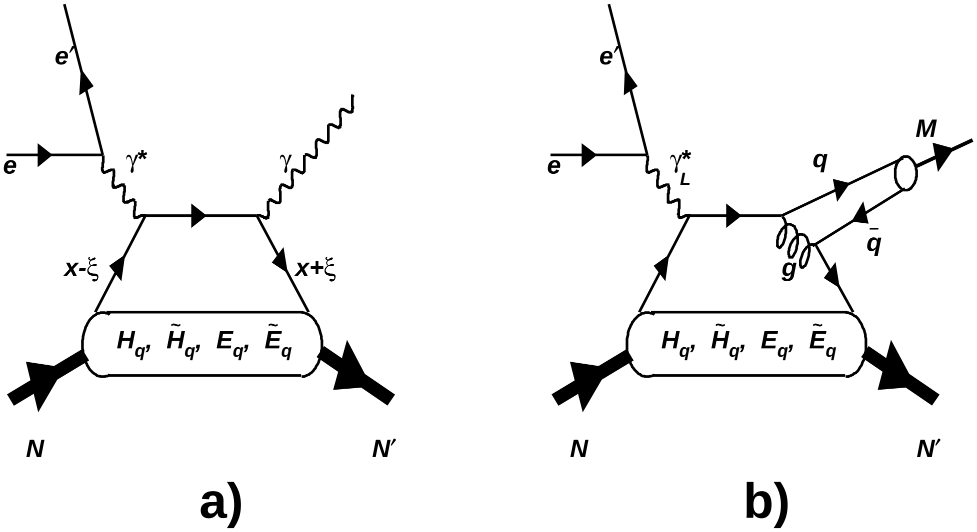

Figure 3.1: "Handbag" diagrams for: (a) DVCS, (b) meson production.

On the light-cone the non-perturbative amplitude (represented by the lower blobs in Fig. 3.1)can parameterize at leading twist as [37]:

$$
\begin{aligned}
&\frac{P^+}{2\pi}\int dy^- e^{ixP^+y^-}\langle p^{'}|\bar{\Psi}^q_\beta(-\frac{y}{2})\Psi^q_\alpha(\frac{y}{2})|p\rangle\Big|_{y^+=\vec{y}_\perp=0} \\
&= \frac{1}{4}\Big\{(\gamma^-)_{\alpha\beta}\Big[H^q(x,\xi,t)\;\bar{N}(p^{'})\gamma^+N(p)\;+\;E^q(x,\xi,t)\;\bar{N}(p^{'})i\sigma^{+\kappa}\frac{\Delta_\kappa}{2M_N}N(p)\Big] \\
&+\;(\gamma_5\gamma^-)_{\alpha\beta}\Big[\tilde{H}^q(x,\xi,t)\;\bar{N}(p^{'})\gamma^+\gamma_5N(p)\;+\;\tilde{E}^q(x,\xi,t)\;\bar{N}(p^{'})\gamma_5\frac{\Delta^+}{2M_N}N(p)\Big]\Big\} \qquad (3.1)
\end{aligned}
$$

where Ψ^q is the quark field operator of flavor q, N is the nucleon spinor, and M_N the nucleon mass. The variables p and p' are the initial and final nucleon momenta, and $P = (p + p')/2$. The GPDs are termed H^q, $\tilde{H}^q$, E^q, and $\tilde{E}^q$, and depend upon three kinematic variables: x, ξ, and t. The variable ξ is the longitudinal momentum fraction of the transfer $\Delta = p' - p$ with $2\xi^1 \to x_B/(1 - x_B/2)$ in the Bjorken limit,

---

[1] $\xi = x_B\frac{1+\frac{Delta^2}{2Q^2}}{2-x_B+x_B\frac{Delta^2}{2Q^2}}$

and $t = \Delta^2$ is the overall momentum transfer in the process. x is the momentum fraction of the struck quark in the quark loop and, as such, is not directly accessible experimentally. One can identify two regions for the GPDs : when $x > \xi$ both partons represent quarks, whereas for $x < -\xi$ both partons represent antiquarks. In these regions, the GPDs are the generalizations of the usual parton distributions from DIS. H^q and E^q are spin-independent, and $\tilde{H}^q$ and $\tilde{E}^q$ are spin-dependent functions. There are sets of GPDs for each quark flavor q.

In the forward limit ($\Delta \to 0$), the GPDs H and $\tilde{H}$ reduce to the quark density distribution $q(x)$ and quark helicity distribution $\Delta q(x)$ respectively, obtained from DIS :

$$H^q(x,0,0) = \begin{cases} q(x), & x > 0\,, \\ -\bar{q}(-x), & x < 0\,. \end{cases} \tag{3.2}$$

$$\tilde{H}^q(x,0,0) = \begin{cases} \Delta q(x), & x > 0\,, \\ \Delta\bar{q}(-x), & x < 0\,. \end{cases} \tag{3.3}$$

The functions E and $\tilde{E}$ are not measurable through DIS because the associated tensors in Eq. (3.1) vanish in the forward limit ($\Delta \to 0$). Therefore, E and $\tilde{E}$ are new leading-twist functions which are only accessible through hard exclusive electroproduction reactions. Similarly, the region $-\xi < x < \xi$ is absent in DIS which corresponds to the limit $\xi \to 0$. In this region, the GPDs behave like a meson distribution amplitude, and contain completely new information about the nucleon structure.

Furthermore, at finite momentum transfer, there are model-independent sum rules that relate the first moments of these GPDs to the standard elastic form factors:

$$\int_{-1}^{+1} dx\, H(x,\xi,t) = F_1(t)\,, \tag{3.4}$$

$$\int_{-1}^{+1} dx\, E(x,\xi,t) = F_2(t)\,, \tag{3.5}$$

$$\int_{-1}^{+1} dx\, \tilde{H}(x,\xi,t) = g_A(t)\,, \tag{3.6}$$

$$\int_{-1}^{+1} dx\, \tilde{E}(x,\xi,t) = h_A(t)\,, \tag{3.7}$$

where $F_1(t)$ and $F_2(t)$ represents the elastic Dirac and Pauli form factors, respectively, while g_A is the axial vector, and h_A is the pseudoscalar form factor.

Also as Ji [8] pointed out, there is a sum rule that relates the second moment of the quark helicity-independent GPDs to the fraction of the nucleon spin (J) carried by the sum of the quark spin and orbital angular momentum:

$$\int_{-1}^{1} dx\; x\;\left(H(x,\xi) + E(x,\xi)\right) = 2J\,. \tag{3.8}$$

This sum rule, combined with DIS data on the helicity distributions, will allow us to identify how the nucleon spin is distributed among its constituents, and shed light on the "spin-puzzle".

The GPDs reflect the structure of the nucleon; they are independent of the reaction that probes the nucleon, and therefore provide a unified description of a wide variety of inclusive and exclusive hard processes.

3.1.2 Revealing GPDs

From a phenomenological point of view, the extraction of the GPDs from data is not a simple task. It requires an extensive experimental program and detailed analyses with controlled theoretical corrections. Although the field is rapidly expanding, we expect that, as a first step, phenomenological parameterization of GPDs will be used to fit the experimental data. Existing parameterizations include general constraints that are derived from DIS and form factor measurements. One of the commonly used parameterizations implements a factorized ansatz for the t-distribution, and defines the t-independent part of the GPD as a sum of two terms (e.g. for H^q):

$$H^q(x,\xi) \,=\, H^q_{DD}(x,\xi) \,+\, \theta(\xi-|x|)\,\frac{1}{N_f}\,D(\frac{x}{\xi})\,, \tag{3.9}$$

where H^q_{DD} is the part of the GPD that is obtained as a one-dimensional section of a two-variable double distribution (DD) [39]. The second term in Eq. (3.9), the so called D-term, is introduced to ensure the non-trivial properties of GPDs, the polynomiality of their Mellin moments [8]. In Figure 3.2, two models of the GPD H at $t = 0$, are presented. The two surfaces correspond to models without (left-hand surface) and with (right-hand surface) the D term in the parameterization [40]. The t-dependence of the GPD is parameterized in terms of the Dirac form factor $F_1^q(t)$ for a quark flavor q, determined through empirical parameterizations for the proton and neutron Dirac form factors:

$$H^q(x,\xi,t) \,=\, H^q(x,\xi)F_1^q(t), \tag{3.10}$$

Using such models, experimentally accessible quantities can be calculated and compared with the measurements.

GPDs enter into Compton form-factors (CFFs) as integrals over x, and therefore only ξ is accessible experimentally (neglecting the Q^2 dependence):

$$\left\{\mathcal{H},\mathcal{E},...\right\}(\xi) = \int_{-1}^{1} dx\, C^{(\pm)}(\xi,x)\left\{H,E,...\right\}(x,\eta)_{|\eta=-\xi}\,, \tag{3.11}$$

where "..." denotes similar other twist-two and twist-three GPDs. Coefficient functions $C^{(\pm)}$ read for the even and odd parity sectors:

$$\xi\, C^{(\mp)}_{(0)i}\,(\xi,x) = \frac{Q_i^2}{1-x/\xi-i0} \mp \frac{Q_i^2}{1+x/\xi-i0}\,. \tag{3.12}$$

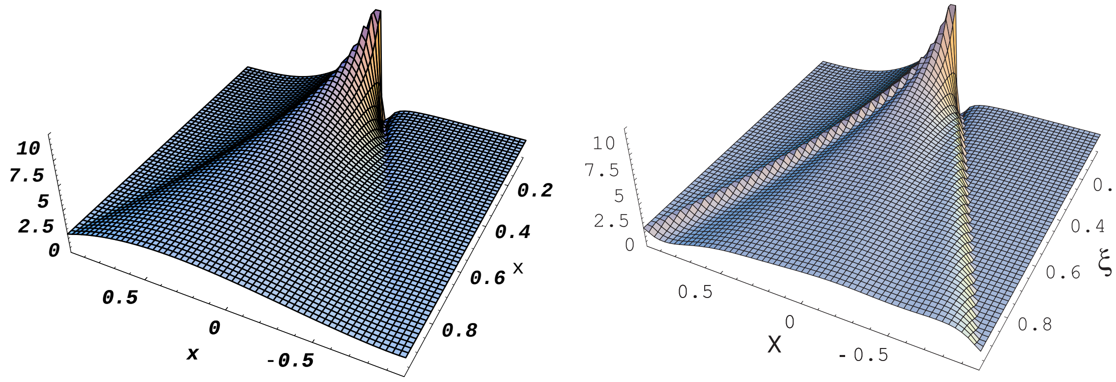

Figure 3.2: Model calculations of the GPD H as a function of ξ and x at $t = 0$. The left-hand surface is a model without the D-term in the t-independent part of the parameterization. The right-hand surface includes the D-term in the parameterization [40]. DIS measures a line at $\xi = 0$, distribution for $x > 0$ corresponds to quarks and for $x < 0$ corresponds to antiquarks.

Measurements of cross sections alone are not sufficient to experimentally map out the surface shown in Figure 3.2. It is important to also measure spin observables. For example, the beam spin asymmetry in DVCS allows access to the imaginary part of the amplitude proportional to the GPDs at the $x = \xi$ point, $H(\xi, \xi, t)$ for instance. A combination of these, and other observables, such as target spin asymmetries, beam charge asymmetry, angular asymmetries of lepton pair in heavy, time-like photon production will be needed to fully constrain the GPDs.

Quark flavor separation of GPDs requires systematic studies using both proton and neutron (deuterium) targets, and measurements of the production of different meson species. Reactions with vector or scalar mesons in the final state are sensitive to unpolarized (H and E) or polarized ($\tilde{H}$ and $\tilde{E}$) GPDs, respectively.

The modified CLAS detector in Hall B with the 12 GeV CEBAF accelerator is an ideal place to conduct systematic studies of exclusive production of photons and mesons in hard scattering processes. In Figure 3.3 the kinematical coverage in Q^2 and x_B is shown for an upgraded CLAS with an 11.5 GeV electron beam. In the range of high x_B, 0.1 to 0.6, not reachable at any other facility, one can cover the range of Q^2 up to 8 $(\mathrm{GeV/c})^2$.

3.1.3 Deeply Virtual Compton Scattering

DVCS is the cleanest tool for constraining GPDs from experimental data. Presently DVCS is in the most advanced stage of theoretical studies compared with other deep exclusive reactions. The DVCS amplitude has been derived explicitly in a light-cone framework [38] and in a parton model approach [41] up to twist-three accuracy. At the twist-two level, 8 GPDs are involved in the description of the DVCS amplitude (GPDs

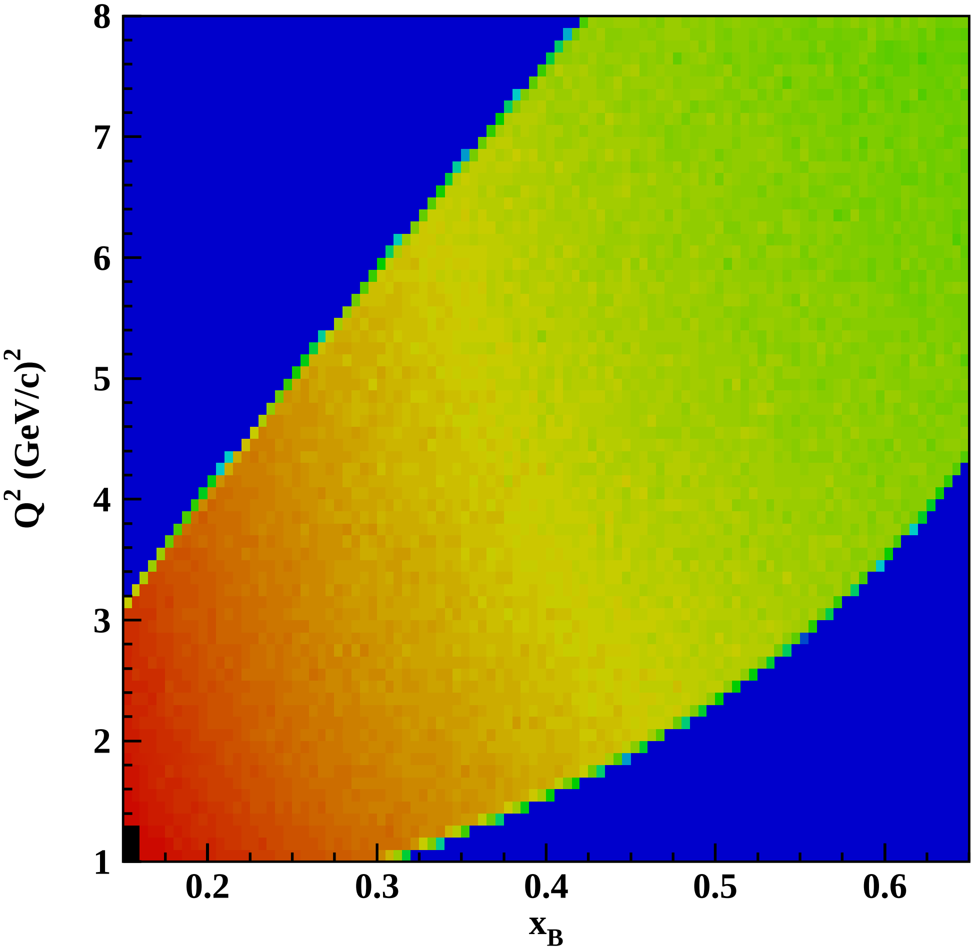

Figure 3.3: The kinematic coverage of an upgraded CLAS for an electron beam energy of 11.5 GeV for the reaction $ep \to epX$.

H^q, $\tilde{H}^q$, E^q, and $\tilde{E}^q$, and 4 new functions from the gluonic transversity distribution). It has been shown in the Wandzura-Wilczek approximation that all twist-three amplitudes can be determined by 4 twist-two GPDs [42], and at twist-three, only 4 new GPDs which correspond to antiquark-gluon-quark correlations enter in the DVCS amplitude.

The leptoproduction of a real photon has the same final state as the Bethe-Heitler (BH) process (see Figure 3.4). The experiment measures DVCS through interference with the BH process. The measured differential cross section can be written as:

$$\frac{d\sigma}{dx_{\mathrm{B}}dydtd\Phi} = \frac{\alpha^3 x_{\mathrm{B}} y}{8\,\pi\,Q^2\sqrt{1+\epsilon^2}} \left|\frac{\mathcal{T}}{e^3}\right|^2 , \tag{3.13}$$

where y is the lepton energy fraction, $y = P_1 \cdot q_1 / P_1 \cdot k$, and Φ is the azimuthal angle between lepton and hadron planes. ϵ is the polarization of the virtual photon, and e is the electron charge. In Eq. (3.13), $\mathcal{T}$ is the scattering amplitude given by:

$$\mathcal{T}^2 \ = \ |\mathcal{T}_{BH}|^2 \ + \ |\mathcal{T}_{DVCS}|^2 \ + \mathcal{I} \, , \tag{3.14}$$

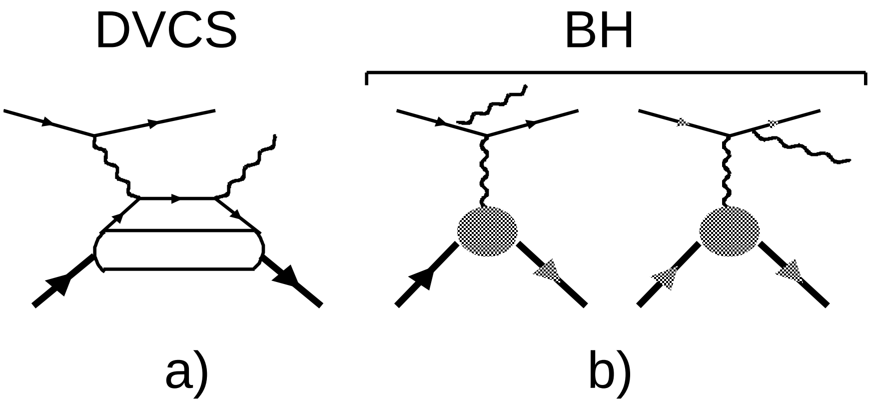

Figure 3.4: Feynman diagrams for DVCS and Bethe-Heitler processes contributing to the amplitude of $ep \rightarrow ep\gamma$ scattering.

where $\mathcal{T}_{DVCS}$ and $\mathcal{T}_{BH}$ are complex amplitudes for the DVCS and BH process, and $\mathcal{I}$ is the interference term:

$$\mathcal{I} \;=\; \mathcal{T}^{*}_{DVCS}\mathcal{T}_{BH} \;+\; \mathcal{T}_{DVCS}\mathcal{T}^{*}_{BH}\,. \tag{3.15}$$

In Ref. [38] the cross section for the hard leptoproduction of a real photon off the nucleon is derived for all possible hadron and lepton polarizations involved. Each component in the cross section is intriduced in terms of sum of Fourier moments in the azimuthal angular dependence[2]. The interference term, $\mathcal{I}$, is the most interesting quantity since it contains linear combination of GPDs, the Fourie decomposition has a for:

$$\mathcal{I} = \mathcal{K}\cdot\left\{c_0^{\mathcal{I}} + \sum_{n=1}^{3}\left[c_n^{\mathcal{I}}\cos(n\phi) + s_n^{\mathcal{I}}\sin(n\phi)\right]\right\}\,, \tag{3.16}$$

where $\mathcal{K}$ is a kinematic parameter. The coeficents $c_0^{\mathcal{I}}$, $c_1^{\mathcal{I}}$ and $s_0^{\mathcal{I}}$ arise at the twist-two level. The additional angular dependance, i.e., c_1^{DVCS}, s_1^{DVCS}, $c_2^{\mathcal{I}}$, and $s_2^{\mathcal{I}}$ is given in terms of twist-three GPDs. The moments $c_3^{\mathcal{I}}$ and $s_3^{\mathcal{I}}$ arise from the twist-two double helicity-flip gluonic GPDs alone.

These moments can be extracted from the measurements of beam (longitudinal) and/or target (longitudinal, transverse) spin asymmetries, and the lepton beam charge asymmetry.

Beam single spin asymmetry

Experimentally, the simplest observable to measure is the beam single spin asymmetry where only the imaginary part of the DVCS amplitude and the interference term, proportional to the beam helicity, survive. In the Fourier decomposition the imaginary part is presented as series of $\sin(n\phi)$ moments of the azimuthal angle, with $n = 1, 2, 3$. In the interference term the leading $\sin(\phi)$ moment, s_1, arises at the twist-two level,

---

[2] Azimuthal angle, ϕ, is the angle between lepton and hadron planes.

while sin(ϕ) moment in the DVCS amplitude squared and sin(2ϕ) moment in the interference term arise at the twist-three level and are suppressed by 1/Q. $s_1^{\mathcal{I}}$ has a linear dependence on imaginary part of CFFs:

$$s_1^{\mathcal{I}} \sim Im\left(F_1\mathcal{H} + \frac{x_{\rm B}}{2-x_{\rm B}}(F_1+F_2)\widetilde{\mathcal{H}} - \frac{\Delta^2}{4M^2}F_2\mathcal{E}\right) \tag{3.17}$$

where $F_1(t)$ and $F_2(t)$ represents the elastic Dirac and Pauli form factors, respectively.

The ongoing theoretical efforts are supported by recent experimental results on the beam spin asymmetry [13, 43] and cross section measurements [44]. The CLAS measurement [13] at 4.2 GeV is the first fully exclusive experimental result on DVCS. In Fig.3.5, the experimentally measured ϕ asymmetry is presented together with theoretical calculations from Ref. [38]. The most intriguing physics outcome of this measurement is the smallness of the amplitude of the sin(2ϕ) component, indicating that higher-twist contributions are small. The comparison with model calculations also shows the importance of antiquark-gluon-quark ($\bar{\rm q}$Gq) GPDs.

In Ref.[13] the number of single photon final states was extracted from the analysis of the shape of the missing-mass spectra in the reaction $ep \to epX$. At higher energies the missing-mass technique, though still useful, will be insufficient to fully separate single photon and π^0 production if only the scattered electron and recoil proton are detected. Detection of a photon will be required for the identification of the DVCS process. The main background will still be from π^0 events. A combination of cuts on missing mass and missing momentum of the $ep\gamma$ system will be used to suppress pion contamination.

The CLAS^{++} detector will have much larger coverage for photons than existing CLAS detector. This enhanced capability to detect photons will play an important role in reducing the background from π^0 production by effectively vetoing $\pi^0 \to \gamma\gamma$ events.

The DVCS cross section and spin asymmetries will be measured over the full range of kinematics, as shown in Fig.3.3, and in a large number of kinematical bins simultaneously. In Fig.3.6, the data points and a choice for possible binning of the future data are presented. In the figure, simulated data on the beam spin asymmetry in the reaction $\vec{e}p \to ep\gamma$ are shown in 56 bins of x_B, Q^2, and t (total of 1064 points). The outer horizontal scale corresponds to the x_B range, divided into 4 bins, shown by the solid lines. The outer vertical scale represents the Q^2 range of the data. Larger bins at higher Q^2 are necessary to compensate for the fast drop of cross section. In each bin of Q^2 and x_B, several bins on t are shown. The average value of $-t$ is shown in the upper corner of each plot.

The leading-order amplitudes that are directly proportional to linear combination of GPDs will be defined as sin($\phi_{\gamma\gamma*}$) moments of the measured distributions. In Fig.3.7 the sensitivity of such measurements to the models at $x_B = 0.35$ and $-t = 0.3$ (GeV/c)^2 for $Q^2 = 2.75$ (GeV/c)^2 (Fig.3.7.a) and $Q^2 = 5.4$ (GeV/c)^2 (Fig.3.7.b) are

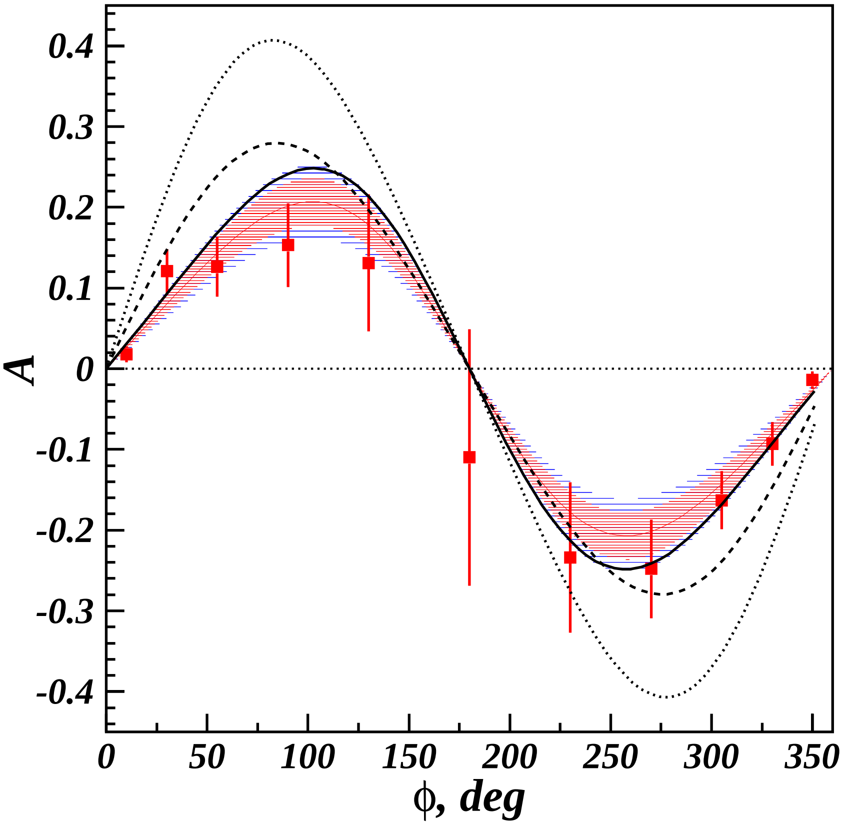

Figure 3.5: The beam spin asymmetry as a function of azimuthal angle measured in the reaction $\vec{e}p \rightarrow ep\gamma$ at a beam energy 4.25 GeV using the CLAS detector. The red shaded region corresponds to a fit to the data with $\sin\phi$ moment of 0.202 including statistical errors, the blue shaded region includes systematic uncertainties, added linearly to the statistical uncertainties. The curves are model calculations from Ref. [38].

shown. Data are simulated assuming 2000 hours of running at a luminosity of 10^{35} cm^{-2} sec^{-1} with an upgraded CLAS detector. Error bars include statistical errors only. As input to the simulation, cross sections calculated by Ref. [45] based on Ref. [46] have been used. The different curves in the figure correspond to different model assumptions. The dashed curve assumes no ξ dependence in the parameterization of GPDs [47], the solid curve has a ξ dependence, and also accounts for valence (b_{val}) and sea (b_{sea}) quark contributions. One sees that there is sufficient resolution to separate the models at both Q^2 values.

DVCS in Polarized Target Measurements

In the case of the four Compton Formfactors (CFFs) $\mathcal{F} = \{\mathcal{H}, \mathcal{E}, \widetilde{\mathcal{H}}, \widetilde{\mathcal{E}}\}$ there are eight observables given by the first harmonics $\cos(\phi)$ and $\sin(\phi)$ of the interference term, which are accessible away from the kinematical boundaries in polarized beam and target experiments. Thus, experiments with both longitudinally and transversely polarized target can measure all eight Fourier coefficients $c^{\mathcal{I}}_{1,\Lambda}$ and $s^{\mathcal{I}}_{1,\Lambda}$ and, thus, also

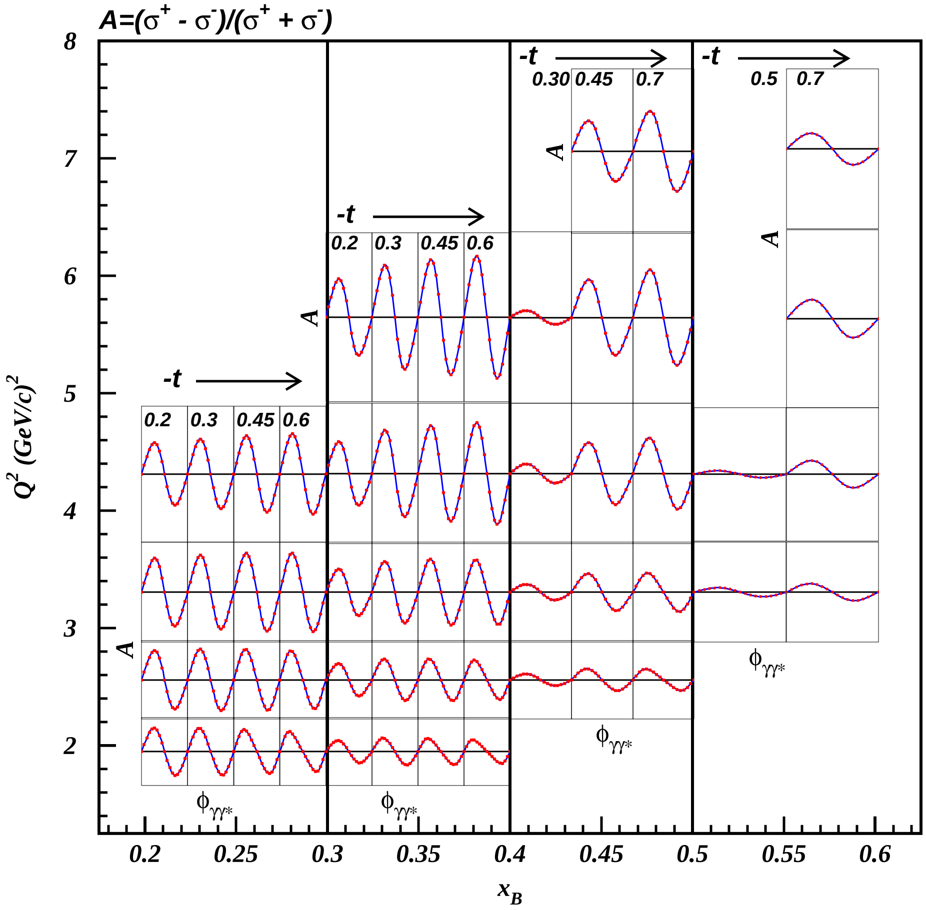

Figure 3.6: Kinematical coverage for $\vec{e}p \rightarrow ep\gamma$ beam spin asymmetry measurements in DVCS. Possible binning of future data is shown. The outer horizontal scale corresponds to the x_B range, divided into 4 bins. The outer vertical scale represents the Q^2 range. Larger bins at higher Q^2 compensate for the fast drop of cross section. Each histogram is a beam spin asymmetry distribution as a function of $\phi_{\gamma\gamma*}$ for a certain t bin. The average value of $-t$ is shown in the upper corner of each plot.

$\Re\text{e}/\Im\text{m}\,\mathcal{C}^{\mathcal{I}}_{\Lambda}$ with $\Lambda = \{\text{unp}, \text{LP}, \text{TP}_x, \text{TP}_y\}$. Knowing these $\mathcal{C}$ functions, we can invert them to obtain the CFFs:

Consequently, the four Fourier coefficients $c^{\mathcal{I}}_{0,\Lambda}$ as well as the four twist-two DVCS coefficients $c^{\text{DVCS}}_{0,\Lambda}$ can serve as experimental consistency checks. Alternatively, they can be used to extract CFFs. Thus, experiments with longitudinally polarized target have the potential to extract the real part of all four CFFs as well as two linear combinations of their imaginary parts from the interference term alone.

Numerical estimates for the nucleon spin asymmetry, A_{UL}, have been done in Ref. [38]. In Figure 3.8 two surfaces, corresponding to two models of GPDs, are presented. The distribution on the left includes twist-two and twist-three GPDs in the Wandzura-Wilczek parameterization [42], and the distribution on the right is the same parameterization with antiquark-gluon-quark correlations. At the kinematics

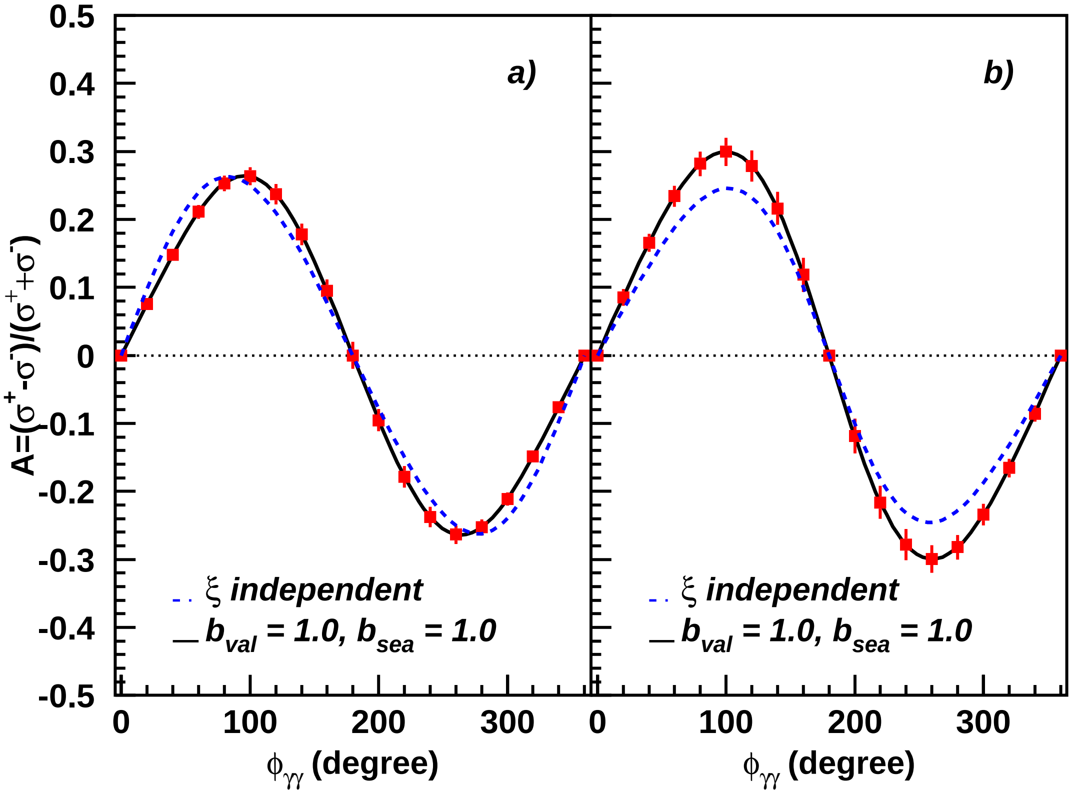

Figure 3.7: Expected data for the $\vec{e}p \rightarrow ep\gamma$ beam spin asymmetry at $x_B = 0.35$ and $-t = 0.3$ (GeV/c)^2, and a) $Q^2 = 2.75$ (GeV/c)^2 and b) $Q^2 = 5.4$ (GeV/c)^2. Only the expected statistical errors are shown. Data are simulated assuming 2000 hours of running at a luminosity of 10^{35} cm^{-2} sec^{-1} with the upgraded CLAS detector. Calculations according to [45] (see text for explanations).

accessible with a 12 GeV beam the asymmetry is found to be 35% at Q^2 $= 2\ (GeV/c)^2$ and decreases with increasing Q^2.

DDVCS : Deeply Double Virtual Compton Scattering

The DDVCS process is the extension of the DVCS reaction to the regime where the final state photon is *virtual* (time-like) instead of being real, and therefore decays into a lepton pair. The motivation for studying this reaction lies in the fact that it gives direct access to the GPDs. One drawback in the GPD study through "standard" DVCS or exclusive meson electroproduction is that one accesses, in general, GPDs integrated over x, or at a specific point, $x = \xi$ (i.e., so one measures directly, in a concise notation, $H(\xi, \xi, t)$ for instance), which is certainly an important gain of information, but clearly not sufficient to map out the GPDs independently in the

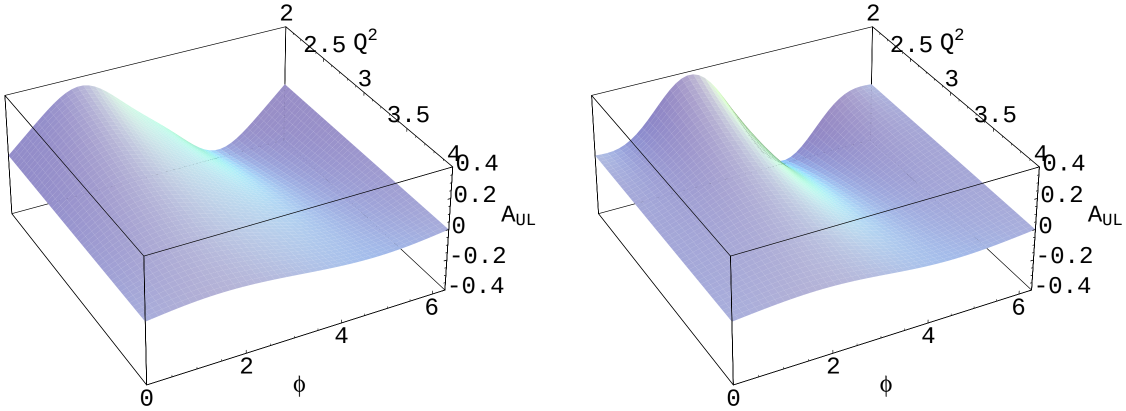

Figure 3.8: Nucleon spin asymmetry as a function of ϕ and Q^2. Surface on the left includes twist-two and twist-three GPDs in the WW-parameterization, and on the right is the same parameterization with antiquark-gluon-quark contribution.

three variables (x, ξ, t). It is, therefore, a non-trivial task to actually extract the GPDs from the experimental observables. In the absence of any model-independent "deconvolution" procedure at present, one will therefore have to rely on some global model fitting procedure.

DDVCS provides a way around this because the virtuality of the final state photon can now be varied, by measuring the invariant mass of the decay lepton pair, which yields an additional lever arm. Figure 3.9 illustrates this, where the *plus*-components of the longitudinal momentum fraction of the quarks and photons are indicated. In the DDVCS case, the kinematics of the two photons (incoming and outgoing) is described by two variables, ξ and ξ', which can be independently varied, whereas in DVCS only ξ could be varied. It can be shown [48, 49] that with DDVCS, when one measures an observable proportional to the imaginary part of the amplitude (for instance, the beam asymmetry, like in the DVCS case, arising from the interference with the associated "time-like" Bethe-Heitler process), one will in general access, in a concise notation, $H(2\xi' - \xi, \xi, t)$. Because the three variables can now be varied independently, this will allow the GPDs to be mapped along each of the three axes.

Actually, for kinematical reasons, only a limited region in the (x, ξ) plane is accessible, as $\frac{q'^2}{Q^2}$ (where $q'^2 > 0$ is the virtuality of the outgoing photon) will always be less than 1 : $0 < 2\xi' - \xi < \xi$ (see Figure 3.10). Nevertheless the gain of information on the GPDs is tremendous as no deconvolution is involved.

Figure 3.11 shows the predicted beam spin asymmetries resulting from the interference between the DDVCS and the associated Bethe-Heitler processes, for different q'^2 values at typical JLab kinematics.

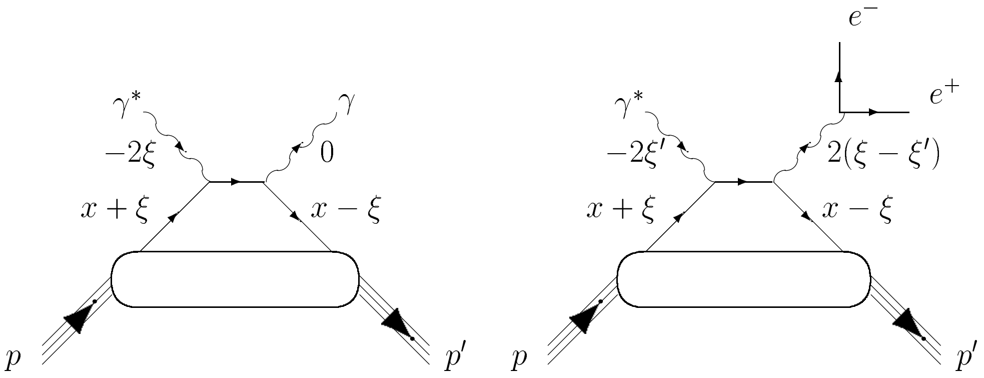

Figure 3.9: "Handbag" diagrams for DVCS (left) and DDVCS (right). The +-component of the longitudinal momentum fractions of the quarks and photons are indicated on the figure. For DVCS, this component is zero for the outgoing <u>real</u> photon whereas it is non-zero for the DDVCS case.

The downside of the DDVCS process is the very low cross sections involved. Indeed, due to the extra $\alpha_e \approx 1/137$ coupling introduced by the decay of the outgoing photon into the lepton pair, the cross section is about a factor 300 [48] less than the DVCS process at $q'^2 \approx 0.3$ GeV^2 for instance. One should tend explore the q'^2 region away from the ρ pole, i.e $q'^2 \approx 0.6$ GeV^2, since the ρ can also decay into lepton pairs and "spoil" the interpretation of the data. The first estimates from Ref. [48] seems to show that the most favorable region for q'^2 is up to 0.3 (GeV/c)^2 where asymmetry is in the range 0.25 to 0.35.

Experimentally, the idea is to concentrate on e^+e^- pairs, as the identification of positrons or electrons is rather straightforward with the CLAS Electromagnetic Calorimeters and Cherenkov counters, compared to muon pairs. Detecting the initial scattered electron, the recoil proton, and the decay positron, and requiring the missing mass $e'pe^+X$ to be consistent with 0 (the electron mass) will cleanly select the reaction. There is already first evidence that this final state has been identified in current 4.2 GeV CLAS data. In Figure 3.12 the missing-mass squared distribution for selected events in the reaction $e^-p \rightarrow e^-pe^+X$ is presented. The peak near "0" corresponds to missing electrons. In Figure 3.13 the invariant mass distribution of (e^+e^-) pairs is shown, after a cut on the missing mass on previous graph, to select electrons. It clearly shows a peak at "0" that corresponds to e^+e^- pairs from Dalitz decay of π^0s, and from photons. A broad peak around 0.5 GeV^2 could correspond to the ρ^0 mass.

Again, CLAS^{++} will be able to access this fundamental reaction and therefore yield direct access to the GPDs in a unique way.

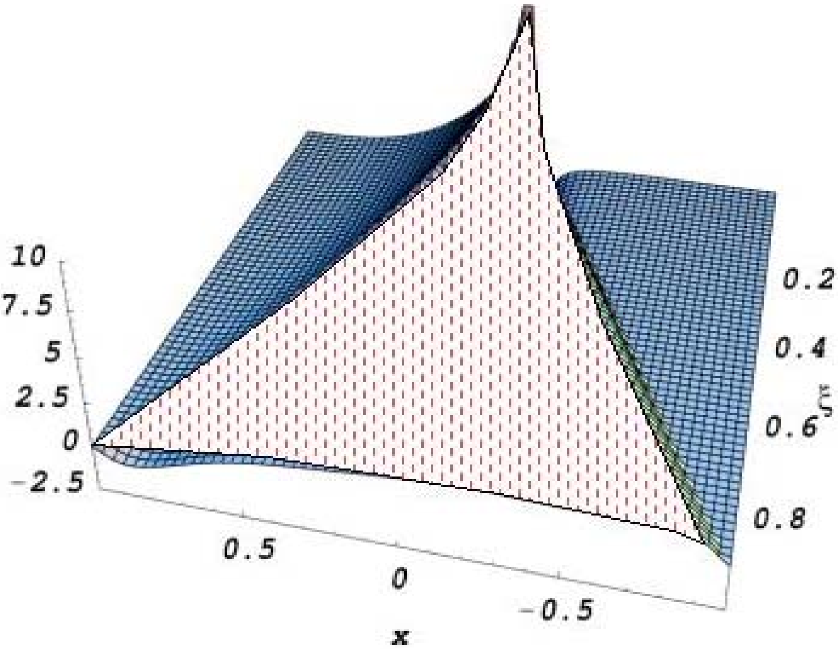

Figure 3.10: Modeling of the shape of the H GPD in the (x, ξ) plane [37]. The "hatched" region represents what is accessible with DDVCS due to the kinematical constraint $q'^2/Q^2 < 1$.

Timelike Compton scattering

As was shown above, the spin asymmetries in DVCS give access to the imaginary part of the scattering amplitude, and therefore to GPDs at the point $x = \xi$. Additionally, a broader surface can be mapped out in the double DVCS process. The real part of the amplitude is not accessible in the spin observables, and it enters in the cross section in the form of integrals of GPDs along x. One of the important aspects of measuring the real part is the sensitivity to the D-term introduced in the modeling of GPDs [39, 40]. In DVCS the real part of the amplitude can be accessed in the measurement of a lepton beam charge asymmetry, which is proportional to the real part of the Bethe-Heitler DVCS interference term [50]. This requires the existence of lepton beams with both polarities. Very recent HERMES data on the beam charge asymmetry [51] shows a positive asymmetry on the order of 0.1. Although the reaction channel is not exclusive and the statistical errors are large, the obtained asymmetry shows the importance of the D-term in the parameterization of GPDs.

The information on the real part of the scattering amplitude can also be obtained from photoproduction of heavy lepton pairs (see Figure 3.14). This process, called Timelike Compton Scattering (TCS), is an inverse process to DVCS and shares many features of DVCS. In the case of TCS, the BH process also contributes at the amplitude level, and therefore linear combinations of GPDs can be accessed through BH-TCS interference. Detailed evaluation of the TCS process is done in Ref. [52].

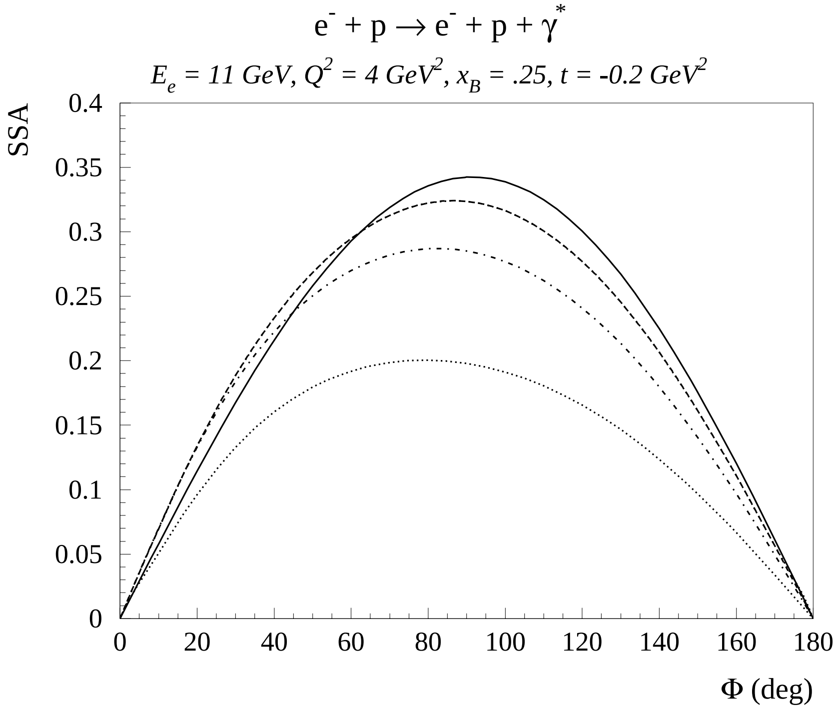

Figure 3.11: Beam single spin asymmetry (SSA) versus azimuthal angle, ϕ, for the reaction $ep \to e'pe^+e^-$ (DDVCS+Bethe-Heitler) for different virtualities of the lepton pair. Calculations from [48].

As in the case of DVCS, the experiment measures TCS in the interference with the BH process. One can measure the interference part of the amplitude in the angular distribution of the lepton pair. In the case of an unpolarized photon beam the angular harmonics are proportional to the real part of the Compton amplitude, while the use of circularly polarized photons introduces an additional term in the interference amplitude proportional to the imaginary part.

DVCS with N→ Δ

The reaction $ep \to e'\Delta\gamma$ (which we refer to as ΔVCS) is the equivalent of the DVCS process but with a Δ resonance in the final state. It has been shown recently [53] that this reaction could be interpreted as well in terms of Generalized Parton Distributions (see Figure 3.15). Like "transition" $N-\Delta$ form factors, these are "transition" $N-\Delta$ GPDs, and they are in principle different from the nucleon GPDs. The $N-\Delta$ GPDs contain the same type of information as the standard nucleon

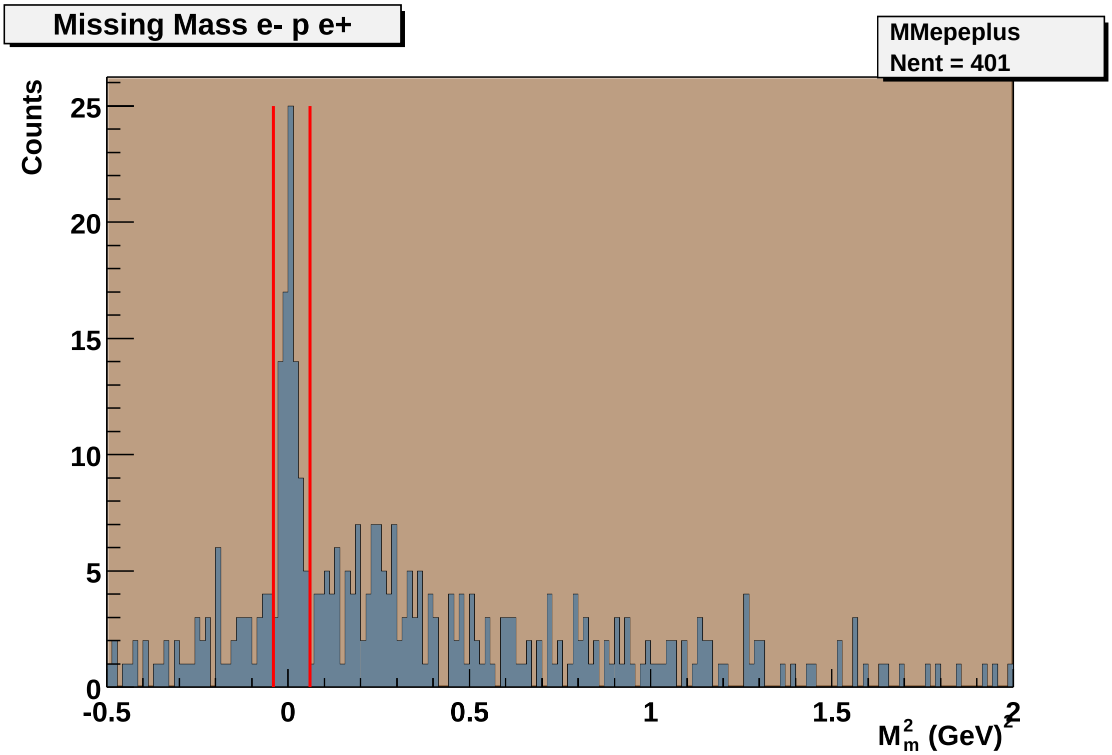

Figure 3.12: Missing-mass squared distribution in the reaction $e^-p \to e^-pe^+X$ from CLAS data at 4.2 GeV.

GPDs, i.e. the quark longitudinal and transverse momentum distributions in the Δ, their spin distribution and, potentially, similarly to Ji's sum rule, the contribution of the quarks to the orbital momentum of the Δ.

There are, at leading order and leading twist in QCD, three $N - \Delta$ GPDs, which are traditionally called : C_1, C_2, and H_M. In the large N_c limit (valid at the 30% level) and relying on SU(3), these can actually be related to the nucleon GPDs as : $C_1 \approx \tilde{H}$, $C_2 \approx \tilde{E}$, and $H_M \approx E$. On the one hand, these relations, although not extremely precise, allow one to interpret the ΔVCS reaction in terms of nucleon GPDs, and therefore access a different *flavor* combination of the GPDs. For instance, in DVCS, one accesses in general the combination $\frac{4}{9}\tilde{H}^u + \frac{1}{9}\tilde{H}^d$, whereas in ΔVCS, the combination that is accessed is the isovector part $\tilde{H}^u - \tilde{H}^d$. One can, therefore, carry out a *flavor* decomposition of the GPDs in this manner.

On the other hand, "large N_c/SU(3)" relations allow one to make numerical estimates and calculations for observables (cross sections, asymmetries,...) related to the ΔVCS process. For instance, similar to the DVCS process, the interference with the associated Bethe-Heitler mechanism, where the outgoing photon is emitted by the incoming or scattered electron, produces a beam spin asymmetry, which has been estimated by Vanderhaeghen et al. [53] (see Figure 3.16).

Recently, first evidence for the observation of the $ep \to e'\Delta\gamma$ reaction has been found in CLAS. The analysis consisted of selecting $e'n\pi^+$ final states in CLAS data

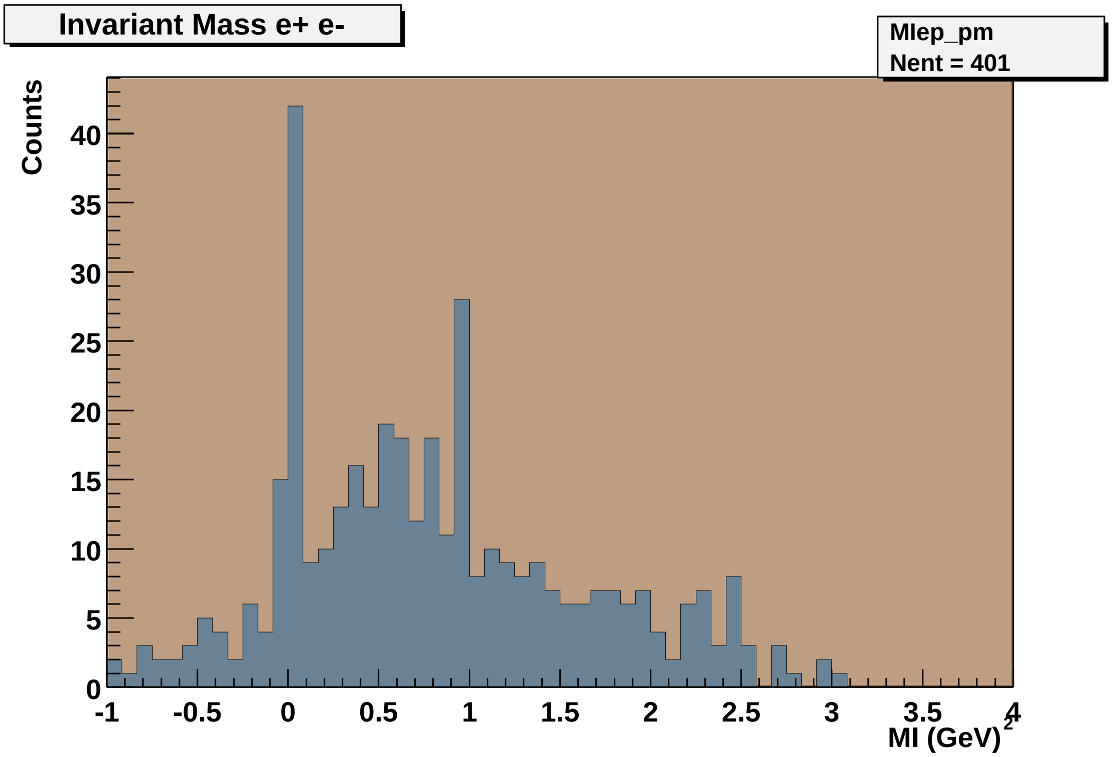

Figure 3.13: Invariant mass squared of e^+e^- pairs from CLAS data at 4.2 GeV. The peak at "0" corresponds to photons, while the broad peak around 0.5 GeV^2, corresponds to ρ^0 meson mass.

taken with a 4.2 GeV incident electron beam. Selecting events whose missing mass is around zero, to be compatible with a missing photon (see Figure 3.17-a), and imposing a $W > 2$ GeV cut so that one is above the resonance region, peaks corresponding to the Δ and also higher-mass N^* resonances clearly became visible in the $n\pi^+$ invariant mass spectrum, indicating $\Delta\gamma$ and $N^*\gamma$ final states, Figure 3.17-b. Although the statistics is currently not enough to extract a significant beam asymmetry to be compared to the theoretical calculations of Figure 3.16, the observed signals are very encouraging and call for a dedicated study.

It should be kept in mind that, like in standard DVCS, there is contamination of the ΔVCS signals by $\Delta\pi^0$ final states at this stage, as the current resolution of CLAS does not permit the separation of the two processes. The upgrade of CLAS with a high-resolution calorimeter will allow one to uniquely identify the final ΔVCS single photon. Combined with a significant increase of luminosity, this promises to provide access to clean and numerous ΔVCS and N^*VCS events. A new way to study baryon spectroscopy is opening up, with these transition N^* GPDs, where not only the t-dependence, currently accessed through the transition form factors, but also their x-dependence can be accessed. This reflects the longitudinal momentum profiles of the quarks in the N^*'s. One can speak of a 3-dimensional picture of the nucleon and its resonances.

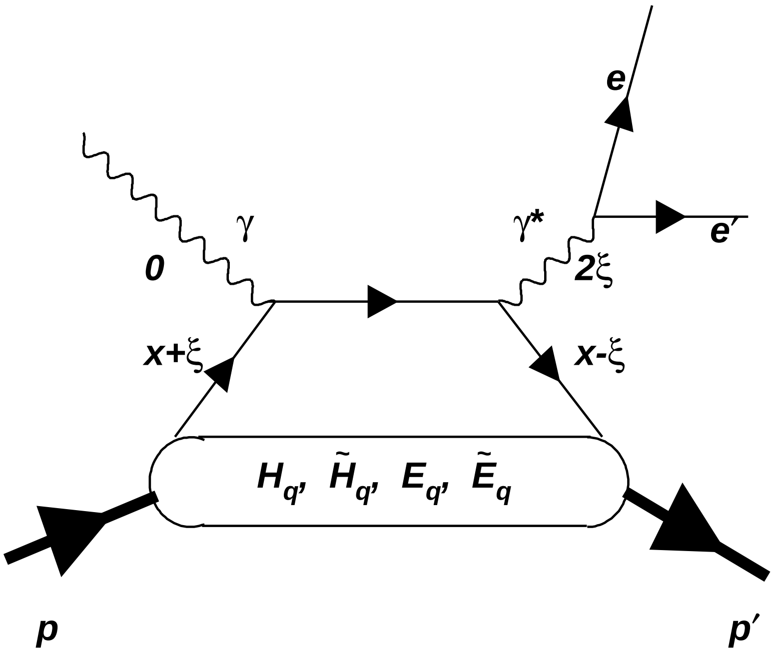

Figure 3.14: "Handbag" diagram for heavy lepton pair photoproduction, called Timelike Compton Scattering.

3.1.4 Deeply Virtual Meson Production

As shown in Ref. [36], leading-order pQCD predicts that the vector meson channels ($\rho_L^{0,\pm}$, ω_L, ϕ_L) are sensitive only to the unpolarized GPDs (H and E), whereas the pseudoscalar channels ($\pi^{0,\pm}, \eta, ...$) are sensitive only to the polarized GPDs ($\tilde{H}$ and $\tilde{E}$). The leading-order longitudinal cross section $d\sigma_L/dt$ for meson electroproduction is predicted to have $1/Q^6$ behavior, while the "soft" contributions are expected to drop with a faster $1/Q^8$ behavior. It is still uncertain at which Q^2 value one will approximately reach the scaling regime where the pQCD corrections are manageable, and therefore it is important to measure the Q^2 dependence of the forward differential cross section at fixed x_B. In any case, the way the asymptotic behavior is approached is an important source of information on pre-asymptotic effects.

One way to reduce model dependency in the corrections is to look at ratios of cross sections. Indeed, as pointed out in Refs. [36, 54], the correction factors are expected to factorize and will therefore cancel out in the ratios. Another approach to deal with pre-asymptotic corrections is the transverse spin asymmetry (TSA) for a proton target polarized perpendicular to the beam direction. TSA is less sensitive to higher-twist effects and to next-to-leading-order corrections (see Ref. [37]). The asymmetry has a linear dependence on the GPDs. This gives, for example, a unique possibility to measure the small contribution of the GPD E in vector meson production. This opens up then the possibility to extract the total angular momentum contributions

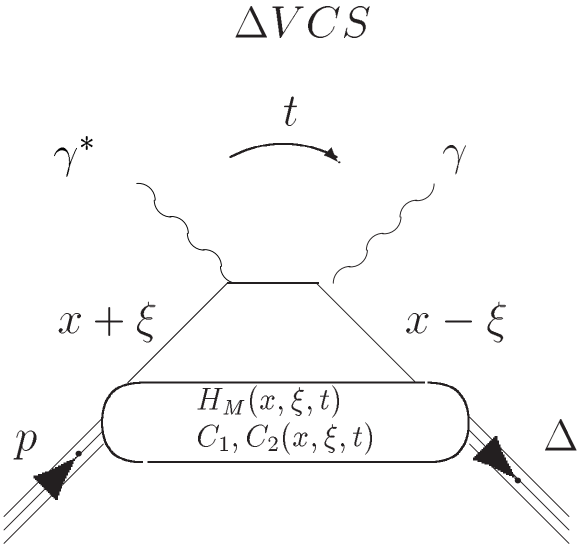

Figure 3.15: “Handbag” diagram for ΔVCS. Three “transition” GPDs contribute at leading twist to the process : C_1, C_2, and H_M. The longitudinal momentum fractions of the quarks (x, ξ) are indicated on the figure, as well as the definition of the momentum transfer t.

J^u and J^d of the u- and d-quarks to the proton spin.

Production of vector mesons

The vector meson channel is the most accessible as it allows a rather straightforward separation of the longitudinal and transverse parts of the cross section through its decay angular distribution. At large x_B the dominant contribution comes from the two-quark exchange mechanism [46, 47]. The quark exchange process can be calculated within the handbag approximation, although due to the presence of the gluon exchange (see Figure 3.1.b), large corrections are expected to the leading order.

So far only σ_L for ρ^0 production has been measured at moderate W values [55]. Calculations made in Refs. [46, 47], where corrections are modeled taking into account $k_\perp$ degrees of freedom, predict the magnitude of the cross section reasonably well. Dedicated measurements to investigate the onset of the scaling behavior of ρ_L electroproduction in the valence region ($x_B > 0.1$) are being performed with CLAS using a 6 GeV electron beam [56], where the longitudinal part of the cross section will be extracted using the angular distribution of the vector meson decay products.

The same technique for longitudinal/transverse (L/T) separation will be used also at high energies. In Figure 3.18 the results of a simulation of ρ electroproduction with an 11 GeV beam and the upgraded CLAS are presented. In the simulation it is assumed that $\sigma_T \sim 1/Q^8$ (dotted line) and $\sigma_L \sim 1/Q^6$ (dashed line). Statistical errors on the points correspond to 400 hours of beam time at a luminosity 10^{35} cm^{-2}sec^{-1}. Study of the Q^2 dependence of the separated cross sections will be a necessary step in order to understand the approach to the scaling regime. The upgraded CLAS with

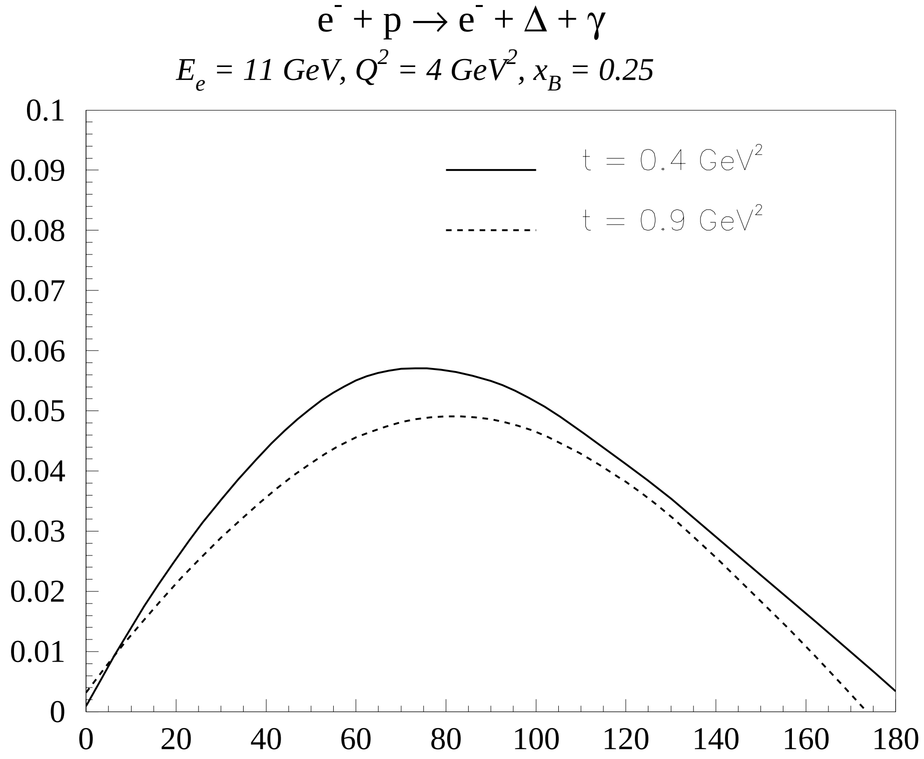

Figure 3.16: Predictions for the beam asymmetry arising from the interference of the ΔVCS and the associated Bethe-Heitler process for typical JLab kinematics. Calculations from Ref. [53].

a high energy electron beam will allow an L/T separation for Q^2 up to 8 (GeV/c)^2 for vector meson production.

Production of pseudoscalar mesons

In the case of pseudoscalar mesons, a Rosenbluth (L/T) separation is needed to extract the longitudinal part of the cross section. This will require one to combine measurements at different beam energies. The prime candidates for these studies are pion and η electroproduction. For the identification of the reaction $ep \rightarrow en\pi^+$, it is sufficient to detect the scattered electron and the π^+, while for clean identification of the reactions $ep \rightarrow ep\pi^0$ and $ep \rightarrow ep\eta$, the detection of two photons from the meson decay, in addition to the scattered electron and the recoil proton, will be necessary. In Figure 3.19 a Rosenbluth separation is simulated for the $ep \rightarrow en\pi^+$ reaction. Differential cross sections are shown as a function of Q^2, and are scaled by Q^6. The open asterisks correspond to σ_L, and the filled asterisks to σ_T. The unseparated cross section shown with the filled squares. Using results at beam energies of 6, 8, and 11 GeV, the L/T separation can be done up to $Q^2 \sim 6(GeV/c)^2$, while the unseparated

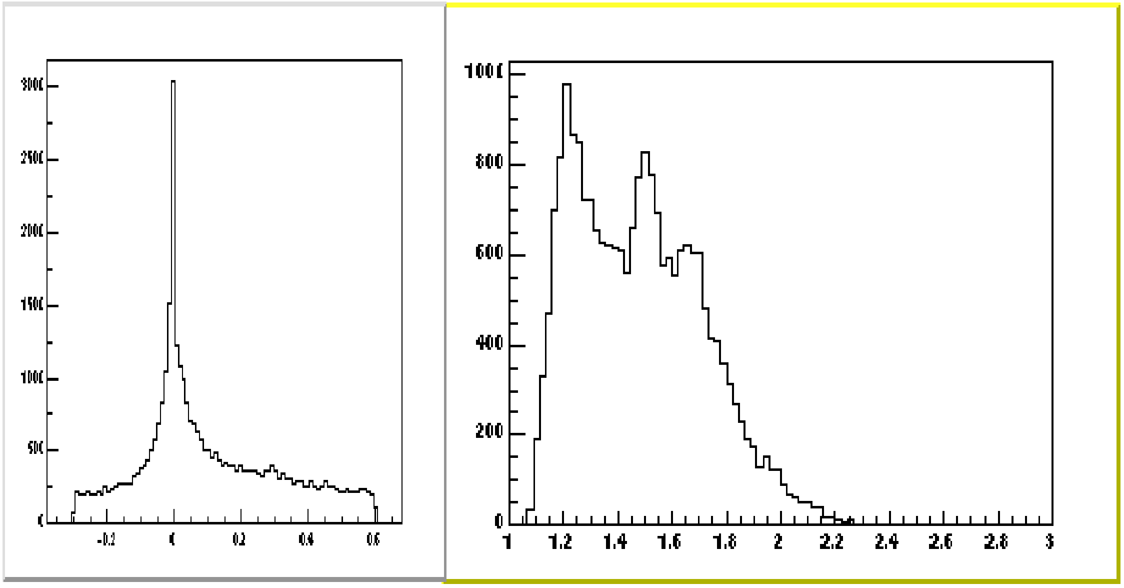

Figure 3.17: a (Left) : Squared missing-mass spectrum for $ep \to e'n\pi + X$ in GeV^2. The peak centered at ≈ 0 corresponds to missing γ's or π^0's. b (Right) : Invariant mass spectrum of the $n\pi^+$ system for $W > 2$ GeV, therefore corresponding to $\Delta(N^*)(\gamma, \pi^0)$ final states.

cross section can be measured up to much higher Q^2.

Significant suppression in hard exclusive production of pseudoscalar mesons on neutrons compared to protons was recently predicted in the GPD framework [54]. Striking differences were also predicted for the relative rates of π^0 and η production in the case of free protons and neutrons compared to coherent production off the deuteron. In addition to a simple test of GPD predictions, measurements of ratios of π^0 and η production from deuteron and proton targets will provide a unique possibility to probe $\Delta d/\Delta u$ in a model independent way from unpolarized target measurements.

Generalized Parton Distributions for $N \to \Lambda, \Sigma$ transitions

The study of hard exclusive processes with strangeness production gives access to the flavor non–diagonal GPDs [58]. The $N \to Y$ GPDs, which can be related to $N \to N$ GPDs via flavor SU(3) relations, provide a new tool for studying the non–perturbative structure of nucleon–hyperon transitions. When one writes the form factor sum rules for strangeness changing GPDs [37], one gets contributions from two additional form factors, $f_3^{N\to Y}(t)$ and $g_2^{N\to Y}(t)$, which are related to second class currents[3]. Both of these form factors are proportional to flavor SU(3) effects ($\sim m_s$) and are absent for transitions without strangeness change. The sum rules are given by:

---

[3] g_2 is often called “weak electricity”.

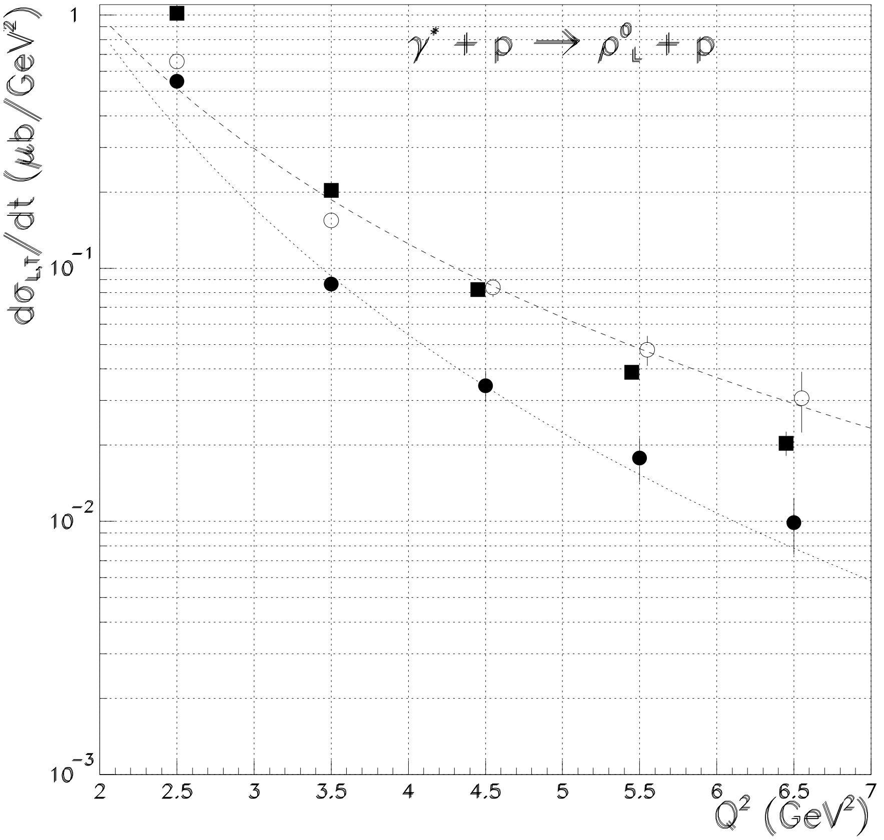

Figure 3.18: Simulation of the L/T separated cross section $d\sigma/dt$ for ρ electroproduction with an 11 GeV electron beam for 400 hours of beam time at luminosity 10^{35} cm^{-2} sec^{-1}. Black squares are the total (unseparated) cross section ($\sigma_{tot} = \sigma_T + \epsilon\sigma_L$), full circles are σ_T, decreasing like $1/Q^8$ (dotted line), open circles are σ_L, decreasing like $1/Q^6$ (dashed line).

$$\int_{-1}^{1} dx\; H^{N\to Y}(x,\xi,t) = f_1^{N\to Y}(t) - \xi\frac{m_Y + m_N}{2m_N} f_3^{N\to Y}(t) \tag{3.18}$$

$$\int_{-1}^{1} dx\; E^{N\to Y}(x,\xi,t) = f_2^{N\to Y}(t) + \xi f_3^{N\to Y}(t) \tag{3.19}$$

$$\int_{-1}^{1} dx\; \tilde{H}^{N\to Y}(x,\xi,t) = g_1^{N\to Y}(t) + \frac{m_Y - m_N}{2m_N} g_2^{N\to Y}(t) \tag{3.20}$$

$$\int_{-1}^{1} dx\; \tilde{E}^{N\to Y}(x,\xi,t) = g_3^{N\to Y}(t) + \frac{1}{\xi} g_2^{N\to Y}(t). \tag{3.21}$$

It is interesting to point out that these additional contributions also violate the symmetry of GPDs under the $\xi \to -\xi$ transformation [59]. The SU(3) flavor symmetry works well for the form factors g_1,f_1, and g_2, as shown in studies of semileptonic decays [60]. These studies are, however, insensitive to f_3, g_2, and f_2. While, as noted

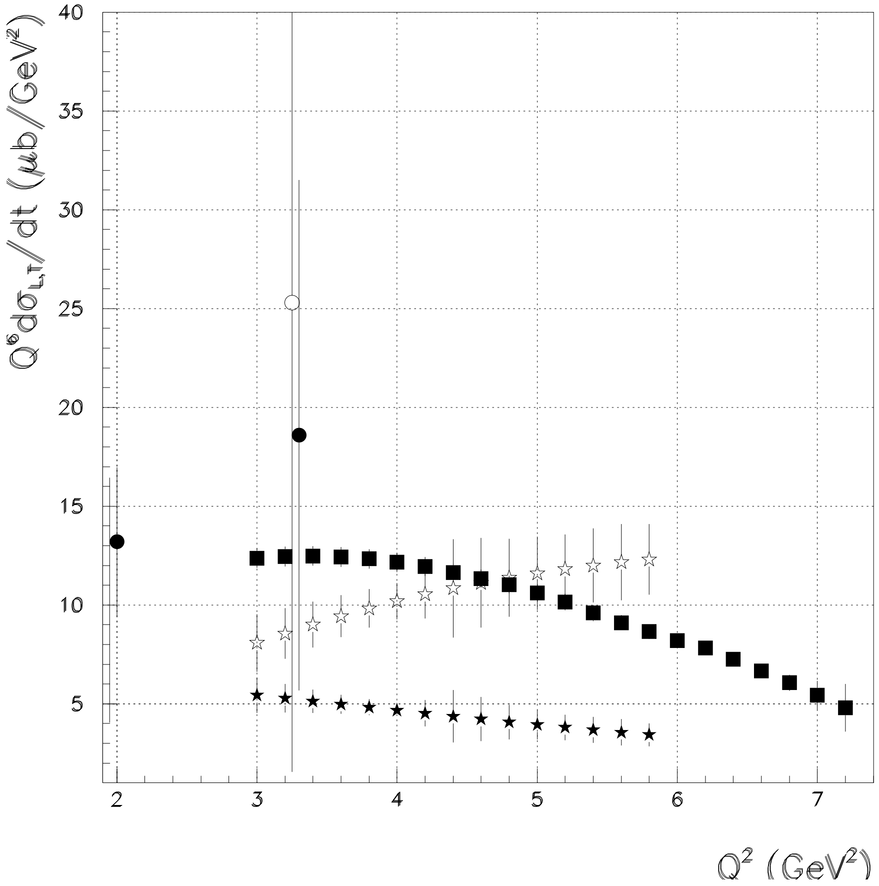

Figure 3.19: Separated differential cross section $d\sigma/dt$ (multiplied by Q^6) for π^+n as a function of Q^2. The existing data [57] are displayed with circles, open asterisks correspond to σ_L, filled asterisks to σ_T. Points are the results of the simulations with 6, 8 and 11 GeV beams. Filled squares correspond to unseparated differential cross section.

above, f_3 and g_2 are expected to be proportional to the strange quark mass (and as such their effect can be non–negligible), the g_3 form factor can be linked to the contribution of the kaon pole via generalized partial conservation of axial current (PCAC) relations:

$$g_3^{N\to Y}(t) \simeq \frac{2g_{KNY}f_K}{m_K^2 - t}, \tag{3.22}$$

where g_{KNY} is the KNY coupling constant, and $f_K \simeq 159$ MeV is the kaon decay constant. Given the t dependence of Eq. 3.22, with the similar relation obtained for the contribution of the pion pole to the pseudoscalar form factor, one notices that because of the large disparity between the pion and kaon masses, the SU(3) symmetry breaking effects are sizeable for $g_3^{N\to Y}(t)$. While these effects are suppressed (by ξ, $m_Y - m_N$) for the H, E, and $\tilde{H}$ GPDs, they are very strong for $\tilde{E}$. In fact the $\tilde{E}$ GPD diverges in the limit $\xi \to 0$ and this divergence is totally dominated by weak electricity. The transverse spin azimuthal asymmetry in the production of kaons on the nucleon is thus a very promising observable, as it is sensitive to the $\tilde{E}^{N\to Y}$ function.

In Fig. 3.20 the transverse spin asymmetries are shown [37] for the $K^+\Lambda$, $K^+\Sigma^0$, and $K^0\Sigma^+$ channels for different values of $-t$. The thick lines correspond (for the top two panels) to predictions based on asymptotic kaon distribution amplitudes, while the thin lines correspond to Chernyak–Zhitnitsky amplitudes. The asymmetries are as large as those predicted for the $\pi^+ n$ channel and, what is more appealing, they can be accessed without the need of a polarized target, simply by measuring the decay distribution of the recoiling hyperon produced off an *unpolarized* target.

The bottom panel shows the sensitivity to the antisymmetric parameter η^a_K that appears in the K^0 electroproduction pole contribution[4], as shown in Eq. 3.23:

$$B^{pole}_{K^0\Sigma^+} = \frac{4}{3}\eta^a_K\Big(\frac{3}{2\xi}\Big)\frac{f_K g_{KN\Sigma}(2m_N)}{m_K^2 - t}. \tag{3.23}$$

The study of flavor non–diagonal GPDs via hard exclusive kaon electroproduction processes gives access to a set of new observables related to the flavor SU(3) symmetry breaking. The yields obtained in the strange channels are comparable with those obtained from non–strange channels and can even dominate (depending on the specifics of distribution amplitudes and polarized parton distributions). This is in sharp contrast with the situation one finds at lower energies where one finds hundreds (if not thousands) of π^+ events for every K^+ identified. The spin asymmetries predicted are as large for the strange as they are for the non–strange reactions.

3.1.5 Large Momentum Transfer Meson Electroproduction

Introduction.

We have seen in Chapter I, (see, e.g., Figure 1.3) that the GPD's as functions of x and t provide a picture of the correlation of longitudinal and transverse momentum distributions, x and $k_\perp$, of quarks in the nucleon. These in turn may be transformed to provide x vs $b_\perp$ distributions $f(x, b_\perp)$, where $b_\perp$ is the impact position of the struck partons. To fully map the small $b_\perp$ core of the distributions, it is necessary to measure reactions at high t, while still retaining the factorizability inherent in the handbag mechanism. This can be realized in *form factor type* measurements, and importantly in deep exclusive reactions in the *high* t - *low* Q^2 regime, which is complementary to the *low* t - *high* Q^2 regime previously discussed. As we have indicated, *form factor type* exclusive reactions as a function of t measure moments $< x^m >= \int x^m f(x, b_\perp)dx$; that is the m'th moments of the x distributions at a particular $b_\perp$. m depends on the reaction studied. For example, for elastic scattering $m = 0$ and in Compton scattering $m = -1$.

---

[4] In contrast with π^0 electroproduction, K^0 electroproduction can have a pole contribution.

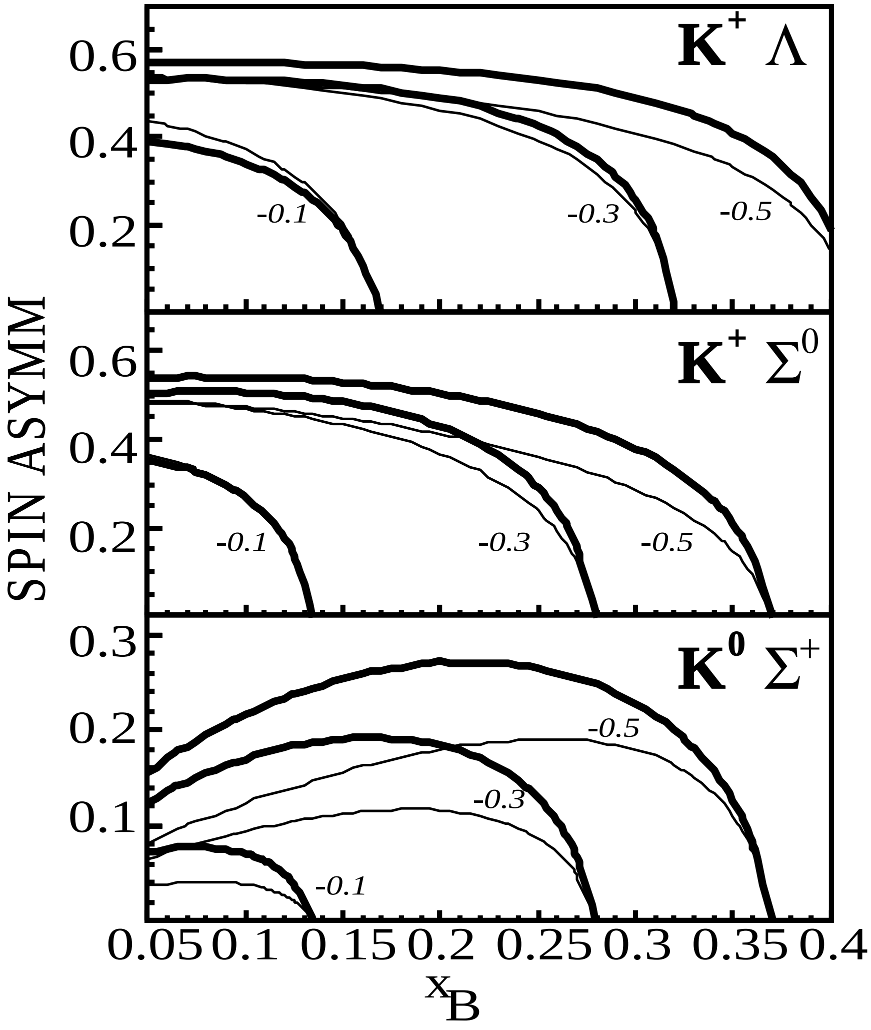

Figure 3.20: Transverse spin asymmetries for the $K^+\Lambda$, $K^+\Sigma^0$, and $K^0\Sigma^+$ channels at different values of t. See text for details.

An important component of our GPD program will be to measure exclusive deep virtual meson and photon production in the *high* t - *low* Q^2 regime, simultaneously with our measurements at *low* t - *high* Q^2. These reactions will provide x^{-1} moments for the small $b_\perp$ components of the correlations function, and combined with the $m = 0$ moments obtained in of the high Q^2 form factor measurements will give powerful constraints on the nucleon's short distance parton wave functions.

As in the *low* t - *high* Q^2, measurement of a variety of pseudoscalar, and vector mesons in the final states will provide selective access to the different flavor characteristics of the various GPD's, e.g. $H, E, \tilde{H}, \tilde{E}$. Referring to Figure 3.21, it can be seen that for low t one can easily project a maximum Q^2 greater than 10 $(GeV/c)^2$, while at low Q^2 one can easily attain a maximum t greater than 10 $(GeV/c)^2$.

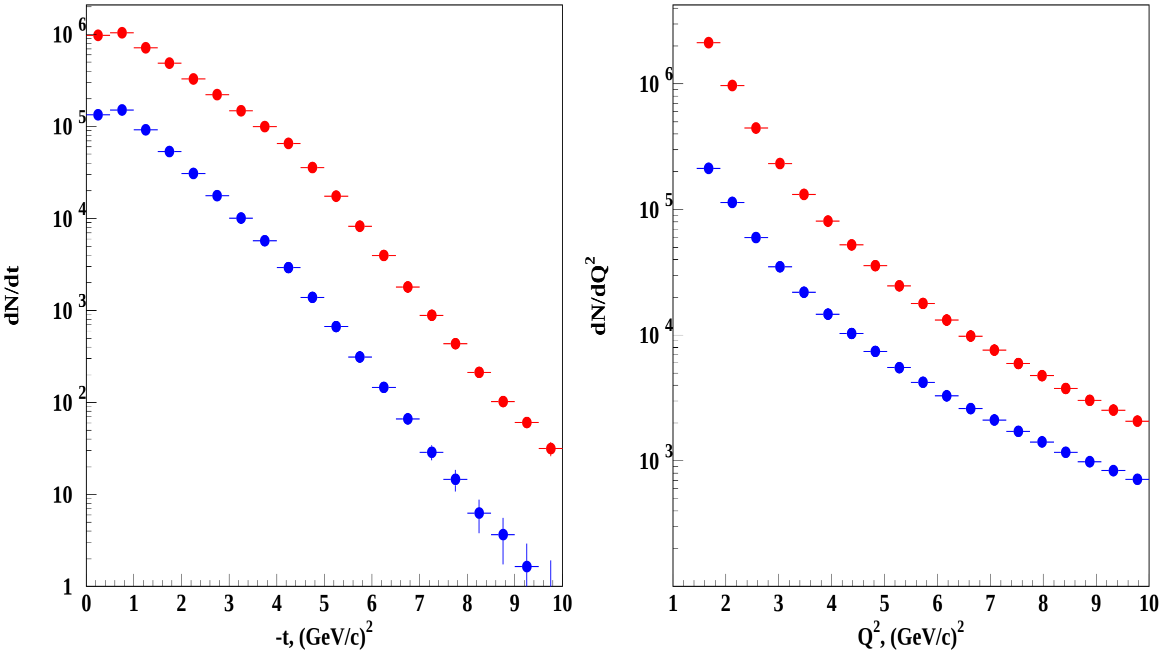

Figure 3.21: Simulated number of the events dN/dt as a function of $-t$ at $Q^2 = 1.5 \div 2.5$ (GeV/c)^2 and dN/dQ^2 as a function of of Q^2 at $-t < 1$ (GeV/c)^2 for π^0 (red points) and η (blue points), in the reaction $e^-p \rightarrow e^-p(\pi\eta), (\pi^0, \eta \rightarrow \gamma\gamma)$. The cross section is assumed to follow the t and Q^2–dependences obtained by fitting our 6 GeV data. The experiment is assumed to run for 2000 hrs at a luminosity of 1×10^{35} cm^{-2}s^{-1}

Physics of *high* t - *low* Q^2 exclusive reactions.

The prototype reaction in this kinematic region is real or virtual wide angle Compton scattering off protons, in which the hard parton-level subprocess is factorized, with the remaining soft proton matrix elements described by *new* form factors [14, 15].

These new form factors represent the x^{-1} moments of the GPD's at large momentum transfer. Similar mechanisms can be applied to electroproduction of pseudoscalar and vector mesons with high momentum transfer, which factorize into hard meson electroproduction off partons and soft proton matrix elements described by similar form factors as appear in Compton scattering. In contrast to the deeply virtual meson production the theory predicts cross section for longitudinally and transversely polarized photons, with the longitudinal cross section dominating at $Q^2 > 1$ GeV^2. Also,the higher twist contributions decrease as m^2/t in contrast to m^2/Q^2 which is the case in *high* Q^2 - *low* t reactions.

The cross section for meson electroproduction $ep \to epM$ can be written as follows

$$\frac{d^4\sigma}{dsdQ^2dtd\phi} \sim (\frac{d\sigma_T}{dt} + \epsilon\frac{d\sigma_L}{dt} + 2\epsilon cos2\phi\frac{d\sigma_{TT}}{dt} + \sqrt{2(1+\epsilon)}cos\phi\frac{d\sigma_{LT}}{dt})$$

where ϕ denotes the azimuthal angle between the hadronic and leptonic scattering planes and ϵ is the ratio of longitudinal to transverse photon flux. The theory predicts all terms in this equation: $\sigma_L, \sigma_T, \sigma_{TT}$ and σ_{LT}.

For illustration, the longitudinal π^0 electroproduction cross section has the following form,

$$\frac{d\sigma_L^{\pi^0}}{dt} \sim \left(R_A^{\pi^0}(t)\int_0^1 d\tau\phi_M(\tau)f_0^{(q)}(\tau, s, Q^2, t)\right)^2, \tag{3.24}$$

where $\phi_M(\tau)$ is the meson distribution amplitude as a function of its internal valence quark momentum fraction τ, and $f_0^{(q)} = f(\tau, s, t, u)$ is the parton-level amplitude. $R_A^{\pi^0}(t)$ is the axial form factor which is composed of the spin dependent GPD's as follows:

$$R_A^{\pi^0}(t) \sim (e_u R_A^u - e_d R_A^d)$$
$$R_A^q(t) = \int_{-1}^1 \frac{dx}{x}\tilde{H}^q(x, 0, t)$$

$\tilde{H}^q(x, \xi, t)$ is the GPD function for quark of flavor q.

Thus, the key ingredients of the reaction which are probed are the GPD's $\tilde{H}^q(x, 0, t)$, with $H^q(x, 0, 0) = \Delta_q(x)$, the pion distribution function $\phi_M(\tau)$, and the single quark hard scattering amplitude $f_0^{(q)}(\tau, s, Q^2, t)$.

Expected rates.

We have simulated the expected rates as a function of t and Q^2. Our event generator is an extrapolation of the results obtained from our recent 6 GeV experiment, in which we have fit the data on π_0, η, η' and ρ with power law dependences in t and

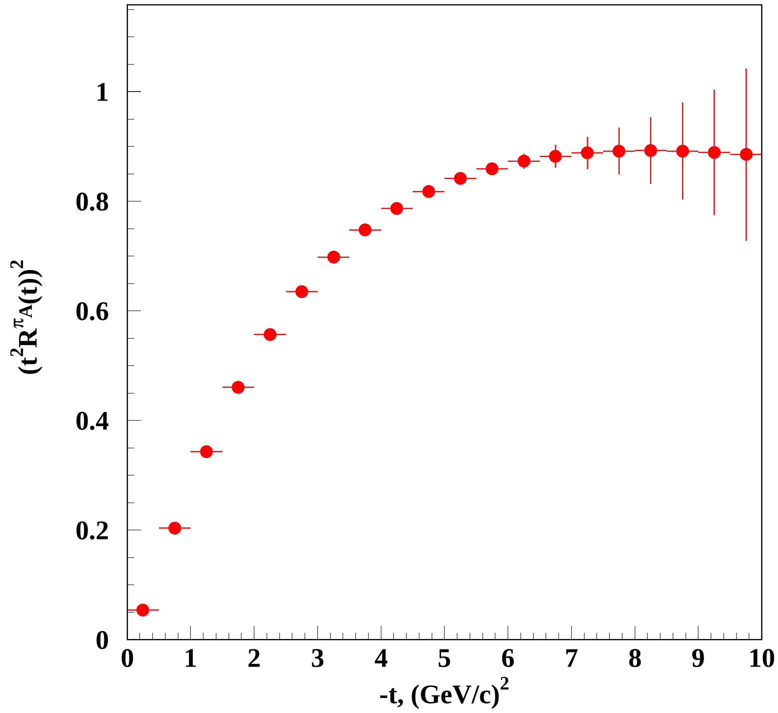

Figure 3.22: Simulated extraction of the form factor $(t^2 R_A^{\pi^0})^2$ from Eq. 3.24 compared with theory[14, 15], assuming statistical accuracies obtained as in figure 3.21.

Q^2. This has been fed into the CLAS^{++} Monte Carlo simulator, to obtain detected events under the assumption of a 2000 hr run with a luminosity of 1×10^{35} cm^{-2}s^{-1}. The trigger consisted of the coincidence of an electron, proton and the two decay photons. Even with such a restrictive trigger the result yields very favorable counting rate over the entire range of t and Q^2. Figures 3.21 and 3.22 illustrate some of the results of the simulation. With such favorable statistics we can envision performing L-T separated t distributions over a large range of t.

3.2 Inclusive Nucleon Structure Functions

3.2.1 Overview

Polarized and unpolarized structure functions of the nucleon offer a unique window on the internal quark structure of stable baryons. The study of these structure functions provides insight into the two defining features of QCD — asymptotic freedom at small distances, and confinement and non-perturbative effects at large distance scales. From measurements of structure functions we can infer the fraction of the nucleon momentum and spin carried by quarks, and, via perturbative evolution, by gluons.

After more than three decades of measurements at many accelerator facilities worldwide, a truly impressive amount of data has been collected, covering several orders of magnitude in both kinematic variables (x, the fraction of the nucleon momentum carried by the struck quark, and the momentum transfer squared, Q^2). However, there are still important regions of the kinematic phase space where data are scarce and have large errors, where significant improvements are possible through experiments at Jefferson Lab with an 11 GeV electron beam.

One of the most interesting open questions is the behavior of the structure functions in the extreme kinematic limit $x \to 1$, where nearly all of the nucleon momentum is carried by a single quark. In this region the nucleon wave function is dominated by valence quarks, which give the overall charge and baryon number of the nucleon, and effects from the virtual sea of quark-antiquark pairs are suppressed. Understanding of this region requires determining relative size of the contribution from u and d valence quarks, as well as quarks with spin parallel and antiparallel to the nucleon spin. Simple phenomenological models, like the spin-flavor symmetric quark model, predict significantly different behavior from perturbative QCD, or from quark models with hyperfine interactions. Observables such as the neutron to proton structure function ratio, F_2^n/F_2^p, and the polarization asymmetry, A_1, very sensitive at large x to the details of the quark wave function in the nucleon, and provide excellent laboratories for studying the systematics of spin-flavor symmetry breaking in the nucleon.

In addition to measurements of valence quark structure at large x, the 12 GeV upgrade will allow a detailed study of the phenomenon of quark-hadron duality. Quark-hadron duality refers to the observation, first made by Bloom and Gilman [61], that the structure function in the resonance region, when suitably averaged over an appropriate energy interval, closely follows the scaling structure function measured at higher energies, where the interaction is dominated by single quark scattering. The phenomenon of quark-hadron duality has so far only been shown to exist in the proton structure function F_2^p, but has not yet been studied for neutrons. Duality in other structure functions, such as the longitudinal structure function F_L, or the spin structure functions g_1 and g_2, is only just beginning to be explored. Understanding the duality between descriptions of a nucleon using either quark or hadronic degrees of freedom in different physical processes and under different kinematical conditions will provide an important key to understanding the consequences of QCD for hadronic structure. Furthermore, both unpolarized and polarized structure functions are not well known at low to moderate Q^2 and x. An improved data sample in this region would allow one to study issues like higher-twist contributions to the structure functions, and improve perturbative QCD analyses by increasing the Q^2 range covered.

The CLAS^{++} detector will allow significant contributions to be made to these studies, particularly in two cases:

- Measurements of the neutron structure function F_2^n in the region of very large x, where we will employ a novel technique (recoil proton detection) to eliminate contamination from nuclear effects, and

- Measurements of polarized structure functions of the proton and deuteron in the region of moderate to high x.

In both cases, the possible luminosity of the experiment is limited by other factors, so that the relatively low luminosity of CLAS will be largely compensated by its very large acceptance.

3.2.2 Neutron structure function at large x

Valence quark distributions

Although a large body of structure function data exists over a wide range of x and Q^2, the region $x > 0.6$ is not well explored. For $x \geq 0.4$ the contributions from the $q\bar{q}$ sea are negligible, and the structure functions are dominated by the valence quarks.

Knowledge of the valence quark distributions of the nucleon at large x is vital for several reasons. The simplest SU(6) symmetric quark model predicts that the ratio of d to u quark distributions in the proton is $\frac{1}{2}$, however, the breaking of this symmetry in nature leads to a much smaller ratio. Various mechanisms have been invoked to explain why the d distribution is softer than u. For instance, if the interaction between quarks that are spectators to the deep inelastic collision is dominated by one-gluon exchange, the d quark distribution will be suppressed, and the d/u ratio will tend to zero in the limit $x \to 1$ [62, 63, 64, 65, 66, 67]. This assumption has been built into most global analyses of parton distribution functions [68], and has never been tested independently. On the other hand, if the dominant reaction mechanism involves deep-inelastic scattering from a quark with the same spin orientation as the nucleon, as predicted by perturbative QCD counting rules, then d/u tends to $\approx 1/5$ as $x \to 1$ [69]. Determining d/u experimentally would lead to important insights into the mechanisms responsible for spin-flavor symmetry breaking. In addition, quark distributions at large x are a crucial input for estimating backgrounds in searches for new physics beyond the Standard Model at high energy colliders [70].

Because of the 4:1 weighting of the squared quark charges between the up and down quarks, data on the proton structure function, F_2^p, provide strong constraints on the u quark distribution at large x,

$$F_2^p(x) \;=\; x\sum_q e_q^2(q(x)+\bar{q}(x)) \;\approx\; x\left(\frac{4}{9}u(x)+\frac{1}{9}d(x)\right) \; . \tag{3.25}$$

The determination of the d quark distributions, on the other hand, requires in addition the measurement of the neutron structure function, F_2^n. In particular, the d/u ratio can be determined (at leading order) from the ratio of neutron to proton structure functions:

$$\frac{F_2^n}{F_2^p} \;\approx\; \frac{1+4d/u}{4+d/u} \; , \tag{3.26}$$

provided $x \geq 0.4$ so that sea quark contributions can be neglected.

Up to now, data on F_2^n have been extracted primarily from inclusive scattering off deuterium. Unfortunately, theoretical uncertainties in the treatment of nuclear corrections have led to ambiguities in the extracted F_2^n at large x. In particular, inclusion of Fermi motion and nucleon off-shell corrections in the deuteron can lead to values for F_2^n/F_2^p that differ by 50% already at $x = 0.75$ [71, 72] compared with values extracted assuming the presence of Fermi motion corrections only. The differences are even more dramatic if one extracts F_2^n on the basis of the nuclear density model [73]. The tagged structure function method for measuring F_2^n proposed here on the other hand virtually eliminates the uncertainties from nuclear models.

Resonance region

In addition to the deep-inelastic region, it is also important to map out the neutron resonance region, where at present there are essentially no data. Resonance transition and elastic form factors provide fundamental information on the structure of the neutron, and therefore are very interesting in their own right.

Measurements [74, 75] at Jefferson Lab of the unpolarized structure functions on hydrogen in the resonance region have previously been used to verify Bloom-Gilman duality [61, 76]. These have inspired considerable interest in quark-hadron duality [77], and neutron data will add more valuable information. Within a simple harmonic oscillator quark model, Close and Isgur [78] found that the neutron structure functions should exhibit systematic deviations from local duality, and that duality should occur at higher W for the neutron than for the proton. Understanding duality could prove to be crucial for mapping the transition from hadronic to quark-gluon degrees of freedom, and the measurements proposed here would allow one to identify the basic principles which underly this transition. Furthermore, if the systematics of Bloom-Gilman duality are understood quantitatively, duality could provide a powerful tool for accessing the large x region.

Although precision electron-proton scattering experiments have been performed in a straightforward manner with hydrogen targets, it has been necessary to infer experimental information on the structure of the neutron from nuclear (typically deuteron) data. The procedure of unfolding neutron data from inclusive nuclear cross sections, via the subtraction of Fermi motion effects and contributions from various nuclear constituents, leads to ambiguities dependent on the models and reaction mechanisms employed. This is particularly true for measurements in the elastic and resonance regions at high x and moderate Q^2.

To illustrate this, consider the inclusive resonance electroproduction cross section spectra shown in Fig. 3.23. These data were obtained at Jefferson Lab at $Q^2 = 1.5$ (GeV/c)^2 for hydrogen and deuterium targets at matched kinematics. Although the three prominent resonance enhancements are obvious in the hydrogen data, only a hint of the first (the $\Delta(1232)$) is identifiable in the deuterium data. At

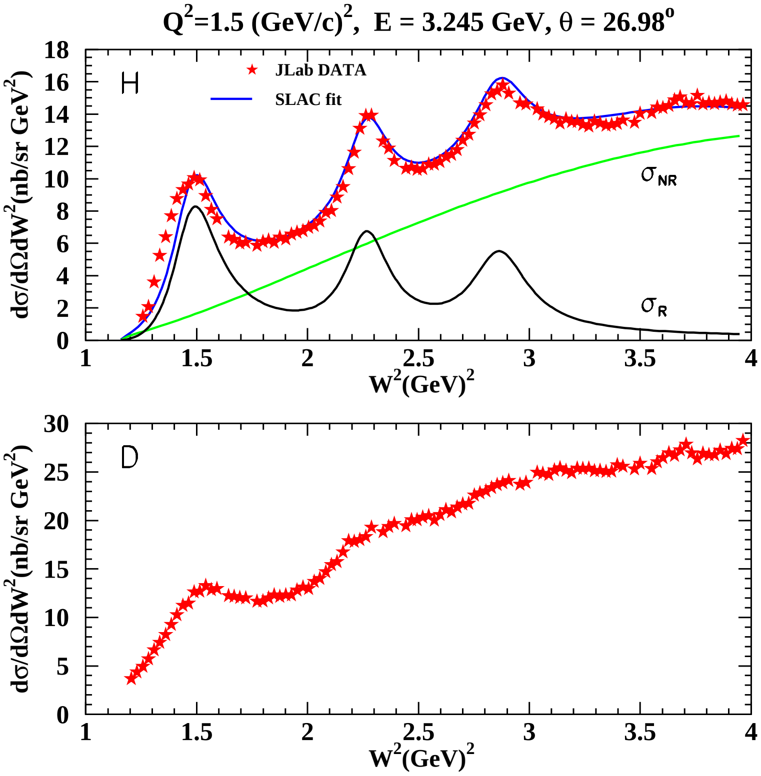

Figure 3.23: Inclusive resonance electroproduction cross sections from Jefferson Lab at $Q^2 = 1.5$ (GeV/c)^2 [79]. Cross sections are shown as a function of invariant mass squared for hydrogen (top) deuterium (bottom) targets at matched kinematics. The hydrogen spectrum is plotted with global resonant and non-resonant fits.

$Q^2 > 2$ (GeV/c)^2, no discernable structure remains in the deuterium data. Neutron extraction from such data requires careful modeling of the resonant and non-resonant components for the neutron (as was done with the hydrogen data). Calculations must account for the nuclear effects of binding, Fermi motion, and nucleon off-shellness, and the model-dependence introduced by each of these steps leads to a substantial uncertainty in the neutron resonance structure functions. For this reason very little neutron resonance transition form factor data exist.

Tagged structure functions

The measurement of the tagged structure functions in semi-inclusive scattering from the deuteron with a slow recoil proton detected in the backward hemisphere, $e + D \rightarrow e + p + X$, will allow the structure function of the free neutron to be extracted with minimal ambiguities associated with the nuclear model dependence [80, 81, 82]. Within the nuclear impulse approximation, in which the deep inelastic scattering takes place incoherently from individual nucleons, the differential semi-inclusive cross section can be written as a product of the deuteron spectral function, $\mathcal{S}$, and an effective (bound) neutron structure function, $F_2^{n(eff)}$ [82]:

$$\frac{d\sigma}{dx dW^2 d\alpha_{sp} d^2 p_T} \approx \frac{2\alpha_{em}^2 (1-\nu/E)}{Q^4} \alpha_{sp} \mathcal{S}(\alpha_{sp}, p_T)\ F_2^{n(eff)}(W^2, Q^2, p^2)\ . \tag{3.27}$$

Here $W^2 = (p_d + q - p_s)^2$ is the invariant mass squared of the unobserved hadronic final state, with p_s the momentum of the spectator proton, p_d the momentum of the initial state deuteron, and $p = p_d - p_s$ the momentum of the struck neutron. The variable $\alpha_{sp} = (E_s - p_s^z)/M$ is the light-cone momentum fraction carried by the spectator proton and p_T its momentum component perpendicular to the direction of $\vec{q}$, with $E_s = \sqrt{M^2 + \vec{p}_s^{\,2}}$ the spectator proton energy and M its mass. The degree to which the struck neutron is off-shell is given by

$$M^2 - p^2 \approx 2\vec{p}_s^{\,2} + 2M\epsilon\ , \tag{3.28}$$

where ϵ is the deuteron binding energy. In the limit $p^2 \to M^2$, the effective neutron structure function $F_2^{n(eff)}(W^2, Q^2, p^2) \to F_2^n(W^2, Q^2, M^2) \equiv F_2^n(x, Q^2)$, the free neutron structure function. The p^2 dependence of $F_2^{n(eff)}$ depends strongly on the theoretical assumptions made about the off-shell behavior of the photon—bound-nucleon scattering amplitude. The ratio $R_n \equiv F_2^{n(eff)}(W^2, Q^2, p^2)/F_2^n(W^2, Q^2)$ of the bound to free neutron structure functions in the relativistic spectator model of Ref. [83] is shown in Fig. 3.24 for several values of x, as a function of the momentum of the spectator, $|\vec{p}_s| = |\vec{p}|$. Although the effect at low $|\vec{p}_s|$ is small, the deviation from unity increases sharply with increasing momentum, especially at larger values of x where the EMC effect is more pronounced. A similar behavior is observed in the non-relativistic model of Ref. [84], where the assumption of weak binding in the deuteron allows one to calculate the off-shell dependence up to order p^2/M^2 [84].

On the other hand, the color screening model for the suppression of point-like configurations (PLC) in bound nucleons [73], which attributes most or all of the EMC effect to a medium modification of the internal structure of the bound nucleon, predicts somewhat larger (by a factor of 2 or 3 [82]) deviations from unity than those in Fig. 3.24. It is important, therefore, that the tagged structure functions be measured for kinematics where the difference $p^2 - M^2$ is as small as possible, to minimize theoretical uncertainties associated with extrapolation to the nucleon pole. Since the deviation of the bound to free structure function ratio from the free limit is proportional to $2\vec{p}_s^{\,2} + 2M\epsilon$, sampling the data as a function of $\vec{p}_s^{\,2}$ should provide guidance for a smooth extrapolation to the pole. In practice, considering a momentum interval of 70–200 MeV/c would allow the dependence on p^2 to be constrained. Existing 6 GeV data from experiment E94-102 (E6) will help to study the high-virtuality behavior of the bound structure function.

Moreover, extrapolation from the minimum $|\vec{p}| \approx 70$ MeV/c, where the bound neutron is only around 10 MeV away from its mass-shell, should be relatively free

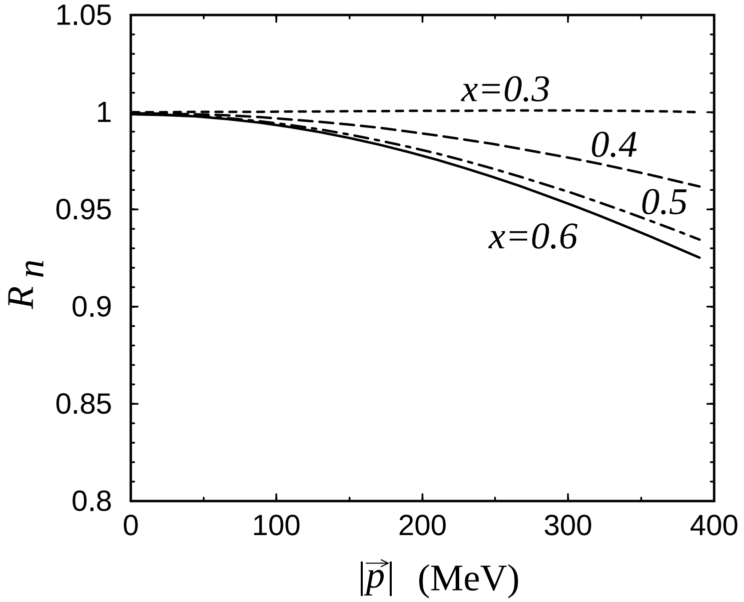

Figure 3.24: The ratio $R_n \equiv F_2^{n(eff)}(W^2, Q^2, p^2)/F_2^n(W^2, Q^2)$ of the bound to free neutron structure functions as a function of the spectator proton momentum in the model of Ref. [83].

of ambiguities. This is also supported by recent $^4\text{He}(\vec{e}, e'\vec{p})$ polarization transfer experiments at Mainz and Jefferson Lab which indicate that the magnitude of the off-shell deformation is rather small [85]. These experiments measured the ratio of transverse to longitudinal polarization of the ejected protons, which is related to the medium modification of the electric to magnetic elastic form factor ratio. Using model independent relations derived from quark-hadron duality, one can relate the small, but non-zero medium modification observed in the form factors to a modification at large x of the deep inelastic structure function of the bound nucleon [86], which suggests an effect of $\leq 3\%$ for $x \leq 0.8$. The typical momentum of the knocked out protons in the experiments was ~ 50 MeV, although the results of the analysis were found not to depend strongly on the proton momentum [86]. These considerations lead us to expect that the extrapolation of the bound neutron structure function to the nucleon pole should introduce minimal uncertainty into the extracted structure function of the free neutron.

In addition to determining the free neutron structure function, tagged structure function measurements on the deuteron could allow one to discriminate between different hypotheses on the origin of the nuclear EMC effect [82]. In particular, one may be able to distinguish between models in which the effect arises entirely from hadronic degrees of freedom — nucleons and pions, and models in which the effect is attributed to the explicit deformation of the wave function of the bound nucleon itself. By comparing ratios of semi-inclusive cross sections at different values of x, which further reduces the dependence on the deuteron spectral function [73], one can discriminate between models such as the PLC suppression and Q^2 rescaling models, which predict a fast drop with α_{sp}, and nuclear binding models, in which the α_{sp} dependence is quite weak [82]. Furthermore, these studies would enable one to test the validity of factorization in nuclear DIS, and determine the boundaries of the traditional convolution approach to describing nuclear structure functions.

Final state interactions

Another possible source of uncertainty lies in the rescattering, or final state interactions (FSI), of the spectator proton and the deep-inelastic remnants, X, of the scattered neutron. Extraction of the free neutron structure function is most reliable in the kinematic region where the FSI effects are small, and where different nuclear models for the deuteron spectral function, $\mathcal{S}$, lead to similar results. The choice of backward angles is designed to minimize these effects. Production of backward protons also suppresses contributions from direct processes, where a nucleon is produced at the $\gamma^* N$ interaction vertex.

The magnitude of FSI effects has been estimated in Ref. [82] within the framework of the distorted wave impulse approximation (DWIA) [87]. Although a direct calculation of the FSI contribution to the cross section requires knowledge of the full dynamics of the spectator proton–neutron remnant system, which is currently unavailable, one can estimate the uncertainty introduced through neglect of FSI by comparing with the calculation of FSI effects in the high-energy $d(e,e'p)n$ break-up reaction [87]. The effective p–X interaction cross section, σ_{eff}, can be approximated [88] by that extracted from soft neutron production in the high-energy DIS of muons from heavy nuclei [89]. The effect of the FSI is to modify the spectral function $\mathcal{S} \to \mathcal{S}^{DWIA}$ [87], where

$$\mathcal{S}^{DWIA}(\alpha_{sp}, p_T \approx 0) \sim \mathcal{S}(\alpha_{sp}, p_T \approx 0) \left[1 - \frac{\sigma_{eff}(Q^2, x)}{8\pi < r_{pn}^2 >} \frac{|\psi_D(\alpha_{sp}, < p_T >) \psi_D(\alpha_{sp}, 0)|}{S(\alpha_{sp}, p_T \approx 0) / \sqrt{E_s \; E_s(< p_T^2 >)}} \right] . \tag{3.29}$$

Here $< r_{pn}^2 >$ is the average separation of the nucleons within the deuteron, E_s is the spectator nucleon energy, and $E_s(< p_T^2 >) = \sqrt{M^2 + p_z^{s\ 2} + < p_T^2 >}$ is the energy evaluated at the average transverse momentum $< p_T^2 >^{1/2} \sim$ 200–300 MeV/c transferred for the hadronic soft interactions, with effective cross section σ_{eff}. The steep momentum dependence of the deuteron wave function, $|\psi_D(\alpha_{sp}, < p_T >)| \ll |\psi_D(\alpha_{sp}, p_T \approx 0)|$, ensures that FSI effects are suppressed in the extreme backward kinematics.

The effects of FSI are illustrated in Fig.3.25, which shows the ratio of the light-cone spectral function including FSI effects within the DWIA to that without [82]. At extreme backward kinematics ($p_T \approx 0$) one sees that FSI effects contribute less than $\sim 5\%$ to the overall uncertainty of the $d(e,e'n)X$ cross section for $\alpha_{sp} \leq 1.5$.

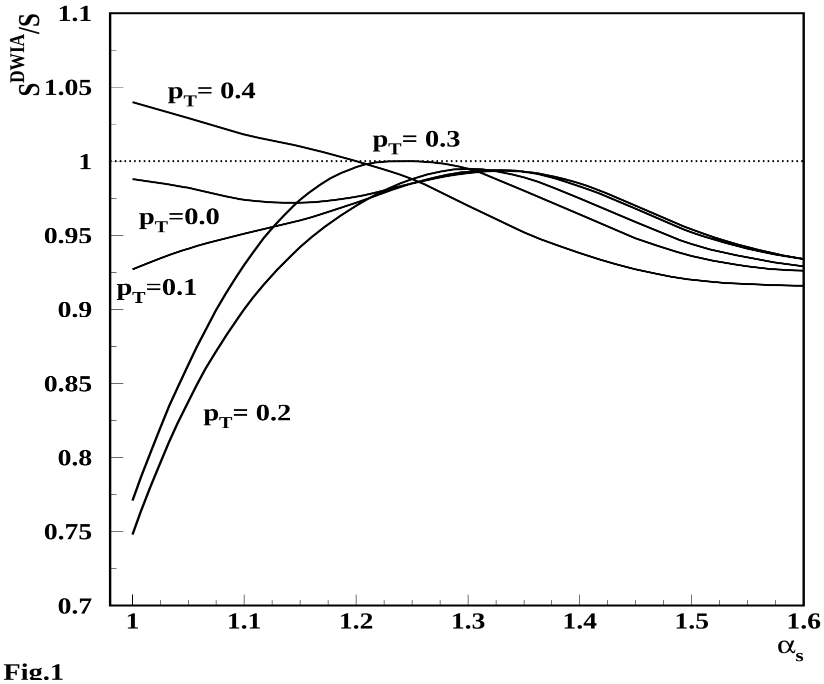

Fig.1

Figure 3.25: Spectral function calculated with and without FSI effects within the DWIA [82]. The curves correspond to different values of the spectator proton transverse momentum (in GeV/c).

This number can be considered as an upper limit on the uncertainties due to FSI. At larger p_T (≥ 0.3 GeV/c) and small α_{sp} (≈ 1) the double scattering contribution (which is not present for the extreme backward case, see Eq. (3.29)) plays a more important role in FSI [87].

At very large x values ($x \geq 0.7$) the factorization approximation itself breaks down [83], and higher order corrections to Eq. (3.27) must be included if one wants accuracy to within a few %. To avoid theoretical ambiguities one should therefore restrict the analysis to spectator momenta below $\approx 150 - 200$ MeV/c.

Of course, in order to identify any residual nuclear effects, it would be ideal to repeat this experiment by detecting spectator neutrons. Comparing the bound proton structure function with the free proton structure function would then allow one to correct the bound neutron structure function for any remaining nuclear effects.

Expected results

We have simulated the expected results from a 40 day (100% efficient) run at 11 GeV in CLAS^{++} with the recoil detector described in Section 5.3. A minimum momentum of 70 MeV/c was assumed for proper detection of a proton moving perpendicular to the detector axis, and accordingly more (due to energy loss) for protons at different angles. A simple model is used of the acceptance of both CLAS^{++} for the scattered electrons and of the recoil detector for protons. To select events where the neutron is close to on-shell, the recoil momentum is required to be less than 180 MeV/c. The spectator proton is also required to make an angle of at least 110 degrees with the

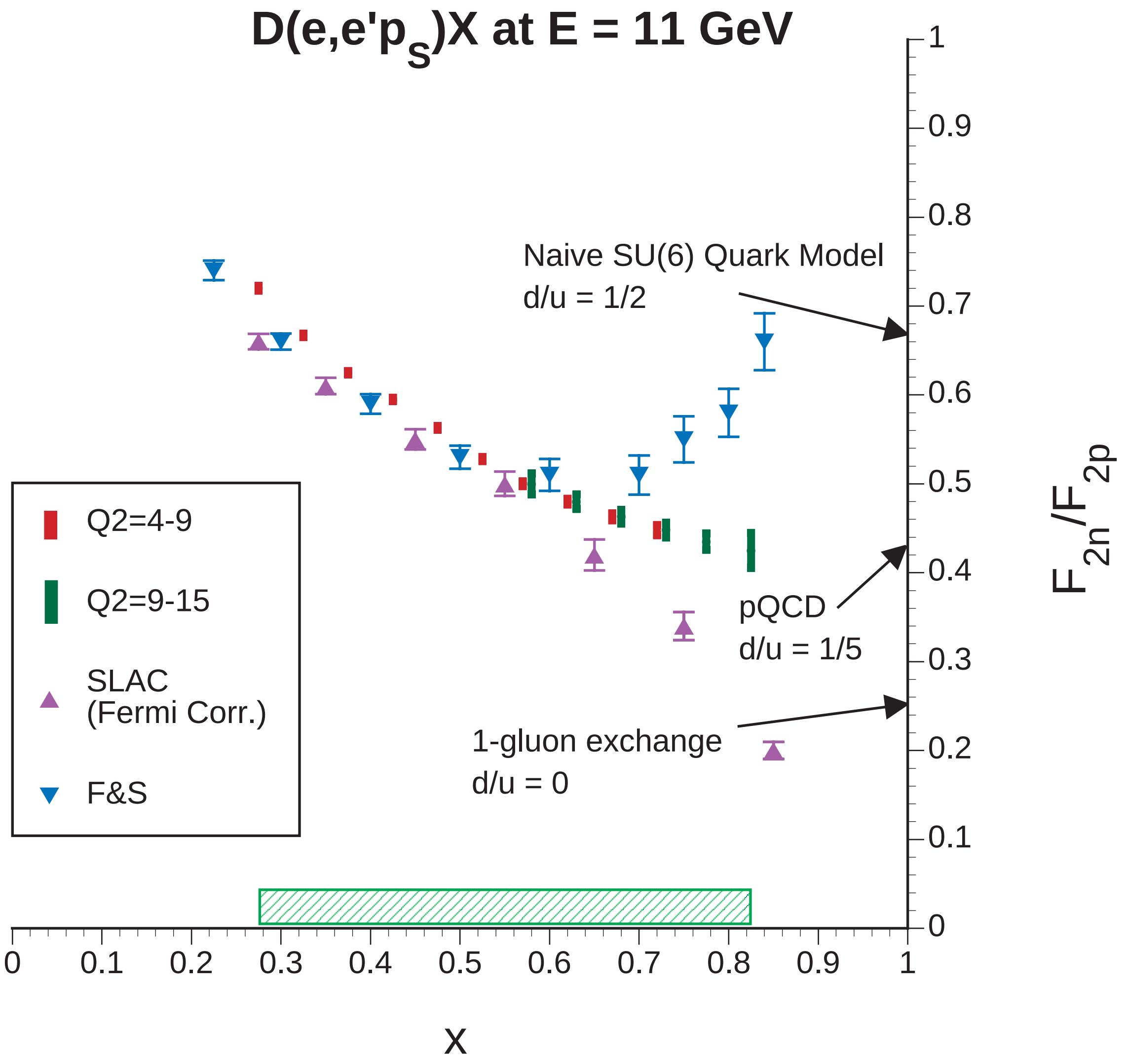

Figure 3.26: Ratio of the neutron and proton structure functions, F_2^n and F_2^p, as a function of x. The red and green vertical bars indicate the expected statistical precision of the proposed experiment for two different bins in Q^2, based on a 40 day run with full reconstruction of the kinematics via detection of a backward moving spectator proton. The triangles indicate existing (deuterium and proton) data from SLAC (with systematic and statistical error bars combined), analyzed in two different ways, as explained in the text.

direction of the momentum transfer vector, $\vec{q}$.

Under these conditions, a total of 1.7 M coincident events is expected, and 700 k events with recoil momentum below 100 MeV/c. The average spectator light-cone fraction for these kinematics will be $\alpha_{sp} = 1.1$. A range in W from the elastic peak to about $W = 4$ GeV will be covered. Restricting the kinematics to $W > 1.8$ GeV (where resonant final states have little influence), data for x between 0.1 and 0.85 will be collected, with sufficient statistics to bin in several Q^2 bins from 1 to 15 (GeV/c)^2 and to study the dependence on the recoil momentum.

As an example, we show in Fig. 3.26 the statistical precision which can be achieved for the ratio F_2^n/F_2^p at high x. The estimated systematic errors, which include experimental and theoretical uncertainties due to FSI effects and possible medium modifications of the nucleon structure function, are indicated by the band along the abscissa. The arrows along the ordinate indicate predictions of different models for the $x \to 1$ limit, as discussed in Section , which cannot be excluded by present-day data due to the uncertainty in the nuclear effects [72]. The data shown, indicated by triangles, are extracted from proton and deuteron cross sections measured at SLAC (with systematic and statistical error bars combined), analyzed according to different prescriptions for subtracting the nuclear corrections. In one case (upward pointing triangles), the deuterium data were corrected only for Fermi motion [71], while in the other case (downward pointing triangles) a parameterization of the EMC effect based on effective inter-nucleon distances extrapolated to the deuteron [73] was used. Clearly, while the current data cannot discriminate between any of the theoretical predictions, the F_2^n/F_2^p data obtained using the new method will allow us (for the first time) to differentiate unambiguously between different expectations for this ratio.

3.2.3 Spin Structure Functions

Measurement goals

While the behavior of the spin-averaged quark distributions at large x still awaits definitive resolution, our lack of understanding of the spin-dependent distributions at large x is even more striking. For instance, there are a number of qualitatively different predictions for the polarization asymmetry, A_1, which (in lowest order in perturbative QCD) is given by the ratio of the spin-dependent to spin-averaged quark distributions,

$$A_1(x) = \frac{\sum_q e_q^2 \, \Delta q(x)}{\sum_q e_q^2 \, q(x)} , \tag{3.30}$$

where e_q is the quark charge. Arguments based on perturbative one-gluon exchange suggest that this should approach unity as $x \to 1$ for proton, neutron and (neglecting nuclear correction) deuteron targets [69]. In contrast, nonperturbative models such as those based on SU(6) spin-flavor symmetry predict that $A_{1p} = 5/9$, $A_{1n} = 0$ and

$A_{1d} = 1/3$ [63, 64, 65]. Presently, the world data set is unable to determine the veracity of these predictions.

Although SU(6) symmetry imposes strict relations between the individual quark distributions, such as $\Delta u = -4\Delta d$, in nature this symmetry is strongly broken. Nonperturbative models which break SU(6) symmetry typically involve a hyperfine interaction, derived for instance from one-gluon exchange or pion exchange, which has the effect of suppressing the d quark distribution relative to the u [63, 64, 66, 67]. If the u quark is dominant as $x \rightarrow 1$, the asymmetries A_{1p}, A_{1n} and (in the absence of nuclear effects) A_{1d} will all tend to unity, and distinguishing between the predictions derived from perturbative QCD will require very accurate data at $x \sim 0.6 - 0.8$. On the other hand, the one-gluon exchange model predicts qualitatively different behavior for the ratios of individual distributions $\Delta q/q$, especially for the d quark. While the asymptotic $x \rightarrow 1$ limit in perturbative QCD is $\Delta d/d \rightarrow 1$, one-gluon exchange predicts $\Delta d/d \rightarrow -1/3$ as $x \rightarrow 1$, so that even the sign of the predictions differs.

The ratio $\Delta d/d$ can be extracted from semi-inclusive measurements of pions in the current fragmentation region (see section on semi-inclusive processes). A program of inclusive and semi-inclusive double spin asymmetry measurements using an energy upgraded CEBAF, in conjunction with polarized proton and deuteron targets, can substantially improve our ability to distinguish between the various descriptions of the nucleon.

The large acceptance coverage of CLAS combined with the high luminosity available at an energy upgraded CEBAF will allow access to a large range of x and Q^2. This will enable precise measurements to be made of moments, or integrals, of the g_1 structure function, and thereby tightly constrain theoretical descriptions of the transition from low to high Q^2 [90, 91, 92]. Understanding this transition is vital for a number of reasons. Through the phenomenon of quark-hadron duality, as discussed in the previous section, one can relate the physics of nucleon resonances, which are described by coherent scattering from constituent quarks at low energy, to the dynamics of single quark scattering which governs the scaling structure function at high energy.

While the phenomenon of quark-hadron duality has been observed in the spin-independent F_2 structure function [74, 61], it has not yet been established for spin-dependent structure functions. Because the g_1 structure function is given by a difference of cross sections, which need not be positive, the workings of duality will necessarily be more intricate for g_1 than for the spin-averaged F_2 structure function. Unlike the unpolarized structure functions, spin 1/2 and 3/2 resonances contribute with opposite signs. For fixed Q^2 values less than 1 $(\mathrm{GeV/c})^2$, the $\Delta(1232)$ resonance pulls the g_1 structure function below zero, in contrast to the positive value observed in DIS. This is also related to the physics which drives the dramatic variation of the integral of the g_1 structure function from its large and negative value at $Q^2 = 0$ (where it is related to the Gerasimov-Drell-Hearn sum rule) to a positive value at large Q^2 (where it is related to deep inelastic sum rules such as the Bjorken sum rule) [90]. Duality may be realized for polarized structure functions if one averages over a complete set of resonances [78]. To achieve a more complete understanding of duality it is necessary to determine the conditions under which duality occurs in both polarized and unpolarized structure functions.

In the context of QCD, one can relate quark-hadron duality to an operator product expansion of moments of structure functions [76]. According to the twist expansion, moments can be expressed in terms of a power series in $1/Q^2$, where the coefficients of each of the terms in the series are related to matrix elements of quark and gluon operators of a certain twist (which is equal to the difference between the mass dimension and spin of an operator) [91, 92]. The leading, Q^2-independent term is related to matrix elements of quark bilinear operators, and gives rise to the scaling of the structure function. The higher order terms involve matrix elements of mixed quark–gluon field operators, and characterize the effect of background color electric and magnetic fields on quarks [93]. Because of the $1/Q^2$ suppression, extraction of the higher twist matrix elements, which reflect the role played by quark-gluon correlations in the nucleon, requires structure function moments over a large range of Q^2, from ~ 0.5 (GeV/c)^2 to several (GeV/c)^2. Measurement of moments of the g_1^p and g_1^d structure functions using CLAS^{++} would therefore significantly improve our understanding of the workings of QCD at low energy.

Future installation of a transversely polarized target will, in addition, allow measurements of the g_2 structure function, which is the cleanest example of a higher twist effect in the nucleon. Although the g_2 structure function does not have a simple parton model interpretation, the x^2-weighted integral of g_2 is directly related to the color electric and magnetic polarizabilities of the nucleon [93]. In particular, the x^2 moment of the combination $2g_1 + 3g_2$ gives the pure twist-3 matrix element, d_2, which reflects the strength of nonperturbative quark-gluon correlations in the nucleon. Furthermore, the large kinematic coverage of CLAS^{++} ($0.1 \leq x \leq 0.85$) will allow hitherto unverified sum rules involving g_2 [94, 95] to be tested accurately. A program of transversely polarized structure function measurements would thus open up a whole additional avenue for exploring the transition between asymptotic freedom and confinement physics.

Experimental parameters

For the measurements of spin structure functions in CLAS at 11 GeV, we anticipate that a dedicated polarized target similar to the existing EG1 target will be built (see corresponding sections of the technical section of the CDR). It will contain dynamically polarized solid ammonia ($^{15}NH_3$ and $^{15}ND_3$) at about 1K temperature in a 5 Tesla field.

For longitudinal asymmetry measurements, the magnet axis will point along the beam direction. In this case, the acceptance of the target will fully match the acceptance of the upgraded CLAS. For transverse asymmetries, the holding field of 5 Tesla will point sideways. Assuming optimized coil openings, we expect a maximum acceptance of ±20 degrees horizontally and ± 35 degrees vertically. The Møller electrons will be ejected sideways, where they can be contained in massive shielding plates. The electron beam will go through a chicane of one upbending and two downbending magnets, so that it will enter the polarized target pointing down and then be bent into the normal beam line to the electron dump.

For the following rate estimates, we assume 40 ideal runnning days (corresponding to 3 calendar months) for each target configuration and both NH_3 and ND_3, and a beam polarization of 70% on average. We expect average target polarizations of 80% for NH_3 and 40% for ND_3 targets, in agreement with recent experience at JLab and SLAC. The overall dilution factor (ratio of events from polarized nucleons to all events) for these targets is about 0.13 for NH_3 and 0.23 for ND_3, due to the presence of ^{15}N in the ammonia and liquid helium coolant as well as entrance and exit foils. We will run with about 30 nA beam current, rastered over the surface of the targets of length 1.5 cm, yielding an overall luminosity of about 10^{35} cm^{-2}s^{-1}. Note that this luminosity is only a factor 5 lower than the highest luminosity that can typically be achieved for solid state polarized targets. This makes CLAS a superior choice for measurements with these targets, since the large solid angle (about one steradian) compensates for the limited luminosity, and all kinematic points can be measured simultaneously.

Expected results

The precision that can be achieved for the asymmetry A_{1p} is shown in Fig. 3.27. These data will clearly distinguish between the SU(6) symmetric quark model prediction of 5/9 and the pQCD prediction of unity for the limit $x \rightarrow 1$, and dramatically improve our knowledge of the proton's spin structure at high x. The difference between these predictions is even more striking for the deuteron, where we will also be able to significantly improve on existing data, as shown in Fig. 3.28. The high precision data on both the proton and deuteron that will be accumulated for several bins in Q^2 will constrain the logarithmic and $1/Q^2$ scaling violations of the spin structure functions g_1, and determine their higher moments, as well as allow duality for spin structure functions to be studied in detail.

Finally, the structure function g_{2p} will be determined from data with transverse target polarization. We will again improve significantly on the existing SLAC data, with smaller error bars and finer binning in x and Q^2. This will allow the evolution of this structure function to be studied and the twist-3 matrix element d_2 to be extracted with three times smaller statistical error than at present.

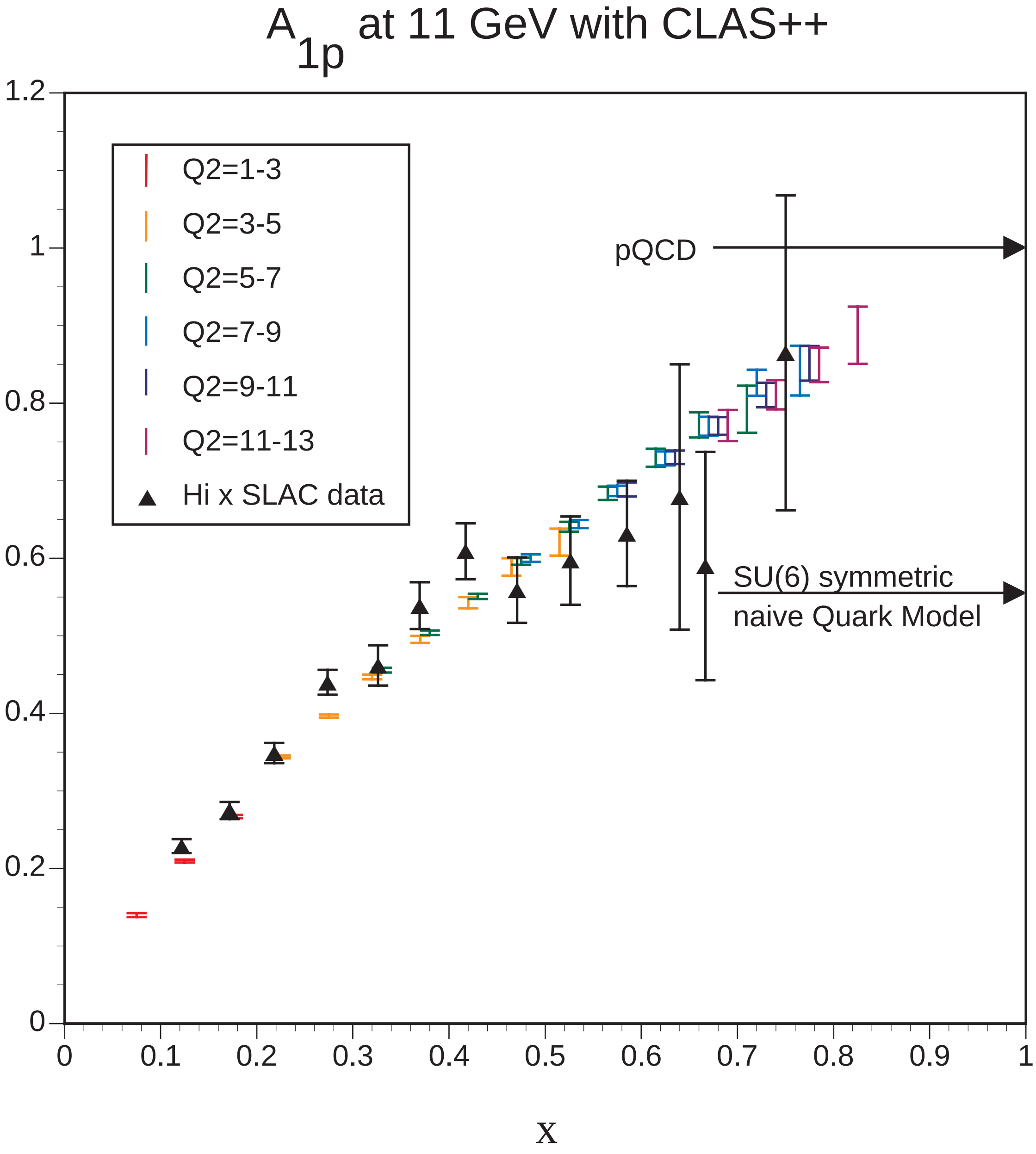

Figure 3.27: Expected data with statistical errors for A_{1p} from 40 days of running with 11 GeV beam. Several bins in Q^2 are indicated by slightly offset error bars. Existing SLAC data (from E130, E143 and E155) are shown as well. The predicted approach to the limit $x = 1$ for two different models is indicated.

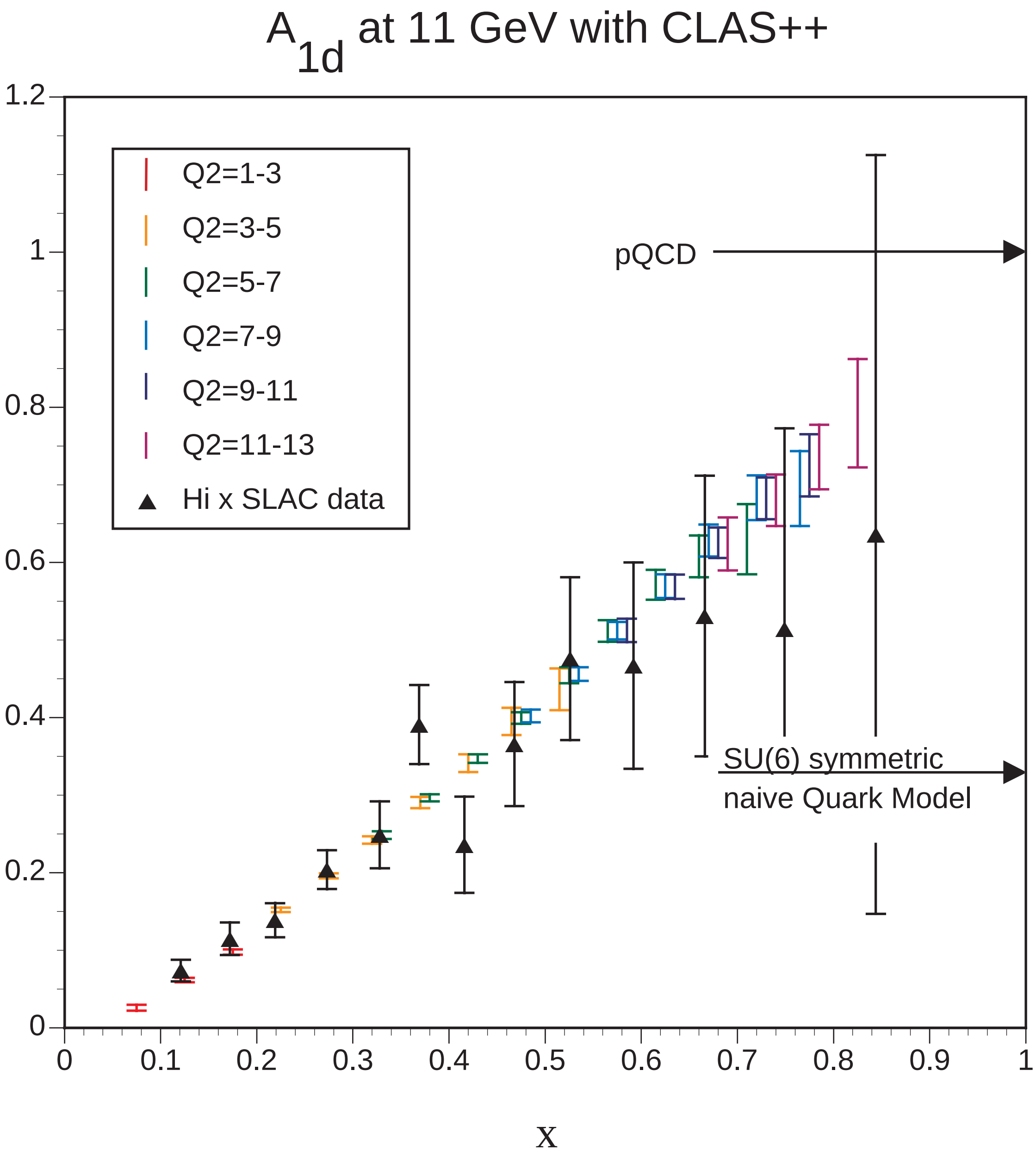

Figure 3.28: Expected data with statistical error bars for A_{1d} for the deuteron from 40 days of running with 11 GeV beam. All symbols are as in Fig. 3.27.

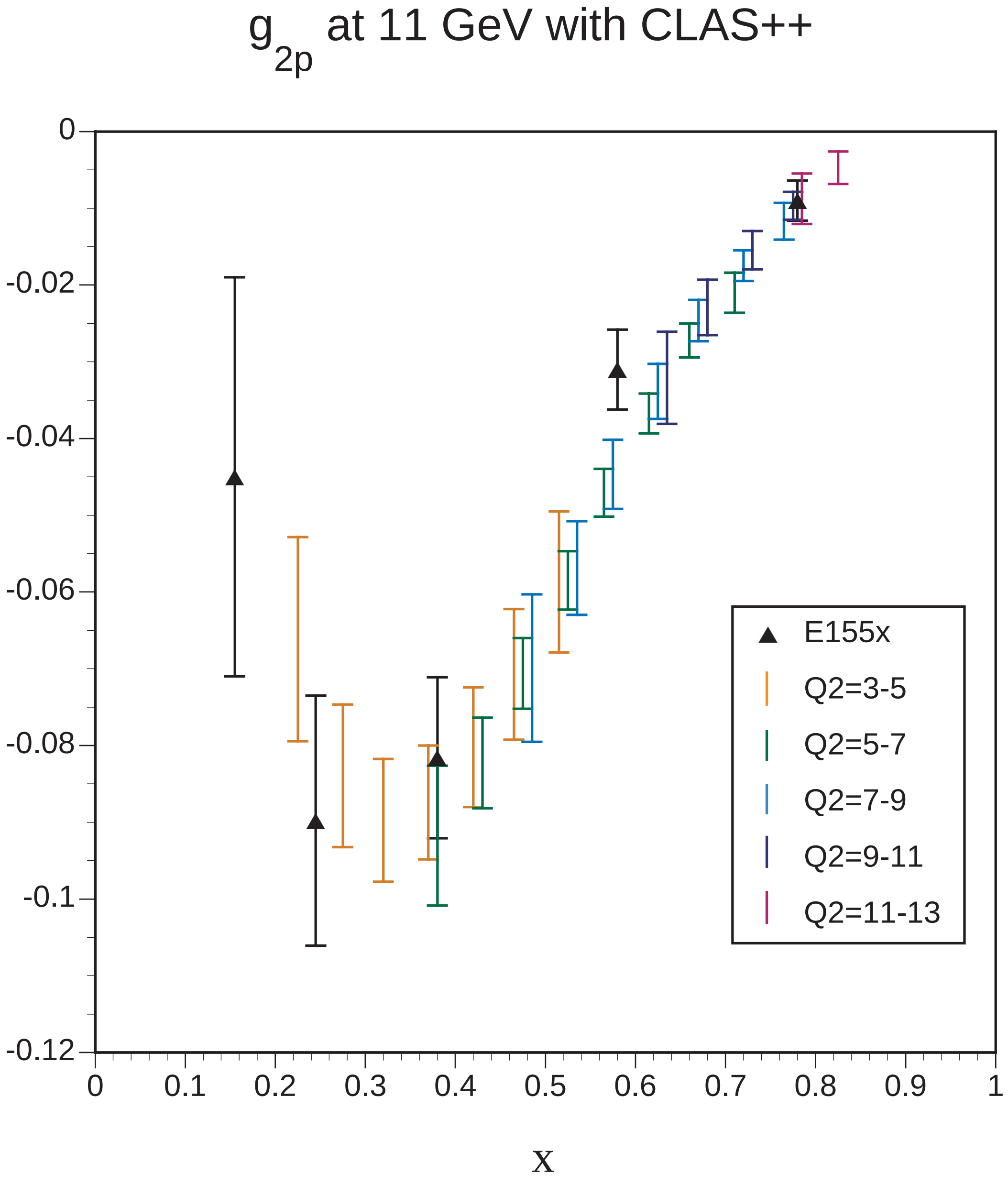

Figure 3.29: Expected statistical error bars on the structure function g_{2p} for the proton from 40 days of running with 11 GeV beam with transverse target polarization.

3.3 Semi-Inclusive DIS

Semi-inclusive deep inelastic scattering (SIDIS) has been used extensively in recent years as an important testing ground for QCD. Studies so far have concentrated on better determination of parton distribution functions, distinguishing between the quark and antiquark contributions, and understanding the fragmentation of quarks into hadrons. The use of polarization in leptoproduction provides an essential new dimension for testing QCD.

Spin and azimuthal asymmetries in distributions of final state particles in deep inelastic scattering (DIS) play a crucial role in the study of the spin structure of hadrons in terms of their elementary constituents [19, 96, 20, 21, 25]. In particular measurement of the azimuthal angle dependence of the observed hadron allows access to various transverse momentum dependent (TMD) distributions [17, 18, 19, 20, 21, 23] containing direct information about the quark orbital motion [26, 25, 28].

It is also argued that in both semi-inclusive [97] and in hard exclusive [98, 53, 99] pion production, scaling sets in for cross section ratios and, in particular, for spin asymmetries at lower Q^2 than it does for the absolute cross section. The very good agreement of the HERMES data with the SMC data, taken at 6-12 times higher average Q^2, shows that the semi-inclusive asymmetries are Q^2 independent within the present accuracy of the experiments [100]. This makes it possible for the measurement of spin-asymmetries to be a major tool for the study of different parton distribution function (TMD,GPD) measurements in the Q^2 domain of a few GeV^2.

The total cross section for single pion production by longitudinally polarized leptons scattering off unpolarized protons is defined by a set of structure functions and contains two main contributions. The beam spin-independent part of the cross section (σ_{UU} in Ref. [20]) arises from the symmetric part of the hadronic tensor, and the helicity (λ_e) dependent part (σ_{LU})[96] arises from the antisymmetric part:

$$\begin{aligned}\frac{d\sigma_{UU}}{dx_B dy\, dz d^2P_\perp} &= \frac{4\pi\,\alpha^2\, s}{Q^4}\, x_B \Big\{ \Big(1-y+\frac{1}{2}y^2+\frac{1}{4}\gamma^2\Big)\,\mathcal{H}_T + (1-y-\frac{1}{4}\gamma^2)\,\mathcal{H}_L \\ &\quad -(2-y)\sqrt{1-y-\frac{1}{4}\gamma^2}\,\cos\phi\;\mathcal{H}_{LT} + (1-y-\frac{1}{4}\gamma^2)\,\cos 2\phi\;\mathcal{H}_{TT}\Big\},\end{aligned}$$

$$\frac{d\sigma_{LU}}{dx_B dy\, dz d^2P_\perp} = \lambda_e \frac{4\pi\,\alpha^2\, s}{Q^4}\; x_B\, \sqrt{y^2+\gamma^2}\sqrt{1-y-\frac{1}{4}\gamma^2}\,\sin\phi\;\mathcal{H}'_{LT}, \qquad (3.31)$$

where ϕ is the azimuthal angle between the scattering plane formed by the initial (k_1) and final (k_2) momenta of the electron and the production plane formed by the transverse momentum of the observed hadron ($P_\perp$) and the virtual photon (see Fig.3.30). The target mass corrections are explicitly included in the kinematics via the term $\gamma^2 = 4M^2x_B^2/Q^2$.

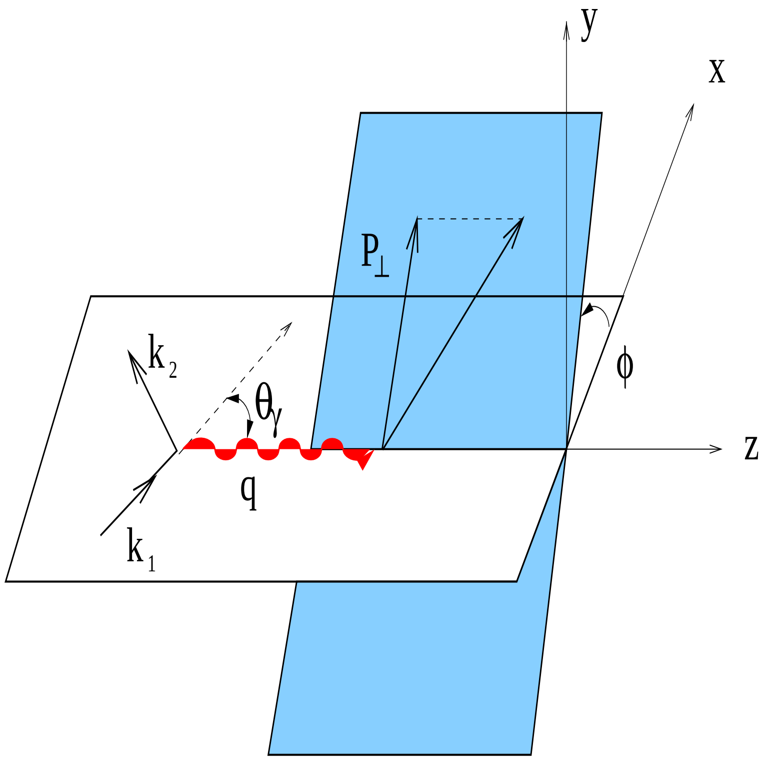

Figure 3.30: Kinematics for the pion electroproduction.

The relevant kinematical variables are defined as: $x_B = Q^2/2P_1 \cdot q, y = P_1 q/P_1 \cdot k_1$, $z = P_1 \cdot P/P_1 \cdot q$, where $Q^2 = -q^2$, $q = k_1 - k_2$ is the momentum of the virtual photon, and P_1 and P are the target and observed final-state hadron momenta, respectively.

The structure functions $\mathcal{H}_T, \mathcal{H}_L, \mathcal{H}_{TT}, \mathcal{H}_{LT}$, and $\mathcal{H}_{LT'}$ are related to the transverse and longitudinal photon contributions and their interference. Additional single and double spin-dependent contributions with corresponding structure functions appear in the SIDIS cross section for polarized targets or if one considers polarimetry in the final state. Assuming that the quark scattering process and the fragmentation process factorize, and that the fragmentation functions scale and depend only on the fractional energy, z, the structure functions could be presented as a convolution of a distribution function and a fragmentation function. Both assumptions have yet to be experimentally confirmed at JLab energies.

At the leading-twist level, the quark structure of hadrons is described by three distribution functions: the number density, or unpolarized distribution function, $q(x)$; the helicity distribution, $\Delta q(x)$; and the transversity distribution, $\delta q(x)$. If the transverse momentum k_T of partons also included, the number of independent distribution functions at leading twist increases to six [20, 21, 24] (three of which reduce to $q(x), \Delta q(x)$ and $\delta q(x)$ when integrated over k_T). Because they in general depend on the longitudinal and transverse momentum, these "3-dimensional" TMD functions

distribution functions		chirality	
		even	odd
twist 2	U	$\mathbf{q}$	$h_1^\perp$
	L	$\boldsymbol{\Delta}\mathbf{q}$	$h_{1L}^\perp$
	T	$f_{1T}^\perp \quad g_{1T}$	$\delta\mathbf{q} \quad h_{1T}^\perp$
twist 3	U	$f^\perp$	$\mathbf{e}$
	L	$g_L^\perp$	$\mathbf{h}_L$
	T	$\mathbf{g}_T \quad g_T^\perp$	$h_T \quad h_T^\perp$

Table 3.1: List of twist-2 and twist-3 distribution functions accessible in SIDIS.

provide a more complete picture of nucleon structure. Relaxing the time invariance condition, two additional functions ($f_{1T}^\perp, h_1^\perp$) are permitted [18, 22, 101, 25, 26, 23], bringing the total number of distribution functions to eight.

With better experimental accuracy it may be possible to isolate the higher-twist effects in hard processes, which arise from the quantum mechanical interference of partons in the interacting hadrons. The higher-twist terms are important for understanding long-range quark-gluon dynamics and may be accessible through measurements of certain asymmetries[30, 96, 21, 20], where they appear as leading contributions. Higher-twist structure functions are important at CEBAF energies because of the phenomenon of parton-hadron duality [61], or 'precocious scaling' [76, 91]. The full list of twist-2 and twist-3 distribution functions (those that survive after the k_T-integration are denoted in boldface) contributing to the double-polarized cross section in SIDIS is shown in Table 3.1 (see [20]):

Parton distribution functions cannot be computed in perturbative QCD. They are universal and do not depend on the particular hard process. Once measured in SIDIS no extra input is needed in order to compute analogous quantities in hadron-hadron collisions. Until recently the TMD distribution functions had mainly academic interest. They appear in azimuthal moments of double-polarized cross sections in single-hadron production in DIS [20, 21]. As shown recently in Ref.[23], the interaction of active parton in the hadron and the target spectators lead to gauge-invariant TMD parton distributions in DIS. Brodsky et al. [25] discussed final state diffractive scattering, which gives rise to interference effects in the DIS cross section[102]. A non trivial phase structure of QCD amplitudes due to rescattering results in *time-reversal odd* (T-odd) effects and the appearance of single-spin asymmetries at leading twist[25, 26]. This opens up a unique possibility to access T-odd distribution functions in single-spin asymmetry measurements in semi-inclusive DIS [25, 26].

A major issue in studies of semi-inclusive scattering is the separation of contributions from current fragmentation (active parton) and target fragmentation (spectators). It was argued [103] that, within perturbative QCD, it is possible to introduce new universal functions, so-called "fracture functions", describing the target hadron once it has fragmented into a specific final state hadron. These fracture functions depend on the initial and final hadrons, as well as on the quark flavor, and are functions of two momentum fractions, Bjorken x_B and the Feynman z variable.

A key goal is to carefully study the transition between the nonperturbative and perturbative regimes of QCD using simultaneous measurements of the Q^2 and x_B dependencies of cross sections and beam/target spin asymmetries for different final state hadrons with extraction of the corresponding structure functions and separation of the contributions of different distribution and fragmentation functions.

3.3.1 Single-Spin Asymmetries

Single-spin asymmetries (SSA) in hadronic reactions have been among the most difficult phenomena to understand from first principles in QCD. Large SSAs have been observed in hadronic reactions for decades [104, 105]. Recently, significant SSAs were reported in SIDIS by the HERMES collaboration at HERA [106, 107] (for a longitudinally polarized target), the SMC collaboration at CERN (transversely polarized targets) [108], and the CLAS collaboration at JLab[16] (polarized beam). In general, such single-spin asymmetries require a correlation of a particle spin with a production or scattering plane. In hadronic processes, such correlations can provide a window to the physics of final and initial state interactions.

Single-spin asymmetries in SIDIS give access to subtle distribution and fragmentation functions, which cannot easily be accessed in other ways. The list of novel physics observables accessible in SSAs includes the chiral-odd distribution functions, such as the transversity (δq) [30], the *time-reversal odd* fragmentation functions, in particular the Collins function ($H_1^{\perp}$) [19], and the recently introduced [18, 22, 25, 26, 28] *time-reversal odd* distribution functions ($f_{1T}^{\perp}, h_1^{\perp}$). These latter functions arise from interference between amplitudes with left- and right-handed polarization states, and only exist because of chiral symmetry breaking in QCD. Their study therefore provides a new avenue for probing the chiral nature of the partonic structure of hadrons. Furthermore, it was demonstrated recently that a nonzero orbital angular momentum of partons in the nucleon is crucial in forming the target SSA. The interference of different amplitudes arising from the target hadron's wavefunction that gives single-spin asymmetries [25], also yields the Pauli form factor $F_2(t)$ and the GPD $E(x, \xi, t)$ [109, 24] entering Deeply Virtual Compton Scattering[110, 111].

Unpolarized target

Assuming factorization of the quark scattering and fragmentation processes, the distribution and fragmentation functions responsible for a non-zero $\mathcal{H}'_{LT}$ in SIDIS were first identified by Levelt and Mulders [96]. They include the twist-3 unpolarized distribution function $e(x)$ introduced by Jaffe and Ji [30], and the polarized fragmentation function $H_1^{\perp}(z)$ first discussed by Collins [19]. The first ever extraction of the twist-3 distribution function from CLAS data [112] is shown in Fig.3.31. With a certain approximation for the twist-3 function $e(x)$, the beam SSA could become a major source of information on the T-odd polarized fragmentation function.

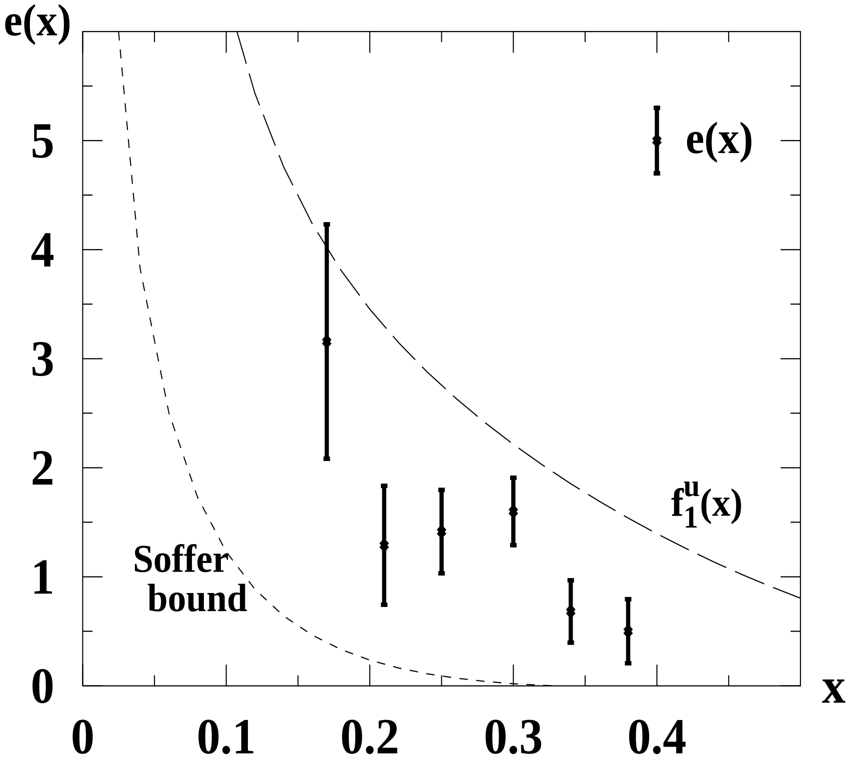

Figure 3.31: The flavor combination $e(x) = (e^u + \frac{1}{4}e^{\bar{d}})(x)$ vs. x, extracted from the CLAS beam-spin azimuthal asymmetry. The error bars are due to statistical errors of the CLAS data with $\langle Q^2 \rangle = 1.5\,\mathrm{GeV}^2$. A fit to published HERMES data[106] on target SSA was used in the parameterization of the Collins function. For comparison $u(x)(f_1^u(x))$ and the twist-3 Soffer bound are shown.

Beam SSAs do not require polarized targets and are free of dilution. They could be measured at the highest accessible luminosities. This makes them an important tool for factorization studies using measurements of different final state hadrons.

Polarized targets

For polarized targets, several azimuthal asymmetries already arise at leading order. The following contributions were investigated in Refs. [19, 20, 21, 113, 25, 28]:

$$\begin{aligned}
\sigma_{LT}^{\cos\phi} &\propto \lambda_e S_T y(1-y/2)\cos(\phi-\phi_S)\sum_{q,\bar{q}} e_q^2 x g_{1T}^q(x) D_1^q(z), && (3.32)\\
\sigma_{UL}^{\sin 2\phi} &\propto S_L 2(1-y)\sin 2\phi \sum_{q,\bar{q}} e_q^2 x h_{1L}^{\perp q}(x) H_1^{\perp q}(z), && (3.33)\\
\sigma_{UT}^{\sin\phi} &\propto S_T(1-y)\sin(\phi-\phi_S)\sum_{q,\bar{q}} e_q^2 x \delta q(x) H_1^{\perp q}(z), && \\
&+ S_T(1-y+y^2/2)\sin(\phi+\phi_S)\sum_{q,\bar{q}} e_q^2 x f_{1T}^{\perp q}(x) D_1^q(z), && (3.34)
\end{aligned}$$

where ϕ_S is the azimuthal angle of the transverse spin in the photon frame and $D_1^q(z)$ is the spin-independent fragmentation function. The subscripts "U, L, T" in $\sigma_{BT}^{W(\phi)}$ ($W(\phi) = \sin\phi, \cos\phi, \sin 2\phi$) stand for the unpolarized "U", longitudinally polarized "L", and transversely polarized "T" states of the beam (first index) and target (second index). Corresponding moments can be measured as
$A_{BT}^W = \int \sigma_{BT}(\phi) W(\phi) d\phi / \int \sigma(\phi) d\phi$.

The latter two equations above describe single-spin asymmetries involving the first moment of the Collins fragmentation function integrated over the transverse momentum of the final hadron. The leading-twist SSA $\sigma_{UL}^{\sin 2\phi}$ is kinematically suppressed at low x_B compared to the sub-leading $\sin\phi$ moment [114]. A recent measurement of the σ_{UL} contribution by HERMES[106] is consistent with a zero $\sin 2\phi$ moment. However, at the large x_B values accessible at JLab, the $A_{UL}^{\sin 2\phi}$ asymmetry is predicted [114] to be large (see Fig.3.32). The leading-twist distribution function $h_{1L}^{\perp}(x)$, accessible in that measurement, describes the transverse polarization of quarks in a longitudinally polarized proton.

The $\sin\phi$ moment of the SIDIS cross section with a transversely polarized target (σ_{UT})[101] contains contributions both from the Sivers effect (T-odd distribution)[18] and the Collins effect (T-odd fragmentation)[19]. Contributions to transverse SSAs from T-odd distributions of initial quarks ($f_{1T}^{\perp q}(x)$ term) and T-odd fragmentation of final quarks ($H_1^{\perp q}(z)$ term) could be separated by their different azimuthal and z-dependencies.

Assuming that the transversity of the sea is negligible ($\delta\bar{q} = 0$) and ignoring the non-valence quark contributions in pion production, the single-spin transverse asymmetry arising from fragmentation becomes:

$$A_{UT}^{\pi^+} \propto \frac{4\delta u(x)}{4u(x)+\bar{d}(x)} \frac{H_1^{\perp u\to\pi^+}(z, P_\perp)}{D_1^{u\to\pi^+}(z, P_\perp)}, \tag{3.35}$$

$$A_{UT}^{\pi^-} \propto \frac{\delta d(x)}{d(x)+4\bar{u}(x)} \frac{H_1^{\perp d\to\pi^-}(z, P_\perp)}{D_1^{u\to\pi^-}(z, P_\perp)}, \tag{3.36}$$

$$A_{UT}^{\pi^0} \propto \frac{4\delta u(x)+\delta d(x)}{4u(x)+\bar{d}(x)+d(x)+4\bar{u}(x)} \frac{H_1^{\perp d\to\pi^0}(z, P_\perp)}{D_1^{u\to\pi^0}(z, P_\perp)}. \tag{3.37}$$

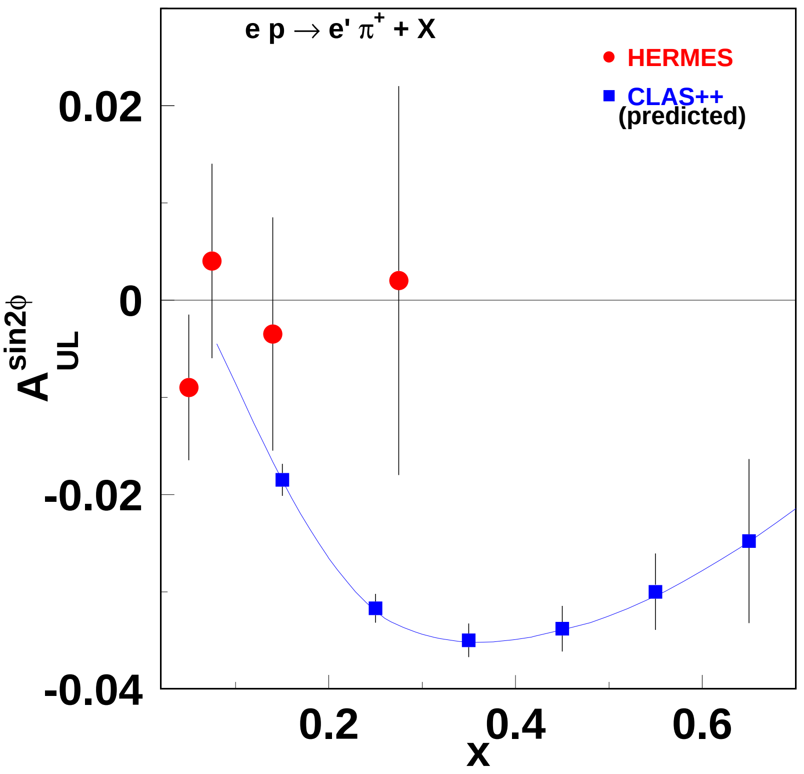

Figure 3.32: Dependence on x of longitudinally polarized target SSA, $A_{UL}^{\sin 2\phi}$. Circles are HERMES data for $A_{UL}^{\sin 2\phi}$, and squares represent expected statistical errors from CLAS at 11 GeV with 2000 hours of data taking. The curve is the prediction from Ref.[114].

The target single-spin asymmetry from polarized quark fragmentation extracted for CLAS kinematics at 12 GeV is plotted in Fig. 3.33. The estimate was done assuming $\delta q \approx \Delta q$ and an approximation for the Collins fragmentation function from Ref.[114]. Additional cuts were applied on z ($z > 0.5$) and the missing mass of the $e'\pi^+$ system ($M_X(\pi^+) > 1.1$ GeV). The curves have been calculated assuming a luminosity of $10^{35}\mathrm{cm}^{-2}\mathrm{s}^{-1}$, with a NH^3 target polarization of 85% and a dilution factor 0.176, with 2000 hours of data taking. The asymmetry is integrated over all hadron transverse momenta. The extraction of the transversity from $A_{UT}^{\sin\phi}$ could be performed via Eqs. (3.35-3.37) using parameterizations for the unpolarized distribution functions $u(x)$ and $\bar{d}(x)$.

The SIDIS cross section with a longitudinally polarized target in the sub-leading order contains an additional contribution to the $\sin\phi$ moment (σ_{UL}) [113, 101, 115]:

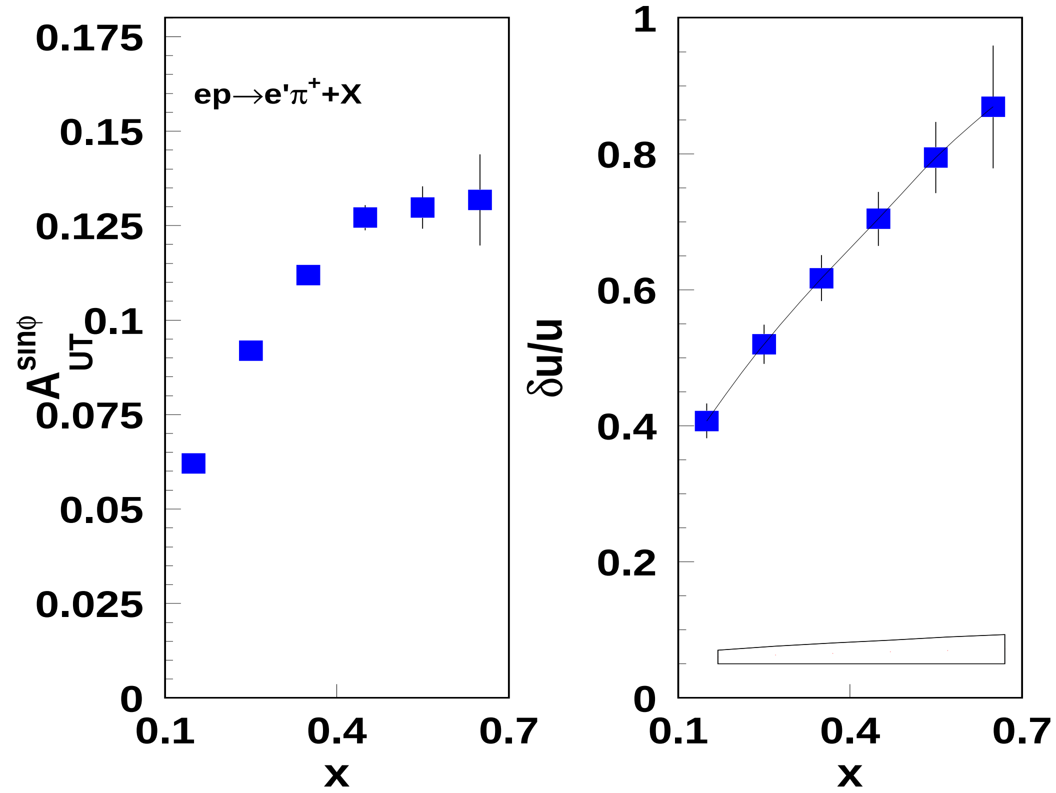

Figure 3.33: Projected transverse spin asymmetry ($A_{UT}^{\sin\phi}$) in single π^+ production with CLAS at 12 GeV (left plot) and the expected precision of the extracted $\delta u/u$ (right plot). The line is the Monte Carlo generated $\delta u/u$ and the band represent uncertainty due to unknown fragmentation function.

$$\sigma_{UL}^{\sin\phi} \quad \propto \quad S_L \sin\phi\,(2-y)\sqrt{1-y}\frac{M}{Q}\sum_{q,\bar{q}} e_q^2 x^2 h_L^q(x) H_1^{\perp q}(z). \tag{3.38}$$

The $\sin\phi$ moment of the cross section measured at CLAS is in good agreement with the HERMES measurement, which indicates that the asymmetry observables are not sensitive to the beam energy (see Fig.3.34). There are several different approaches[53, 116, 25] to the interpretation of the sign flip of the target SSA at large z observed by HERMES[106], and more data are needed to separate the different contributions.

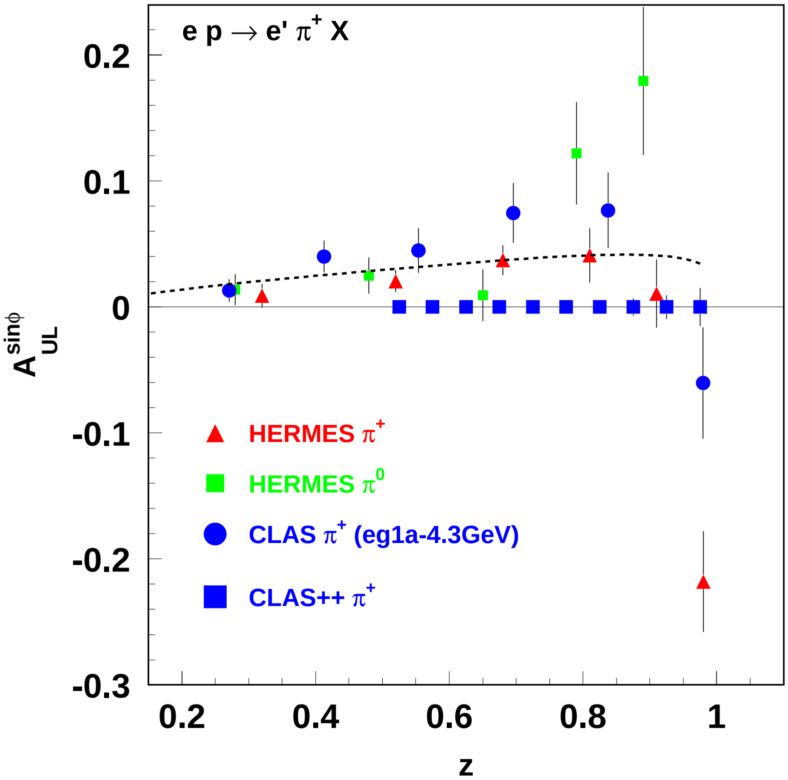

Figure 3.34: $A_{UL}^{\sin\phi}$ as a function of z from CLAS compared to HERMES [106, 107]. Squares are projection of CLAS 12 GeV. The curve is the prediction from [115] for HERMES kinematics.

3.3.2 Flavor Decomposition

The SIDIS cross section for a polarized beam and a polarized target contains contributions σ_{LT} and σ_{LL} proportional to the beam helicity (λ_e) and the transverse (S_T) and longitudinal (S_L) components of the target spin with respect to the virtual photon direction [20]. The most well-known result for leptoproduction is the double-polarized asymmetry integrated over the final hadron transverse momentum:

$$\sigma_{LL} \propto \lambda_e S_L y(1-y/2)\sum_{q,\bar{q}} e_q^2 x\Delta q(x) D_1^q(z).$$

The semi-inclusive double-polarization asymmetries with a longitudinally polarized target (σ_{LL}) have been the subject of considerable interest recently, both theoretically and experimentally. On the experimental side, luminosity has been one of the main constraints limiting measurements beyond $x = 0.5$. While the polarized u-quark

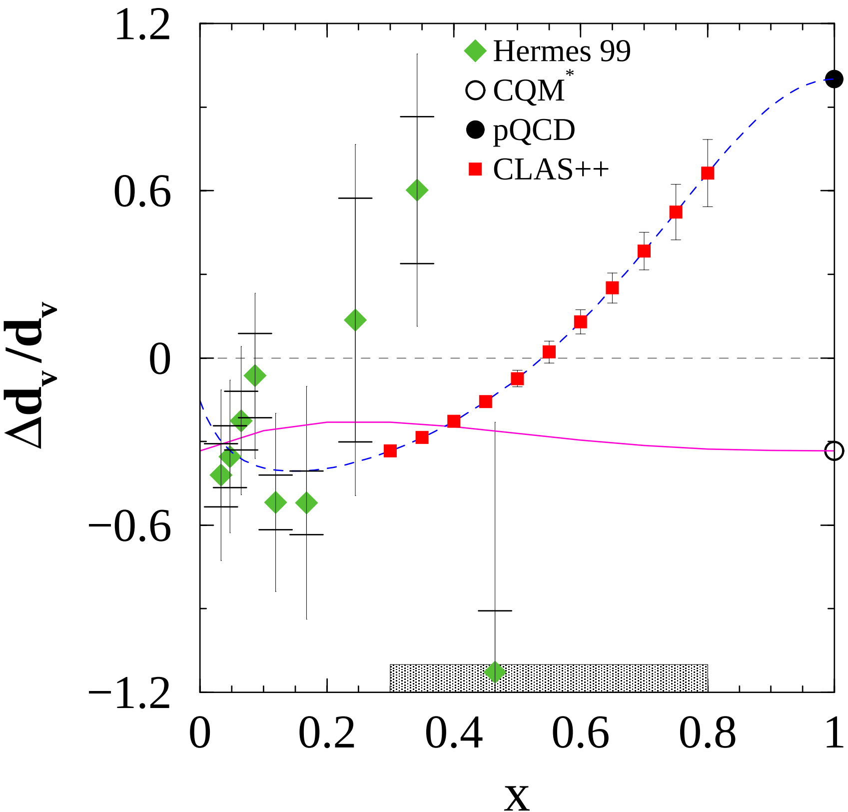

Figure 3.35: Projection of CLAS $\Delta d/d$ measurements at large x, compared with the constituent quark model (CQM) and pQCD-based parameterizations.

distribution is reasonably well established experimentally, the polarized d-quark distribution is poorly known, especially at large x, where there are significant differences between predictions derived from non-perturbative and perturbative models of QCD. The data shown in Fig. 3.35 represent the present knowledge of Δd at large x. An energy and luminosity upgraded CLAS will allow measurements in the x region above 0.5. Assuming factorization, SIDIS measurements may be used to extract polarized distribution functions using polarized proton and deuteron targets. The extraction of polarized-quark distribution functions from semi-inclusive asymmetries could be done either using the purity technique [100] or the method based on the extraction of spin asymmetries in the difference of π^+ and π^- counts [117].

3.3.3 Semi-Exclusive Meson Production

In the processes of semi-exclusive electroproduction, the final meson is produced at short distances via hard-gluon exchange [118, 119, 120], with a characteristic rapidity gap between the current fragmentation region and target fragmentation region. This mechanism is expected to dominate the cross section in the kinematic regime where

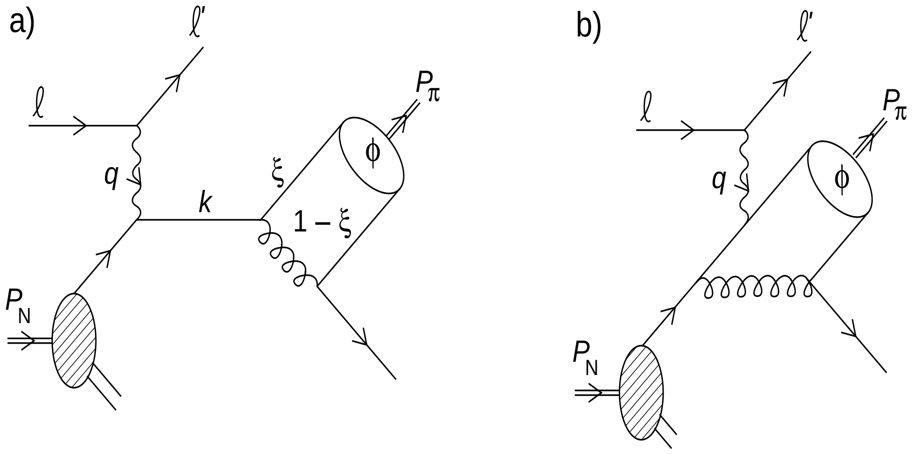

Figure 3.36: Leading contributions to the amplitude of the reaction $u + e^- \to e^- + \pi^+ + d$.

the ejected meson picks up most of the virtual photon momentum (or large z) [119]. Phenomenological fragmentation functions are not required to describe this important class of deep-inelastic processes, since the mechanism of meson production from a quark is described exactly by pQCD. One can view it as a first step in solving the problem of meson formation in hard processes. It is essential that in the theory of semi-exclusive reactions, formation of the final hadronic state is described in terms of quark distribution amplitudes, therefore providing a connection between inclusive and exclusive reactions (see Fig. 3.36). It was also noted that with CEBAF upgraded to 12 GeV, the semi-exclusive channel allows one to reach high virtuality of the exchanged gluon, corresponding to about $Q^2 \sim$30 GeV^2 for the exclusive case of the pion form factor [121].

It was shown in Ref.[118] that higher twist effects may be isolated in semi-exclusive pion production for moderate values of Q^2. Significant $\cos\phi$ and $\cos 2\phi$ moments (see Fig.3.37) were predicted in the exclusive limit ($z \to 1$).

An important physics implication of connection between inclusive and exclusive reactions is that the corresponding subprocess, $\gamma^* q \to \pi q$, is an essential component of the formalism of Deeply Virtual Meson production. Semi–inclusive measurements may therefore produce model–independent information necessary to extract (polarized) Generalized Parton Distributions from deeply–virtual exclusive electroproduction of mesons.

The CLAS^{++} detector can provide complete kinematic coverage of semi-exclusive electroproduction reactions in the deep-inelastic region.

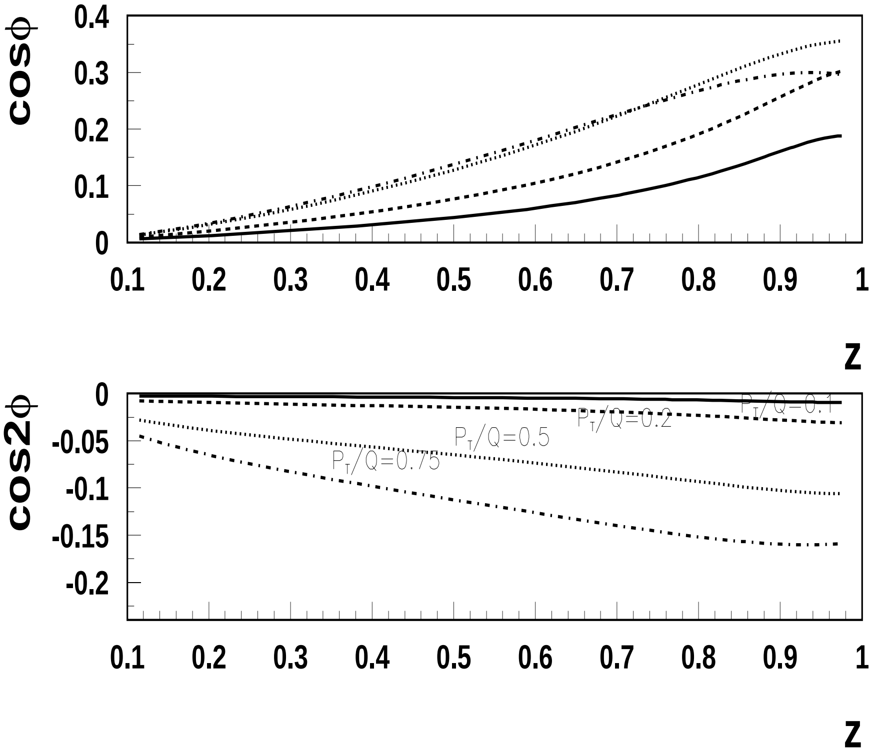

Figure 3.37: Azimuthal moments in unpolarized cross section as a function of z for different values of transverse momentum of the final π^+.

3.3.4 Conclusions

In summary, with upgraded energy and luminosity, CLAS can study single- and double-spin asymmetries, involving essentially unexplored chiral-odd and time-odd distribution functions, like transversity[29, 30], Sivers[18, 25, 26, 28] and Collins[19] functions and shed light on the quark transverse momentum distributions and the orbital angular momentum [19, 21, 20, 109, 122]. With good particle identification, single- and double-spin asymmetries can be extracted for different hadrons, enabling flavor decomposition of different distribution functions. Measurement of SSAs with K^+ (see Fig. 3.38 for the ratio of K^+, π^+ yields) in comparison with SSA for π^+ would provide an experimental test of factorization and u-quark dominance at JLab energies[123].

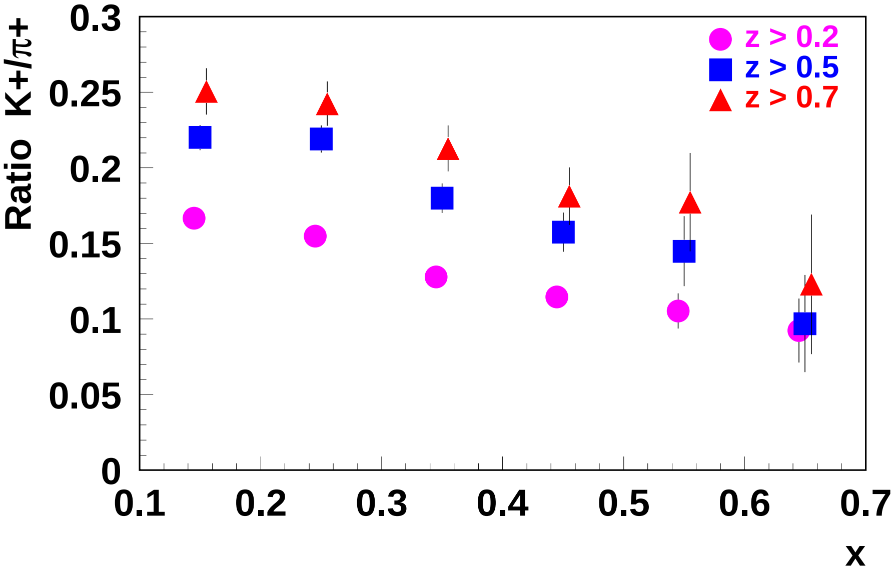

Figure 3.38: The expected ratio of K^+ to π^+ as a function of x_B from CLAS with 12 GeV, based on studies from the LEPTO event generator.

3.4 Properties of QCD from the Nuclear Medium

3.4.1 Introduction

Quantum Chromodynamics, the theory of the strong force, exhibits several exotic features not found in the other elementary forces. One such feature is confinement, the property that the binding forces between the elementary constituents of hadrons grow with increasing separation distance. Understanding this phenomenon is one of the central topics in hadronic nuclear physics. Intimately related to confinement is the process of hadronization, where hard interactions with an individual parton create longitudinal regions of high energy density that generate a spray of new particles emerging in a somewhat correlated direction. One consequence of confinement is that colored objects such as isolated quarks or gluons may not be observed directly, so that their properties must be inferred through indirect means.

A second exotic feature of QCD is the property of color transparency, the tendency of small-sized color singlet configurations to have a reduced interaction cross section. This is expected to be manifested, e.g., in reactions where an emerging particle could interact with nearby hadrons, such as a modified final state interaction from a nuclear target.

The following sections describe several approaches to gaining new understanding of these QCD properties by using the nuclear medium. Studies of the transparency of nuclei to colored quarks emerging from hard interactions are hoped to reveal the time scales of the hadronization process. Kinematic broadening of the transverse momentum spectra from the resulting hadron may yield additional clues concerning the energy loss of the colored quark, and its correlations with the emitted soft gluons. For these two topics, a large program is proposed to characterize the dependencies on Q^2, ν, p_T, z, helicity, hadron mass and size, and quark flavor. In a second thrust, nuclear transparency to vector mesons is suggested to provide definitive demonstrations of the existence of color transparency in the few-GeV^2 kinematic regime, using coherent reactions and also incoherent reactions at fixed coherence length. The magnitude of the effect predicted by models is quite large in both these approaches, offering the hope of a definitive observation of color transparency effects at JLab energies. Finally, quasielastic scattering in nuclei is proposed as an additional test of the role of the valence quarks in elastic scattering.

A related topic is the study of properties of nucleons interacting with each other at small distances. These can be isolated using deuteron electrodisintegration where a backward-moving pseudo-spectator proton is measured and used to characterize the initial state momenta of both nucleons. Modifications to the neutron's structure function due to this short-range interaction can therefore be determined, yielding new information on structural alterations of strongly interacting six-quark systems.

Since the following sections represent distinct scientific ideas, they are presented as independent projects. However, it should be appreciated that most of these experiments will be done in parallel by sharing the same beam time. This economy is simply the result of the broad kinematic coverage, good particle identification, and non-restrictive triggers characteristic of CLAS.

3.4.2 Quark Propagation

Space-time Characteristics of Hadronization

Due to the property of confinement, a struck quark in a hard process will evolve in space-time to produce multiple hadrons through the complex process of hadronization. This behavior is a unique distinctive of QCD. By studying the properties of the particles emerging from deep inelastic scattering (DIS) on a range of nuclei, important information on the characteristic time-distance scales of hadronization can be determined as a function of several variables.

The physical picture of hadronization in a nucleus begins with a hard interaction on a bound quark within the nuclear volume. This is illustrated in Fig. 3.39. For large Q^2 and ν the initial interaction is localized to a very small volume and results in an energetic quark propagating through the nuclear medium. Ultimately this quark emerges bound in a hadron, accompanied by other hadrons generated in the process. The time interval between the $\gamma^* q$ interaction and the hadron being fully reconstituted is often referred to as the *formation time*. If the formation time is much smaller than the nuclear transit time, then the hadron that carries the struck quark will strongly interact with the nuclear medium. This hadron will then be 'lost' in the sense that the event shifts to higher multiplicity and lower particle momenta relative to the same interaction on a smaller nucleus. If, on the other hand, the formation time is much longer than the nuclear transit time, then the formed hadron will not interact with the nuclear medium. (The propagating quark or partially formed hadron is expected to have little interaction with the medium, an expectation that seems to be borne out by the data[31].) In this way, hadron absorption by nuclei can be used to estimate the time scales of the hadronization process.

The observable that is used to quantify this absorption is the *hadronic multiplicity ratio* R^h_M. This quantity is defined by

$$R^h_M = \frac{\left\{ \frac{N_h(z,\nu)}{N_e^{DIS}(\nu)} \right\}_A}{\left\{ \frac{N_h(z,\nu)}{N_e^{DIS}(\nu)} \right\}_D} \tag{3.39}$$

In this expression, N_h is the number of hadrons produced in DIS events and N_e^{DIS} is the number of associated DIS electrons. The numerator corresponds to target nucleus A, and the denominator corresponds to deuterium. ν is the energy transferred by the electron, and z is the hadron energy divided by ν ($0 < z < 1$). In

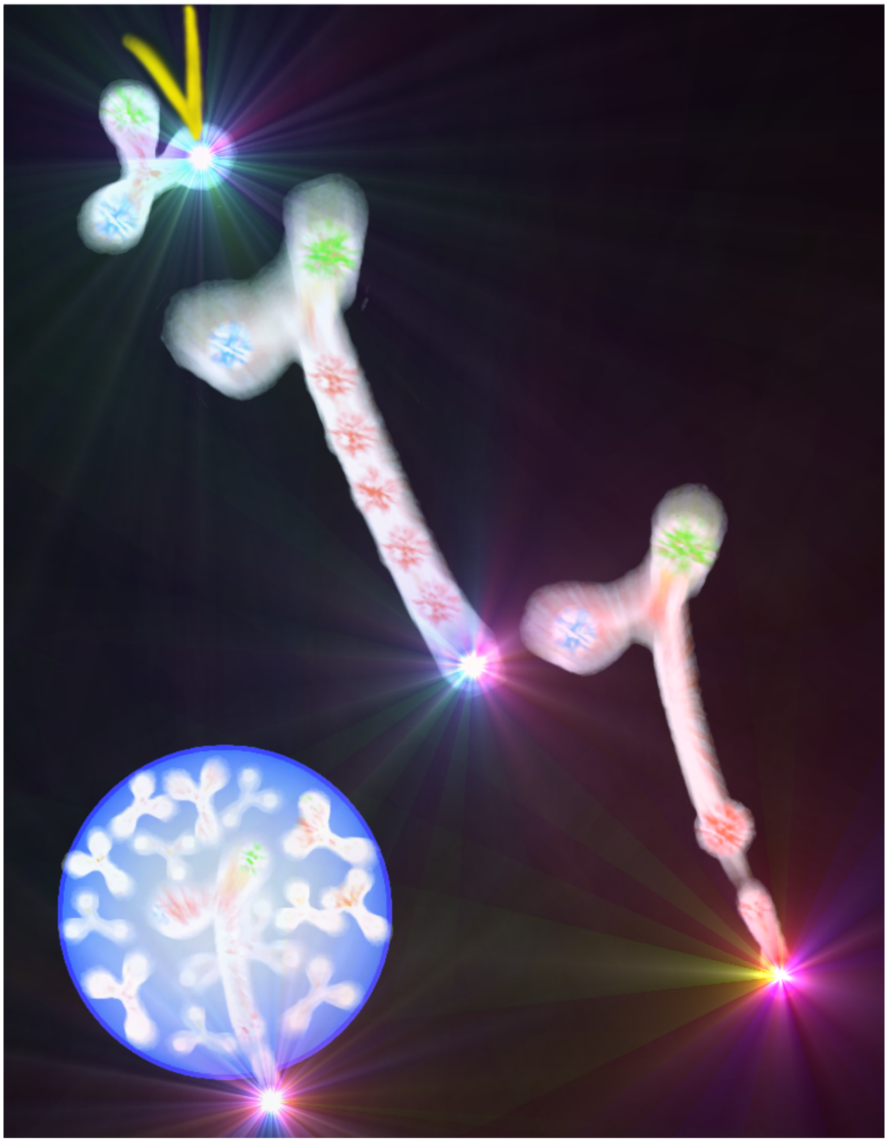

Figure 3.39: Artist's conception of the hadronization process in the valence quark regime. In the upper left corner, a quark undergoes a hard interaction with a virtual photon; in the middle picture the struck quark separates rapidly from the other quarks, forming a region of high energy density in which several proto-hadrons begin to form; in the bottom right-hand corner the struck quark emerges as part of a newly-formed hadron. In the bottom left corner of the figure, this process is visualized implanted in a nucleus; by varying the nuclear size, the distance scales involved can be probed, since the fully formed hadron will interact with the nuclear medium.

the QCD-improved parton model, R^h_M is given by ratios of sums over products of the quark distribution functions with fragmentation functions.

There are several scientific issues surrounding the hadronization distance scale studies. An important example is the fundamental process of gluon emission. The present understanding of gluon emission by the propagating quark is that it occurs both in vacuum and within the nuclear medium; within the nuclear medium it is additionally stimulated by multiple scattering from the nuclear partons. The propagating quark loses energy as a result. In a hot nuclear medium an additional dynamic of thermally stimulated gluon absorption and emission comes into play, while this is irrelevant in the cold nuclear medium. At some point the propagating quark evolves into a hadron, and the copious production of gluons ceases. The balance between gluon emission and hadronization, and the relationships between the two, are not established theoretically or experimentally, and this is a major theme addressed by the measurements identified here. Most experimental efforts, as will be discussed below, have focused on formation of either pions or protons; the proposed CLAS^{++} measurements will address a much broader spectrum of hadrons, as seen in the table in this section, which lists nearly 20 hadron species that will be accessible.

In the following, two model approaches will be discussed in order to give a flavor for the physics issues addressed by the proposed data. The first is the gluon bremsstrahlung model[124][125], which predicts $R^h_M(\nu, z, A)$ and other quantities for leading (highest momentum) pions. The second is a model based on leading-twist-four pQCD calculations[126], which, starting from a measurement of $R^h_M(\nu, z, A)$ for one nucleus A, can predict $R^h_M(\nu, z, A)$ for other nuclei.

In the gluon bremsstrahlung model, a time and energy dependent energy loss by gluon emission is modulated by a hadronization model. First, the time dependence of the energy loss in vacuum by gluon emission is described by:

$$\begin{aligned} \Delta E_{radiated}(t) = & \\ & \frac{\epsilon}{2} t Q^2 \Theta(t_1 - t) \ + \\ \epsilon\nu(1 - z_h)\Bigg\{ & (1 + ln(\frac{t}{t_1}))\Theta(t - t_1) \ + \\ & ln(\frac{Q^2}{\lambda^2})\Theta(t - t_2) \ \Bigg\} \end{aligned} \tag{3.40}$$

In this equation, if the transverse momentum of the gluon is k_T and the strong coupling constant is α_s, then $\epsilon = \frac{4\alpha_s(k_T^2)}{3\pi}$, λ is the lower limit of k_T (taken to be small), $t_1 = \frac{(1-z_h)}{x_{Bj} m_N}$, $t_2 = \frac{Q^2}{\lambda^2} t_1$, and $x_{Bj} = \frac{Q^2}{2m\nu}$. This form of the equation assumes $Q^2 >> \lambda^2$ so that $t_1 < t_2$. The time derivative of Eqn. (3.40) gives $\frac{dE}{dx}$ for the quark. This equation incorporates two time scales, t_1 and t_2. As is evident from Eqn. (3.40), the term in the first line is non-zero from the interaction time up until t_1, and after

Table 3.2: Final-state hadrons potentially accessible for formation length and transverse momentum broadening studies in CLAS. The rate estimates were obtained from the LEPTO event generator for an 11 GeV incident electron beam. (The criteria for selection of these particles was that $c\tau$ should be significantly larger than nuclear dimensions, and their decay channels should be measurable by CLAS^{++}.)

hadron	$c\tau$	mass (GeV)	flavor content	detection channel	production rate per 1k DIS events
π^0	25 nm	0.13	$u\bar{u}d\bar{d}$	$\gamma\gamma$	1100
π^+	7.8 m	0.14	$u\bar{d}$	direct	1000
π^-	7.8 m	0.14	$d\bar{u}$	direct	1000
η	0.17 nm	0.55	$u\bar{u}d\bar{d}s\bar{s}$	$\gamma\gamma$	120
ω	23 fm	0.78	$u\bar{u}d\bar{d}s\bar{s}$	$\pi^+\pi^-\pi^0$	170
η'	0.98 pm	0.96	$u\bar{u}d\bar{d}s\bar{s}$	$\pi^+\pi^-\eta$	27
ϕ	44 fm	1.0	$u\bar{u}d\bar{d}s\bar{s}$	K^+K^-	0.8
K^+	3.7 m	0.49	$u\bar{s}$	direct	75
K^-	3.7 m	0.49	$\bar{u}s$	direct	25
K^0	27 mm	0.50	$d\bar{s}$	$\pi^+\pi^-$	42
p	stable	0.94	ud	direct	1100
$\bar{p}$	stable	0.94	$\bar{u}\bar{d}$	direct	3
Λ	79 mm	1.1	uds	$p\pi^-$	72
$\Lambda(1520)$	13 fm	1.5	uds	$p\pi^-$	-
Σ^+	24 mm	1.2	us	$p\pi^0$	6
Σ^0	22 pm	1.2	uds	$\Lambda\gamma$	11
Ξ^0	87 mm	1.3	us	$\Lambda\pi^0$	0.6
Ξ^-	49 mm	1.3	ds	$\Lambda\pi^-$	0.9

that point it is zero; after t_1, the terms in the second line contribute, and after time $t_2(> t_1)$, the second and third lines contribute, essentially reflecting the constraints of energy conservation. After the initial hard interaction of the virtual photon with the quark, the quark emits gluons at a constant rate up until the time t_1. From that point until t_2, the rate of energy emission is reduced; a Sudakov-type form factor ultimately cuts off the gluon emission. Finally, a hadronization model evolves the colored quark into a colorless hadron. It is instructive to give a few numerical examples for the kinematics accessible to CLAS^{++}; the example will be for the longest-lived leading hadron, which is characterized by $z = 0.5$, $Q^2 = 9\ GeV^2$, and $\nu = 9\ GeV$. For this hadron, $t_1 = 0.9\ fm$, and for this time interval the energy loss is $\frac{dE}{dx} = 3.9\ GeV/fm$. After 0.9 fm, the energy loss is reduced because of the factor $\nu(1 - z_h)$ to an average value 0.4 GeV/fm. The hadronization model evolves the colored quark to a colorless

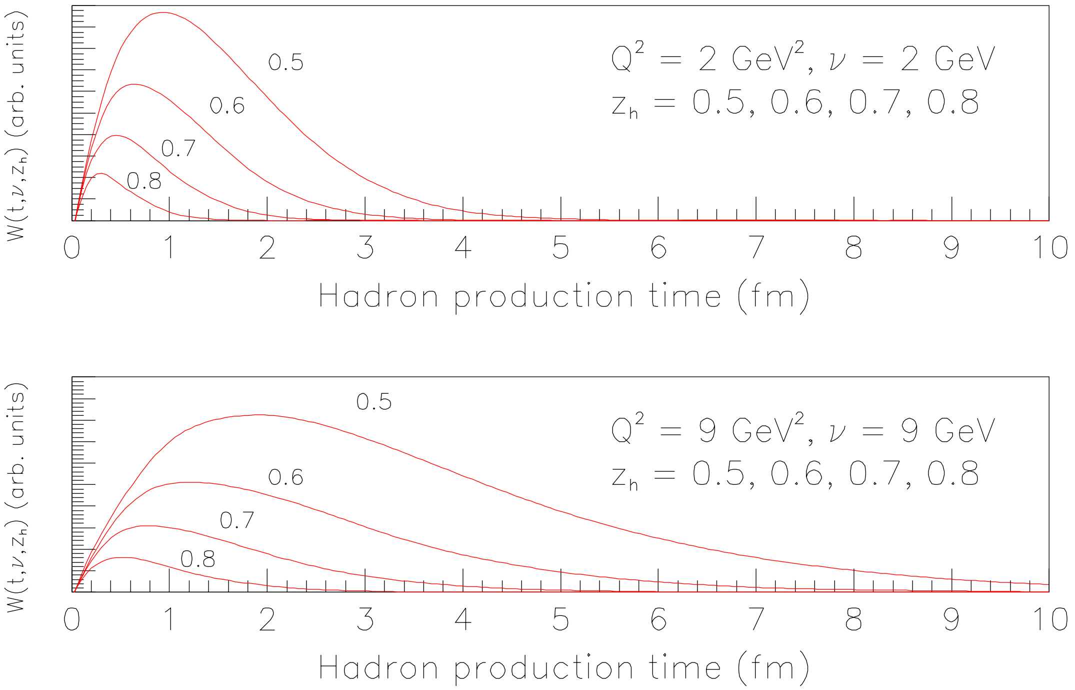

Figure 3.40: Distribution function $W(t, \nu, z_h)$ for leading hadrons as a function of hadron production time, for $Q^2 = 2\,GeV^2$, $\nu = 2\,GeV$, and $Q^2 = 9\,GeV^2$, $\nu = 9\,GeV$, in the gluon bremsstrahlung model. See text for discussion.

hadron in a mean distance of 3.5 fm; this distribution, however, has a long tail, extending to greater than 15 fm, as discussed below. As a check, the averaged energy losses mentioned above sum to 4.7 GeV, which, considering a small reduction due to the form factor, is quite consistent with $z = 0.5$.

The hadronization model mentioned above is based on a color dipole representation of the radiated gluons. Assuming that the leading hadron originates from a $q\bar{q}$ pair made up of the leading quark and the antiquark from the last emitted gluon, the leading dipole wavefunction can then be projected onto a hadron wave function. This projection produces a distribution function expressing the probability that the dipole evolves into a quark as a function of time, ν, and z_h. It is given by:

$$W(t, \nu, z_h) \propto \int_0^1 \frac{d\alpha}{\alpha}\, \delta\left[\alpha - 2\left(1 - \frac{z_h \nu}{E_q(t)}\right)\right] \int \frac{dk_T^2}{k_T^2}\, \delta\left[k_T^2 - \frac{2\nu}{t}\alpha(1-\alpha)\right] \times$$

$$\int dl_t^2\, \delta\left[l_T^2 - \frac{9}{16}k_T^2\right] \int_0^1 d\beta \delta\left[\beta - \frac{\alpha}{2-\alpha}\right] |\Psi_h(\beta, l_T)|^2. \tag{3.41}$$

In the above equation, α is the fraction of the light-cone momentum carried by the struck quark, δ signifies a Dirac delta function, $E_q(t) = \nu - \Delta E_{radiated}(t)$ is the energy of the struck quark as a function of time (c.f. Eqn. (3.40) for $\Delta E_{radiated}$), and $\Psi_h(\beta, l_T)$ is the light-cone wave function for the hadron with β and $1-\beta$ the fractions of the light-cone momentum carried by the two quarks in the leading hadron, with l_T their relative transverse momentum. Plots of this distribution function are shown in Fig. 3.40 (vertical axis is in arbitrary units). In the upper panel are distributions for $z = 0.5,\ 0.6,\ 0.7,\ 0.8$ for $Q^2 = 2\ GeV^2$ and $\nu = 2\ GeV$. The lower panel shows the same quantities for $Q^2 = 9\ GeV^2$ and $\nu = 9\ GeV$. As can be seen from these plots, for $z \rightarrow 1$ the hadronization distances are always smaller than the radius of the ^{14}N nucleus (2.6 fm, the smallest nucleus proposed for study here), while for $z = 0.5$ in the bottom panel, a non-negligible probability exists for hadronization to occur outside even a large nucleus such as ^{197}Au with a radius of 6-7 fm. Therefore, according to this model, this range in ν and Q^2 is particularly well-suited for studying the z dependence of the hadron formation time, or studying the ν dependence for hadrons with $z = 0.5$, using a range of nuclei. The connection of this quantity to experimental data is achieved by integrating over time to yield the fragmentation function $D^h(\nu, z_h) = \int_0^\infty dt W(t, \nu, z_h)$.

All of the above discussion was for quarks propagating through vacuum. Inserting this process into nuclei brings at least two further effects. First, multiple scattering of the quarks with the nuclear partons stimulates additional gluon emission, increasing the energy loss. Second, interactions of the formed hadrons with the nuclear medium modify the fragmentation functions. The current version of the gluon bremsstrahlung model can include the effect of medium-induced soft gluon radiation. For most of the kinematics accessible to CLAS^{++}, it is a few-percent effect within this model. However, for particular kinematic conditions, it can become more significant. The largest differences in the predictions of R^h_M with and without the medium induced radiation are found for lowest Q^2, highest ν, largest nuclei, and minimal z, which for this model is $z = 0.5$. A plot that illustrates this is shown in Fig. 3.41. The medium-induced radiation produces a shift in the prediction of R^h_M of more than 10% for the heavier nuclei under these particular kinematic conditions in this model. This demonstrates that there may be some experimental sensitivity for establishing the importance and magnitude of medium-induced radiation of gluons.

The modification of the fragmentation functions by the nuclear medium is treated in the gluon bremsstrahlung model with a path integral approach [127] that provides a prescription for evolution of the $q\bar{q}$ wave packet as it passes through the nuclear medium. Rather than a simple nuclear absorption, this provides a quantum-mechanical distortion of the wave function of the forming $q\bar{q}$ pair in addition to a nuclear attenuation. Effects such as color transparency and nuclear shadowing and anti-shadowing emerge naturally in this approach.

Turning now to the second model approach, the twist-four pQCD model [126]: in this approach, the nuclear modification is interpreted as being entirely due to

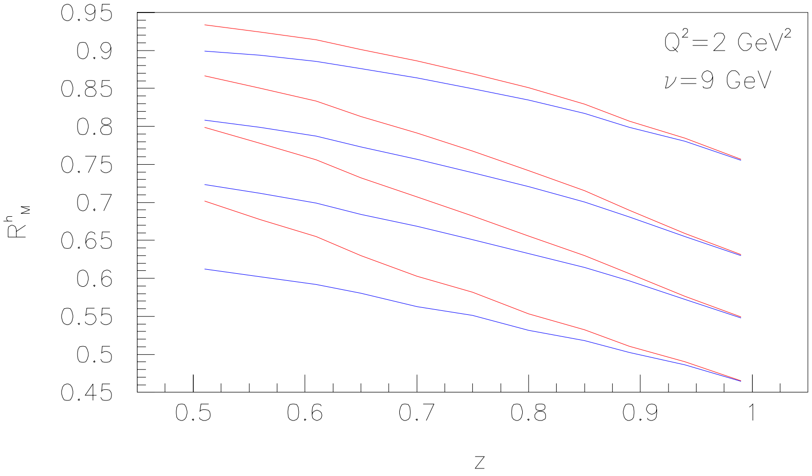

Figure 3.41: Calculations from the gluon bremsstrahlung model for R^h_M for (top to bottom) ^{14}N, ^{40}Ar, ^{84}Kr, ^{197}Au for $\nu = 9\ GeV$ and $Q^2 = 2\ GeV^2$ with (blue lines) and without (red lines) medium-induced gluon radiation. No difference is seen for the highest z, however for lower z there is more suppression due to medium-induced radiation, particularly for the heavier nuclei where the effect exceeds 10%.

energy losses passing through the nuclear medium, due to multiple scattering and soft gluon emission. The inclusion of the leading terms of higher-twist contributions leads to a prediction for medium-modified fragmentation functions with one adjustable parameter. In principle, predictions can be obtained for two or more nuclei by fixing the parameter for one nucleus and predicting the behavior for the other nuclei.

In this approach, the cross section for semi-inclusive DIS is written in the conventional way as a contraction of the lepton tensor with a hadronic tensor:

$$\frac{d\sigma^h_{\rm DIS}}{d\vec{p}_{e'}dz_h} = \frac{1}{E'}\frac{\alpha^2_{\rm EM}}{2\pi s}\frac{1}{Q^4}L_{\mu\nu}\frac{dW^{\mu\nu}}{dz_h}, \tag{3.42}$$

where the hadronic tensor is given by

$$\frac{dW^{\mu\nu}}{dz_h} = \sum_q \int dx f^A_q(x,Q^2) H^{(0)}_{\mu\nu} \widetilde{D}_{q\to h}(z_h,Q^2). \tag{3.43}$$

In these expressions, the scattered electron momentum and energy are $\vec{p}_{e'}$ and E', α_{EM} is the electromagnetic coupling constant, and s is the square of the initial-state four-momentum. The term $f^A_q(x,Q^2)$ is the nuclear quark distribution function, $H^{(0)}_{\mu\nu}$ represents hard scattering and is identical to that for ep scattering, and $\widetilde{D}_{q\to h}(z_h,Q^2)$

is a modified fragmentation function that is the source of the nuclear modification. This term is defined as the ordinary twist-two vacuum fragmentation functions plus a new term:

$$\widetilde{D}_{q\to h}(z_h, Q^2) \equiv D_{q\to h}(z_h, Q^2) + \Delta D_{q\to h}(z_h, Q^2). \tag{3.44}$$

The new term has the following form:

$$\begin{aligned} \Delta D_{q\to h}(z_h, Q^2) = \int_0^{Q^2} \frac{dp_T^2}{p_T^2} \frac{\alpha_s}{2\pi} \int_{z_h}^1 \frac{dz}{z} \times \\ [\Delta\gamma_{q\to qg} D_{q\to h}(z_h/z) + \Delta\gamma_{q\to gq} D_{g\to h}(z_h/z)] \end{aligned} \tag{3.45}$$

where p_T is the hadron's momentum component transverse to the virtual photon direction, α_s is the strong coupling constant, and the functions $\Delta\gamma$ are modified splitting functions; in this expression, the D terms are again the ordinary twist-two vacuum fragmentation functions. The modified splitting functions $\Delta\gamma$ are complicated expressions that contain a quark-gluon correlation function with four independent twist-4 parton matrix elements. These arise from keeping the leading twist-four terms in the twist expansion, and represent double-scattering processes at the partonic level. (The splitting functions also contain terms that preserve infrared stability and unitarity.) An LPM-like interference (LPM, or Landau-Pomeranchuk-Migdal effect [128],[129],[130]) is observed in the behavior of these amplitudes when the gluon formation time is much larger than the nuclear size. The strength of the quark-gluon correlation function within nuclei is the free parameter available in this approach. For a given process, such as DIS, it can be fixed for one nucleus and used to predict the behavior for other nuclei.

The two model approaches highlighted in the above discussion have in common the fundamental role of gluon emission. However, they are very different with respect to the precise source of the nuclear medium modification effects. In the gluon bremsstrahlung model, it is the interaction of formed hadrons with the nuclear medium that modifies the fragmentation function. By contrast, in the twist-four pQCD model it is the in-medium multiple scattering and induced gluon emission that is responsible. If hadronization typically occurs on the few-fm distance scale, the first picture is more appropriate. If the typical distance scale is tens of fm, the second picture may be more valid. While much has been written about hadronization distances, it has not been rooted in data, and our *experimental* understanding of these issues is extremely poor.

Exploratory studies of R_M^h have been carried out at HERMES using 12 and 27 GeV positron beams on nitrogen and krypton targets; the higher energy nitrogen data have been pubished to date[31],[32]. These studies have been interpreted as being dominated by hadronization, and characteristic formation times for negative

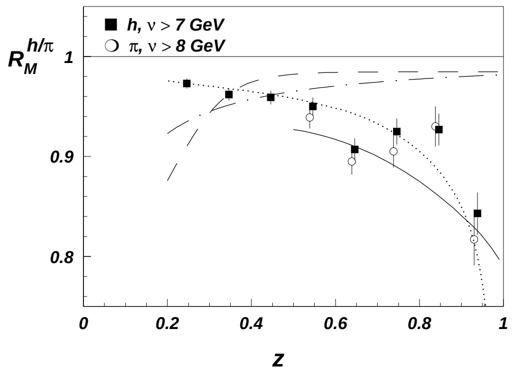

Figure 3.42: The z dependence of R_M^h from the Hermes data for ^{14}N plotted against the results from the gluon bremsstrahlung model (solid curve) and various parameterizations.

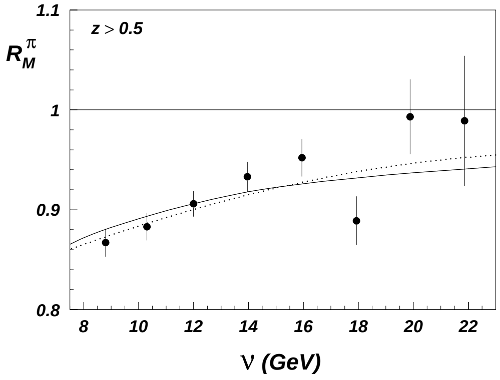

Figure 3.43: The ν dependence of R_M^h from the Hermes data for ^{14}N plotted against the results from the gluon bremsstrahlung model (solid curve) and various parameterizations.

and positive pions, and protons, have been derived. One result of this work was to conclude that the proton formation time is more than a factor of two greater than that for pions, and that there is a strong dependence on $z = \frac{E_{hadron}}{\nu}$. The formation time for positive pions was the same as that for negative pions, within the errors. Based on their limited statistics, they did not observe a significant dependence of the formation time on Q^2.

The HERMES nitrogen analysis employed a phenomenological formalism [131] that characterizes the hadronization process by a single time constant, the formation length, which is the characteristic parameter of a decaying exponential $P_q(x_1 - x_2) = exp[(x_1 - x_2)/\tau_f]$ representing the probability that the propagating object struck at coordinate x_1 is still a quark at coordinate x_2. The probability that the object is a hadron is then $1 - P_q$. The propagating object interacts with a quark-nucleon cross section σ_q while it is a quark, and a hadron-nucleon cross section σ_h while it is a hadron. The probability of interaction with the medium is taken as proportional to the nuclear density. Predictions for R_M^h are obtained by integration over z and impact parameter for spherical nuclei of varying radii. The parameters of the formalism are then σ_h and σ_q (assuming a Fermi form of the nuclear density), and any parameters that are built into τ_f.

The functional form of τ_f is not known from a fundamental theory, and several have been proposed. The HERMES analysis tested three basic forms and was able to eliminate two of the three based on the observed z dependence. Within the above phenomenological framework, the form that most closely represented their data was $\tau_f = c_h(1 - z)\nu$, where c_h is a constant depending on the hadron type. This functional form is visible in the gluon bremsstrahlung model expression for energy loss

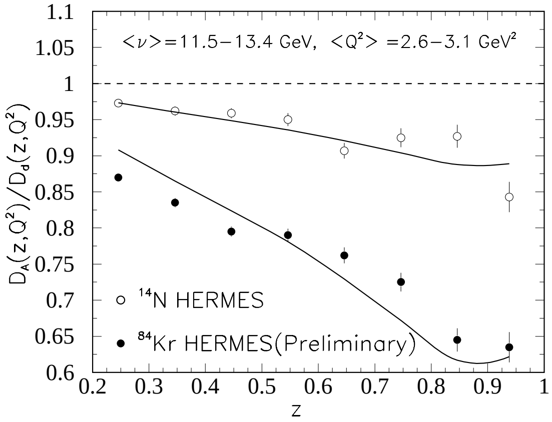

Figure 3.44: The z dependence of R_M^h from the Hermes data for ^{14}N and ^{84}Kr plotted against the results from the twist-four pQCD model.

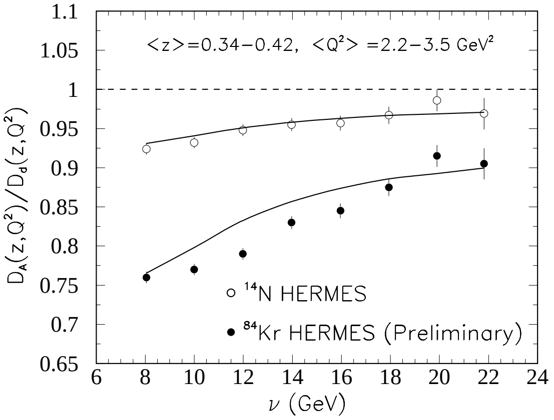

Figure 3.45: The ν dependence of R_M^h from the Hermes data for ^{14}N and ^{84}Kr plotted against the results from the twist-four pQCD model.

by gluon emission in Eqn. (3.40) and is approximately reflected in the time integral of Eqn. (3.41). (While the linear dependence on ν was common to all models as simply a relativistic boost, the less obvious form of the z dependence was predicted in advance by the gluon bremsstrahlung model in 1995.) Their analysis found $c_{\pi^+} = c_{\pi^-} = 1.4\ fm$, while for all hadrons (primarily protons) they found $c_h = 3.5\ fm$.

See Figures 3.42 and 3.43 for a comparison of the gluon bremsstrahlung model to some of the HERMES data. See Figures 3.44 and 3.45 for a comparison of the twist-four pQCD model to some of the HERMES data.

While many assumptions necessarily go into such an analysis, the HERMES pioneering studies offer tantalizing hints concerning the nature of hadronization. For instance, the longer formation time for protons compared to pions is what one might qualitatively expect, since the proton is larger and more massive than the pion. Similarly, one would expect positive and negative pions to have the same formation time, since they are the same size and mass. However, without further experimental study, the only progress that can be made is in the theoretical arena. For instance, the gluon bremsstrahlung model[124],[125] predicts a strong Q^2 dependence of $R_M^h(z)$ as can be seen in Figures 3.46 and 3.47. According to this model, the strong z dependence of $R_M^\pi(z)$ disappears with increasing Q^2. This prediction can only be tested with more data. Very little dependence of R_M^h on Q^2 was seen at HERMES, however, the study was based on integrating over both $z > 0.5$ and $\nu > 8\ GeV$ to obtain sufficient statistical accuracy, which may mask any Q^2 dependence. Similarly, a dependence on transverse momentum p_T, predicted by color string models, was not seen, however, the same integration over $z > 0.5$ and $\nu > 8\ GeV$ had to be performed to have statistical errors comparable to the systematic errors. Further, while there is an interesting suggestion that larger or more massive particles have a longer formation

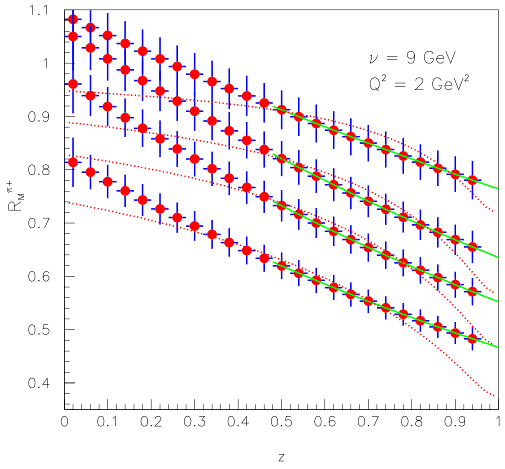

Figure 3.46: Z dependence of the hadronic multiplicity ratio for (top to bottom) ^{14}N, ^{40}Ar, ^{84}Kr, ^{197}Au for $\nu = 9\ GeV$ and $Q^2 = 2\ GeV^2$. The solid line is a gluon bremsstrahlung model calculation for $z > 0.5$ for pions. The dotted line shows the parameterization based on the HERMES 27 GeV data[31], which is independent of Q^2.

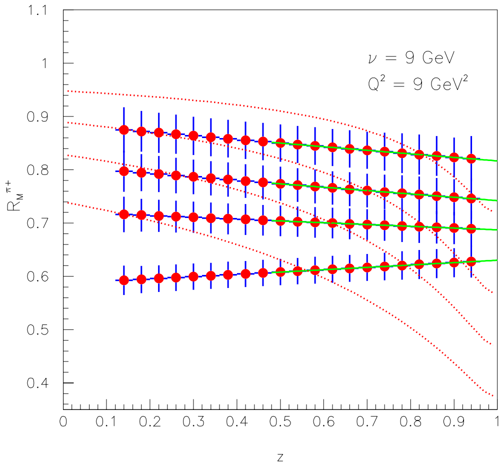

Figure 3.47: The same plot as in Fig. 3.46 for $\nu = 9\ GeV$ and $Q^2 = 9\ GeV^2$. The errors shown in both figures are a combination of statistical and systematic errors for 30 days of running at design luminosity. Note the dramatic change in the gluon bremsstrahlung model prediction for the higher Q^2 data.

length, there are still numerous outstanding questions. For instance, is this a mass effect or a size effect? Is there contamination from knocked-out protons or pions rather than particles created through a fragmentation process? Are there other reaction mechanisms contaminating the event sample? What is the flavor dependence of the formation time? How realistic is the relatively simple picture of hadronization within the nucleus on which these analyses are based?

These questions can be well-addressed by CLAS^{++} in a natural extension to the approved 6 GeV measurement[132]. The limited information available on the Q^2 dependence of R^h_M will be easily remedied by the high luminosity available after the 12 GeV upgrade. This can be seen in Figures 3.46 and 3.47 which show the wide range of Q^2 available for study, at large energy transfer; the z dependence can be determined in bins in ν and Q^2, rather than integrating over these variables. The large kinematic coverage of CLAS^{++} allows many bins in ν and Q^2 to be accessed in a simultaneous measurement. This can be seen from Fig. 3.48, where the z dependence of R^h_M is plotted in 24 bins in ν and Q^2 spanning the range $\nu = 3 - 9\ GeV$ and $Q^2 = 2 - 9\ GeV^2$. A group of 13 additional bins with similar coverage has been omitted to improve readability of the figure. The green lines show the gluon bremsstrahlung model[124],[125] prediction for pions with $z > 0.5$, and the red data

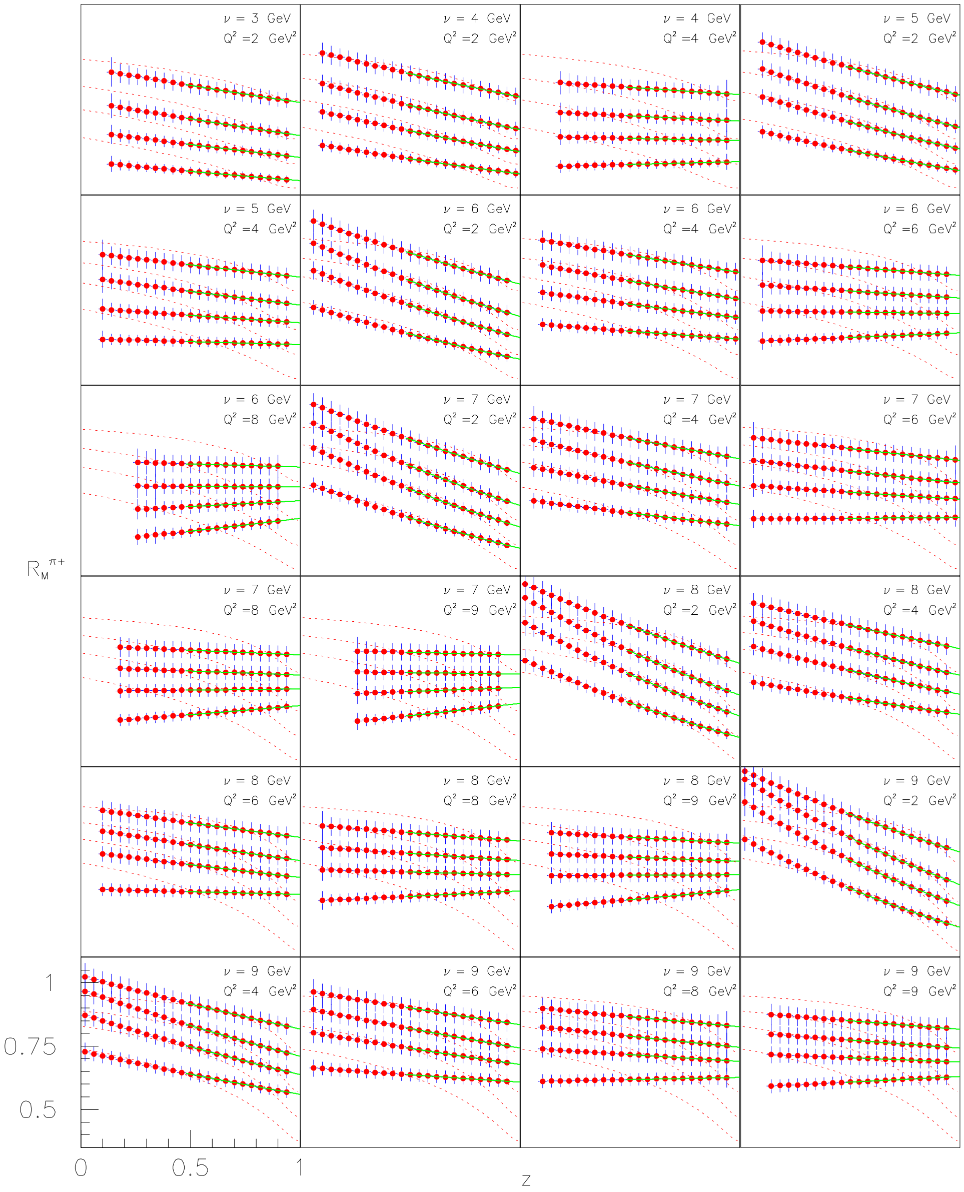

Figure 3.48: Z dependence of the hadronic multiplicity ratio for (top to bottom in each plot) ^{14}N, ^{40}Ar, ^{84}Kr, ^{197}Au for 24 bins in ν, Q^2. The solid line is a gluon bremsstrahlung model[124],[125] calculation for $z > 0.5$ for pions. The dotted line shows the parameterization based on the HERMES 27 GeV data[31], which is independent of Q^2. 13 bins with $Q^2 = 3$ and $Q^2 = 5\ GeV^2$ have been omitted to permit readability of this figure.

points indicate CLAS^{++} kinematic coverage. For reference, the red dashed lines indicate the parameterization derived by HERMES for pions, which depends on z and ν but not on Q^2. The errors on the data points are combined statistical and systematic errors; unlike the lower-rate channels described below, these data are dominated by systematic errors.

In a similar way, the p_T dependence can be isolated because of the increased luminosity. One particular interest is the behavior of R^h_M at high p_T, e.g., $p_T > 1\ GeV$. In that region, R^h_M has been seen to be *greater* than 1.0 by $10 - 20\%$ and rapidly rising with p_T in both the HERMES data as well as earlier EMC data. This effect may be compared to the Cronin effect in p-A scattering[133],[134]. Here the interesting region of $p_T > 1\ GeV$ is in the tail of the p_T distribution, therefore, one of the major benefits of the higher luminosity is to probe this effect out to higher p_T with improved statistical accuracy. The second benefit is again that multivariable dependences of R^h_M can be explored, e.g. in bins of z and ν.

The issue concerning contamination from potentially knocked-out protons (or pions) can be addressed by studying particles of a similar mass which were not preexisting in the nucleus, such as Λ particles or neutral kaons. In Fig. 3.49 are plots of invariant mass distributions that will serve to identify these particles in CLAS^{++}. These plots were made by taking the output of a LEPTO [135] (fragmentation event generator) simulation of 11 GeV electrons on protons and neutrons, applying an acceptance and resolution function, and reconstructing the data by going through all combinations of $p\ \pi^-$ and $\pi^+\pi^-$ events for Λ and $K0$, respectively, to simulate the semi-exclusive event analysis as closely as possible. The signal peaks for these particles are clearly visible in the upper two spectra, which show the distributions as a function of missing mass. The lower two spectra plot ν on the vertical axis; as can be seen, there is coverage over essentially the entire ν range. This will allow hadronization studies to be performed just as in the case of the proton and pions. An important background reduction not reflected in these plots is that these events will come from detached vertices; a cut on the vertex position should eliminate most of the background in the real experiment. Because these particles are identified through charged particle channels, the resolution for their transverse momentum will be adequate to study momentum broadening(discussed in the following section).

As another example of relevant neutral particle channels, Fig. 3.50 shows the spectrum of particles obtained by combinatoric analysis of all photon pairs, using the same method as for the above Λ $K0$ analysis. This approach takes advantage of the large acceptance of CLAS^{++} for neutral particles, using the new calorimeters in the central detector as well as the new and existing forward calorimeter components. While the raw backgrounds here are more substantial and the mass resolution is broader, it is still clear that the signal is more than adequate to carry out systematic formation length studies. (Further background reduction may be possible after additional study of the event topologies.) The application of this experimental capability to formation length studies brings entirely new information to bear on the problem, since it allows

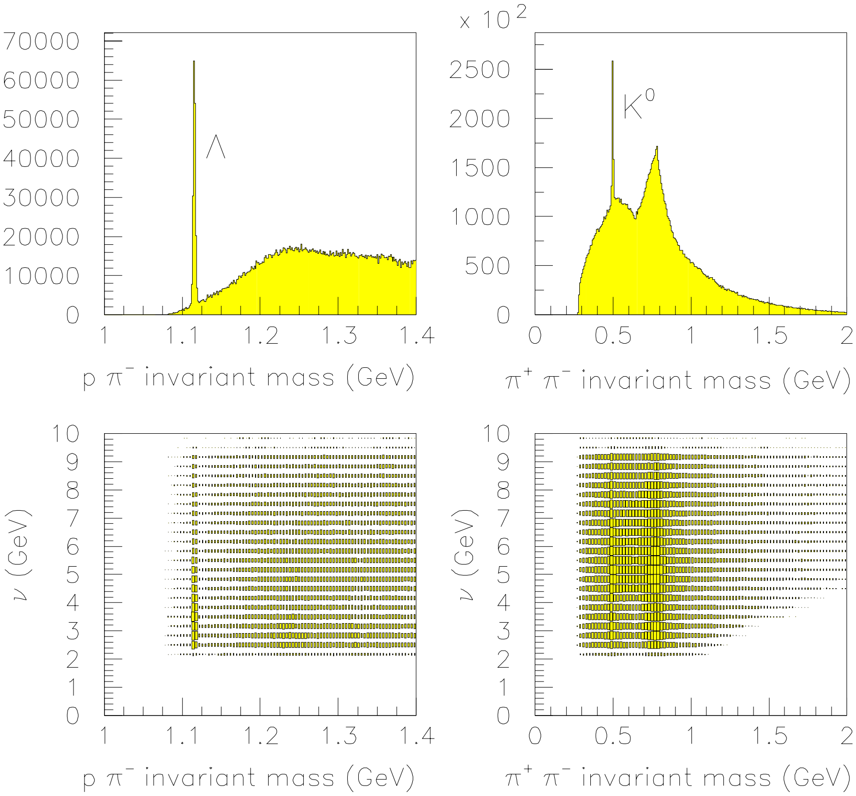

Figure 3.49: Expected data from a LEPTO simulation at 11 GeV, showing production of lambda baryons and neutral kaons for a few PAC hours of data acquisition time. A parametric acceptance and resolution function has been applied. It is expected that a significant reduction in the background can be achieved by identifying detached vertices for both of these particles.

comparison of the neutral pion channel to the charged pion channels, and comparison of the η to the $K0$, which has a different flavor content but a similar mass.

The flavor and mass dependence can be further studied by using a wide array of particles that are known to be stable over a distance scale much larger than nuclear dimensions. In the table in this section is a list of nearly twenty particles which should be accessible to formation length studies in CLAS^{++} over some kinematic range. A quite impressive advance in understanding formation lengths can be attained by systematically studying the production of all of these particles for a series of nuclei, providing strong constraints on model calculations. Because of the large acceptance and good particle identification characteristics of CLAS^{++}, all of these particles emerge from the same data set. Because of the high luminosity, the dependence on multiple variables can be studied even for the particles that have a low

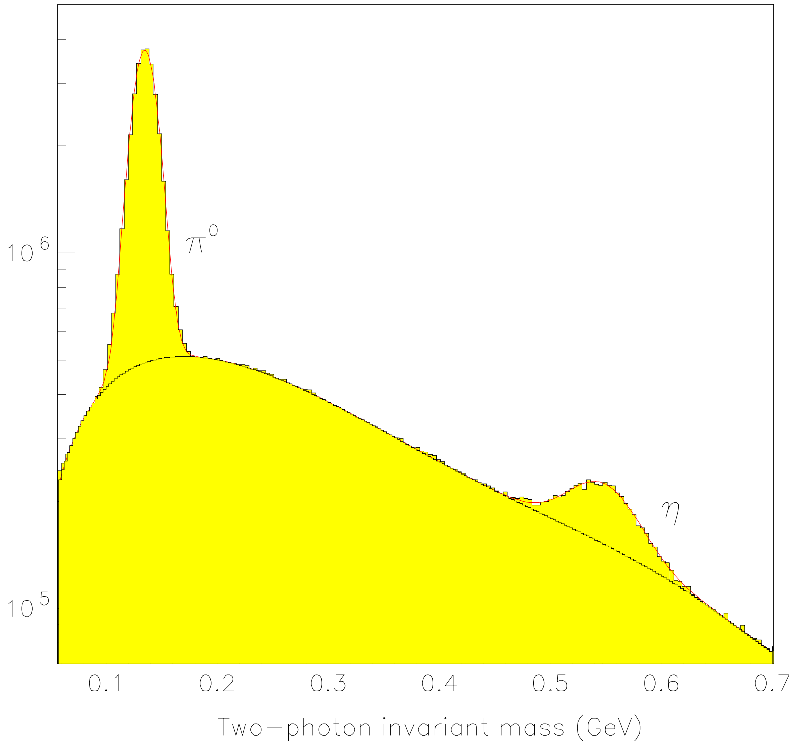

Figure 3.50: Expected data from a LEPTO simulation at 11 GeV, showing production of neutral pions and eta mesons for a few PAC hours of data acquisition time. A parametric acceptance and resolution function has been applied.

production cross section or for which the acceptance is small. The ability to carry out studies on a number of different particles will help to evaluate if this simple picture of hadronization within nuclei is adequate. If a consistent picture emerges, then one can have confidence in that picture; if not, a more sophisticated framework can be developed.

In conclusion, the opportunity exists to thoroughly and systematically study the space-time characteristics of hadronization by determining the variable dependences of the formation length, and exploring manifestations of quark energy loss from medium-induced gluon bremsstrahlung. The studies can be carried out as a function of Q^2, ν, p_T, z, helicity, hadron mass and size, and quark flavor. This large program is expected to yield a wealth of new insights into the nature of the gluon emission and hadronization process, which is a direct manifestation of confinement.

Transverse momentum broadening

As a struck quark traverses the color field presented by a nucleus, it scatters off the partons in the medium, losing energy primarily by radiation of gluons. The gluon emission, which is a fundamental prediction of QCD, may have a coherent character similar to that of the Landau-Pomeranchuk-Migdal (LPM) effect [128],[129],[130] in the QED energy loss of charged particles passing through atomic matter. This coherence, in combination with the non-Abelian nature of QCD radiation, predicts that the energy loss will be *quadratic* in the distance the quark travels through a nuclear medium, in strong contrast to the energy loss in quantum electrodynamics.

A number of theoretical studies have linked the broadening of the transverse momentum to the energy loss due to gluon radiation[136],[137]. Specifically, if the transverse momentum broadening through a nuclear medium of thickness L is expressed as $< p_T^2 >_L$, then the energy loss per unit length $-dE/dx$ is given approximately by

$$\frac{-dE}{dx} = \frac{\alpha_s}{\pi} N_c < p_T^2 >_L \tag{3.46}$$

where N_c is the number of colors and α_s is the strong interaction coupling constant. Further, the broadening is expected to be proportional to L, i.e., to vary for nuclei as $A^{\frac{1}{3}}$. As a result, the total energy loss is predicted to scale as L^2, a novel behavior quite unlike the QED energy loss of particles traveling through ordinary atomic matter. An observation of the quadratic energy loss would be a striking confirmation of the importance of coherence behavior in these processes, such as the LPM effect.

Transverse momentum broadening has also been theoretically linked to a correlation function between hard quarks and soft gluons[138]. Therefore, these studies offer one avenue for studying partonic correlations. All of these simple interpretations depend on the assumption that the quark travels independently in the medium, which in turn requires an understanding of the hadronization time scales discussed in the previous section.

A further interest in this study is to gain a greater understanding of the 'Cronin effect,' the overabundance of high p_T events in heavier nuclei relative to light nuclei[133],[134]. This effect, while seen most prominently in hadron-nucleus scattering, is also seen in DIS studies on nuclei[139]. An advantage of DIS for these studies relative to hadron beam studies is that the probe does not multiple scatter or otherwise interact before undergoing the interaction being studied. The primary limitation of the study of this phenomenon in DIS to date is statistical accuracy, since the events of interest are for $p_T > 0.5\ GeV$, where the rate is correspondingly low. Since one of the chief contributions CLAS^{++} brings to these studies is high luminosity, it should be possible to determine the kinematic dependences that accompany the effect, such as the dependence on the coherence length[134].

In general, p_T broadening will ultimately be predictable within the context of quark propagation models, and therefore will provide further discrimination power to differentiate among the models.

Experimentally, the determination of transverse momentum broadening for channels including only charged particles will be straightforward (see the table earlier in this section). A detailed study with a realistic simulation is required to estimate the

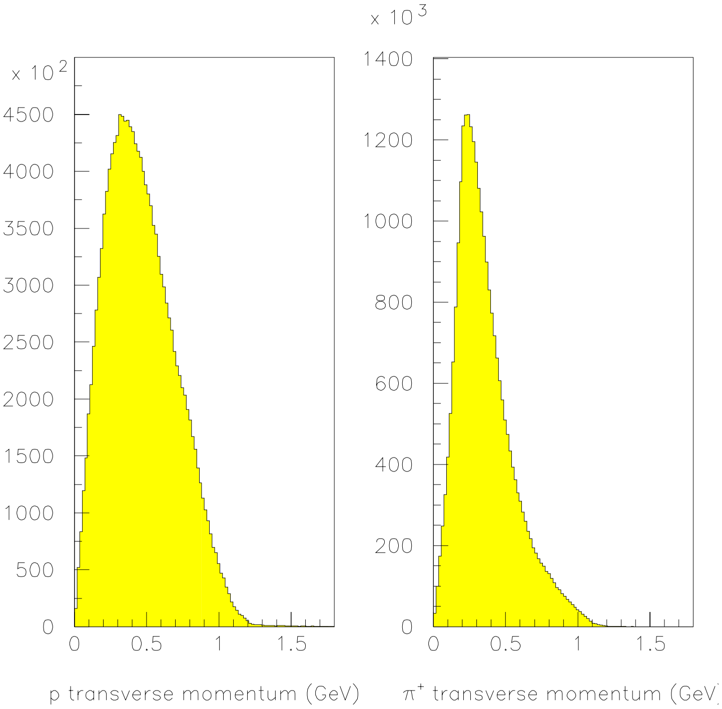

Figure 3.51: Expected data from a LEPTO simulation at 11 GeV, showing transverse momentum distributions for protons and positive pions for a few PAC hours of data acquisition time. A parametric acceptance and resolution function has been applied. For this simulation, the LEPTO parameter describing the intrinsic quark momentum distribution is set to its nominal value of 0.44 GeV. The quantity shown is expected to broaden measurably for nuclear targets due to partonic multiple scattering, and the high momentum tail is expected to be enhanced in heavier nuclear targets compared to deuterium.

transverse momentum resolution for a number of these channels. A substantial body of new information will clearly become available from this data.

3.4.3 Color transparency in coherent vector meson production

The factorization property of hard scattering reactions is a result of the fundamental property of QCD, the phenomenon of asymptotic freedom, that leads to decreased interactions between quarks and gluons at short distances. Qualitatively, the presence of a hard probe allows one to create small size quark-gluon configurations whose interactions can be described in pQCD.

Small size configurations (also called point-like configurations, PLCs) of quarks and gluons produced in hard scattering reactions [140] will interact weakly with nuclear matter. This leads to the fundamental prediction of QCD, the existence of *color transparency* (CT), *i.e.* nuclear matter becomes transparent to a small color singlet object (see e.g. Refs. [141, 142] and references therein).

With the availability of high energy and high intensity electron beams, a new possibility in the experimental investigation of CT phenomena opens up, namely exclusive reactions. Electroproduction of vector mesons off a deuteron in fully exclusive reactions is one of them:

$$e + d \rightarrow e' + V + d' \tag{3.47}$$

where "V" is the ρ, ω, or ϕ vector meson. The decay products of the vector meson, as well as the scattered electron and the recoiling deuteron, will be detected in the final state. The detection of the nuclear response in coincidence with the produced final hadron state is the key element in the investigation of the space-time picture of hard exclusive reactions.

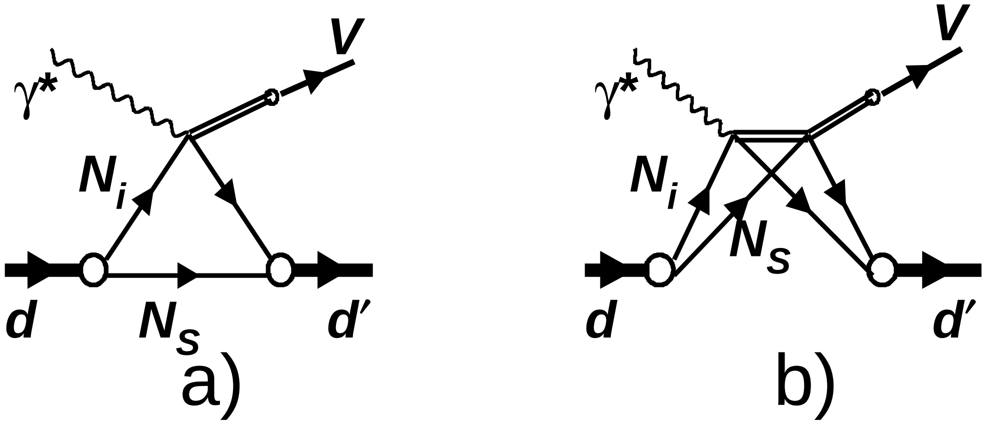

Figure 3.52: Leading mechanisms for coherent production of a vector meson on deuterium. a) dominates at $-t < 0.4(GeV/c)^2$, and b) at $-t > 0.5(GeV/c)^2$.

Coherent production of vector mesons off deuterium can be described by single- and double-scattering mechanisms. In Figure 3.52, the schematic diagrams for these processes are shown. Figure 3.52.a corresponds to single scattering (dominant at $-t < 0.4(GeV/c)^2$), where only one nucleon participates in the interaction and, therefore, the t dependence will follow the deuteron form factor. Figure 3.52.b corresponds to the rescattering mechanism (dominant at $-t > 0.6(GeV/c)^2$, where the photon interacts with one of the nucleons inside the target, and produces an intermediate hadronic state that subsequently rescatters from the second nucleon before forming

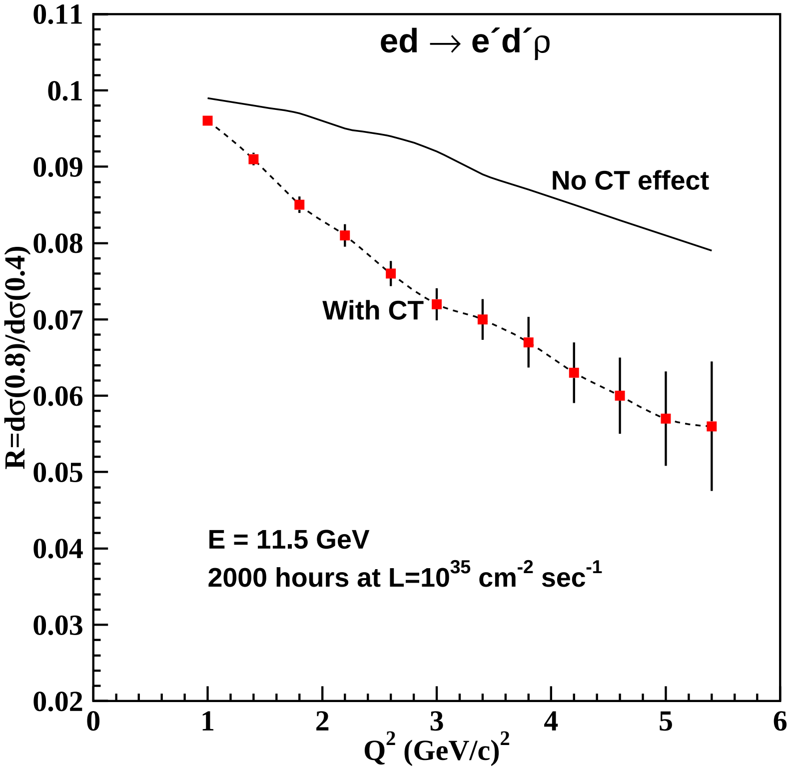

Figure 3.53: Expected errors on the ratio of cross sections for ρ^0 production at $-t = 0.4$ and 0.8 (GeV/c)^2 for 2000 hours of running at luminosity of 10^{35} cm^{-2} sec^{-1}.

the final state vector meson. This process has a harder t dependence than the first one, and this is where evidence of CT will manifest itself.

Coherent production is well established experimentally in the photoproduction of the ρ meson off the deuteron [143]. The key point in the investigation of CT phenomena is measuring the re-interaction process at different Q^2. The reduction of the transverse size of the produced wave packet with increased Q^2 will be detected through diminished re-interaction [144, 145]. The change of the slope of the t dependence at high t, with an increase of Q^2 at fixed coherence length, $l_c(x) = \frac{2\nu}{m_V^2+Q^2}$ with $m_V^2 \simeq 0.5$, will indicate a change of the reaction mechanism. The ratio of two differential cross sections at the same Q^2 and l_c but at different t, the first one in the double scattering region (t_1), Figure 3.52.b, and the second one in the single (t_2) scattering region, Figure 3.52.a, is particularly sensitive to this change while being insensitive to systematic uncertainties.

There is already a dedicated experiment planned to run on CLAS using a 6 GeV electron beam and the deuterium target [146]. This measurement will be the first exploratory measurement of the coherent production of vector mesons on the deuteron target, and will cover a range of Q^2 up to 3.5 (GeV/c)^2. At 12 GeV and with an upgraded CLAS, one can extend these measurements up to 6 (GeV/c)^2, where the effect is expected to be on the order of 50%. In Figure 3.53, the simulated Q^2 dependence of the ρ^0 electroproduction cross sections ratio at $-t = 0.8$ (GeV/c)^2 and at $-t = 0.4$ (GeV/c)^2 are shown. Error bars represent the expected statistical error and correspond to 2000 hours of running CLAS at a luminosity of 10^{35} cm^{-2}sec^{-1}. The solid curve corresponds to Glauber calculations without CT effects and the dashed curve includes CT effects.

3.4.4 Q^2 Dependence of Nuclear Transparency for Incoherent ρ^0 Electroproduction

Introduction

One of the major goals of Jefferson Lab (JLab) is to explore and study the interface between the nucleonic picture of the strong interaction and the partonic one. Although the standard nuclear models are successful in reproducing the overall picture of hadrons interacting at large distances, and QCD is convincing in the description of the quarks interacting weakly at short distances (Perturbative QCD), the physics connecting the two regimes is almost nonexistent. When probing distances comparable to those separating the quarks, classical nuclear physics should break down at some point, yet the nucleonic picture still describes many features of the strong interaction. The alternative is to look for the onset of experimentally accessible phenomena which are naturally predicted by QCD. Color transparency (CT) could be a potential candidate. Its basic concepts imply that in exclusive hard processes at large momentum transfer (Q), the hadron has more chance to escape intact from a nuclear target if its wave-function fluctuates into a configuration which contains only valence quarks with small transverse separation. This small size object should lead to a vanishing absorption when it propagates through the nucleus. In this proposal, we hope to observe a clean signal of the onset of CT. By studying the onset of color transparency, one could improve our understanding of the dynamics of bound states in QCD and therefore help to build a detailed picture of photon and electron interactions with nuclei at intermediate energies.

The color transparency phenomenon illustrates the power of exclusive reactions to isolate simple elementary quark configurations. For a hard exclusive reaction such as vector meson electroproduction on the nucleon, the scattering amplitude at large momentum transfer is suppressed by powers of Q^2 if the hadron (vector meson in this case) contains more than the minimal number of constituents. This is derived from the QCD based quark counting rules. Therefore, the hadron containing only valence quarks dominates the cross section. Moreover, each quark, connected to another one by a hard gluon exchange carrying momentum of order Q, should be found within a distance of order $1/Q$. Therefore, at large Q^2 one selects a very special quark configuration where all connected quarks are close together, forming a

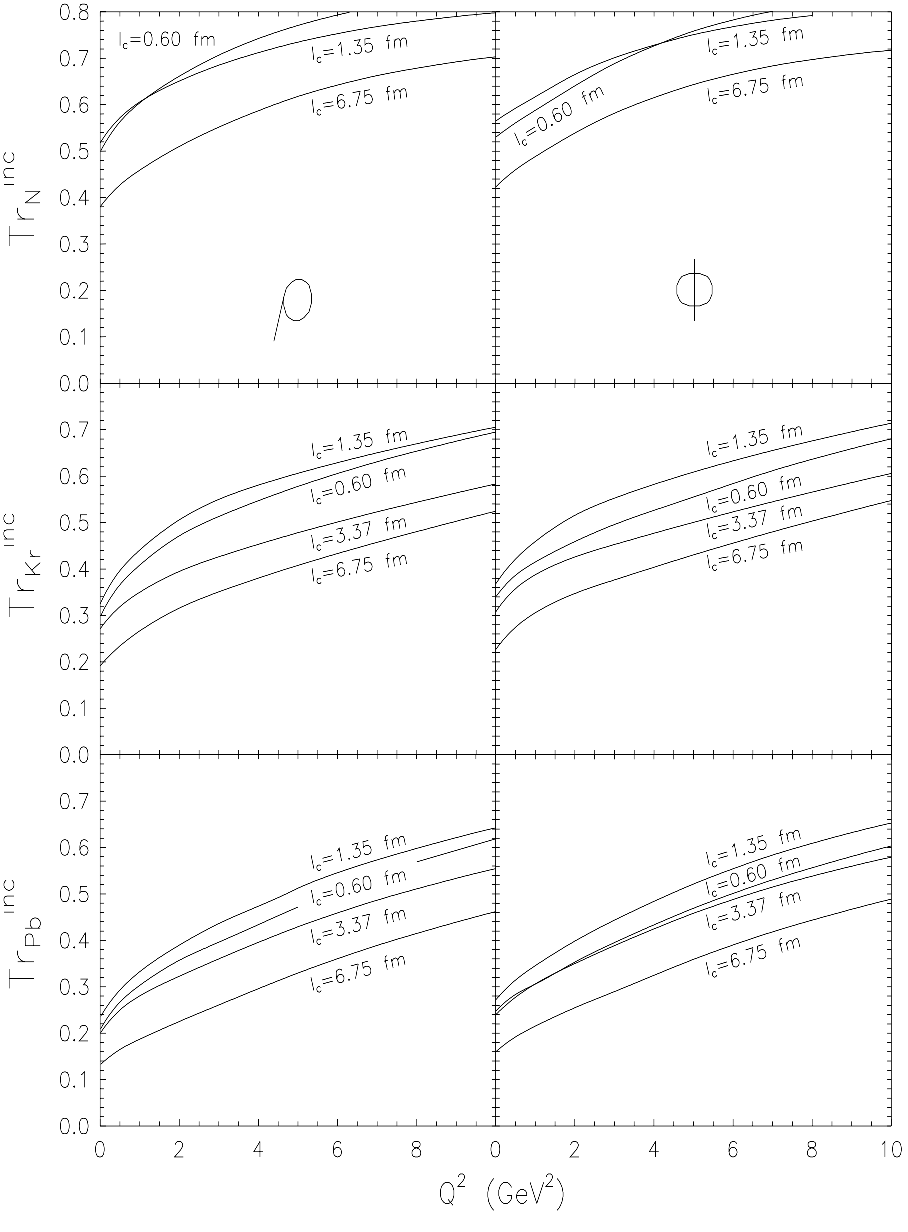

Figure 3.54: Q^2 dependence of the nuclear transparency for exclusive ρ electroproduction on nuclear targets ^{14}N, ^{84}Kr and ^{208}Pb. The CL is fixed at $l_c = 0.6$, 1.35, 3.37 and 6.75 fm.

small size color neutral configuration called *Point Like Configuration* (PLC). During a formation time $\tau_f = 2\nu/(M_{v'}^2 - M_v^2)$, where M_v is the mass of the vector meson in its ground state and $M_{v'}$ its first orbital excitation mass, the *mini hadron* evolves to a normal hadron. Such an object is unable to emit or absorb soft gluons. Therefore, its strong interaction with the other nucleons becomes significantly reduced, and then the nuclear medium becomes more transparent. Consequently, the signature of CT is an increase in the nuclear transparency T_A with increasing hardness of the reaction. T_A is defined as the ratio of the measured exclusive cross section to the cross section in absence of initial and final state interaction (ISI and FSI). It can be measured by taking the ratio of nuclear per-nucleon (σ_A/A) to free nucleon (σ_N) cross sections :

$$T_A = \frac{\sigma_A}{A\sigma_N} \tag{3.48}$$

A number of experiments have searched for an increase in the nuclear transparency. Unfortunately only few of them were able to claim confirmation of CT. The first experiment to investigate CT was performed by Carroll *et al.* [147] at Brookhaven National Laboratory. Quasielastic (p,2p) scattering from each of several nuclei was compared to pp elastic scattering in hydrogen at incident proton momenta of 6, 10, and 12 GeV/c. Its results do not support a monotonic increase in transparency with Q^2 as predicted by CT : the transparency increases for Q^2 from 3 to 8 GeV^2, but then decreases for higher Q^2, up to 11 GeV^2. This subsequent decrease was explained as a consequence of soft processes that interfere with perturbative QCD in free pp scattering but which are suppressed in the nuclear medium [148]. Due to the simplicity of the elementary electron-proton interaction compared to proton-proton one, the quasi-free A(e,e'p) reaction was suggested as an alternative [3-5]. Unfortunately, both the SLAC [149],[150] and JLab [4,5] experiments failed to produce evidence of CT even for the Q^2 values as large as 8 GeV^2. The clearest signal of CT was observed in the E791 experiment [151] at Fermilab. The A-dependence of the diffractive dissociation into di-jets of 500 GeV/c pions scattering coherently from carbon and platinum targets was measured. It was found that the cross-section can be parametrized as $\sigma = \sigma_0 A^\alpha$, with $\alpha = 1.6$. This result is quite consistent with theoretical calculations [7-9] including CT effects and is obviously inconsistent with a cross-section proportional to $A^{2/3}$ which is typical of inclusive π-nucleus interactions. Another Fermilab experiment, E665 [152] reported interesting indications of CT using a 470 (GeV/c) muon beam. Exclusive diffractive ρ-meson production from nuclear targets was used to determine the nuclear transparency. The increase of the nuclear transparency with Q^2 was only suggestive of CT because the statistical precision of the data was not sufficient.

CT effects at moderate energies are more problematic than they are at high energies. Other mechanisms that contain no explicit QCD dynamics may contribute, interfering with identification of the CT signal. The experimental studies of CT were

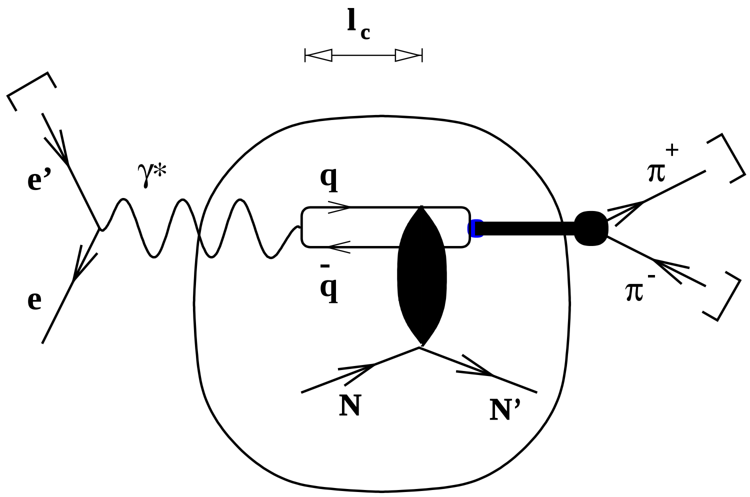

Figure 3.55: Exclusive leptoproduction of the ρ^0 meson.

mainly focused on the quasi-elastic electron scattering (e,e'p) process. In these measurements inelastic corrections could mock [153] the CT signal. The existence of such processes was confirmed by the measurements of the total cross sections of neutron [154] and neutral K-meson [155] interactions with nuclei. Due to these inelastic corrections, the cross-section is smaller, i.e. the nuclear medium is more transparent than is expected from the Glauber approximation. This effect increases with the ejectile energy. Thus, it will also increase with Q^2 because the energy $\nu = Q^2/2m_N$ and Q^2 are correlated in the quasi-elastic peak. The first order inelastic correction has been estimated in Ref. [153]. It was found that the growth of nuclear transparency with Q^2 in quasi-elastic electron scattering off nuclei could imitate the onset of CT up to $Q^2 \sim 20$ GeV^2.

Exclusive incoherent electroproduction of vector mesons off nuclei has also been suggested [156] as a sensitive way to detect CT. In these processes, a fluctuation of the virtual photon gives rise to a quark-antiquark ($q\overline{q}$) pair that travels through the nuclear medium evolving from the initial state, with Q^2 dependent size (the transverse size of the hadronic fluctuation is $r_\perp \sim 1/Q$), to develop the vector meson detected in the final state. Therefore increasing the photon virtuality Q^2, one can 'squeeze' the size of the produced ($q\overline{q}$) wave packet. In the laboratory frame, the photon fluctuation can propagate over a distance l_c known as the *coherence length* . The coherence length can be estimated by making use of the uncertainty principle and Lorentz time dialation as $l_c = 2\nu/(Q^2 + M_{q\overline{q}}^2)$, where ν is the energy of the photon in the laboratory frame, $-Q^2$ is its squared mass and $M_{q\overline{q}}$ is the mass of the ($q\overline{q}$) pair. In the case of exclusive ρ^0 electroproduction, the mass of $q\overline{q}$ is dominated by the ρ^0 mass. The produced small size colorless hadronic system will then propagate through the nuclear medium with reduced attenuation because its cross section is proportional to its size ($\sigma(r) \propto r^2$). The effect of the nuclear medium on the particles in the initial and final states can be characterized by the nuclear transparency. Our ultimate goal is searching for a rise of T_A with Q^2 as a signal for the onset of CT. However, one has to be careful to take into account all the other effects that can imitate this signal. Indeed, the HERMES experiment [157] has shown that T_A increases when l_c varies from long to short compared to the size of the nucleus. This is due to the fact that the nuclear medium seen by the $(q\overline{q})$ fluctuation becomes shorter; thus the $(q\overline{q})$ interacts less. This situation occurs when Q^2 increases at fixed ν. This so-called *coherence length effect* (CL) must be kept under control to avoid mixing it with the CT effect. A simple way to do so is to keep l_c fixed, which is the approach proposed here.

Count rates and expected uncertainties

The 12 GeV JLab upgrade will reach energies optimal for studies of the onset of CT. The high luminosity will be a key parameter in obtaining good statistical precision for experiments of practical duration. CLAS^{++} would be the right place to host measurements of exclusive vector meson electroproduction on nuclei. These measurements would be a natural extension of an approved CLAS experiment [158]. The nuclear transparency of incoherent ρ^0 production on nuclear targets can be measured up to $Q^2 = 7.5$ GeV^2 and for fixed l_c values. Binning the data in a way which keeps l_c constant represents a simple prescription to eliminate the CL effect from the Q^2 dependence of the nuclear transparency. Moreover, because the chosen values of l_c are shorter than the mean free path of the vector meson in the nuclear medium, it is obvious that there is no nuclear shadowing in the initial state. For fixed CL, the Glauber model predicts *no* variation of T_A with Q^2. According to recent work by Kopeliovich and collaborators [159], an important increase of the nuclear transparency with Q^2 is predicted as a signal for the onset of CT. The suggested reaction was exclusive incoherent ρ^0 electroproduction on nuclei for fixed l_c values. The authors have developed a quantum mechanical approach based on the light cone QCD Green function formalism. This formalism naturally incorporates the interference between the CL effect (ISI) and CT effect (FSI). Due to quark-hadron duality, it becomes equivalent to the full multichannel problem in the hadronic presentation. These calculations have succeeded in describing the coherence length dependence of the nuclear transparency reported by the HERMES collaboration [157] and are also in good agreement with the FNAL E665 measurements [152].

In Fig. 3.4.4, we show the predicted nuclear transparency [159] ratio as a function of Q^2 for incoherent ρ^0 electroproduction on nitrogen and krypton at fixed l_c values. The model predicts a large increase of the nuclear transparency as a function of Q^2. Such measurements would be important to disentangle the CL effect from the onset of CT and are crucial for the study of the kinematic conditions for which exclusive

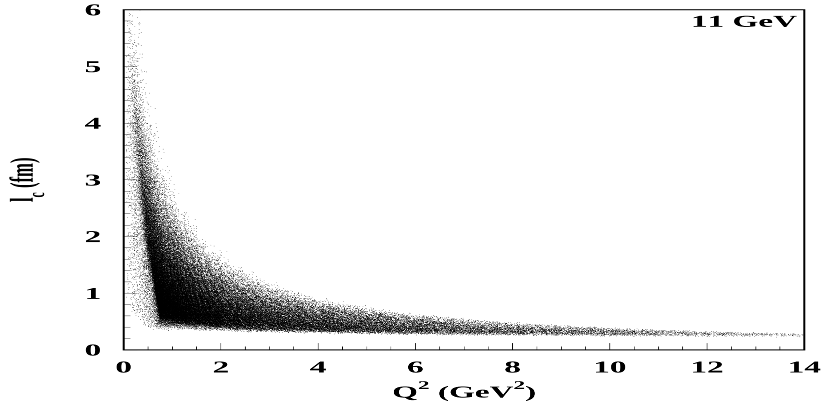

Figure 3.56: The correlation between the coherence length, l_c, and Q^2.

vector meson electroproduction is dominated by the contribution of small size configurations. Information on the mini-hadron evolution to its normal size and its reduced final state interaction with a spectator hadron can also be obtained. In general these measurements are important to understand the dynamics of vector meson production in the nuclear medium and to study the microscopic structure of hadrons where color effects probably have an important role.

The nuclear transparency ratio, $T_A = \sigma_A / A\sigma_N$, for incoherent ρ^0 electroproduction on copper (A $= {}^{63}Cu$) as a function of Q^2 could be measured. The schematic of the reaction is given in Fig. 3.4.4. The incident electron scatters off the target nucleus and exchanges a virtual photon. The photon interacts with one of the nucleons inside the nucleus and eventually produces a ρ^0 meson. The ρ^0 decays into two pions. The electron beam energy would be 11 GeV. The luminosity assumed is $10^{35} cm^{-2} s^{-1}$ for deuterium and $10^{34} cm^{-2} s^{-1}$ for copper. The scattered electron will be detected to determine Q^2. The coincident detection of the two pions will allow the identification of ρ^0 particles using their reconstructed invariant mass.

Since the coherence length effect can imitate the color transparency effect, we will study the Q^2 dependence of T_A at fixed l_c values. Although these measurements will cover a coherence length range from 0.5 to 4.5 fm, none of the l_c values covers the whole range in Q^2. Therefore, we need to consider at least two values of the coherence length, $l_c = 0.5$ fm covering high Q^2 region from 1. to 7.5 GeV^2 with reasonable count rates, and $l_c = 2$ fm which covers Q^2 from 0.5 to 1 GeV^2. The bins in l_c are 0.1 fm wide centered at 0.5 and 2 fm. The three independent kinematical variables W, Q^2 and the momentum transfer, t, are generated according to their experimental distributions. W and Q^2 are generated according to the flux of virtual photons $\Gamma(W, Q^2)$ exchanged between the incident electron and the target :

$$\Gamma(Q^2, W) = \frac{\alpha}{8\pi^2} \times \frac{W}{ME^2} \times \frac{W^2 - M^2}{MQ^2} \times \frac{1}{1-\epsilon} \tag{3.49}$$

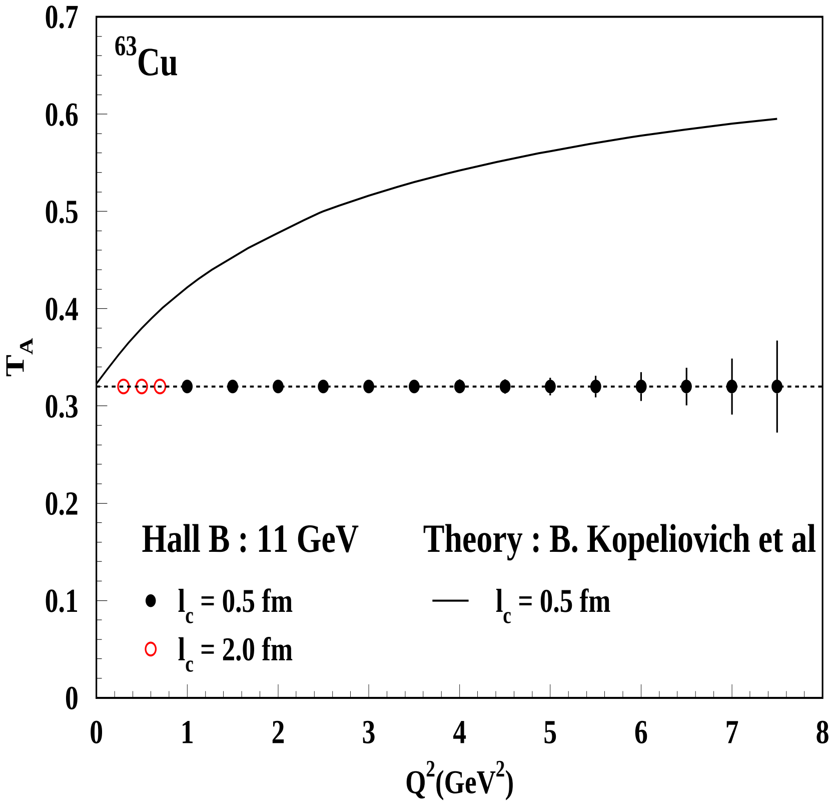

Figure 3.57: Expected error bars for the proposed measurements and predictions of [20].

where M is the mass of the target. E and E' are respectively the energies of incident and scattered electrons, $\nu = E - E'$ is the energy of the virtual photon, and the variable $\epsilon = [1 + 2(Q^2 + \nu^2)/(4EE' - Q^2)]^{-1}$ is its polarization. The momentum transfer, t, is generated according to the experimental differential cross section $\frac{d\sigma}{dt}$ reported in [160] and fitted to the exponential form :

$$\frac{d\sigma}{dt'} = A\exp(-b(W,Q^2) \times t'), \tag{3.50}$$

where $t' = |t - t_{min}|$, and t_{min} is the minimum value of t. Fermi momentum of nucleons inside the nucleus has been taken into account. The momentum of the struck nucleon is generated inside the corresponding Fermi momentum sphere of radius P_F. Experimental values of P_F [161] have been used. The generator considers also the decay of ρ^0 into a pair of pions $\pi^+\pi^-$. Pion angles are generated assuming s-channel helicity conservation. Kinematical cuts have been applied to well identify the reaction of interest. We use W > 2 GeV to avoid the resonance region, $z = \frac{E_\rho}{\nu} > 0.8$, to select the elastic process, and $|\Delta E| < 0.2$ GeV cut to reduce the contamination from non-exclusive events, where

$$\Delta E = \nu - E_\rho + t/2M_p \tag{3.51}$$

ΔE is the energy missing from the $\pi^+\pi^-$ pair due to the creation of any additional final state particles (excitations of the recoil nucleus don't affect ΔE within the resolution). The cut on ΔE is closely related to the cut $z \simeq 1$ but has the advantage that it includes the correction for the kinetic energy $-t/2M_p$ of the recoil nucleon and that the inelastic threshold $\Delta E = m_\pi + m_\pi^2/2M_p$ is independent of ν. The cut $-t' < 0.5$ GeV^2 has also been used to select the diffractive process. To exclude coherent production, we use $-t' > 0.1$ GeV^2. Using ρ^0 electroproduction cross sections, $\sigma(W,Q^2)$, using the Vector Meson Dominance model [160], we have been able to estimate count rates for the chosen bins in l_c and Q^2. We have used a run time of 30 days for copper target and 3 days for deuterium. The projected measurements at the proposed values of l_c are presented in Fig. 3.4.4. The curve is the prediction of Ref. [159]. They show a CT effect on the value of T_A at $Q^2 \sim 7.5$ GeV^2 of 70% for copper; the Glauber calculations predict *no* Q^2 dependence of the nuclear transparency. We must recall that data with all possible values of l_c, Q^2 and t' will be taken at the same time and can be used to determine the l_c dependence of the nuclear transparency. A common fit to all available data at fixed l_c with the slope of Q^2 as a free parameter will be performed. One can use $T_A = a + b \cdot l_c + c \cdot Q^2$ form with a, b and c as free parameter. This fit procedure will allow the determination of the Q^2 dependence (parameter c) with greater precision. Using only l_c values of 0.5 and 2. fm, we can obtain 7σ precision on the Q^2 slope parameter c for copper.

Conclusion

The Color Transparency Phenomenon is considered as a promising tool for the understanding of the nucleon structure in terms of quarks and gluons. Furthermore, the onset of CT offers important information about the transition regime between classical nuclear physics and QCD. Measurements of the nuclear transparency for copper with an 11 GeV electron beam have been suggested. The process in question is diffractive incoherent ρ^0 electroproduction which will extend the maximum Q^2 from 4 to 7.5 GeV^2 and the maximum l_c from 1.5 to 4.5 fm. Because of the high luminosity, broad kinematic coverage, and higher beam energy, CLAS^{++} would be the appropriate place for these measurements.

3.4.5 Transparency Studies via Quasielastic Scattering

Nuclear transparency in quasielastic scattering has long been discussed as a way to understand the reaction mechanism for elastic scattering at high momentum transfer. In one picture, it is supposed that hard elastic scattering selects small-sized configurations of the nucleon. If this is the case, then those configurations should have a reduced interaction probability within the nuclear medium, and the nuclear transparency of this reaction should increase as Q^2 increases. Alternatives to this simple picture have also been suggested.

As mentioned in the introduction, multiple experiments may be performed with the same beam time and spectrometer setup. A study of transparency in nuclear systems for quasielastically scattered nucleons is a good example of this. The data to study this effect will naturally accompany that from the quark propagation experiment described in 3.4.2. The kinematic coverage can be seen in Fig. 3.60, since that measurement is also performed using quasielastic scattering (on deuterium). One can reach up to $Q^2 = 14\,GeV^2$, and the entire range shown in that figure is covered. Systematic errors of approximately five percent will be achievable; the statistical errors would probably limit the accuracy at the larger momentum transfers, depending on the number of days devoted to each nucleus. An additional advantage for the Hall B measurement is that quasielastic scattering of neutrons can be measured in addition to measuring protons, simultaneously, since the CLAS electromagnetic shower calorimeters have an efficiency for neutron detection of greater than fifty percent. This unusual capability suggests the opportunity for a higher-precision comparison of proton and neutron quasielastic response.

3.4.6 Nucleon structure modification in tightly bound nucleon pairs

For a complete understanding of QCD at hadronic scales, we need to to learn more about the interplay between the internal (quark) structure of nucleons and the

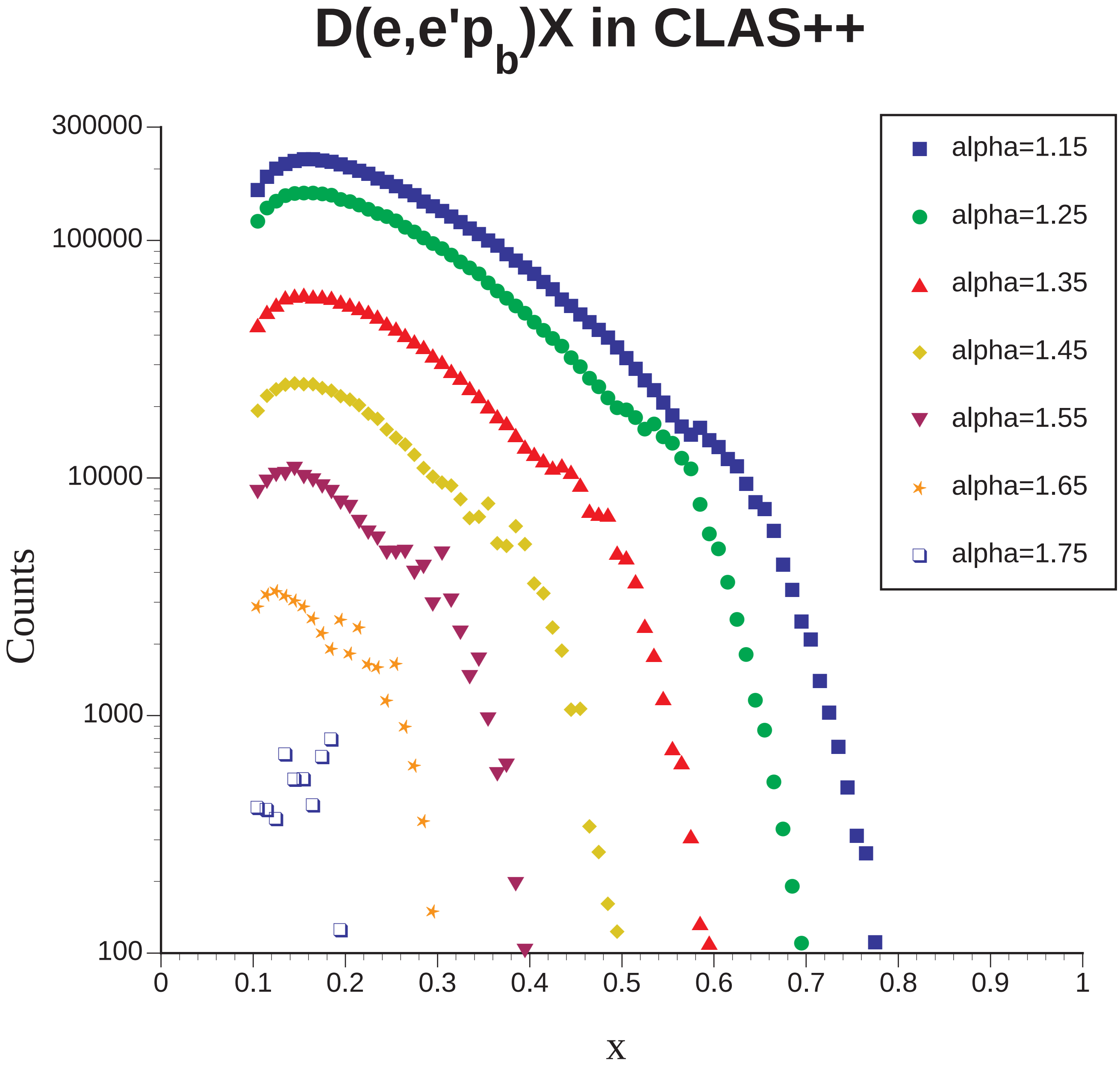

Figure 3.58: Kinematic coverage in Bjorken–x and proton light-cone fraction α_S for the proposed experiment. The count rates have been estimated for a 20 day run with the standard CLAS^{++} configuration.

interaction between two nucleons. In particular, it is of high interest whether nucleons in close proximity to each other change their internal structure or maybe even lose their separate identity to fuse into a "six quark cluster" [162],[163]. Some less dramatic modifications of the nucleon structure that have been proposed include off-shell effects [72], Q^2 rescaling effects and the suppression of small-size configurations (PLCs) in the nucleon wave function [80, 73]. (See the discussion of these effects in Section 3.2.) Deuterium is the optimal system to study such "tightly bound pairs", since there are no additional nucleons interacting with the pair under study and the pair is at rest in the lab, with completely defined kinematics. While the probability for a small internucleon distance configuration in deuterium is rather small compared to heavier nuclei, such configurations can be "tagged" by the emission of a fast proton in the backward hemisphere relative to the momentum transfer vector. We therefore propose to measure the reaction $D(e, e'p_b)X$ with coincident detection of the scattered electron in the forward part of the CLAS^{++} and the fast (above 300 MeV/c) backwards proton in the central detector.

In the simple spectator picture, the backwards moving proton does not participate in the scattering process and can serve as a tag of the initial state momenta of both nucleons. By measuring the momentum of this backward proton, we can correct the observed electron kinematics for the initial motion of the unobserved struck neutron and extract the modified neutron structure function $F_2^{n(eff)}(x, Q^2, p^2)$. This technique is very similar to that described in Section 3.2, but the emphasis here is not on nearly on–shell neutrons, but rather on the opposite kinematic extreme of fast–moving neutrons where off-shell effects and other internal structure changes are much more pronounced. We can extract the dependence of the structure function $F_2^{n(eff)}(x, Q^2, p^2)$ at fixed x and Q^2 on the spectator momentum p over nearly the full range, from about 70 MeV/c to 700 MeV/c, by combining the results of the experiment described in Section 3.2 with the one proposed here. We will simultaneously cover a large range in x and Q^2, allowing us to make detailed comparisons with different models mentioned above, including the rather striking change in the shape of the structure function F_2 predicted for a non-trivial six quark configuration [162],[163].

For the proposed experiment, we will use CLAS^{++} in the standard configuration, with a liquid deuterium target and the fully instrumented central detector to tag the backward proton. We estimated the expected number of counts for a 20 day run with full luminosity (10^{35} cm^{-2}s^{-1}). The results are shown in Fig. 3.58 as a function of the "ordinary" Bjorken variable $x = Q^2/2m\nu$ in the lab and for several bins in the light cone fraction α of the backward proton. One can clearly see the kinematic shift due to the motion of the struck neutron, which we can fully correct using the proton kinematics. We clearly will have good statistics for a large range in x and in α (the highest bin corresponds to more than 600 MeV/c momentum opposite to the direction of the $\mathbf{q}$ vector), drastically extending the kinematic coverage and statistical precision of the existing data from the analog experiment at 6 GeV (E94-102).

nu

3.5 Baryon Form Factors

3.5.1 Introduction

The internal structure of the nucleon is a defining problem for nuclear physics. The most basic observables which reflect the composite nature of the nucleon are its electromagnetic form factors. Indeed, historically the first direct indication that the nucleon is not elementary came from measurements of the form factors in elastic electron–proton scattering [164]. The elastic electric and magnetic form factors characterize the distributions of charge and magnetization in the nucleon as a function of spatial resolving power. Further, the elastic and transition form factors can be described and related to other observables through the use of generalized parton distributions. Therefore, this topic connects strongly to other thrusts of the 12 GeV program.

3.5.2 Context and Motivation

The nucleon elastic form factors are defined through matrix elements of the electromagnetic current, $J_\mu = \overline{\psi}\gamma_\mu\psi$, as:

$$\langle N(P')|J_\mu(0)|N(P)\rangle = \overline{u}(P')\left(\gamma_\mu F_1(Q^2) + \frac{i\sigma_{\mu\nu}q^\nu}{2M}F_2(Q^2)\right)u(P) \;, \tag{3.52}$$

where P and P' are the initial and final nucleon momenta, and $q = P - P'$ is the momentum transferred to the nucleon, with $Q^2 = -q^2$. The Sachs electric and magnetic form factors are defined in terms of F_1 and F_2 as:

$$G_E(Q^2) = F_1(Q^2) - (Q^2/4M^2)\; F_2(Q^2), \tag{3.53}$$

$$G_M(Q^2) = F_1(Q^2) + F_2(Q^2)\;. \tag{3.54}$$

Electromagnetic transition form factors may be similarly defined. In this case the final state is no longer a nucleon but rather may be a resonance state: $\langle R(P')|J_\mu(0)|N(P)\rangle$.

The elastic form factors at low Q^2 are known to approximately follow a dipole form, $G_D(Q^2) \propto 1/(1+Q^2/Q_0^2)^2$, with $Q_0^2 \approx 0.71$ GeV^2. This behavior can be qualitatively understood within a vector meson dominance picture, in which the virtual photon interacts with the nucleon after fluctuation into a virtual vector meson. However, deviations from the dipole form have been observed, and it is important to understand the nature of the deviations, particularly at larger Q^2.

At the other extreme of asymptotically large Q^2, the elastic form factors can be described in terms of perturbative QCD [165]. Here the short wavelength of the highly virtual photon enables the quark substructure of the nucleon to be cleanly resolved. Just where the perturbative behavior sets in is still an open question, however, which must be resolved experimentally. Evidence from recent experiments at Jefferson Lab and elsewhere suggests that non-perturbative effects still dominate the form factors at least for $Q^2 < 10$ GeV^2. For example, the Q^2 dependence of the G_E and G_M form factors, which is expected to be the same in perturbative QCD, is observed to be rather strong in the G_E/G_M ratio for the proton out to $Q^2 \approx 5$ GeV^2 [166].

Theoretical guidance on the form factors in the transition region can be obtained from lattice QCD. It may be anticipated that these calculations will have achieved a degree of accuracy that easily surpasses that currently available for the neutron at high Q^2 by the time CLAS^{++} is taking data [167]. Challenging these fundamental calculations with high-precision data for both the proton and the neutron out to high Q^2 will provide an important test of their accuracy.

Understanding the transition from the low to high Q^2 regions is vital not only for determining the onset of perturbative behavior. Form factors in the transition region are very sensitive to mechanisms of spin-flavor symmetry breaking, which cannot be described *in principle* within perturbation theory. A classic example is the electric form factor of the neutron, G_E^n [168], which is identically zero in a simple valence quark picture, and whose non-zero value can only be understood in terms of non-perturbative mechanisms, such as the hyperfine interaction between quarks [169], or a pion cloud [170].

The Q^2 dependence of the elastic electric and magnetic form factors of the nucleon reflects the dynamics of the quark constituent degrees of freedom in a region where confinement plays an important role. Because the electromagnetic current couples to the charged quark constituents, one can decompose the form factors into a sum over the various quark contributions:

$$G_{E,M}(Q^2) = \sum_{q=u,d,\cdots} e_q \, G_{E,M}^{(q)}(Q^2) \ . \tag{3.55}$$

To determine the contribution $G_{E,M}^{(q)}$ from each individual quark flavor requires measurement of the form factors of both the proton and neutron. However, at present, precision data at high Q^2 exist only for the proton, as may be seen in Fig. 3.59.

There are other reasons why the study of form factors is of fundamental importance. They contain information on nucleon structure complementary to that which is measured through other processes, such as inclusive scattering. Recent work on generalized parton distributions has provided a unifying framework within which both form factors and structure functions can be simultaneously embedded [172, 173]. For example, the generalized parton distribution, $H(x,\xi,t)$, where $t = (P - P')^2$ and $\xi = n \cdot (P' - P)/M$ with n a light-like vector that corresponds to the matrix element of the Dirac vector current, connects the Dirac form factor F_1 with the unpolarized quark distribution function, $q(x)$, by [172]:

$$\int_{-1}^{1} dx H(x,\xi,t) = F_1(t) \ , \tag{3.56}$$

$$H(x,0,0) = q(x) \ . \tag{3.57}$$

The generalized parton distributions can be measured in processes such as deeply-virtual Compton scattering, or deeply-virtual meson production, at large photon vir-

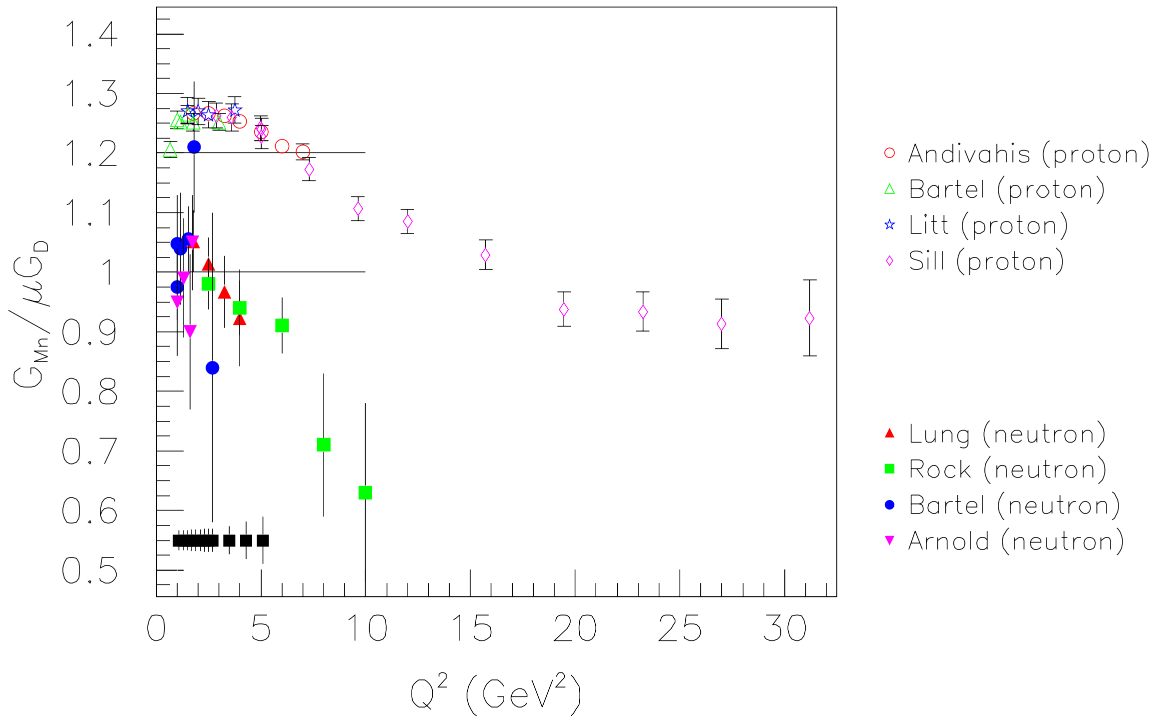

Figure 3.59: The normalized elastic proton and neutron magnetic form factors ($G_{Mn}/G_D\mu_n$, $G_{Mp}/G_D\mu_p$) out to high Q^2. The proton data has been shifted upward by 0.2 for clarity. Note the lack of high-quality data for the neutron at large Q^2. For more information on the referenced data, see [171]. The points plotted at 0.55 indicate the size of the anticipated errors from the CLAS E5 measurement.

tuality Q^2 and small t, where one expects the process to be dominated by single quark scattering (note that here t corresponds to the square of the momentum transfer to the hadron, while Q^2 is the virtuality of the photon).

Of course it is not a priori clear at which Q^2 single quark scattering will dominate, so it is important to take measurements over a range of Q^2. This will also enable one to smoothly match on to the case of real Compton scattering at $Q^2 = 0$.

The elastic and transition form factors can be related to each other in dynamical quark models of the nucleon, and more rigorously, in the limit of QCD with a large number of colors. Therefore, within this framework, they measure different combinations of the same set of generalized parton distributions. The variety of form factor measurements accessible in CLAS^{++} are therefore interrelated and can be interpreted within a unified analysis. Such an analysis will be very important for obtaining reliable information on these fundamental distributions.

From another perspective, the interplay between form factors and structure functions is central to the phenomenon of quark-hadron duality [61, 174, 175, 176, 177], and the transition from quark to hadron degrees of freedom in QCD. Form factors obtained in exclusive reactions can be related through local quark-hadron duality to deep-inelastic structure functions measured in inclusive processes. For elastic scattering, the form factors can be used to predict the behavior of structure functions in the limit $x \to 1$ [61, 178, 179, 180], which is a region very difficult to access experimentally. For the F_1 structure function of the nucleon, for instance, one has at large Q^2 [61, 180]:

$$F_1(x \to 1, Q^2) \;\; \propto \;\; \frac{dG_M^2(Q^2)}{dQ^2} \; . \tag{3.58}$$

Conversely, from data on structure functions at very large x one can extract the elastic form factors as a function of Q^2 and compare with the directly measured values [174, 175].

One can similarly use quark-hadron duality to study not just the elastic case, but the entire spectrum of excited final states, and more generally the transition from resonance production to scaling in deep-inelastic scattering [181]. The form factors which parameterize transitions from the ground state to the excited states, such $N \to \Delta$ or $N \to S_{11}$, contain rich information about the spatial distribution of quarks inside the nucleon.

The $N \to \Delta$ transition form factor is particularly important given the prominent role that the Δ is known to play in hadron structure [170]. The previously observed Q^2 dependence of the $\gamma^* N\Delta$ form factor is qualitatively different from the Q^2 dependence of the form factors of the other resonances [182]. Moreover, the contribution of the $N \to \Delta$ transition to the polarization asymmetry

$$A_1 \;\; = \;\; \frac{\sigma_{1/2} - \sigma_{3/2}}{\sigma_{1/2} + \sigma_{3/2}} \; , \tag{3.59}$$

where $\sigma_{1/2(3/2)}$ is the virtual photoabsorption cross section for total γ^*-nucleon spin projection 1/2 (3/2), is known to be large and negative at low Q^2, while the same asymmetry at large Q^2 is positive. Understanding this transition, and the related non-trivial Q^2 dependence of the Gerasimov-Drell-Hearn sum rule at intermediate Q^2, requires a precise determination of the $\gamma^* N\Delta$ form factor over a large range of Q^2 [183].

The next lowest excited state after the Δ is the negative parity partner of the nucleon, the S_{11} resonance. In the limit of exact chiral symmetry, the masses of the nucleon and its parity partner would be degenerate, so that the properties of the S_{11} form factor reveal fundamental aspects of dynamical chiral symmetry breaking in QCD.

3.5.3 Form Factor Measurements

There are several examples of form factors which should be accessible with CLAS^{++}.

Nucleon Elastic Form Factors

The form factor accessible in CLAS^{++} that reaches the highest Q^2 is the neutron magnetic form factor, $G_{Mn}(Q^2)$. This is obtained by an extension of the method used in Jefferson Lab experiment E94-017[33]. In this method, an unpolarized cryogenic liquid deuterium target is employed as a 'neutron target,' and the ratio of e-n events to e-p events off deuterium is measured. The proton is detected in the drift chambers and identified by time-of-flight, while the neutron is detected in the forward calorimeters with high efficiency. A cut on W selects quasi-elastic kinematics for the neutron and the proton. In the conceptual limit where the neutron and proton are considered as free in the deuteron, the e-n/e-p ratio can be directly related to the free form factors of the proton and neutron. Using the more accurately determined proton form factors and an estimate of the neutron electric form factor, one derives the magnetic form factor from the deuteron quasi-elastic cross section.

There are a number of factors which affect the accuracy of the measured G_{Mn}. While these are the same for low and high Q^2, their relative importances change. As long as G_{Mn} is much larger than G_{E_n}, uncertainty of the latter does not contribute significantly to the uncertainty in G_{Mn}. The proton magnetic form factor must also be quite well-known, and the proton's electric form factor must be reasonably well-determined. In quasi-elastic kinematics, corrections to the ratio due to the binding of the nucleons within the deuteron are expected to become increasingly smaller at high Q^2, and work is in progress to quantify these corrections within a reliable relativistic theory. The solid angles within which the proton and neutron are measured must be known to be equal; this problem is not expected to be very different at high momentum transfer, since these are essentially geometric issues.

The neutron detection efficiency, which must be known accurately in this method, will be more stable at high Q^2. This is because the intrinsic detection efficiency in the electromagnetic shower calorimeter plateaus to a nearly constant value for neutron momenta above approximately 1.75 GeV/c. The detection efficiency was continuously monitored in experiment E94-017 using a novel dual-cell target which allowed two target cells to be simultaneously in the beam. The upstream target contained cryogenic liquid deuterium, while the downstream target contained cryogenic liquid hydrogen. The neutron detection efficiency was thereby continuously measured using the exclusive reaction $p(e, e'\pi^+)n$ from the proton target.

There are two factors which are expected to become much more important at high Q^2; both essentially have to do with isolating the reaction of interest. The first is that the quasi-elastic scattering rate becomes small relative to inelastic processes nearby in the W spectrum. The tails of these processes therefore become an important contamination underneath the region of quasi-elastic scattering. The second effect is the kinematic broadening of the W peak. These two effects, taken together, mean that there may not even be a visible enhancement in the W spectrum due to this process for $Q^2 >$ 8 GeV^2, independent of experimental resolution. Previous measurements of G_{Mn} at high Q^2, using inclusive electron scattering, encountered this limitation[184].

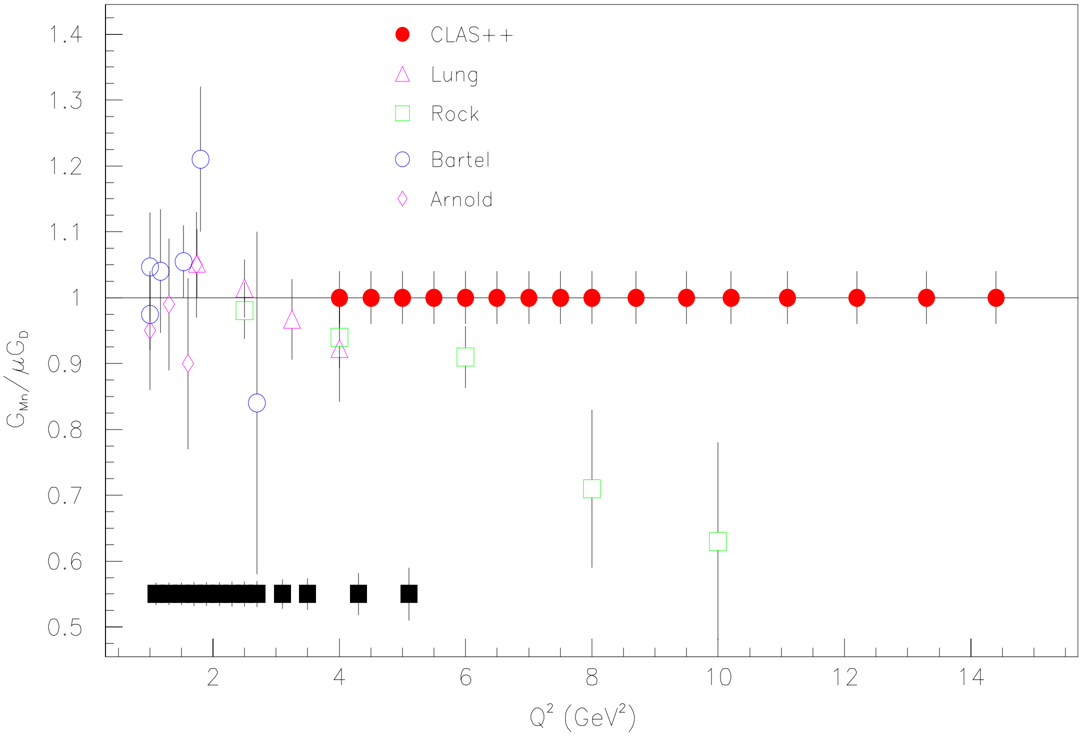

Figure 3.60: Predicted neutron form factor data obtained from CLAS^{++} for a running period of 45 days. For more information on the referenced data, see [171]. The points plotted at 0.55 indicate the size of the anticipated errors from the CLAS E5 measurement.

These difficulties can be overcome in CLAS^{++} using two types of cuts that do not introduce bias into the ratio measurement. First, the angle between the virtual photon and the detected nucleon is very small for quasi-elastic kinematics. Eliminating angles that are not consistent with the quasi-elastic process removes much of the inelastic background. Second, the hermiticity of CLAS^{++}, and its increased capability for detection of neutrals, means that events with in-time charged particles that are inconsistent with quasi-elastic scattering can be vetoed with high efficiency, as can neutral hit pairs reconstructing to the π^0 mass. In this way, the events of interest can be separated from inelastic events.

The expected quality of the measurement feasible is seen in Fig. 3.60. The errors are dominated by systematic errors even at the highest Q^2 as a result of the increased luminosity limit from the upgraded detectors. It is clear from this figure that a substantial improvement of our understanding of the neutron elastic magnetic form factor will result from the upgrade to CLAS^{++}.

Electromagnetic Transition Form Factors

The excitation of nucleon resonances is a prominent feature of strong interaction physics in the non-perturbative domain. CLAS measurements carried out to date on

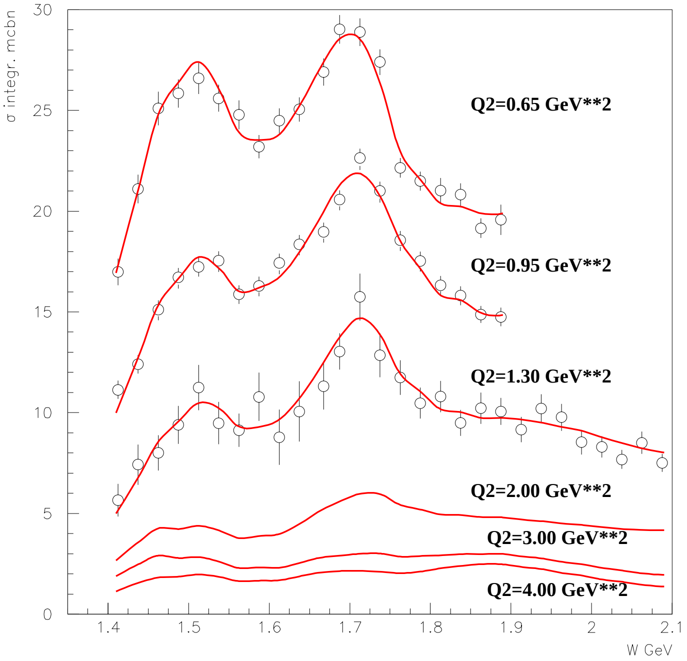

Figure 3.61: Preliminary CLAS data for $\gamma^* p \to \pi^+\pi^- p$ [185], [186] compared to model calculations [187][188]. The photocouplings for all states and the strong couplings for $P_{13}(1720)$, $D_{13}(1700)$ are from a fit to CLAS data, while the strong decays of other states are estimated based on the analysis of [189][190] as described in [187]. The curves for $Q^2 > 1.5\ GeV^2$ are model predictions [187][188] (see text).

excited nucleons in a variety of exclusive channels have yielded precise information on both the dominant and the weakly excited multipoles of the $P_{33}(1232)$ resonance in single pion production [191] and for the $S_{11}(1535)$ excitation in eta production [192]. First data on N^* electromagnetic form factors for many states with masses above 1.6 GeV have been obtained in studies of exclusive $\pi^+\pi^-$ production on the proton at $W < 2.1$ GeV and $Q^2 < 1.5$ GeV^2 [185][186][193]. The analysis of electromagnetic form factors for nucleon excitations < 2.1 GeV in the $\pi^+\pi^-$ channel [193], performed within the framework of the Single Quark Transition Model (SQTM) [194] has demonstrated that the data can be described (Fig. 3.61) with N^* photocouplings consistent to within 30% of the SQTM predictions. This supports the picture that a single quark transition between coherent three-quark configurations in the ground and excited nucleon states is an important mechanism for exciting nucleon resonances for $Q^2 < 1.5$ GeV^2. CLAS^{++} will offer the opportunity to study the evolution of the N^* excitation mechanism from coherent interactions with constituent quarks to hard interactions with a single quark for small distances with Q^2 of the order of 10 GeV^2.

At this transition scale we could perhaps gain access to the quark momentum distribution for excited nucleon states. A phenomenological analysis [187][188] may be adequate to analyze the data, and one could hope to observe manifestations of sea quark contributions to N^* structure as suggested in [195].

Among the electromagnetic transition form factors accessible to CLAS^{++}, those for the $S_{11}(1535)$ and $\Delta(1232)$ are particularly noteworthy. Because the S_{11} resonance has a large branching ratio to (N, η), the resonance transition form factor for the $N \to S_{11}(1535)$ transition offers a unique signature which is likely to provide substantial immunity to background resonances and non-resonant backgrounds. The η meson may be detected through the missing mass technique and also may be detected directly, taking advantage of the enhanced hermiticity and photon reconstruction capability of CLAS^{++}. The prospect of having an overdetermined final state with a substantial acceptance means that a very high quality analysis will be feasible. A clean measurement will be relatively straightforward to obtain.

The $\Delta(1232)$ resonance should also present a favorable opportunity for study out to higher Q^2. Because the resonance is well-isolated, backgrounds will be suppressed, and an adequate count rate will be obtained. As in the previous reaction, overdetermined final states in both the π^+ and π^0 channels should be accessible with relatively high acceptance, ensuring the reliability and completeness of the analysis. This should also help to identify the fraction of non-resonant background, which may be the primary experimental challenge. Improved angular resolution and coverage of the angle ϕ_π^* between the hadronic and lepton scattering planes will permit CLAS^{++} to push the separation of σ_{TT} and σ_{LT} into unexplored regions of Q^2. These structure functions measure the interference between helicity-conserving and non-conserving amplitudes and should vanish in the pQCD limit. Current CLAS data show no evidence of a trend toward this limit in σ_{TT}/σ_{TOT} in the region of the $\Delta(1232)$, although above and below the Δ a rapid decrease in helicity non-conservation is evident (Fig. 3.62). Furthermore, a multipole analysis of σ_{LT} of data from CLAS and Hall C indicate an *increase* in the ratio of the longitudinal-scalar coupling S_{1+} to the magnetic dipole M_{1+} as Q^2 increases, while pQCD strictly requires $S_{1+}/M_{1+} \to \textit{constant}$. Figure 3.63 shows projected errors of a S_{1+}/M_{1+} measurement with CLAS^{++}.

The information on the N^* excitation amplitude is very important in studies of quark-hadron duality as suggested in [196][197]. The approach taken by [187][188] allows extraction of the resonant amplitude averaged over resonant state widths.

A prominent feature of the double charged pion production cross-section is a pronounced resonant structure at $W = 1.7$ GeV (Fig. 3.61) observed for the first time by CLAS. This structure was not seen in previous experiments with real photons [198], nor with hadron probes [189][190]. It was found [185] that this structure could be described in two ways: a) by assuming strong couplings of N^* from recent published analyses [189][190], a new missing baryon state could be implemented with the quantum numbers $P_{13}(1720)$, determined from fitting the data; b) by using known states with drastically modified strong couplings that are significantly different from recent

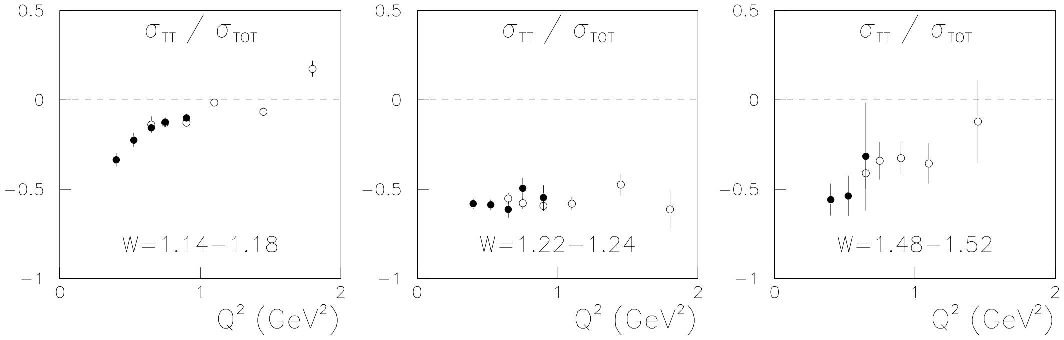

Figure 3.62: CLAS data showing the ratio of σ_{TT} to the total cross section σ_{tot} for three W bins: below the $\Delta(1232)$ (left), at the top of the $\Delta(1232)$ (middle) and in the second resonance region (right).

analyses [189][190].

CLAS^{++} offers promising opportunities for systematic studies of signals from previously unobserved resonant structures in different exclusive channels and in a wide Q^2 range. The quark models predict missing states of two types: a) still unobserved three quark system excitations; b) exotic states such as three quarks confined by an excited gluon potential [195][199]. Numerous missing states at $W > 2.0$ GeV have been predicted[200][201][202][203][204]. These will be accessible to study by CLAS^{++}. The machinery already developed in existing analyses[187][188][205] will be applicable to the new data.

To investigate the feasibility of N^* electromagnetic form factor studies at high Q^2, we performed an evaluation of double charged pion production cross-sections and their decomposition through resonant and non-resonant contributions in the framework of the model for double charged pion production [187][188]. The Q^2 dependence of electromagnetic form factors for all states were evaluated in the SQTM model [194], with the exception of the $P_{13}(1720)$. For that state, the photocouplings from an extrapolation of the recent CLAS data analysis were used. A small number of model parameters for non-resonant mechanisms were fixed to the values from the same analysis, while 3-body phase space was extrapolated assuming a $1/Q^3$ dependence (in the spirit of quark hadron duality) for $A_{1/2}$ N^* helicity dominance with the asymptotic behavior.

The predicted double charged pion production cross-sections for $Q^2 > 1.5$ GeV^2 together with the CLAS data fit [185][186][193] are shown in Fig. 3.61. The predicted cross-section decreases with Q^2 and at $Q^2 = 4.0$ GeV^2 the average value of the predicted cross-sections is approximately one order of magnitude lower than at $Q^2 =$ 0.65 GeV^2. Therefore, with the anticipated order of magnitude increase in luminosity for, it will be possible to carry out studies in the double charged pion production channel for $Q^2 < 4.0$ GeV^2 with high sensitivity.

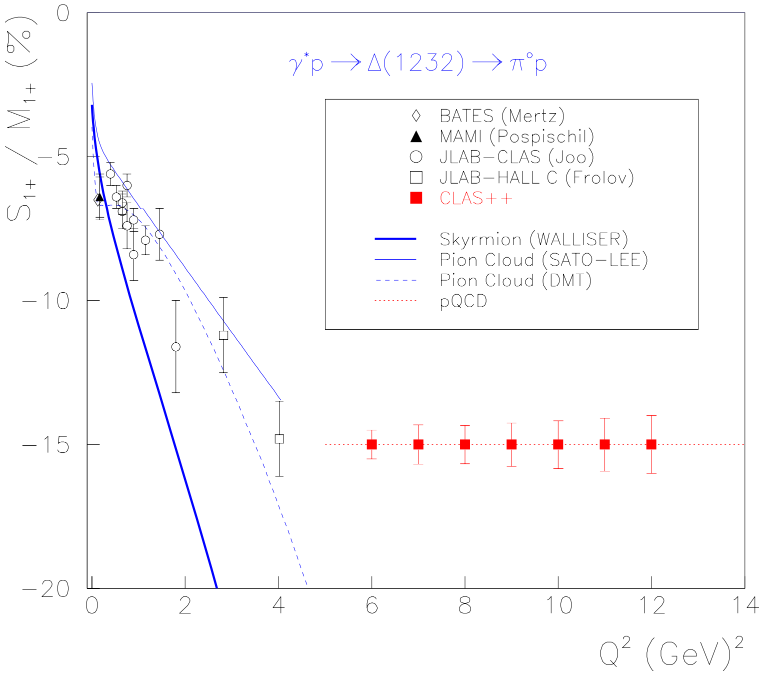

Figure 3.63: The multipole ratio S_{1+}/M_{1+}. The low Q^2 data are from CLAS and Hall C. The red square symbols are projected data at 11 GeV with CLAS$^+$. For a clean separation from single photon events the full final state $ep\pi^o(\gamma\gamma)$ is measured. The errors are dominated by systematic uncertainties in the background amplitudes.

A decomposition of the predicted cross-sections into resonant and non-resonant parts is shown on Fig. 3.64. The relative contribution of the resonance part increases with Q^2 in the overall W interval . The resonant structures observed in CLAS data [185], [186] at $W = 1.5$ and 1.7 GeV survive at high Q^2. Moreover, at $Q^2 > 2.5$ GeV^2 an additional structure at 1.9 GeV appears. This additional structure is composed of high lying $F_{35}(1905)$ and $F_{37}(1950)$ states, not seen at $Q^2 < 2.0$ GeV^2 due to large non-resonant contributions. Therefore, if the predicted fall-off of the non-resonant contributions with Q^2 is confirmed, detailed studies of N^* with masses > 1.9 GeV should be feasible at high Q^2.

In Fig. 3.65 the predicted ratio of resonant to non-resonant cross sections (blue lines) is shown in comparison with this ratio extracted from CLAS data [185][186] (red lines) at W-values corresponding to the peaks for the observed and predicted resonant structures at 1.51, 1.71, and 1.89 GeV. The remarkable feature is a drastic growth of the resonant mechanism contribution with Q^2. The ratio of resonant to non-resonant mechanisms at $Q^2 = 4.0$ GeV^2 exceeds the corresponding quantity at $Q^2 = 0.65$ GeV^2 by almost an order of magnitude. Therefore, even considering the uncertainties in our predictions, studies of high mass N^* states at high Q^2 appear very promising.

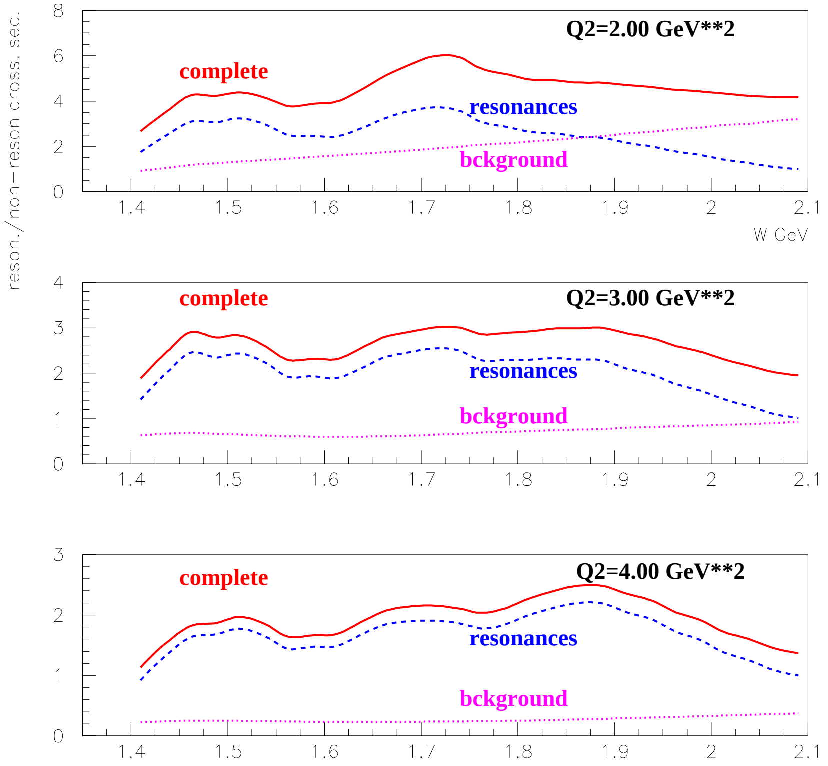

Figure 3.64: Decomposition of predicted [7,8] $\gamma_{virt}p \rightarrow \pi^+\pi^-p$ cross-sections through resonant and nonresonant contributions.

3.6 Exclusive Strangeness Production

Additional information on the structure of the nucleon can be obtained by studying, with CLAS^{++} and the upgraded 12 GeV accelerator, the spin structure of quark pair creation in $N \rightarrow Y$ transitions. It is widely believed that the dominant mechanism by which hadronization and excited particle decays occur is the neutralizing of the color flux by the production of a $q\overline{q}$ pair. Exclusive electroproduction of Λ K final states along with a measurement of the Λ recoil polarization will allow a measurement of the spin-state of the created $s\overline{s}$ quark pair.

Electroproduction from a proton with polarized electrons proceeds through the transfer of circularly-polarized virtual photons. In a simple SU(6) quark model picture, the virtual photon is absorbed predominantly by a u quark. Since only u quarks with the correct helicity (opposite that of the photon) can contribute, the process results in an intermediate state of one polarized u quark recoiling from the unpolar-

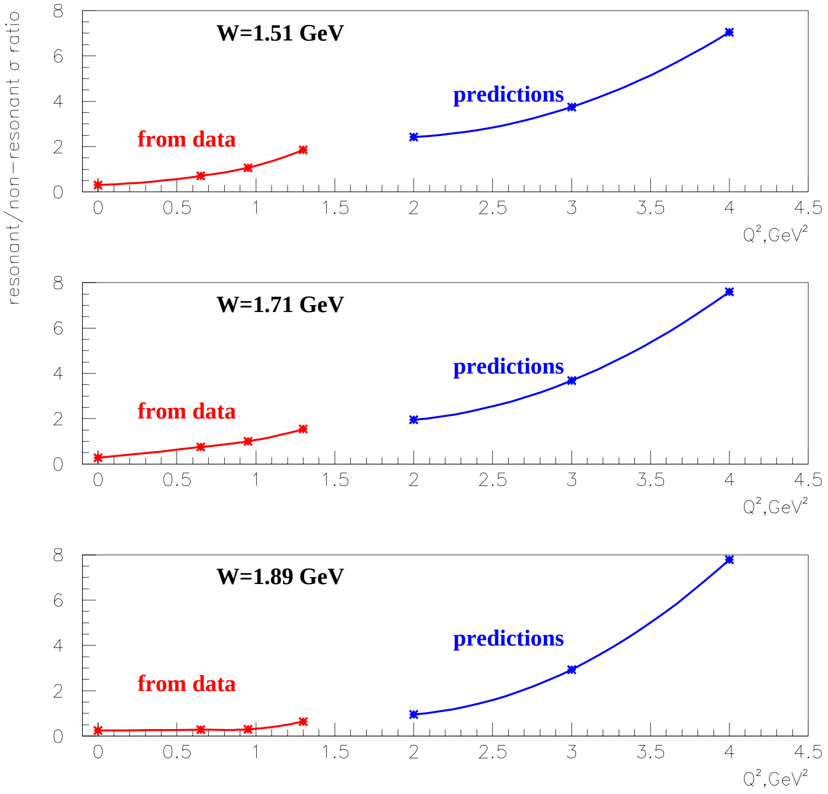

Figure 3.65: The ratio of resonant to non-resonant cross-sections as a function of Q^2, estimated for W values corresponding to the peaks of the resonant structures in the $\gamma_{virt}p \rightarrow \pi^+\pi^-p$ cross-sections.

ized ud spectator system. This intermediate state can then hadronize into a $K^+\Lambda$ final state through the creation of an $s\overline{s}$ pair. Since the K^+ is a pseudoscalar, the polarization state of the $\overline{s}$ quark must be opposite that of the u quark. Measuring the polarization of the Λ reveals the s quark polarization direction, and hence the spin correlation of the $s\overline{s}$ pair in the limit that this amplitude dominates.

Proposed measurements

We propose to measure the exclusive production of $K\ \Lambda$ and $K\ \Sigma$ states, for both pseudoscalar (K^+) and vector ($K^{*+}(892)$) mesons[5] over a large kinematic range. In addition to the scattered electron and the outgoing kaon, decay products of the associated hyperon will be detected.

---

[5] The neutral K^0 and $K^*(892)$ will be measured as well.

The proposed measurements take full advantage of an array of favorable factors:

- The availability of CEBAF's highly polarized electron beams. This allows use of the powerful method of beam polarization asymmetry.
- The self-analyzing nature of Λ decay and the fact that to a first approximation (in the symmetric quark model) the Λ spin is entirely due to the s quark. This fact allows the direct measurement of the polarization of the s quark.
- The vector nature of one-photon exchange. This fact ensures the efficient helicity transfer from the electron to a u quark, governed only by well-known kinematic factors. We must also assume that this amplitude dominates; it is 8 times larger than the corresponding amplitude from the d quark.
- The energy regime of an upgraded CEBAF allows us to explore the resonance region where other amplitudes (interferences between overlapping resonances, for example) may also cause polarization and also reach beyond this regime.
- At higher energy the available phase space will allow a direct comparison between the polarization for exclusive K^+ Λ production with that for $K^{*+}\Lambda$ production. If the effect arises from a common spin correlation projected onto the outgoing hadronic structure, then the Λ polarization should change sign.

In Fig. 3.66 the kinematics achievable with the CLAS^{++} detector and an electron beam of 11 GeV are shown for the $ep \to e'K^+\Lambda$ reaction as a function of Q^2 and W. The black distribution shows the extent of all allowed electron-kaon events. The red distribution incorporates the restrictions in momentum and angles related to the detection of the outgoing electron in coincidence with a kaon; the torus was assumed at maximum field. The coverage for $ep \to e'K^{*+}(892)\Lambda$ production is shown in Fig. 3.66b. For the distribution shown in Fig. 3.66, if one requires an extra proton to be detected (on top of the electron and kaon) the number of expected events (acceptance) goes down by a factor of ∼4 (note that this incorporates the ∼ 64% branching ratio for the $p\pi^-$ decay of the Λ hyperon).

Besides phase space coverage and acceptance, the resolution with which the momenta and angles of the final state particles are reconstructed is also important. When producing K^+ mesons off a proton target (which is the case for most of the experiments described here) one has not one, but two ground states accessible, namely the Λ and the Σ^0 hyperons. The mass separation between these states is only ∼80 MeV. Furthermore, the heavier Σ^0 decays almost exclusively into $\Lambda\gamma$. Detection of the decays products including the 80 MeV photon will allow a clean separation from the direct Λ channel. Since the baryon is most likely produced at large angles, most of the decay products will be measured in the central detector system.

In addition one can employ the missing mass method in kinematic regions where the resolution with which one detects the electron and the kaon is good enough to

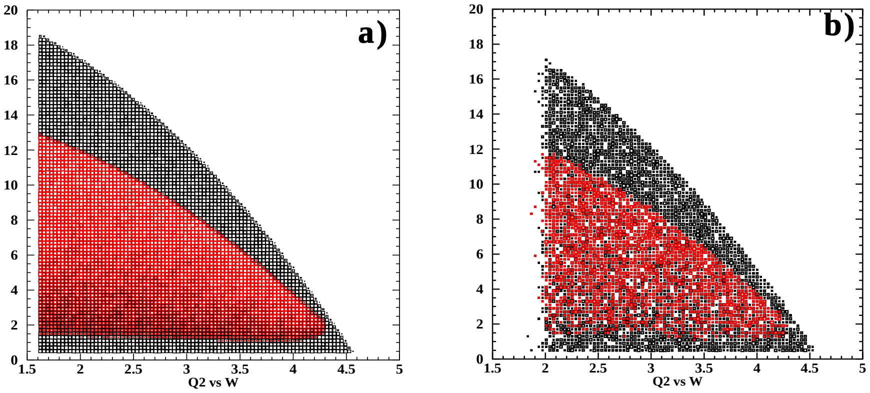

Figure 3.66: Kinematic coverage for the $ep \rightarrow e'K^+\Lambda$ (left) and $ep \rightarrow e'K^{*+}(892)\Lambda$ (right) reactions with CLAS^{++} at 11 GeV. The black distribution shows all kinematically allowed Q^2 and W values while the red distribution requires the outgoing electron and kaon (plus photons for panel b) to be detected in CLAS^{++}.

allow this separation. In the left panel of Fig. 3.67 the width (σ) of the missing mass distribution (for Λ production) is shown as a function of the relative momentum resolution of the detected particles (horizontal axis) and the absolute angular resolution (vertical axis). The cyan (red) portion of the graph shows the regions where the missing mass resolution is smaller than 40 (26.66) MeV, providing a 2(3) σ separation between the Λ and Σ^0 hyperons. The left panel of Fig. 3.67 shows the overlap between Λ and Σ^0 for a missing mass resolution of ∼30 MeV.

Requirements

The requirements needed for the semi–exclusive study of open strangeness systems described here, are listed below (with critical requirements deemed specific to this set of experiments in boldface):

- Good electron identification (electron–π^- discrimination) over all available phase space.
- **Good K^+ identification**. A time-of-flight resolution of 50–80 ps.
- **Good hermeticity**. As the proposed studies rely on three or more particles to be detected in the final state, minimizing the dead regions of the detector will be an essential requirement.
- **Resolution**. At least partial separation of the ground states Λ and Σ^0 via missing mass is desired. For charged particles one will need a resolution of 0.1–0.2% ($\Delta p/p$) in momentum and ∼1 mrad in angle.

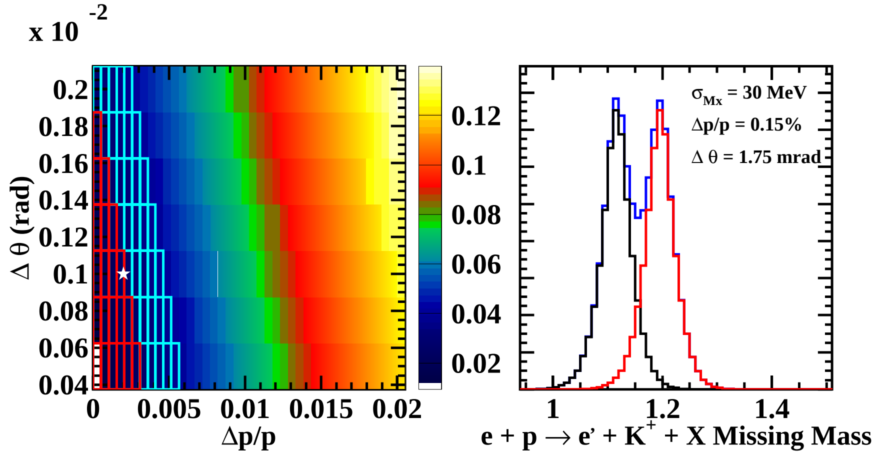

Figure 3.67: Missing Mass resolution (σ) as a function of the relative momentum resolution and absolute angular resolution (left panel). Missing mass reconstruction for $e + p \rightarrow e' + K^+ + Y$ (right panel).

- Neutral particle identification. Some of the reaction channels studied can benefit from the direct detection of neutral (γ, n, etc.) particles. Even partial information (i.e. direction) might be usable in selected cases.

The requirements listed above are common to the strangeness GPD studies described elsewhere in this document. These experiments will benefit if additional particle identification information is available, especially for K^+.

3.7 Electroproduction at very small Q^2

3.7.1 Introduction

The current photoproduction setup of CLAS, producing real bremsstrahlung photons tagged by a magnet spectrometer for the scattered electrons, can not be operated at 11 GeV energies. Instead, we are planning to use quasi-real photons produced when electrons are scattered at very forward angles (*i.e.*, scattering angles about 1^o). Electron scattering at very small angles, with coincidence detection of hadronic final states, is a very attractive alternative to photoproduction experiments. We plan to use a small angle forward electron tagger in coincidence with the detection of multi-particle final states at the CLAS^{++} detector to study electroproduction at Q^2 values of about 10^{-2} GeV^2. Electroproduction at these very small values of Q^2 using unpolarized electrons is equivalent to photoproduction using partially linearly polarized photons [206].

The physics program using this facility will take advantage of polarized photons with relatively high photon fluxes. Since electrons are tagged after their target interactions, this technique allows the use of high electron currents, and permits to achieve high luminosity on thin targets (*i.e.*, gas targets with target recoil detection capabilities) at CLAS^{++}. Knowledge of the photon linear polarization, together with the use of the nearly 4π coverage for hadronic final states of CLAS^{++}, will allow the study of meson spectroscopy in a competitive and complementary experimental environment to the already planned coherent bremsstrahlung production experiments.

There are many physics topics that can take advantage of these beam and detector characteristics,

- meson spectroscopy (especially the study of high mass states, consisting of ordinary mesons, hybrids, and mesons with exotic J^{PC}) using H_2 and ^{4}He targets,
- wide-angle pion Compton scattering,
- time-like Compton scattering,
- J/ψ production near threshold,
- high-t physics,
- study of parton distributions at low Q^2,
- low x_{Bj} physics (shadowing) on heavy targets,
- high mass baryon production, *e.g.*, Ξ baryons.

Kinematics, rates, and backgrounds for this facility are briefly described in the next section. The physics program of the first two items in the list are then described in detail. The third item in the list, time-like Compton scattering, has been described previously in the DVCS section. No detailed discussion of the other topics will be given.

Kinematics and Rates

The kinematic range covered by such a facility, for 11 GeV incoming electrons, is shown in table 3.3. Figure 3.68 shows total electroproduction rates expected in our kinematic range assuming a luminosity of 10^{34} cm^{-2}sec^{-1}. The total inclusive electron rate in the low Q^2 detector will be of about 10 kHz (for ν=8 to 9 GeV).

Electron scattering contains contributions from one-photon exchange (Born process), from QED vacuum polarization loops, and from the emission of additional real photons (radiative corrections). The importance of the internal radiative corrections in relation to the Born process depends on the kinematics. Radiative corrections increase with decreasing Q^2 and increasing ν. We have used the program RADGEN 1.0 [207] to calculate the contributions of internal radiative corrections to the total inclusive cross section. Figure 3.68 shows the ratio of the inelastic (Born) and elastic-radiative tails to the total inclusive cross section versus scattered electron energies.

$E_{scattered}$	1 - 4 GeV
θ	0.5^o - 1.2^o
ϕ	0^o - 360^o
ν	7 - 10 GeV
Q^2	0.003 - 0.029 GeV^2
W	3.9 - 4.6 GeV
x_{Bj}	0.0001 - 0.002

Table 3.3: Kinematic range covered by the low Q^2 tagger.

Inelastic processes represent about 4% of the total cross section in our kinematic range. It is, therefore, essential for our measurements to require a tight trigger coincidence between the forward tagger and the detection of multi-particle final states in the CLAS detector. The total rate of inelastic events is, therefore, expected to be about 400 Hz (for ν=8 to 9 GeV).

Backgrounds to the very forward electron tagger include bremsstrahlung and Møller processes. Bremsstrahlung photon production peaks at very forward angles (about $\delta\theta \approx m_e/E$), therefore their contribution at angles $\theta > 0.5^o$ is very small. We have calculated the Møller electron rates at forward angles. Figure 3.69 shows the angular distribution of Møller electrons for an electron luminosity of 10^{34} cm^{-2} sec^{-1}. The rates of Møller electrons show a minimum about 0.5^o to 1.4^o, which correspond to our tagging angles. These backgrounds have been checked using a GEANT-3 simulations. Most of the background comes from Møller electrons. Hadronic backgrounds are about two order of magnitude smaller. The total expected background is about 6 MHz. This background can be almost totally rejected at the trigger level by energy and clustering thresholds in the low Q^2 detector.

Virtual (‘almost real’) photoproduction presents several advantages over photon bremsstrahlung beams. Only electrons corresponding to photons that have produced hadronic interactions are registered by the tagger, thus allowing a higher beam flux for a comparable accidental rates. This is a major advantage for using thin targets. For “post-tagged”, very low Q^2, beams the tagged electron flux is proportional to the hadronic rate and not to the incoming photon flux, so that the photon flux is not limited by the electron tagging rate. It is, therefore, possible to run higher beam currents into thin targets without an increase in accidental rates. As a consequence, higher luminosities can be achieved using thin (in gm/cm^2) targets than in case of a tagged bremsstrahlung beam.

As discussed earlier, for a luminosity of 10^{34} cm^{-2} sec^{-1} the total tagged electron rate will be of order 6 MHz, producing an inelastic signal of about 400 Hz. To be able to reduce those total electron rates, a selective trigger and tight coincidence window between the low Q^2 tagger signal and a multi-particle signal in CLAS^{++} needs to be achieved. Møller background will produce two clusters containing the full energy

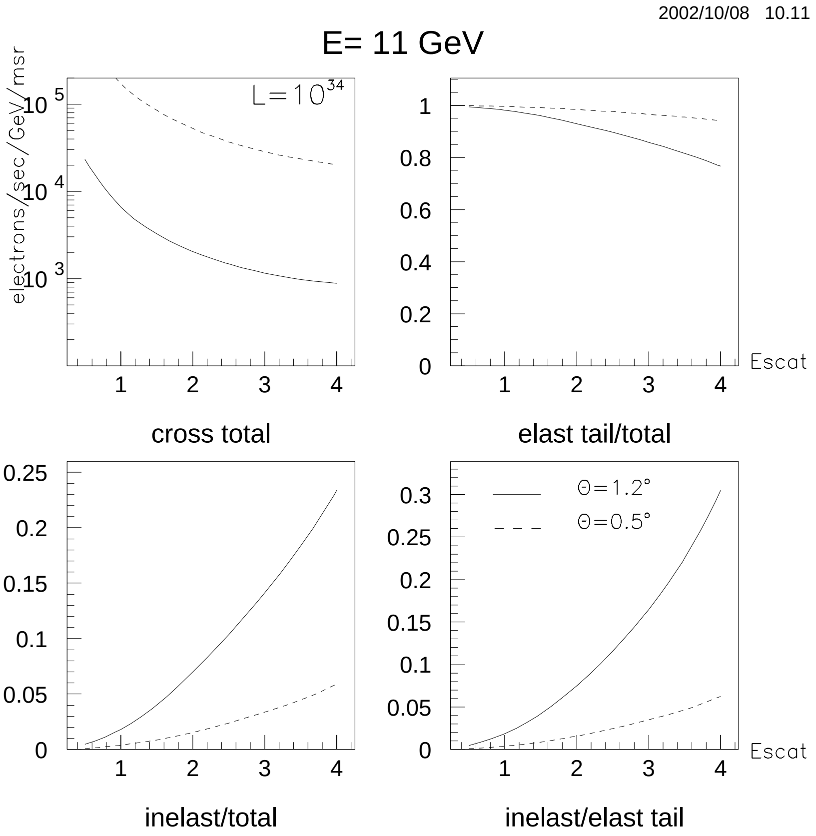

Figure 3.68: Total electroproduction rates at 11 GeV beam energy.

of the beam, instead the signal will produce one cluster with an energy of around 1 to 4 GeV. For a three prong event in CLAS^{++} and energy thresholds in the low Q^2 electron detector, the data acquisition rate will be reduced to a few kHz.

The low Q^2 post-CLAS detector is currently being designed and is expected to be in operation well before the 12 GeV upgrade. Electrons undergoing small angle scattering in the CLAS target will be detected by a downstream spectrometer (about 10 meters downstream of the target) that measures the angles θ, ϕ and the electron energy. The spectrometer will consist of high rate multi-wire proportional chamber, scintillating fibers or traditional drift chamber to measure θ and ϕ of the electrons. The energy will be determined either by using a magnetic spectrometer or by a high resolution highly segmented calorimeter. We expect to achieve virtual photon energy resolution on the order of $\delta(E_\nu)/E_\nu < 0.5\%$.

3.7.2 Meson Spectroscopy on LH_2 Targets

A complete mapping of meson resonances in the mass region of 1 to 3 GeV will be particularly important for a better understanding of the QCD confinement mechanism.

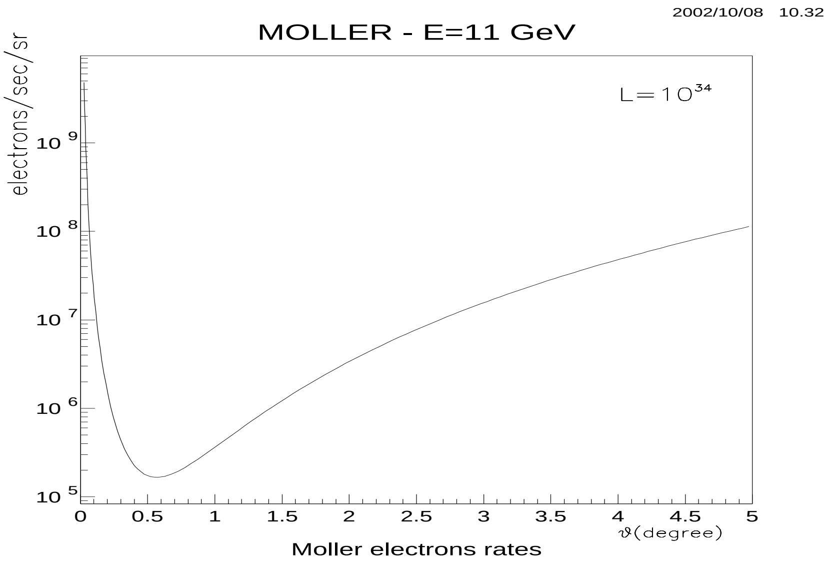

Figure 3.69: Møller electron rates

QCD predicts the existence of several new types of states beyond the naive quark model: glueballs, hybrids, multi-quark $q\bar{q}q\bar{q}$ states [208, 209]. Gluons play a central role in strongly interacting matter – quark confinement is due to gluonic forces. The clearest most fundamental experimental signature for the presence of dynamics of gluon degrees of freedom is the spectrum of gluonic excitations of hadrons. Gluonic excitations of mesons with "exotic" quantum numbers, *i.e.*, quantum numbers not accessible to the $q\bar{q}$ system, would be the most direct evidence for these states. Determining the properties of such states would shed light on the underlying dynamics of quark confinement.

The identification of these states has been difficult, as high mass resonances are generally broad and overlapping, and often have similar quantum numbers (mixing). Hadronic cross-sections are low, so statistics have been limited. Ideally, for a complete mapping of the mesons in this mass region, we will need to study each resonance through as many decay channels and production mechanisms as possible in order to disentangle mixing. To determine meson quantum numbers we use partial wave analysis (PWA) (in a broad sense, fits to the angular distributions of final states). A complete PWA requires high event statistics, as well as high resolution and geometrical detector acceptance. Meson spectroscopy at the upgraded CLAS, using the low Q^2 tagger, will fulfill many of those stipulations. The general idea of PWA is to parameterize the intensity distribution in the space of quantum numbers available to the observed final states. The intensity distribution is written as a sum of interfering and non-interfering amplitudes (partial waves), for example in the reflectivity basis [210]: $I(\tau) = \sum_{\epsilon,k} | \sum_b^{\epsilon} V_{bk}^{\epsilon} A_b(\tau)|^2$. The variable k is the rank of the fit, related to the set of partial waves from the production vertex, τ describes the set of angular distributions that define the decays, and b is an index for the set of quantum number accessible to the final state system. The spin density matrix will define the rank of the production waves, entering the production amplitude V_{bk}. The decay amplitudes, $A_b(\tau)$, are given by geometrical terms of combinations of Clebsch-Gordan coefficients (D functions). A maximum likelihood fit is done to the intensity distribution by a set of given partial waves and reasonable assumptions of the production mechanisms. The goodness of the fit is related to the statistics (number of events per binned data) and the rank of the matrix, number of parameters to be fitted. The fit could then be improved by using higher statistics or (equivalently) by reducing the rank of the fit by having more information about the production mechanisms.

The knowledge of photon polarization simplifies the PWA by giving direct information on the production mechanisms and therefore reducing the rank of the fit. Electroproduction at these very small values of Q^2 using unpolarized electrons *is equivalent to photoproduction using partially linearly polarized photons.* The matrix element for the electron scattering process in the one-photon exchange is:

$$|\mathcal{M}|^2 = (2e^4/Q^2)T_{\mu\nu}L^{\mu\nu}$$

where $T_{\mu\nu}$ is the hadronic tensor (expressed in terms of nucleon structure functions) and $L^{\mu\nu}$ is the virtual photon polarization density matrix. Defining the photon polarization as:

$$\epsilon = [1 + 2\frac{(Q^2+\nu^2)}{Q^2}\tan^2(\theta/2)]^{-1},$$

and the longitudinal polarization $\epsilon_L = \frac{Q^2}{\nu^2}\epsilon$, the polarization density matrix can be written as [206]:

$$\begin{pmatrix} \frac{1}{2}(1+\epsilon) & 0 & -[\frac{1}{2}\epsilon_L(1+\epsilon)]^{1/2} \\ 0 & \frac{1}{2}(1-\epsilon) & 0 \\ -[\frac{1}{2}\epsilon_L(1+\epsilon)]^{1/2} & 0 & \epsilon_L \end{pmatrix}$$

At very low values of Q^2 the virtual photon beam becomes, for all practical purposes, almost a real photon beam, since

$$\epsilon_L = \frac{Q^2}{\nu^2}\epsilon = 10^{-3}\epsilon \approx 0.$$

Since there is no longitudinal contribution, the matrix represents the spin density matrix of real (transverse) photons.

Figure 3.70 shows the values of the photon polarization in our kinematic range. The photon polarization produced by an 11 GeV electron beam ranges between 65% (7 GeV photons) to 20% (10 GeV photons). Since the polarization is measured for

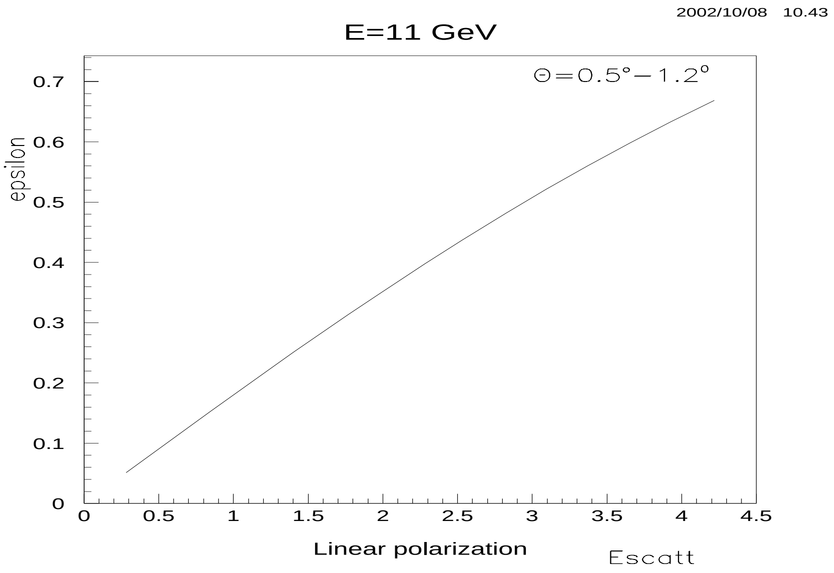

Figure 3.70: Virtual Photon Polarization

each photon, in a sense, all of the photons in the beam are polarized. In contrast, the polarization produced by coherent bremsstrahlung beams is a strong function of the energy of the bremsstrahlung photons.

To illustrate the importance of linear polarization, a simulation of meson production via photoproduction physics was performed (for an electron beam energy of 6 GeV). Events were generated according to t channel phase space with a $\frac{\partial\sigma}{\partial t} \propto e^{5t}$. These events were weighted according to a photoproduction cross-section as a function of polarization and with a one pion exchange production (OPE) mechanism. Included in the description of the cross-section were 4 resonances: $a_1(1260), a_2(1320), \pi_1(1600)$ and $\pi_2(1670)$. Events were then filtered through a *current CLAS geometric acceptance simulation (GSIM).* The events were simulated for $\nu = 4\ GeV$, so the polarization of the virtual photon was $\approx 60\%$ (similar to the one expected in the upgrade).

The effects of polarization can be directly seen in Figure 3.71. Because pion exchange corresponds to unnatural parity exchange the ϕ dependence of the produced 3π system will flip depending on the naturality of the state [211]. These two figures differ only in the direction of the photon polarization and correspond to the two eigenstates of reflectivity. In Figure 3.71 (a) are those events where the photon polarization is normal to the production plane, and (b) are those events where the photon polarization is in the production plane. Due to parity conservation in the production process, states of the same reflectivity but opposite naturality will have opposite ϕ distributions, which may be observed in the figure. It is most clearly seen for the band at the $a_2(1320)$ mass. This distribution is $cos^2(\phi)$ in one figure and $sin^2(\phi)$ in the other. Another band at a mass near 1.7 GeV has the opposite ϕ behavior of the $a_2(1320)$. It corresponds to the $\pi_2(1670)$ which has a naturality

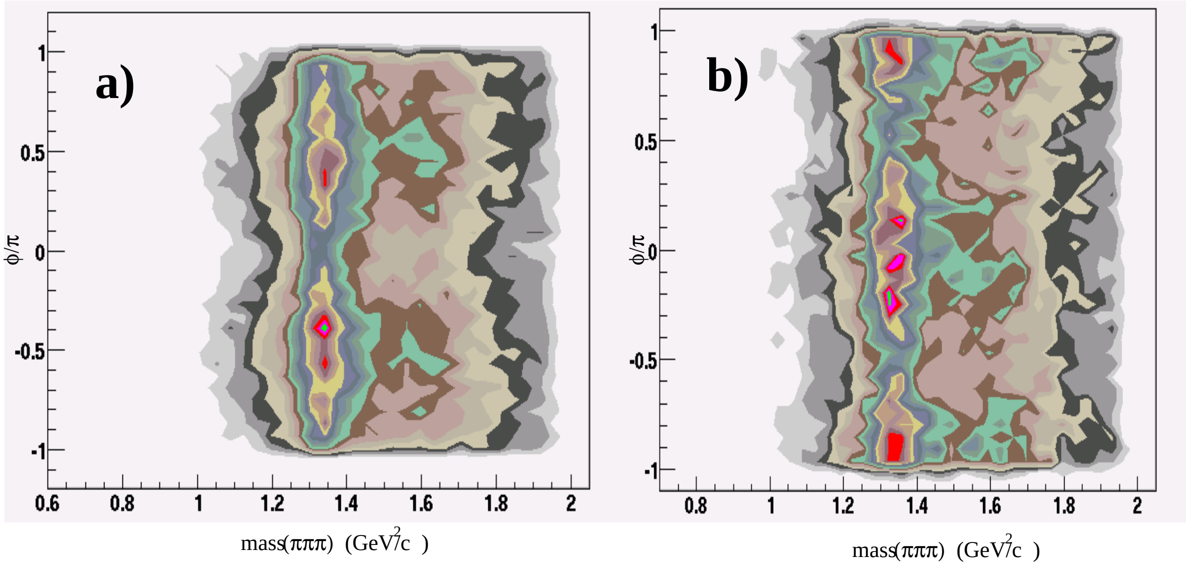

Figure 3.71: The ϕ/π vs Mass$[3\pi)$ for those events with the polarization in the production plane. The simulated polarization was set to 60%.

opposite that of the $a2(1320)$.

In practice, the spin-parity, and therefore the naturality, of a resonance is measured via a partial wave analysis. Using this and the known beam polarization in formation, the naturality of the unknown exchange particle can be determined thus providing key insight into the production mechanism.

Spectroscopy studies of mesons have started at JLab with CLAS at lower energies [212]. Preliminary results of these experiments show the viability of such studies using the current CLAS configuration. PWA of simple final states $(\pi\pi)$ have already been carried out successfully using current CLAS data. CLAS experiment E01-017 studied the reaction $\gamma p \to p\pi^+\pi^-$. For the purpose of this study, we have chosen exclusive final states where a π^+, a π^-, and a proton are detected in CLAS. The $\pi^+\pi^-$ invariant mass distribution shows a clear signal at the mass of the ρ and the f_2. The results of a preliminary PWA of the system is shown in Figure 3.72. The ρ meson is identified as a $J^{PC} = 1^{--}$ state, while s-channel helicity conservation is clearly observed, as the ρ signal is dominated by the $|J_z| = 1$ partial wave. There is also some leakage from the $J^{PC} = 2^{++}$ $f_2(1270)$ partial wave into the 1^{--} wave as observed in Figure 3.72, in the 1^{--} partial wave intensity in the 1.1 to 1.2 mass range. Since the final state is composed of two identical pseudoscalars, there are also purely mathematical ambiguous solutions that at this moment, we have not accounted for but have plans to incorporate as the analysis matures. These ambiguities will be mostly resolved when using linearly polarized photons and larger acceptances.

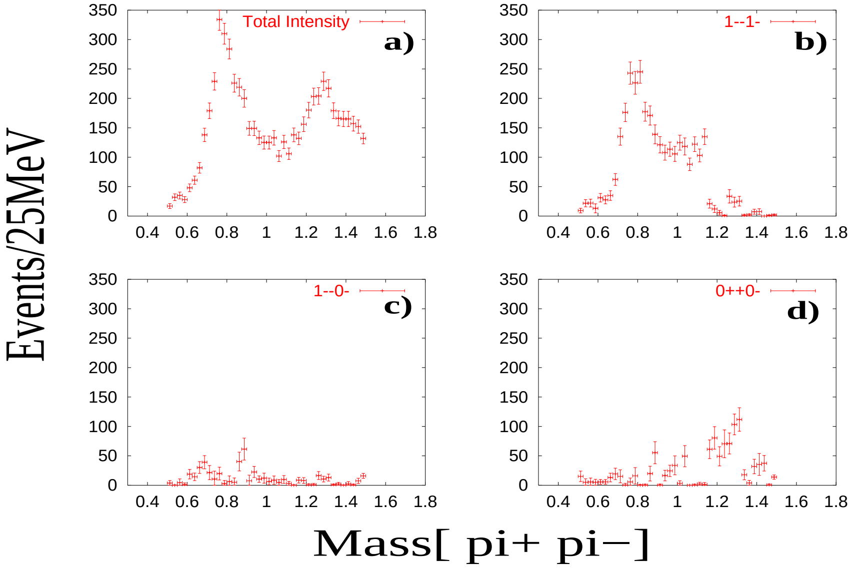

Figure 3.72: CLAS E01-017 preliminary partial wave analysis results of the reaction $\gamma p \to p\pi^+\pi^-$. (a) Total intensity distribution. (b) Intensity for the $J^{PC} = 1^{--}, |J_z| = 1$ wave. (c) Intensity for the $J^{PC} = 1^{--}, |J_z| = 0$ wave. (d) Intensity for the $J^{PC} = 0^{++}$ wave.

Even if events are not fully measured over the entire solid angle, hermiticity will provide information to veto events that are not fully reconstructed, reducing leakages among different waves due to poorly reconstructed events. CLAS^{++} will be able to measure multi-charged and multi-photon particle final states with good acceptances for up to four or five final state particles. PWA of more than four or five final particles becomes difficult and increasingly unreliable, limiting the possible number of decay channels to be analyzed. We plan to obtain the high statistics that will be needed to access channels with four observed particles in the final state by running high beam currents. The rate at which we will be able to obtain data will likely be determined by limits of our DAQ system. In comparison, current CLAS experiments using CLAS bremsstrahlung beams at DAQ rates of 2 KHz were able to achieve comparable statistics (in three particles final states) to previous π beam experiments in about one or two months ("real time") of running.

Another important meson spectroscopy study is of strangeonia. Strangeonia are mesons made of dominantly (valence dominance) $s\bar{s}$ unflavored strange quarkonia. They are associated with the radial and orbital excited states of the $\phi(1020)$ meson, that is known to be composed mainly of $s\bar{s}$ valence quarks. We will study strangeonium states with masses ranging from 1 up to about 2.5 GeV. Given that strangeonium states have intermediate masses between the light (up, down) and heavy (charm, bottom) quarkonia, they are very useful in the study of the QCD confinement potential in the transition region from short to large distance behavior. Particularly,

$s\bar{s}$ excitations provide a range of quark separations where the confinement potential can be explored from the perturbative to the non-perturbative regimes. This character has been pointed out by Gell-Mann and recently by Barnes, Page and Black [213]: "the similarity between the $s\bar{s}$ spectrum, the light meson $n\bar{n}$ and the heavy $Q\bar{Q}$ systems needs to be understood to bridge the gap between Heavy Quark Effective Theory (HQET) and the light quark world in which we live". Strangeonia are poorly understood – of the 22 strangeonium states expected below a mass of 2.2 GeV, only 5 are well identified. The clarification of the strangeonium spectra in this mass range is an important and necessary step for the advance of intermediate mass meson spectroscopy.

3.7.3 Meson Spectroscopy Using Coherent Production on ^{4}He.

Partial wave analysis is a key element in any meson spectroscopy experiment. Use of a linearly polarized photon beam is one way to reduce the number of parameters in the PWA, and therefore reduce the ambiguities and the required statistics. Another way of simplifying the PWA is the selection of a production mechanism that reduces the number of allowed helicity states and/or allowed exchange particles. Such processes can be coherent production of t-channel meson on nuclei. Particularly, coherent production of mesonic states on ^{4}He, where the target nucleus remains intact after the interaction, has several advantages for the PWA. These are due to the spin-0 and isospin-0 of ^4He. This type of reaction is a powerful tool for studying neutral mesons.

Examples of such reactions can be coherent production of $\pi\eta$ and $\pi\eta'$ final states on a ^{4}He target. The attractive feature of these final states is that in P-wave these are $J^{PC} = 1^{-+}$ exotics. Photoproduction of $\pi\eta$ and $\pi\eta'$ on the nucleon proceeds only via C-odd ρ or ω exchanges. Since ^4He has isospin-0, only ω exchange is allowed. Due to spin-0 of ^4He, the helicity of the final state in forward production should be equal to the helicity of the incoming photon, which means that S wave production in the final state is not allowed, and the sum over the helicity of the final state will be reduced to one term. **The key feature of these measurements is that the recoiling helium nuclei remains intact. This requires direct detection of the recoiling ^4He nucleus.**

PWA formalism

In photoproduction (as in the case of pion beams) the mechanism leading to natural parity and unnatural parity exchange (NPE and UPE) in the t-channel do not interfere and contribute to different amplitudes with different angular dependences. If the production mechanism is defined, it provides additional constraints for the PWA.

Differential cross section of t-channel meson photoproduction in the rest frame of the produced state (Gottfried-Jackson frame) can be written as[6]:

$$\frac{d\sigma}{d\Omega} \;=\; |A_0 \;+\; A_-|^2 \;+\; |A_+|^2. \tag{3.60}$$

Here A_0 and A_- are the helicity amplitudes for the UPE, and A_+ is for NPE. The complete expression for helicity amplitudes can be found in [214] and references therein.

In the case of coherent photoproduction of $\pi\eta(\pi\eta')$ on ^4He, when only ω exchange is allowed, A_0 and A_- will vanish and only A_+ contributes. Morover, production of a state with $L = 0$ is forbidden due to helicity conservation in the S-channel (SCHC)[7], and the helicity of the $\pi\eta$ $(\pi\eta')$ system should be that of the incoming photon. Therefore, A_+ can be written as:

$$A_+ \;=\; \sum_{L=1}^{L_{max}} (2L+1)^{1/2}\sqrt{2}L_{1+}Im(D^L_{10}(\Theta,\phi)), \tag{3.61}$$

where L is the total angular momentum of $\pi\eta$ $(\pi\eta')$ system, and the sum is taken up to the highest possible angular momentum of the produced pair in the given mass range. $L_{\lambda+}$ is the amplitude for the production of $\pi\eta$ $(\pi\eta')$ with spin L via NPE. These amplitudes are the parameters in the PWA. The angular distribution of the decay meson will be analyzed in each energy bin to determine the production strength of a particular wave.

The function $D^L_{\lambda 0}(\Theta,\phi)$ defines the angular distribution of the π (or η/η') in the Gottfried-Jackson frame. Θ and ϕ are polar and azimuthal angles of the meson in that frame. Using the standard form for $D^L_{10}(\Theta,\phi)$ the differential cross section for the production of interfering waves with $L \leq 3$ can be written as:

$$\begin{aligned}\frac{d\sigma}{d\Omega} &= |-\sqrt{3}P_{1+}\sin(\phi) \\ &+ \quad -\sqrt{15}D_{1+}\sin(\phi)\cos(\Theta) \\ &+ \quad -\frac{\sqrt{15}}{2}F_{1+}\sin(\phi)(5\cos^2(\Theta)-1)|^2,\end{aligned} \tag{3.62}$$

It should be noted that the cross section is proportional to $\sin^2(\phi)$, which is due to the assumption of SCHC. The measured angular dependence will be an independent test of this assumption. In the PWA only three mass-dependent parameters, P_{1+}, D_{1+} and F_{1+}, need to be determined.

---

[6] Here and in the following we will use notations from Ref.[214].

[7] This is valid at our kinematics where $\frac{\sqrt{-(t-t_{min})}}{E_\gamma} \sim 0$

Experimental issues

CLAS^{++} will have large coverage for neutral and charged particles in the forward direction and nearly 2π coverage at scattering angles $\theta > 45^o$. The detection of a multiparticle final state from many-body decays of final state mesons can therefore be accomplished. The main issue in these measurements will be the detection of the recoiling ^4He nuclei.

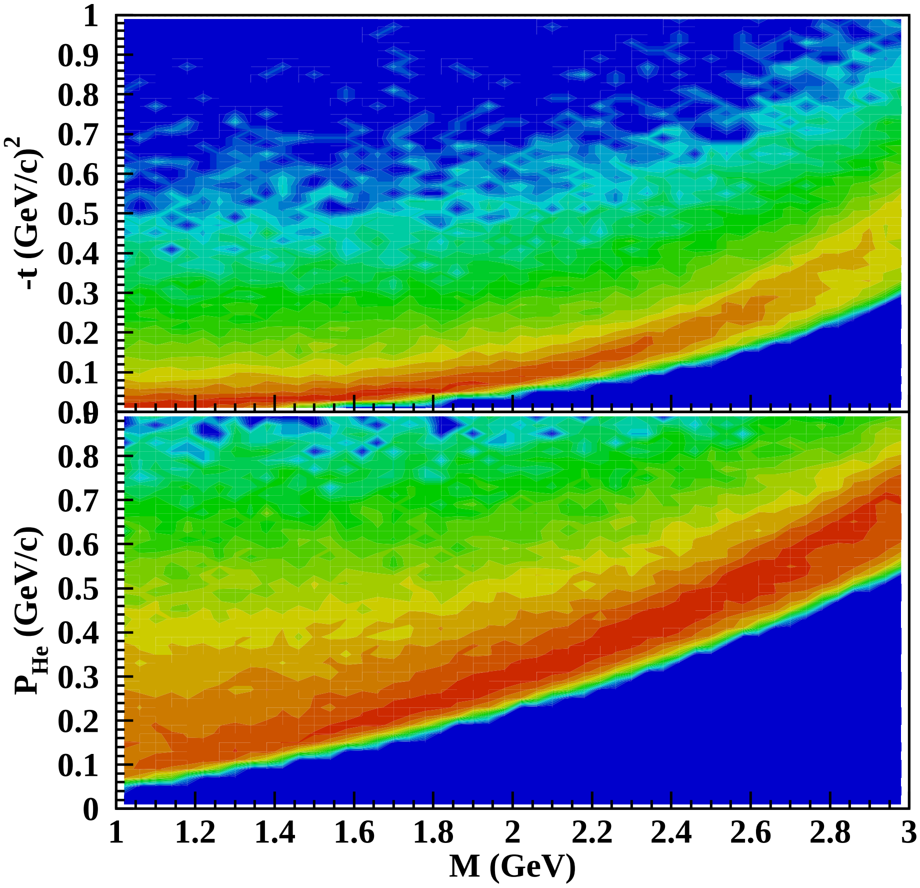

Figure 3.73: Kinematics of proposed measurements. Top plot - four momentum transferred squared as function of the produced t-channel meson mass. The lower edge corresponds to t_{min} for a maximum photon energy of 9 GeV. The lower plot shows the corresponding momentum distribution of recoiling ^4He nuclei.

For reasonable production rates, measurements should be carried out at small momentum transferred, close to t_{min}, to limit the cross section reduction due to the ^4He form factor. This implies that recoiling target nuclei will have very small momenta, as shown in Figure 3.73. For a mass range $M < 2.5$ GeV/c^2 the momentum of the recoiling nucleus is ≤ 0.35 GeV/c. ^4He nuclei with such low momenta will not be able to pass through any size liquid target. A lighter target, e.g. using pressurized gas, is needed. Using a gas target with the conventional photon tagging method is not an option due to severe luminosity limitations. **Electron scattering at small angles opens up a very attractive alternative to conduct experiments on "thin" targets**.

Use of an electron beam has many advantages: the small size of a few hundred μm high precision electron beam will allow use of a small diameter target cell. This will help reduce the thickness of the target walls at a given pressure (density), and therefore reduce the amount of the material in the way of final state particles. Also a small size electron beam will allow better determination of the interaction point in the plane perpendicular to the direction of the beam. For the required luminosity, the density of the target and the beam current can be varied without compromising the signal/accidental ratio.

The proposed detector for tagging very low momentum backward going protons in electron deuteron scattering (for studying the neutron structure), will allow detection of ^4He nuclei for momenta as low as $\sim$ 0.25 GeV/c (corresponding to a transferred momentum squared in the t-channel of $t_{thr} = 0.07$ (GeV/c)^2). A description of the gas target and the detector for low energy protons is presented in Section **??**. To use this detector for meson spectroscopy, the only change required is to replace the deuterium gas in the target cell by helium gas.

Expected rates

In this section, estimates for the production rate of exotic states in the mass range from 1.4 to 1.6 GeV in the $\pi\eta$ decay channel are presented. States with exotic quantum numbers have been reported in previous experiments. We assume that exotic waves will be produced at a rate of 10% compared to the production rate for A_2 in the same decay mode.

The cross section for t-channel meson electroproduction can be expressed as a sum of the cross sections for transversely (σ_T), and longitudinally (σ_L) polarized photons:

$$\frac{d\sigma_{eN\rightarrow eM^0N}}{dQ^2dWdt} = \Gamma_W \cdot (\frac{d\sigma_T}{dt} + \epsilon\frac{d\sigma_L}{dt}) \tag{3.63}$$

were Γ_W is the virtual photon flux, and ϵ is the virtual photon polarization.

For the kinematics of the proposed measurements, Q^2 $\sim$ 0.01 (GeV/c)^2, σ_L can be neglected, and σ_T can be calculated using the VDM formalism from the photoproduction cross section:

$$\sigma_T = \left(\frac{m_\rho^2}{m_\rho^2+Q^2}\right)^2 \cdot \sigma_{\gamma N\rightarrow M^0 N} \tag{3.64}$$

were m_ρ is the ρ meson mass, and $\sigma_{\gamma N\rightarrow M^0 N'}$ is the photoproduction cross section.

Production on nuclei is usually used to enhance the statistics. In the proposed experiment the gain in the production rate (cross section) will be a factor of 16, however the requirement of leaving the ^4He nucleus intact will add an extra form-factor, $F_{He}(t)$, in the amplitude, and the cross section will be:

$$\frac{d\sigma_{eHe\to eM^0He}}{dQ^2dWdt} = \Gamma_W \cdot \frac{d\sigma_{\gamma N\to M^0N}}{dt'} \cdot (4F_{He}(t))^2 \tag{3.65}$$

For A_2, the differential cross section can be extracted from existing experimental data ([215]). At $t' = t_{thr} - t_{min} = 0.05$ (GeV/c)^2, we obtain $\frac{d\sigma}{dt'} \simeq 2\mu b(GeV/c)^{-2}$. The proposed measurements will be carried out using a 10 cm helium gas target at 5 atm pressure. Combined with a beam of up to 500 nA a luminosity of $L = 4 \times 10^{33}$ cm^{-2}sec^{-1} can be achieved. Using the known branching ratios Br($A_2 \to \pi\eta$)= 14% and Br($\eta \to \gamma\gamma$)= 39%, and the upgraded CLAS acceptance for this final state ~ 0.07 one gets 0.05 sec^{-1} for the A_2 electroproduction in this channel. Assuming 10% for the ratio of an exotic wave relative to the A_2 we found 18 hour^{-1} for the detection rate of an exotic in the coherent scattering of the 11 GeV electrons off a helium target.

One should note that $\pi\eta$ or $\pi\eta'$ final states are just examples of reactions that can be studied. Since CLAS^{++} can operate with loose trigger requirements, all possible final states will be recorded in parallel. The spin 0 and isospin 0 of the ^4He target will give the same advantages in PWA for other final states.

3.7.4 Summary

The low Q^2 post-CLAS electron detector is currently being designed and is expected to be in operation well before the 12 GeV upgrade. Electrons that undergo small angle scattering in the CLAS^{++} target will be detected by a downstream spectrometer (about 10 meters downstream of the target) that measures the angles θ, ϕ and the electron energy. The spectrometer will consist of high rate multi-wire proportional chamber, scintillating fibers or traditional drift chamber to measure θ and ϕ of the electrons. The energy will be determined either by using a toroidal magnetic spectrometer or by a high resolution highly segmented calorimeter. We expect to achieve virtual photon energy resolution on the order of $\delta(E_\nu)/E_\nu < 0.5\%$.

Virtual ('almost real') photoproduction presents complementarity to a bremsstrahlung beam. Only photons that had produced hadronic interactions are registered by the tagger, thus allowing a higher beam flux for comparable background accidentals. For "post-tagged", very low Q^2, beams the tagged electron flux is proportional to the hadronic rate and not to the incoming photon flux, so that the photon flux is not limited by the electron tagging rate. It is therefore possible to run higher beam currents into thin targets without an increase in accidental rates.

The addition of a low Q^2 post-CLAS electron tagging detector will extend the rich physics program of CLAS^{++} at 12 GeV. The meson spectroscopy program will provide measurements in a novel manner that will test models and complement measurements made via other methods. The Wide–Angle Pion Compton Scattering and Time-like DCVS program is unique to CLAS and will add significantly to the CLAS^{++} GPD physics program.

Chapter 4

Upgrade Strategy and CLAS^{++} Detector Components

4.1 CLAS Upgrade Strategy

The main goal of the CLAS upgrade is to maintain its capability to obtain high statistics data for exclusive electron scattering reactions at beam energies of 12 GeV. At the higher energies, and in the regions of interest for the physics program at large hadronic invariant masses, particle multiplicities increase and make it more difficult to isolate exclusive processes from an increasing level of multihadron background. In addition, the missing mass resolution decreases which will render the separation of exclusive processes from multihadron background less effective. Lastly, exclusive processes are of interest at high photon virtualities Q^2, where the electroproduction cross section is expected to fall-off with the power of $1/Q^6$. In order to achieve acceptable count rates for these reactions experiments have to be carried out higher luminosities than at 6 GeV. To accomodate these requirements in the CLAS upgrade two major improvements are required:

- the missing mass technique needs to be complemented by a more complete detection of the hadronic final state
- the luminosity that CLAS can operate at needs to be increased by about one order of magnitude to $L = 10^{35}\ cm^{-2}\ s^{-1}$

The coverage for hadronic final states will be increased by complementing the present CLAS detection system by a new central detector that allows detection of charged particles and neutral particles over the full acceptance. Moving this central detector upstream converts the present CLAS detection system into a detector for forward going particles.

Knowing the directions of all particles gives the following analysis options:

- use of kinematical fitting procedures to determine the final state
- veto events with incomplete determination of the final state (this lowers the detection efficiency but avoids contaminating lower multiplicity final states)

The key to operating CLAS at increased luminosity is to keep the occupancy of the drift chambers low. A crucial ingredient is the magnetic shield that protects the tracking system from Møller electrons. The mini-torus can no longer be used since its mechanical structure blocks part of the solid angle. The preferred solution is a short superconducting solenoidal magnet which also serves as a magnet for the momentum analysis of large angle tracks.

The upgrade plan is based on retaining major components of CLAS, the torus magnet, scintillation counters, gas Cerenkov counters, electromagnetic calorimeters, and part of the electronics, while replacing the tracking chambers, adding a new central detector, a pre-shower detector, and a second gas Cerenkov counter. A single-sector exploded view of the upgraded CLAS^{++} detectors is shown in Fig. 4.1. Conceptual designs of the components of the upgrade plan are discussed in more detail in the following sections.

4.2 CLAS Torus Magnet

The original CLAS Toroidal Magnet was designed and fabricated by Oxford Inc. The CLAS^{++} upgrade is based on using the original CLAS Torus with some modifications. At this time the extent of the modifications is not clear, but the concept is to reuse as much of the Torus as possible. At minimum this includes:

- all six coils
- the service module
- the cryogenic supply from the End Station Refrigerator and all associated piping
- the power supplies and bus bars
- vacuum pumping system
- backup AC electrical generator system which provides power upon a loss of site power to keep the computer hardware and vacuum system operational and allows for controlled rundown of the magnet.

The minimum modification required will be to replace all 72 out-of-plane (OOP) supports. These supports keep the coil centered in the vacuum case and support both magnet and gravitational loads. Experience gained from the original CLAS operation

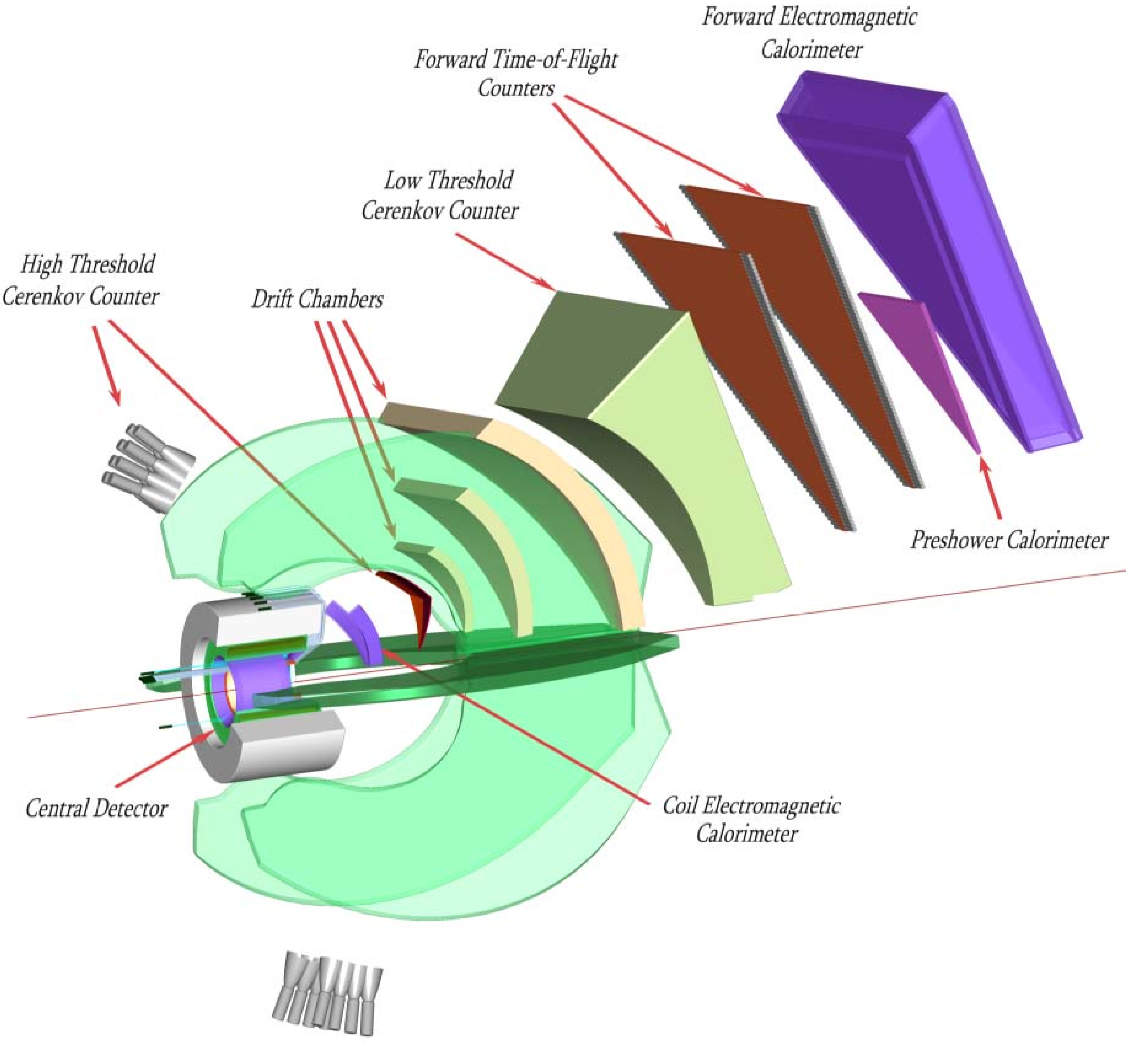

Figure 4.1: Exploded view of the CLAS^{++} detector system for a single Torus magnet sector showing, beginning at the target, the Central Detector system, the inner electromagnetic calorimeter, the high threshold Cerenkov counter, the region 1, 2 , 3 drift chambers, the low threshold Cerenkov detector, the double layer forward time-of-flight counters, the preshower calorimeter, and the forward electromagnetic calorimeter. The light collection system outside of the Torus coils collects the light from the high threshold inner Cerenkov counter.

has shown this to be a requirement for operating a high field solenoid inside the torus at full field. The CLAS Torus will also be modified to allow for the addition of the Central Detector, Solenoid Magnet, and iron flux return. This will require that the backward (upstream) end of the coils are moved out, and the following items will need replacement:

- backward support ring
- forward fixings
- a new cold ring may be needed. The cold ring provides cryogenic distribution to all 6 coils; it also contains quench protection circuitry and temperature stabilization

Issues that require further study:

- impact of iron of the Central Detector affecting Torus field lines
- impact of iron of the CD on Torus OOP and IP support
- hysteresis of iron affecting magnetic field
- quenching and ramping of magnets. Sequencing and interlocking
- swaying of the Torus either beam left or right due to attraction to the iron

After all modifications have been completed, the position and geometry will be surveyed, and the magnetic field will be mapped in the region where particle tracking will be done, i.e. up to about 40° in polar angle, and for all six sectors.

To optimize the installation schedule a cold ring will be procured in advance of the end of 6 GeV CEBAF operations. When the upgrade starts, CLAS will be disassembled, and each of the 6 coils will be removed from the superstructure. The original cold ring will be removed. The top coil will be hung from its support rods, and the coils will be reinstalled in a similar fashion to the original system.

Support for the 20,000kg of iron will be from the floor of the Hall whereas the Torus will remain hung from the superstructure.

4.3 Central Detector

4.3.1 Introduction

The CLAS^{++} detector consists of a forward detector system (FD) which is sensitive to charged and neutral particles emitted at lab angles between 5 and 40 degrees and a central detector (CD) which covers the angular range from 40 to 135 degrees.

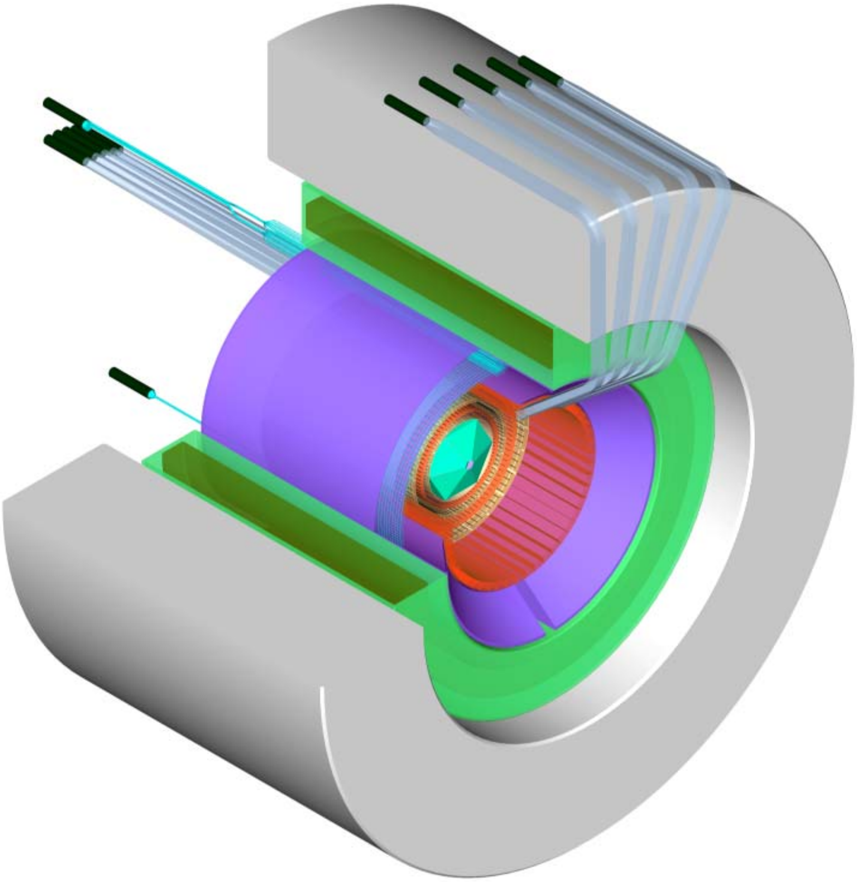

Figure 4.2: Central detector region showing (from the outside to the inside) the flux return iron, the super-conducting solenoid, and the layout of the central EC and TOF, the central tracker, and the microstrip detector assemblies.

The central detector is located within a small superconducting solenoidal magnet which performs a dual function: it curls emitted low-energy MØller electrons into tight spirals which are directed into a cylindrical absorbing tube, and it provides the B-field for the central tracker. The design of the solenoidal field involves a compromise between a desire for a large-radius, high-current solenoid which would curl the MØllers into the tightest radius and the necessity to keep the magnetic forces on the main torus which result from the stray B-field as low as possible. An iron flux-return surrounding the magnet accomplishes these contradictory goals.

A major thrust of the experimental program will be deeply exclusive scattering (DES). DES events are characterized by the presence of the scattered electron and one or two hadrons in the forward spectrometer, and typically one recoil baryon in the central detector. Because we rely on the missing mass technique to identify reactions and to reject background we wish to optimize the missing-mass resolution and to maximize the multi-particle acceptance.

Ideally, we would like to match the contributions of the central and forward detectors to the missing-mass resolution; i.e. $\delta(E + H_{fwd}) \approx \delta(H_{recoil})$. Since we expect the forward electron and hadron to have roughly 5 GeV/c of momentum, and we expect a momentum resolution of 0.1% * P or approximately 0.5% (for each 5 GeV/c particle), then the expected absolute resolution is about 50 MeV/c or better for each. The recoil particle will have a momentum of approximately 1 GeV/c. This momentum must be measured with an accuracy of about 5% to contribute an equal amount to the missing-mass error budget as the other two particles. As presented in the following section on the central tracker, a tracking device which measures a 25 cm long track in a 3T solenoidal magnetic field with a 100 micron accuracy on the sagitta will have a resolution on the perpendicular component of the momentum of about 2.2%. This sets the scale for the accuracy requirements of such a tracker; the value varies linearly with the accuracy, inversely with the B-field value and as the inverse square of the tracking length. Similarly, we expect the forward tracking system to have a polar angle accuracy of about 1 mrad, resulting in an inaccuracy of the perpendicular component of a 5 GeV/c track of about 5 MeV/c. The expected 8 mrad accuracy of the central tracker will likewise result in an 8 MeV/c resolution of the perpendicular component of a 1 GeV/c particle. The absolute momentum and angular resolution of the central tracker is therefore well-matched to the expected resolution of the forward tracker.

In addition to the tracking devices, the central detector consists of an array of scintillator paddles used to measure time-of-flight (CD-TOF) of the charged particles, and a central electromagnetic calorimeter (CD-EC) use to measure the energy of photons emitted in the central region.

With the projected time resolution of 50 ps the CD-TOF will be able to separate pions and protons up to 1.2 GeV/c, and kaons from pions up to 0.6 GeV/c. In addition it will be very important in rejecting the out-of-time hadronic background. This can be accomplished with time resolutions on the order of 1 ns.

The CD-EC will complement photon detection in the forward calorimeter, cover the full azimuthal angular range, and the polar angle range from 40^o up to 135^o. Most of the photons hitting the CD-EC will have energies from 50 MeV to up to 1 GeV. The CD-EC has been designed to have sufficient "depth" to fully contain the energy deposition of 1 GeV photons, and allow detection of photons in this energy regime with approximately the same energy resolution as the forward angle calorimeter.

A layout of the central detector and solenoid is shown in Fig. 4.2.

4.3.2 Superconducting Solenoid Magnet

At the core of the central detector is a superconducting solenoid to provide a central longitudinal magnetic field of up to 5 Tesla. The solenoid magnet serves the following functions:

- determine particle momenta and charge via tracking in the central tracking devices.
- keep Møller scattered electrons from reaching the detectors by guiding them to a shielding pipe made of heavy metal. The maximum luminosity CLAS^{++} can be operated at is limited by the degree to which tracking chambers are shielded from the Møller electrons and secondary particles. This technique has been used successfully during the CLAS eg1 runs, with the magnetic field provided by the 5 Tesla superconducting Helmhlotz magnet wich was used with the CLAS polarized target magnet. This arrangement resulted in better shielding than that provided by the mini-torus magnet which is the standard shielding configuration in CLAS for use in experiments with unpolarized targets.
- provide the magnetic field for a solid-state dynamically polarized target. This requires a 5 Tesla polarizing magnetic field with an inhomogeneity of $\Delta B/B \leq 5 \times 10^{-4}$ for polarized NH_3 material. The polarized target operation adds homogeneity constraints which will require additional correction coils.

Magnet Design

A magnetic design using TOSCA$^{(R)}$ 3D has been performed to establish the basic magnetic requirements, provide 3D field maps for Møller background analysis and to produce basic engineering information about the magnet. A single layer, Superconducting, warm iron yoke magnet was chosen as the optimal configuration. The field excitation ranges from 2T to 5T. The design constraints were as follows:

- reduce the fringe field in the proximity of the CLAS coils to minimize the CLAS's out of plane forces.
- have a sufficiently large internal radius to house the central detectors, and
- an outer yoke radius to fit within the modified CLAS cryostat
- an opening in the forward region to allow detection of particles from 5^o to 40^o.

An important aspect of the iron yoke is to avoid magnetic interference with the toroidal magnet which may otherwise produce unacceptably high out-of-plane forces at the torus coils.

Table 4.1: Magnetic Properties

Type	Superconducting Solenoid
Aperture	0.78 m warm bore
NI 60%Packing factor	4.5 x 10^6 A-Turns
Central Field	2T to 5T
Integral Field	5.5 T.m
Yoke	19 metric sons (1006 Steel) (1.96m OD x 1.10m ID x 1.18m long)
Coil and Cryostat	2.7 metric tons stainless Steel (1.10m OD x 0.78m ID x 1.055ml long)
Stored Energy	‘ 7.64 MJ

Table 4.2: Conductor Parameters

Type	Nb/Ti,wet wind, semi ordered epoxy lay up
Cable Diameter	1.39 mm
Copper/SC ratio	1.75:1.0
Ic (4.2K, 5.3T)	1405 amps
Current Density	14,000 A-T/cm^2
Packing factor	60 %
Current/Turn	354 Amps
Number of Turns	12,653

The magnetic design uses a TOSCA-generated solenoid coil. The yoke, which is a simple cylinder with an outer diameter of 1.96 m. and an inner diameter of 1.10, was modeled as a nonlinear iron (1006 steel). The length of the yoke is 1.18 m. The Superconducting coil is off centered within the yoke by 0.1252 m. The peak field produced within the yoke is 3.1 Tesla and within the coil windings of 6.4 Tesla.

A projective view of the magnet in the cryostat and the flux return yoke is shown in Fig. 4.2. The magnetic properties are summarized in Table 4.3.2, and the conductor parameters are summarized in Table 4.3.2

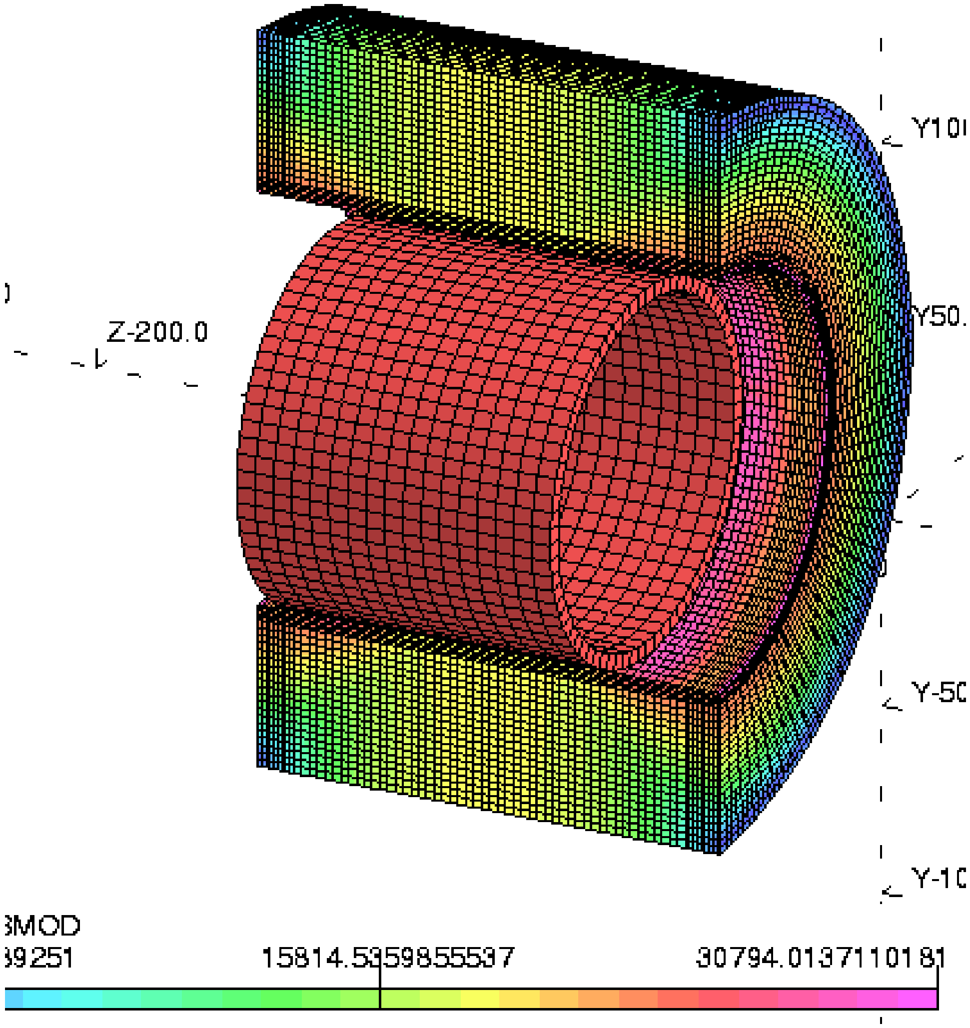

Figure 4.3: Field distribution in the solenoid magnet and the flux return yoke. The central field is 5 Tesla. The field in the iron yoke is typically less than 2 Tesla. Saturation field levels of up to 3 Tesla occur only in a few localized areas near the edges.

The iron flux return reduces the total current required, increases the field homogeneity, and reduces the fringe field. An important aspect of the iron yoke is to avoid magnetic interference with the toroidal magnet which may otherwise produce unacceptably high out-of-plane forces at the torus coils. Since shielding the Møller electrons relies on the fringe field the geometry of the flux return has been optimized to avoid reducing the shielding effect.

Fig. 4.3 shows the magnetic field density distribution in the magnet bore and the flux return iron. The iron is sized to minimize saturation effects, while keeping its size and weight compatible with installation in the Torus magnet. At the bottom the distribution of the magnetic field density in the r-z plane is shown , where z is the axis along the beam line, and r is the radial distance from the solenoid symmetry axis. The distribution along the beam axis varies rapidly while the variation along r is much more uniform. The extended fringe field is important for guiding the Møller electrons far enough away from the interaction region to a shielding pipe (not shown) where they can be absorbed.

4.3.3 Central Electromagnetic Calorimeter

Overview

The central electromagnetic calorimeter is an essential part of the CLAS^{++} Central Detector. It covers detection angles in the polar range of $40^o \leq \theta \leq 135^o$ and in almost the entire azimuthal range $0^o \leq \phi \leq 360^o$. It is designed for the reconstruction of π^o and η by their neutral decays, therefore, for the detection of multi γ - events . The design parameters are defined to meet an operational luminosity of $L \sim 10^{35}$ cm^{-2} sec^{-1}. The following sections describe the technical requirements, the detailed concept design and estimates for the calorimeter performance.

Requirements

The compact structure of the whole Central Detector, which is entirely mounted inside a superconducting solenoid of strong magnetic field, determines the basic parameters of the calorimeter. The available radial space for the calorimeter material, inside the magnet, is limited to ~ 10 cm. The calorimeter must provide adequate energy and spatial resolutions to cleanly identify π^o and η . Typical energies of decay photons, produced under large angles ($> 40^o$) at beam energies of 12 GeV, are up to $E_\gamma \sim 1 GeV$. Reasonable energy resolutions with these size restrictions can only be achieved if very dense materials are used. The π^o and η mass resolutions are function of the energy and angular resolutions. In order to provide sufficient mass resolution, i.e.

$$\delta m \sim 1/3(m_{\pi^o}/2)$$

for π^o and η, it is necessary to have energy resolutions of about

$$(\frac{\sigma}{E_\gamma}) \leq 6\%$$

at $E_\gamma \sim 1$ GeV and angular resolutions of $\delta\theta \sim 0.8^o - 1.4^o$. The angular resolution depends on the number of channels used to measure ϕ and θ. Taking into account that transverse shower dimensions are expected to be of about ~ 20 mm ($\sim 80\%$ containment), the lower limit of the angular resolution is estimated to be $\delta\theta \sim 1^o$. To detect π^o of the lowest energy, the calorimeter must provide an energy threshold of about $\sim 50 MeV$. To prevent major shower energy leakages, for photons under angles close to $\theta = 90^o$ (worst case), the calorimeter should be $\sim 10 - 11$ radiation lengths deep at $E_\gamma = 1GeV$. Table 4.3 shows the main design parameters of the Central Calorimeter.

Total Radiation Length	10 -12
Radial Space (radial thickness)	$\sim$ 10 cm
Energy Resolution	$\approx 6\%/\sqrt{E}$
Angular Resolution, $\delta\theta = \delta\phi$	$\sim 1^o$
Timing Resolution, δt	few ns
Energy Threshold, E_γ^{min}	$\leq 50 MeV$

Table 4.3: Central Electromagnetic Calorimeter parameters

Scintillating Fiber/Tungsten Powder Calorimeter Design

The overall view and basic dimensions of the central calorimeter mounted inside the solenoid magnet are shown on Figure 4.4. Dense Tungsten metal powder is used as the absorber. The calorimeter has a cylindrical shape: thin plastic scintillating fibers run in the direction parallel to the beam and are read out from one upstream end, see Figure 4.5. Fibers are grouped in sectors of equal size. Each sector combines all fibers covering an azimuthal angle range $\Delta\phi \approx \pm 0.6^o$ forming single photo-multiplier tubes readout channels that provide energy, ϕ and timing information. In the radial direction, there are one or two layers of fibers (see Figure 4.6) all bend at same radius with both ends running out of the sensitive volume as shown in Figure 4.7. This circular layer of grouped fibers provides independent measurements of the polar angle θ of the shower. To have resolutions of $\delta\theta \approx 1^o$ there will be a total of about ~ 50 channels per polar angle measurements. To allow all these fibers to run through the main volume, see Figure 4.7, there is a narrow gap not wider then 5 mm along the beam direction for readout purposes. This gap produces only a small reduction in the angular acceptance of the calorimeter (about 1-2%).

The implementation of such topology of scintillating fibers within essentially the same sensitive volume is only possible because of the powder technology, the volume is filled by loose metal powder. Since the so called "green density" of the Tungsten powder to be used as absorber is of about 12 ± 0.2 g/cm^3, the whole structure becomes very efficient, especially providing high sampling ratios and frequencies with fibers as thin as 0.5 - 0.75 mm or even of smaller diameters. This particular feature allows matching two requirements, i.e. to have sufficient energy resolution and small overall dimensions at the same time.

Expected Performance

To estimate the calorimeter response one can use parameterizations based on simulation and previous calorimeter data. We have used parameterizations during the initial design phase for a fast estimation of the calorimeter basic dimensions and

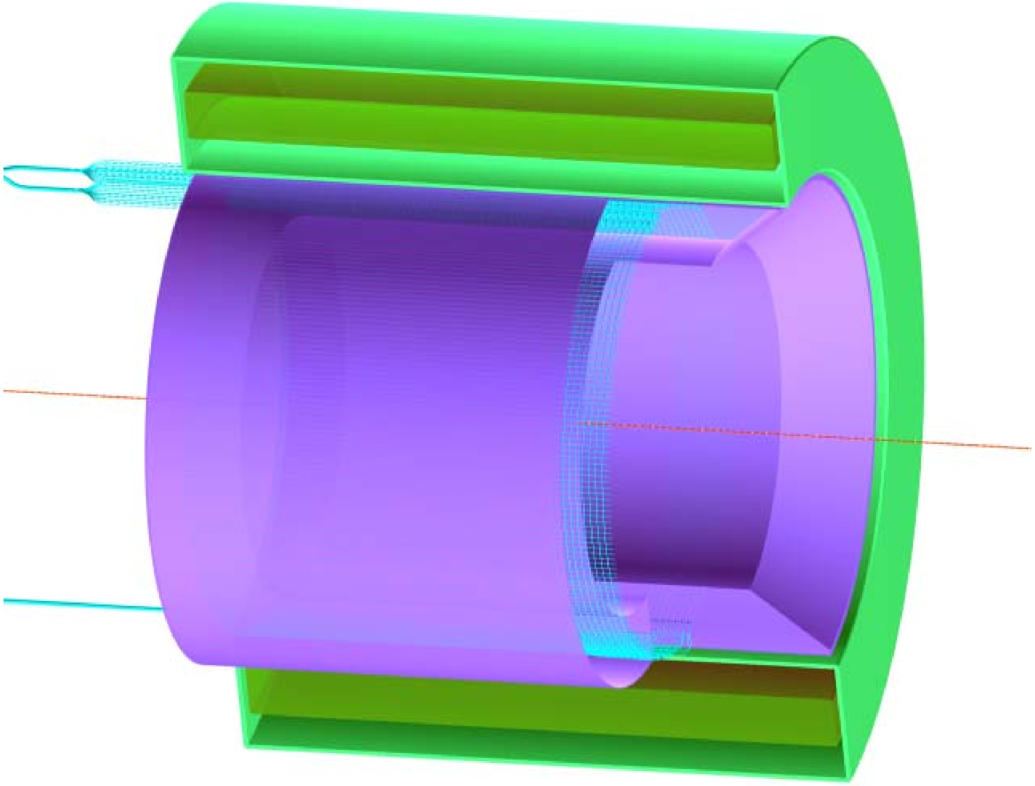

Figure 4.4: A perspective view of the central electromagnetic calorimeter inside the solenoid magnet.

characteristics. The containment of the shower is parameterized using [216]:

$$L(98\%) = 2.5 * [log(\frac{E}{\epsilon}) + 1.2] * X_o(cm)$$

L gives the length in centimeters that contains about 98% of the energy of the shower. E is the energy of the incoming photon, ϵ the critical energy of the material and (X_o) the radiation length of the mix in centimeters . The material in the calorimeter is a mix of tungsten powder and scintillating plastic (Polystyrene) fibers. The radiation length for the mix (X_o) that contains a fraction y of scintillating plastic per volume and a fraction $(1 - y)$ of tungsten powder absorber, is obtained using:

$$\frac{1}{(X_o)} = \frac{y}{X_{Sci}} + \frac{(1 - y)}{X_{Powder}}$$

For the powder with a fraction x of the pure tungsten density the radiation length

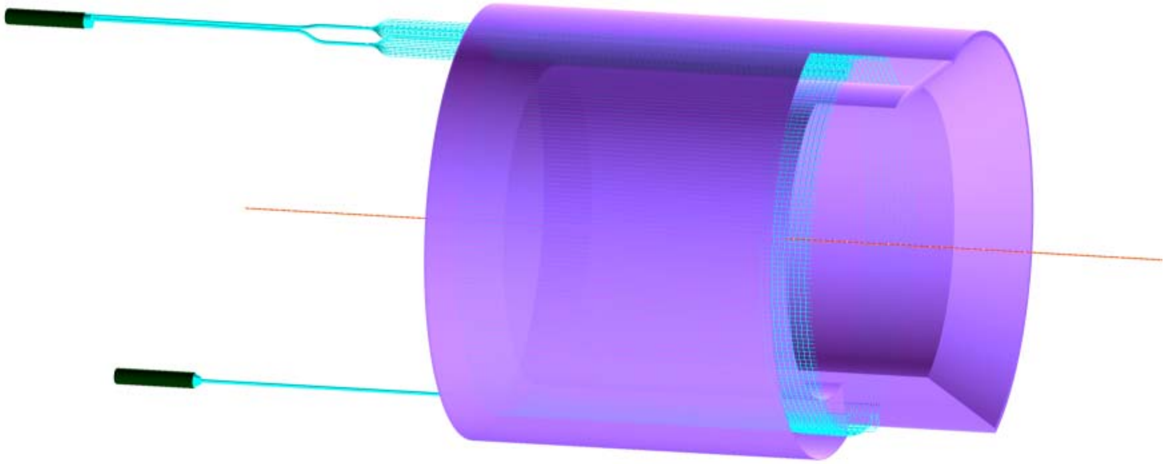

Figure 4.5: Central calorimeter. The tungsten powder volume and some of the axial readout fibers are shown at the left. Some of the radial fibers are indicated at the right side. The radial fibers are brought to the readout end through a slot at the bottom of the calorimeter.

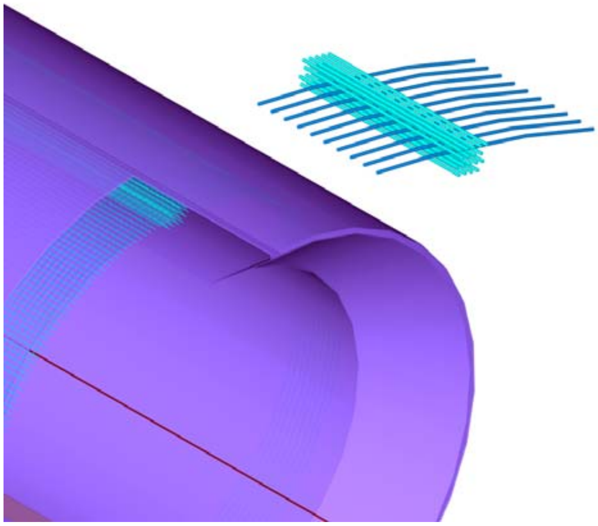

Figure 4.6: Central Calorimeter: radial fibers view. The radial fibers are interleaved with the axial fibers. They provide shower position information along the beam direction. Since they are not used for the energy measurement only a few layers are needed to provide the position information.

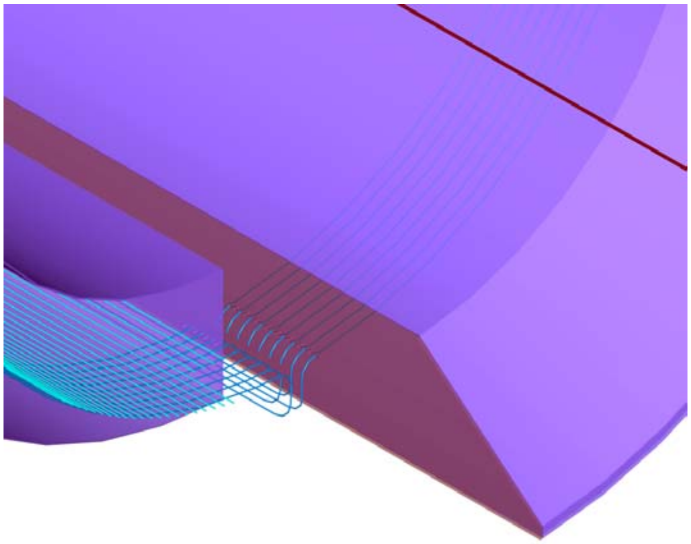

Figure 4.7: Central Calorimeter: radial fibers read out (detail) in the slot at the bottom of the calorimeter.

is

$$X_{Powder} = X_{PureTungsten}/x$$

.

The critical energy of the mix is obtained using:

$$\epsilon = y\epsilon_{Sci} + (1 - y)\epsilon_{Powder}$$

The results are shown in figure 4.8. The values of **L** are plotted versus the fraction of scintillating plastic by volume for three values of the powder density: x= 0.62 (current loose powder), x= 0.8 (cold pressed density currently obtained) and x= 1.0, pure tungsten. One can see that if the radial thickness of the calorimeter, using loose powder at x= 0.62, is limited by $\sim$ 10 cm, then the fraction of scintillating plastic should not exceed $\sim$ 35% per volume.

The other important figure-of-merit is provided by the sampling errors (in the energy measurements). For a given material (x= 0.62), these sampling errors are a function of the fraction of scintillating plastic in the calorimeter y (sampling fraction), and the diameter of the fibers, ϕ (sampling frequency). The corresponding parameterization for sampling errors are given by [217]:

$$(\frac{\sigma}{E})_{sampling} = 0.02 * \sqrt{\frac{\phi(mm)}{f_{sampl}}}$$

where f_{sampl}, the sampling ratio for minimum ionizing particles (mip) is calculated using:

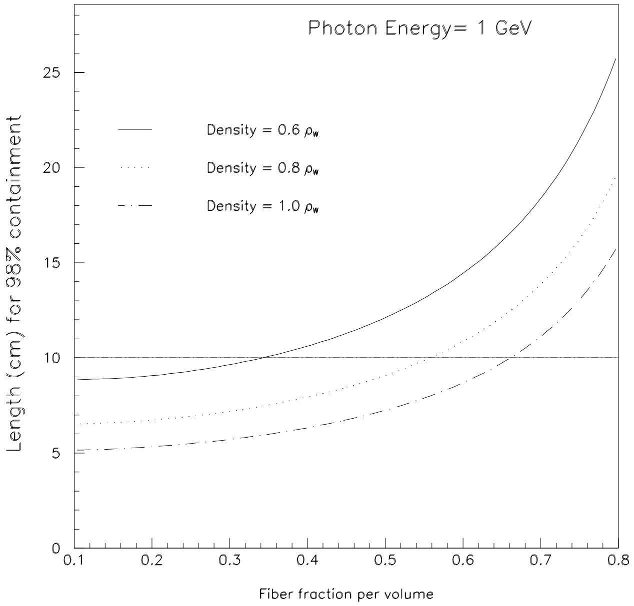

Figure 4.8: Containment versus fraction of plastic.

$$f_{sampl} = \frac{1}{1 + \frac{(1-y)}{y} * x * \frac{dE_W}{dE_{Sci}}}$$

where, dE_W and dE_{Sci} are the energy depositions by minimum ionizing particles in 1cm of tungsten (22.1 MeV/cm) and polystyrene (2.0 MeV/cm), respectively. Figure 4.9 shows the sampling errors versus the fraction of scintillating plastic by volume for four different fiber diameters (0.25, 0.5, 0.75 and 1 mm), at a powder density of x= 0.62. One can see that for an absorber density of 11.8 g/cm^3 (x= 0.62), a tungsten powder based sampling calorimeter built with fibers of 0.5 mm in diameter and with a fraction of scintillating fibers of 35% per volume can reach energy resolutions better than $\sim$ 6% at 1 GeV energies. These resolutions are similar to the one reached by the the KLOE [218] and JETSET [219] calorimeters using larger amount of scintillating fibers. In the same figure also is shown the value obtained by the KLOE collaboration [218] with a sampling calorimeter of 23 cm of radial thickness built at y= 0.5, using lead absorber and 1 mm polystyrene fibers.

Prototyping and Simulations

The proposed sampling calorimeter is made using a new calorimetry construction technology, there are open questions that need to be answered, although some initial tests already have been successfully carried out.

- An important test will be to establish the more efficient assembly procedure when fibers having different directions and shapes are installed in the same

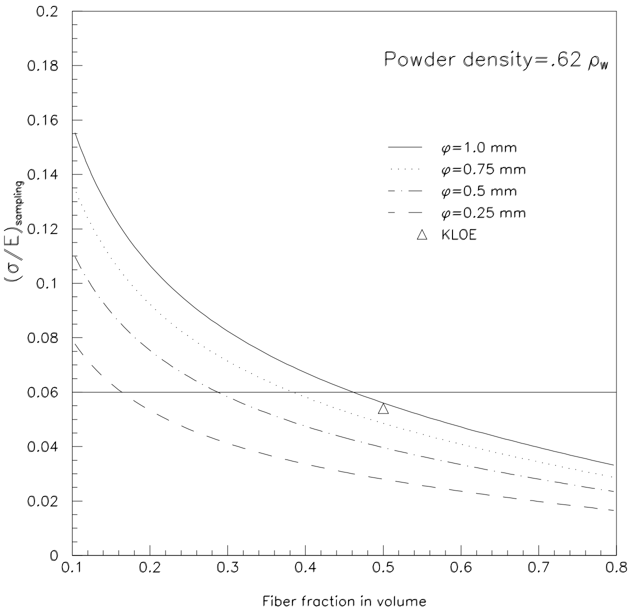

Figure 4.9: Sampling errors versus fraction of plastic.

volume.

- We need to explore the limits on sampling frequencies available with this technique, especially with fibers of small diameters. Small fibers ($\sim 0.25mm$) cannot be used with other techniques (grooving), unless one agrees to have lots of air gaps or glue. Also the technical limits for sampling ratios with Tungsten powder radiator has to be found. First tests have shown that designs are possible with a sampling ratio $\sim$ 17% and 340 polystyrene fibers of 0.5 mm in diameter using loose tungsten powder, A density of not less than 11.8 g/cm^3 can be achieved. Further tests are in progress.

- The main features of the calorimeter with a given realistic geometry need detailed simulation (i.e, using GEANT). This simulation will define the expected energy and angular resolutions to be compared with experimental test values that can be used in planning of physics experiments.

- A prototype consisting of 12 modules is currently being designed to examine all basic properties of the calorimeter. The goal is to test the calorimeter under a photon or electron beam in the very near future. This first full prototype will have 10 cm of thickness (11 radiation lengths) with a fraction of plastic of 35% by volume using polystyrene fibers of 0.75 mm in diameter.

4.3.4 Central Time-of-Flight System

A conceptual view of the central TOF system is shown Fig. 4.10. The active scintillator area consists of a cylinder of radius 26 cm and length 50 cm. The thickness of the

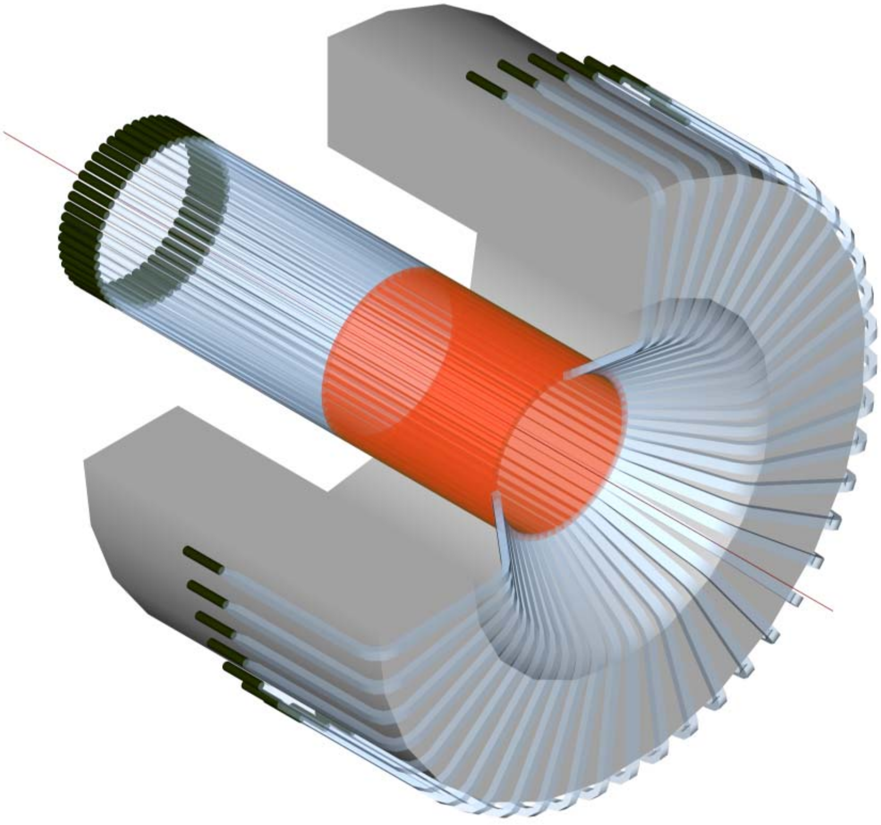

Figure 4.10: Perspective view of the central TOF system. Scintillator material shown in red color. In this option the scintillator light is transported to regions of reduced magnetic field using light guides (shown in translucent light blue color)

detector is 2 cm. It is located inside the solenoidal field and must therefore be able to operate in the high magnetic field. The design goal is to achieve timing resolution of σ =50 ps. This timing resolution allows separation of pions from kaons up to 0.64 GeV/c and pions from protons up to 1.25 GeV/c (Fig. 4.11). This assumes a "4σ" difference in time between the two particles and allows identification of a signal in the presence of other particles with ten times higher rates.

Expected Rates

The rates in the scintillators for the existing CLAS detector have been studied at two different beam currents and used to predict the counting rates at a luminosity of $10^{35} cm^{-2} s^{-1}$ [220]. We summarize the results here for both the central and the forward detector systems. The rates are given in Table 4.13 at two thresholds. The expected integrated rates for the central and forward detectors are approximately equal. The current threshold setting for the counters is 20 mV, but efficient operation can be achieved at a threshold of 30 mV, which reduces the rate considerably (Fig. 4.12). The forward detector elements will have a typical rate per counter at 30 mV of about 750 kHz. At this threshold, the central detector has an integrated

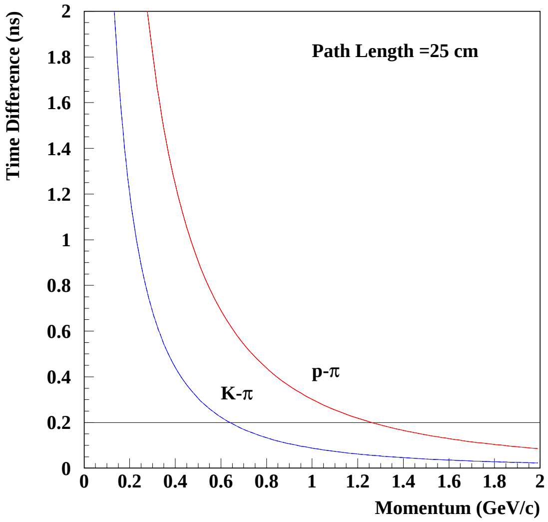

Figure 4.11: Time differences between protons and pions, and between kaons and pions over the 25 cm path length expected for the outer TOF system.

rate of 40 MHz. In order to keep the rates below one MHz per counter, we require approximately 50 channels of electronics.

Options

The traditional scintillator detector array for TOF measurements in the central detector is challenging due to the magnetic field of the solenoid which may operate at several Tesla. Hybrid photomultipliers such as Hamamatsu R7100U-07 and DEP model PP0350G can operate in magnetic greater than 1.5 Tesla with no reduction in pulse height. The field in the region inside the solenoid near the ends of the scintillator is less than 1 T, so hybrid PMTs are an option for use with short light guides.

A second option is to use light guides to bring the light out of the high magnetic field to the region outside the yoke and use standard PMTs. The magnetic field outside the iron yoke of the solenoid is shown in Fig. 4.14. The magnetic field is plotted as a function of z (beam direction) for slices in x (radial distance from the beamline). The slices in x are 16.67 cm wide and the field is plotted for intervals of 2 cm, the average x value is indicated on the plot. The field surrounding the yoke is no less than 70-100 G, where standard magnetic shielding is challenging, though not impossible. We note that in the regions outside the solenoid, the magnetic field of the torus cannot be neglected, although it is not included in the present field tables.

Finally, an alternative technology is being developed which matches our requirements. Atmospheric multi-gap resistive plate chambers (MRPC) are under development for the STAR detector [221]. The resolution of these detectors is about 63 ps as shown in Fig.4.15 at voltages where their efficiency is >98%. Approximately 400

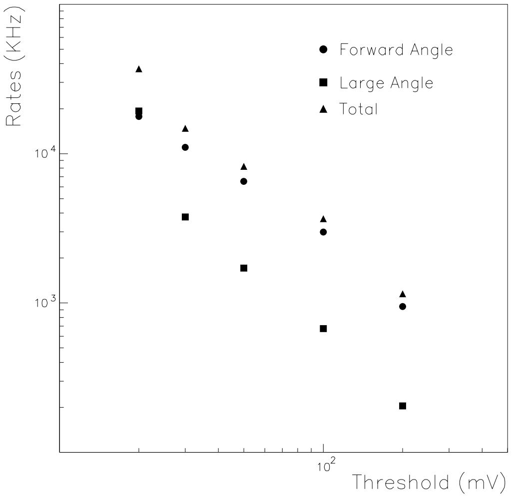

Figure 4.12: Rates summed over all six sectors as a function of threshold at a luminosity of 0.9×10^{34}cm^{-2}s^{-1}. When the threshold is increased by a factor of 2 the count rates drop by a factor of between 2 to 3.

Angular Range	Threshold (mV)	Rate (MHz)
Forward	100	32
Central	100	8
Total	100	42
Forward	20	214
Central	20	243
Total	20	457

Figure 4.13: The scaler rates in the CLAS scintillators extrapolated to a luminosity of 10^{35}cm^{-2}s^{-1}. The rates are summed over all six sectors.

channels of MRPC are required to cover one layer of the TOF cylinder, as each pad covers an area of about 20 cm^2. However, two layers are required to avoid gaps in the detection system. Implementation of two layers would therefore increase the space necessary for the CD-TOF detector by additional 6 cm diameter. A certain drawback of MRPCs is that they do not provide energy loss (dE/dx) information. dE/dx is of particular use at the relatively low momenta in the central region where is could provide additional information for particle identification.

4.3.5 Central Tracker

The central tracker is located inside the central solenoid. Fig. 4.2 shows the layout of the entire area. We are currently pursuing two options for the tracking in the central region. In the first option a gas-filled wire chamber occupies the entire radial space from 5 to 25 cm. In the second option, the radial space from 5 to 11.18 cm is occupied by a silicon strip detector, and the outer radial space is again occupied by a cylindrical wire chamber.

The wire chamber design is cylindrical with axial anode wires arranged as four, 2-layer (staggered) superlayers with inside, inner and outside cathode foils. Foils reduce

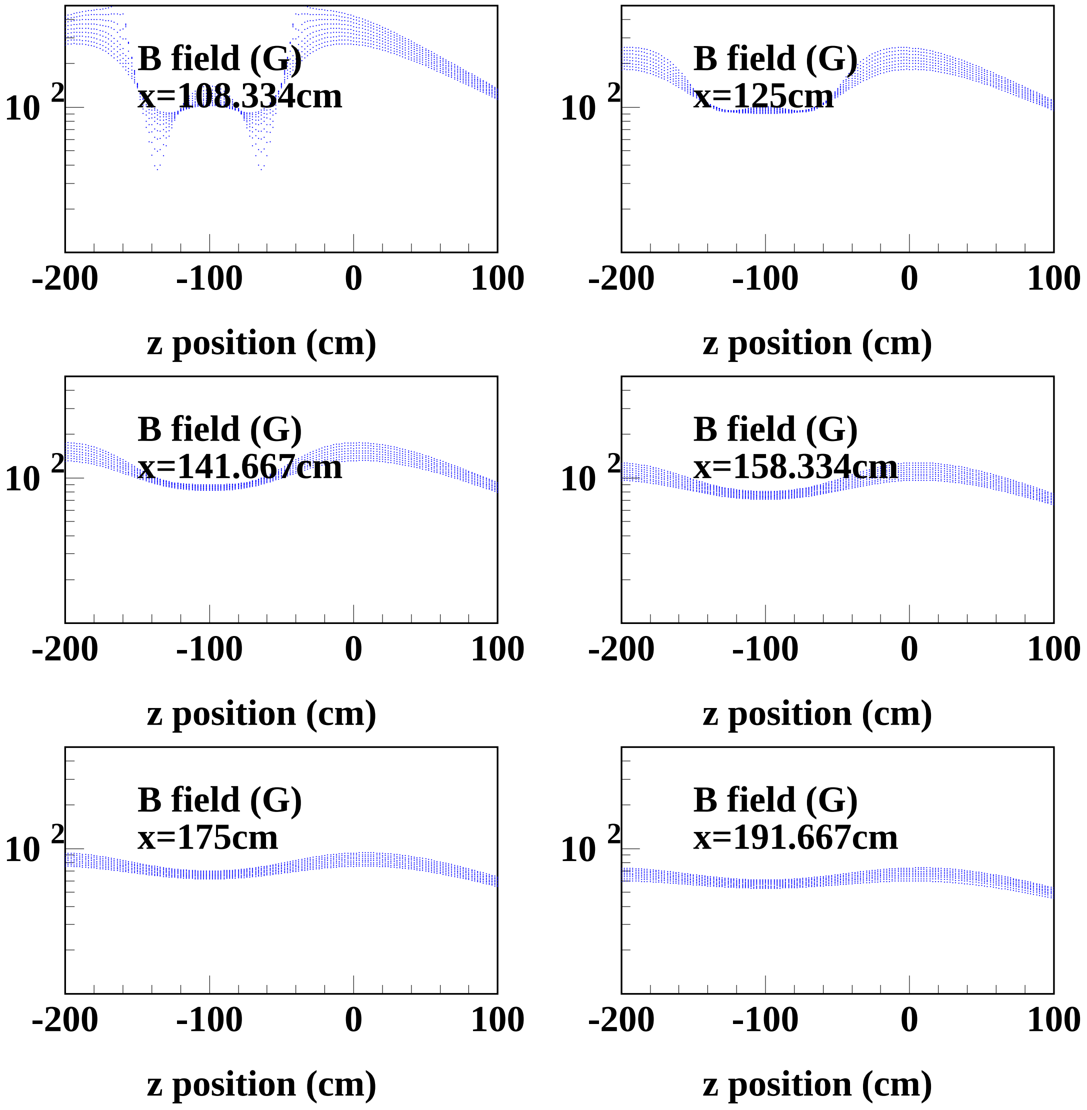

Figure 4.14: Magnitude of the B-field for the solenoidal magnet as a function of z, for various ranges of the radial distance, x. The fields are plotted on a log scale to span the range of values in the figures.

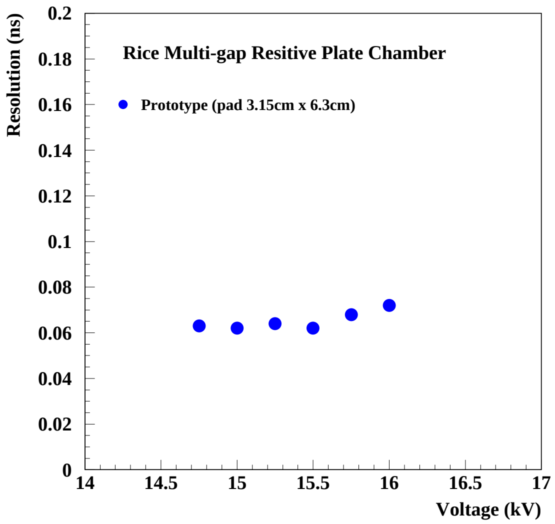

Figure 4.15: Resolution of a prototype multi-gap resistive plate chamber for the STAR detector. The thickness of the detector is less than 2 cm.

the need for additional field wires and lower the wire tension and thus, the thickness of the endplate. The endplates are angled such that the wires all subtend approximately the same range in scattered angle, from 40 to 135 degrees in the laboratory frame. A perspective view is shown in Fig. 4.16 and a detailed view is shown in Fig. 4.17.

There are a total 4 super-layers, 2 layers each, 80 anode wires and 80 field wires per layer, with the drift distance varying from 0.22 to 0.91 cm. The anode wires provide the electric field to produce the avalanches and resulting gas gain. The anode wires will be read out to provide a precise time measurement as well as a phi measurement by converting the drift time into a drift distance. The z-position-sensitive readout is primarily via cathode pads; a drift-time measurement gives a measure of the azimuth, phi, while a charge measurement of several cathode pads gives theta information. When the anode avalanche multiplicity is one, the anode time information will be used for the phi measurement. In case of higher multiplicity on one anode wire, the time information will come from the cathode strips.

The inner-most wire layer has an average radius of 5.53 cm with 80 anode wires in azimuth with 80 field wires between, resulting in a 2.2 mm drift. This layer will be covered with 800 cathode pads, of dimensions 4 mm X 16 mm; the second layer also has 80 anode wires and 800 cathode pads of about 4.5 mm X 18 mm size. Each successive superlayer will have the same channel count (160 anode wires and 1600 cathode pads) but will scale up in size by a factor of 1.5. The accidental rate is proportional to the solid angle of the pads relative to background source times the time window. Compared to the present CLAS detector, we will have roughly the same number of channels per layer as Region 1; and a time window on the inner layer a factor of 10 smaller than Region 1. The major reduction in electromagnetic

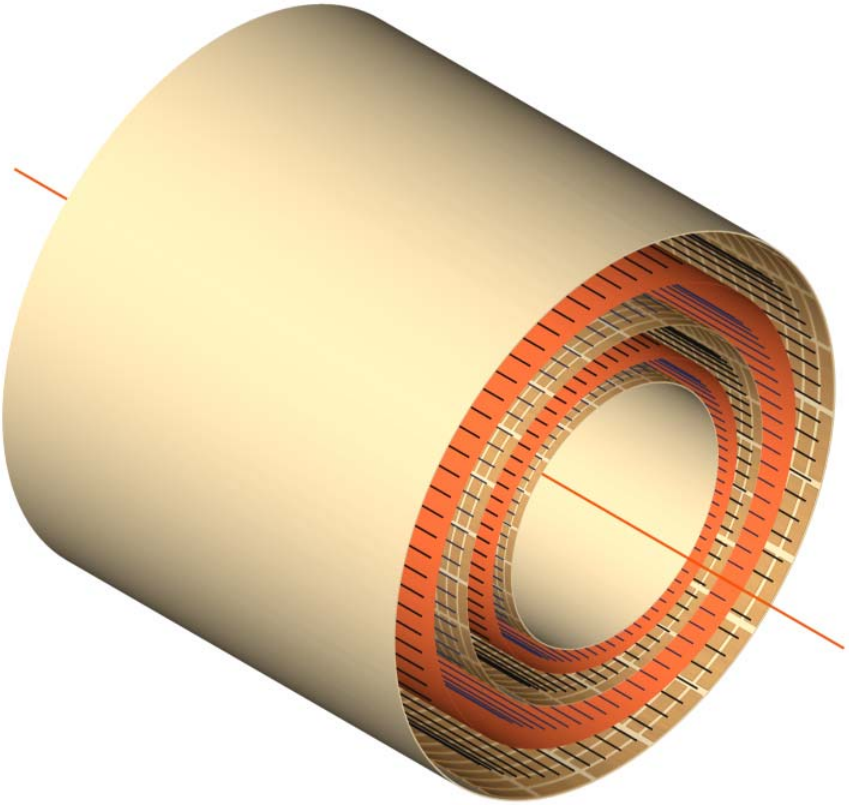

Figure 4.16: Cathode chamber view of two superlayers.

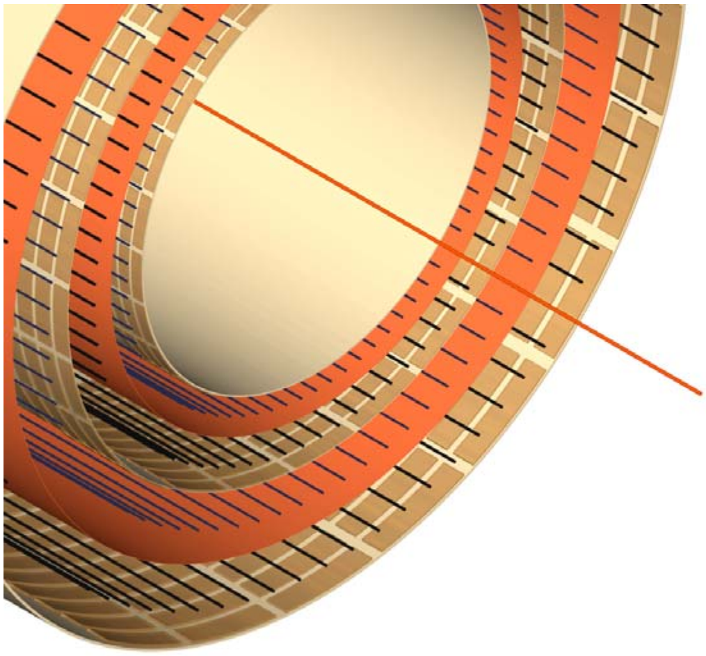

Figure 4.17: Cathode Chamber - cathode pad (yellow) and cathode wire (black) detail

background comes from the solenoidal shielding scheme. Tests using a Helmholtz coil and cylindrical absorber showed that the dominant background was directed forward from the source (the mouth of the absorbing cylinder). We thus expect that the central tracker will be adequately shielded from any Møller background.

Since the momentum resolution from this chamber is expected to be dominated by multiple scattering, the fractional resolution $\delta P/P$ is a constant, independent of momentum. A simple calculation shows that

$$\frac{\delta P_{\perp}}{P_{\perp}} = \frac{\delta S \times 27 \times P}{R_0^2 B} ,$$

where B is the solenoid field in Tesla, P the momentum in GeV/c, R_0 the radial extent of the chamber in meters, and S the sagitta of the track in meters.

For B=3 Tesla, $P = 1$ GeV/c, 20 cm path and a 100 μm accuracy δS, we estimate that

$$\frac{\delta P_{perp}}{P_{\perp}} = 2.2\% .$$

Twenty cm of an Argon-dominated gas mixture and 12 plastic foils of 50 micron thickness each gives a total of .0025 radiation lengths of material. This results in a 1 mrad multiple scatter on the angle of the track. The theta resolution of the cathode chamber will not be this good. The position resolution in z will be about 0.8 mm for the inner-most layer, growing to about 2.7 mm for the outermost layer, resulting in a polar angle resolution of about 8 mrad. The dE/dx loss will be approximately 1.3 keV/cm of Argon for minimum ionizing particles, resulting in a small energy loss for recoil hadrons.

As an alternative option as a central tracker we consider use of six layers of a silicon microstrip detector combined with a gas chamber of the same type as described in the previous section, but radially restricted to the region from 10 cm to 25 cm, while the strip detector would occupy the radial region from 5 cm to 10 cm. At the same time the silicon strip detector would provide track information in the polar angle range from 5^o to 40^o and in the full azimuthal range.

4.3.6 Silicon Strip Detector

The limited radial space available in the Central Detector region for particle detection forces the charge particle tracking detectors to be located very close to the target in order to retain acceptable momentum resolution. Use of a small microstrip detector near the target can provide excellent position resolution, which will provide both position measurements close to the interaction point for excellent angle and vertex resolution, as well as providing good momentum determination for large angle tracks. These aspects are of particular importance in the detection of relatively low momentum protons and recoil hyperons, e.g. $\Lambda \rightarrow \pi^- p$, as well as in resolving the decays

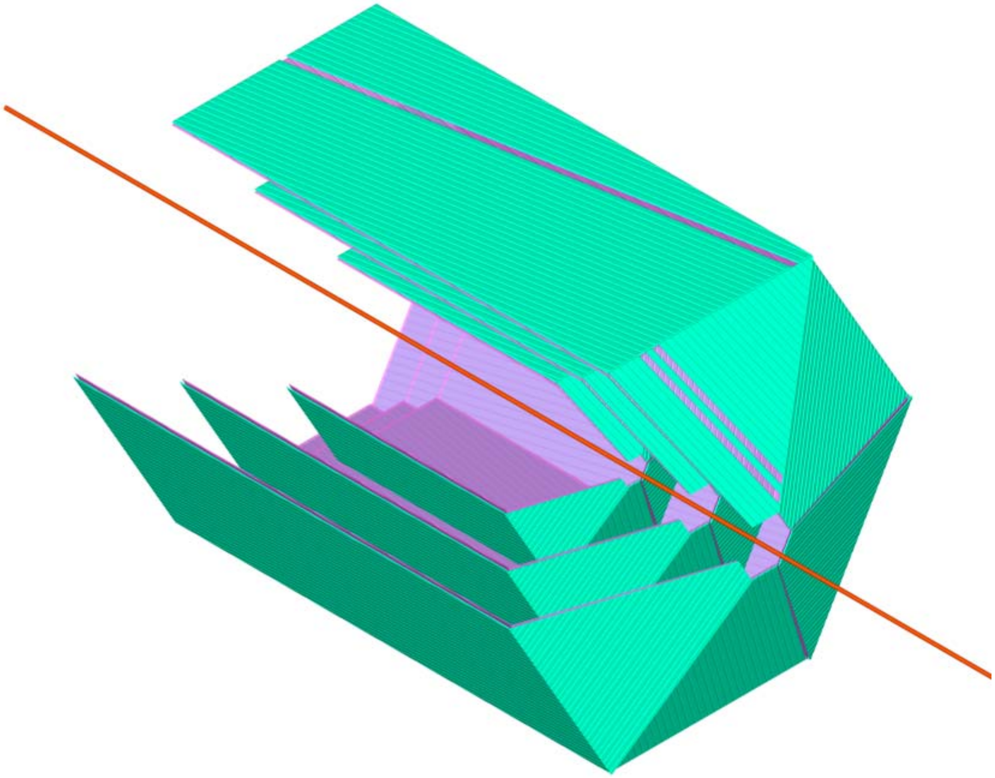

Figure 4.18: Concept of a Silicon Strip Detector covering the angular range from 5^o to 135^o. The orientation of the strips is indicated as well. We anticipate that the signal read out will be in the back. A total number of 50,000 readout channels are needed for full coverage.

vertex of $K_s \rightarrow \pi\pi$. The microstrip detector will also provide tracking at forward angles to aid in the reconstruction of high momentum tracks and in regions which are blocked by the torus coils. The track segments near the target can be linked up with tracks reconstructed in the forward angle tracking chambers to improve angle and momentum resolution. This is especially important for the CLAS^{++} configuration where the first tracking chamber is located at a distance of about 2 meter from the target.

Fig. 4.18 shows a possible conceptual layout of a silicon strip detector, arranged in 6 layers around the target. The six layers (only the 3 superlayers are shown, each contains two stereo layers) provide 3 space points (x, y, z) for a given track. Alternating layers have strips at different angles to provide stereo readout and resolve ambiguities. In the large angle region the strips can be arranged to provide $\pm 10^o$ readout. This will provide near optimal momentum resolution for tracks in the longitudinal solenoid field, while at the same time giving good polar angle resolution due to the excellent position resolution. In the forward region the strips are arranged to have a much larger crossing angle, giving excellent angle resolution for forward going tracks down to angles of 5^o. The graph shows also a possible strip layout of the silicon wafers. A strip pitch of 300μm is assumed which is expected to result in a position resolution of better than 100μm. The first two layers may consist of 100μm thick silicon wavers, while the four outer layers, which are considerably larger could be as thick as $280\mu m$. Using thinner wafers for the inner layers would allow detection of recoil protons down to lower momenta. To limit the effect of multiple scattering, we consider the possibility of having strips on either side of the wafer for the outer four layers, which would reduce the multiple scattering effect considerably, and improve the momentum resolution. However, such design considerations will have to be carefully balanced against complications in the detector construction, and the reduction of the readout signal for minimum ionizing particles, among others.

Signal readout of the SSD

Requirements

The SSD considered for CLAS^{++} has sections of various lengths. The longer sections are about 20 cm long and the shorter sections are about 4.6 cm. The total inter-strip capacitance should be less than 10 pF to minimize signal loss and noise and the coupling capacitance should be larger than 10 pF/cm for AC-coupled strips. A strip resistance of less than 30 Ω/cm is desirable to minimize signal dispersion. The operating bias voltage, which is related to the full depletion voltage of teh detector, should be in the range of 50V to 200V. The poly-silicon bias resistor should be about 2.5 MΩ for low thermal noise and production uniformity.

Readout Electronics

Although the number of channels for this detector is less than in other SSDs, channel density is expected to be similar. This requires the use of high density custom chips mounted in close proximity to the detector and includes amplifiers, discriminators, buffers, logic and driver circuitry. Power dissipation and cost are two variables which must be kept in check. The followowing high density custom chips are in operation in different experiments and are good representatives of the current state of the art in high density, low power and low cost readout electronics for SSDs:

ABCD

- Detector signals are amplified and shaped. A level/edge discriminator with programmable threshold followd and data are stored in the binary pipleline at 25 ns intervals, For every trigger, data from three consecutive events are transferred from the pipeline to the de-randomizing buffer and compressed for serial readout. Readout is effected via a token ring. Six chips can be read out on one optical fiber.

AToM

- Detector signals are amplified and shaped. A level discriminator follows and clocks bits into the pipeline at about 67 ns intervals corresponding to the Time-Over-Threshold (TOT) for the shaped detector pulse. For this type of shaper, the number of pulses is logarithmically proportional to the charge injected, yielding 4-bit resolution for position interpolation. For every trigger, a region of every channel's pipeline of up to 2 μs is searched and the results stored into a sparce/storage buffer. Readout is effected via token ring on diffferential serial lines. Only a single hit can be recorded for each channel and is readout as a 16-bit header, followed by 16 bits of data and terminated by a 16-bit trailer.

SVX4

- Detector signals are integrated and stored in teh analog pipeline. Digitization is effected by means of a Wilkinson-type ADC (ramp down and comparator) and a counter (7-bit). The counter value is then stored in a FIFO where data is sparcified. An 8-bit output bus provides the data in a sequence of bytes identifying the chip, the time slice in teh pipeline, the channel number and the data.

The ABCD chip is a multihit binary readout chip that provides leading ege timing information only. As a result, time walk of the order of 15 ns is inevitable and this must be taken into account when considering the required spatial resolution.

The AToM chip provides leading edge timing information and a course digitization for position interpolation. Additionally, the peaking time is adjustable which is of interest for detectors with strips of different lengths. However, this chip dissipates considerably more power and dose not have multi-hit capability.

The SVX4 chip. although functionally attractive, has been designed strictly for experiments where bunch crossings provide an acquisition trigger. Therefore, the SVX4 is not useful for the application with CLAS^{++} at Jefferson Lab.

As most chips used so far have been custom designed, availability is questionable. The possible alternatives are:

- Single chip implementations - ABCD, AToM,..
- Multi-chip readout implementations have ben used in the past where one custom chip may include several anplifiers/discriminators and a second custom chip include the logic/buffer/drivers. (RHIC-Phenix, STAR, LHC-Atlas)
- Design a custom chip for Jeffferson Lab.

Instrumentation

The readout chips, in die form are attached to a substrate that is attached to the SSD. The substrate provides a pitch transition from the detector (300 μm) to the readout chips (50 μm), allows mounting the chip closase to the strip, allows a certain degree of thermal matching and mechanical support, provides the routing for bias voltages and control signals and serves as a support for the output cable/fiber assemblies.

The substrate(s) may be FR-4 or polyimide High Density Interconnect (HDI) (a.k.a. flex interconnect). Ceramic substrates (Al_2O_3, BeO, AIN) are attractive for their thermal performance. For example, AIN has a coefficient of thermal exoansion very similar to silicon. On the other hand, BeO has very high thermal conductivity. The wire bond pads must be gold-plated for reliable bonding.

The strips are wire bonded to pads on the substrate. These pads are routed to the appropriate chips and wire bonded to the pads on the chips. All chips' padsare wire bonded and routed out through bonded HDI assemblies.

The logic signals on the HDI assemblies are routed away from the detector along the support structure and connect to optical fiber driver boards. Multiplexing may be implemented through high-speed optical links (5 GHz) or by use of Wavelength Division Multiplexing (WDM) and multimode optical fibers.

Radiation damage

Silicon detectors at hadron machines have suffered from radiation damage and some had to be replaced after some years of operation. The main cause of the radiation damage at hadron machines was found to be due to low energy protons or neutrons. This situation led to the development of radiation hard doped silicon wafers. Proton yields of up to $10^{15}\mathrm{cm}^{-2}$ are considered a limit for the operation of such silicon wafers. For an electron beam environment the main background is due to Møller electrons. The SSD will be shielded by the superconducting magnet from nearly all low energy Møller electrons. The remaining source of background is then dominated by low momentum protons knocked out of the target in (quasi-) elastic ep scattering with minimal momentum transfer. At 11 GeV these rates are far below a critical level where significant radiation damage may occur on a time scale of 10 years of operation.

Prototyping

Silicon strip technology has matured during the past decade and is now widely used in high energy and nuclear physics applications. Yet, detectors have often very specific applications in experiments, are usually custom made, and require some prototyping effort. We are currently in contact with the Brookhaven National Laboratory Instrumentation group[222] to construct one segment of the proposed detector, which would then be tested in Hall B in conjuntion with the solenoid magnet currently planned for the DVCS experiment. The prototype work is expected to commence in early 2003.

We also like to point out the excellent experience made with silicon strip detectors implemented in the ep energy measureing arrangement installed in Hall A by the Clermond-Ferrand group [223]. These detectors operate at considerably higher luminosities than what is anticipated for CLAS^{++}.

4.4 The Forward Detector Concept

4.4.1 Forward Detector - Overview

The Forward Detector (FD) detects charged and neutral particles in the angular range between 5 and 40 degrees. The new detector is designed to provide extended particle identification, better charged particle tracking resolution, improved two-photon separation, nearly full azimuthal coverage for photon detection and greatly reduced sensitivity to background compared to the present CLAS. The FD consists of the following detector elements beginning with the one closest to the target:

- The small angle part of the silicon microstrip detector (see Fig. 4.18)
- The high threshold Cherenkov counter (HTCC)
- Coil calorimeter (coilEC)
- Tracking chambers (R1, R2, R3) with axial and stereo readout
- Low threshold Cherenkov counter (LTCC)
- Time-of-flight scintillator arrays (FTOF)
- Preshower electromagnetic calorimeter (preEC)
- CLAS forward electromagnetic calorimeter (FEC)

We give here a brief description of every element in the FD system. A more detailed description is provided in the sections following this overview.

High threshold Cherenkov detector

The bulk of the FD provides active coverage in the azimuthal range not blocked by the main torus coils. Electron identification and pion rejection is accomplished using a new Cherenkov detector HTCC operated with a light radiator gas such as CO_2. This will provide pion rejection for momenta up to 4.9 GeV.

Coil electromagnetic calorimeter

The coil electromagnetic calorimeter (coilEC) provides photon detection in the regions shadowed by the torus magnet coils. In conjunction with the microstrip detector is can discriminate photons from charged tracks.

Tracking chambers

Forward tracking of charged particles is accomplished by **three sets of chambers**, analogous to the present CLAS drift chambers and named accordingly, Regions 1, 2 and 3 (R1, R2, R3). These chambers will cover less than half the polar angular range of the present setup. By keeping the channel count constant, we are able to decrease the cell size and active time window by more than a factor of two, resulting in better spatial resolution and decreased sensitivity to backgrounds.

Low threshold Cherenkov counter

The LTCC is the modified CLAS Cherenkov Detector operated with a highly dense gas to allow pion identification for momenta above 3 GeV/c.

Forward time-of-flight detector

The FTOF array consists of scintillator strips recycled from the existing CLAS TOF detector. The new array will consist of a double layer of 5cm thick scintillator paddles each 5cm wide. This will provide a much improved timing resolution as the amount of light collected in the photomutipliers is increased by a factor of several.

Preshower electromagnetic calorimeter

The forward electromagnetic calorimeter (FEC) currently used in CLAS will be augmented by a more highly segmented pre-shower electromagnetic calorimeter (preEC) located immediately in front of the FEC. It will provide better spatial resolution; especially needed for the detection of the two photons from high-energy π^o decays. The FEC will be used as is.

Expected performance of the forward detector

The forward spectrometer will be able to detect all charged and neutral particles emitted in the polar angular range of 5 to 40 degrees; providing momentum resolutions of $\delta P/P = 0.005 + 0.001 * P$ for charged particles and energy resolutions of $\delta E/E \leq 9\%\sqrt{(E(GeV)}$ for photons. Particle identification is accomplished using time-of-flight information, Cherenkov counters, and electromagnetic calorimetry. In addition, kinematical fitting can be applied in some cases. Electrons and π^- can be separated for momenta up to 5 GeV/c using gas threshold Cherenkov counters, and above 5 GeV in electromagnetic calorimeters. Kaons(protons) can be separated from pions for momenta up to 3(4.5) GeV using the upgraded time-of-flight arrays, and above 3 GeV using the low threshold Cherenkov counter as a veto for kaons. Only the direction of the momentum vector can be measured for charged particles headed for the main torus coils. All of the detectors can operate in the background environment expected at luminosities of $10^{35} s^{-1} cm^{-2}$.
In the following sections we describe the detector components of the forward detector in more detail.

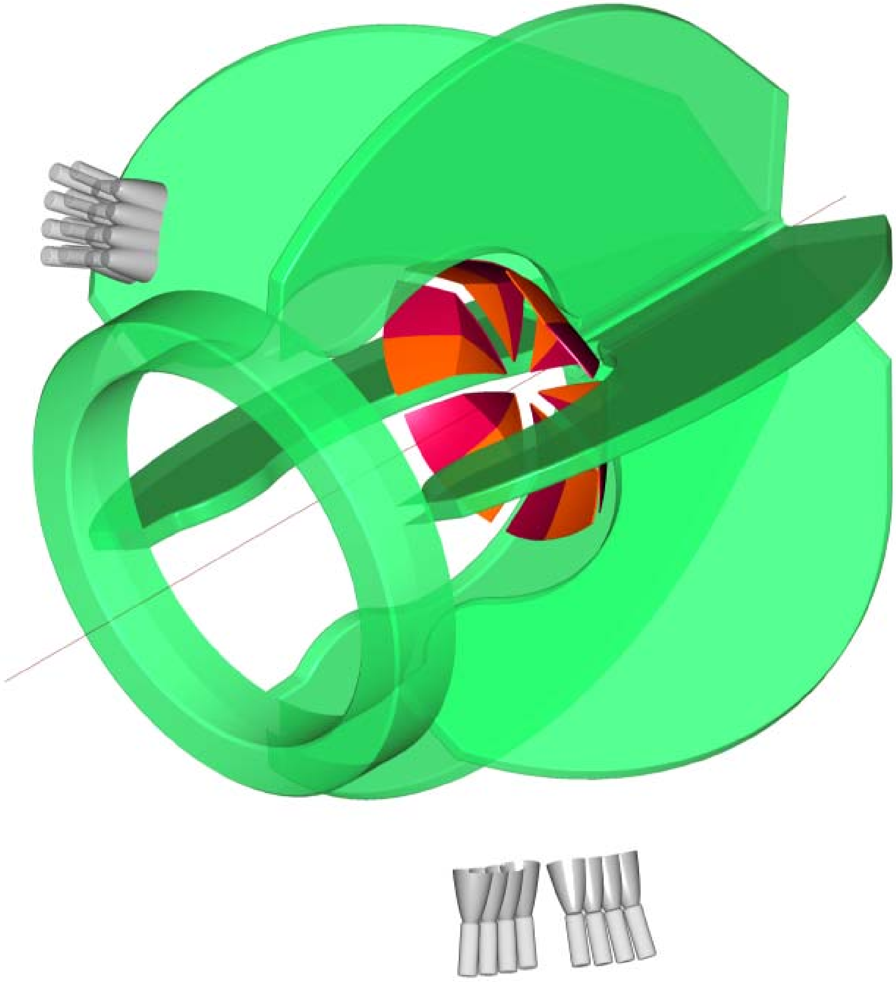

Figure 4.19: Concept of the High Threshold Cerenkov Detector located inside the Torus coil arrangement.

4.4.2 High Threshold Cerenkov Counter (HTCC)

The HTCC is the first active detector downstream of the microstrip tracker. Its main function is to aid in the identification of electrons and pions. A relatively light gas such as CO_2 will be used as a radiator. This will provide a threshold for the detection of charged pions of 4.9 GeV/c. In combination with the CLAS FEC, this will provide highly efficient electron identification. A pion rejection factor of > 2000 can be achieved this way for the entire momentum range up to 4.9 GeV.

The HTCC will also be used in combination with the LTCC for charged pion identification in the critical momentum range from 2.9 - 4.9 GeV. In this momentum range the HTCC does not detect pions while the LTCC does, this way providing identification of both electrons and charged pions. The HTCC is located in front of the Torus magnet and the first forward tracking chamber. A conceptual view is shown in Fig. 4.19.

The very limited space available for the HTCC puts serious constraints on the optics and the performance of the mirror system and the photon detectors. Figure 4.20 illustrates the optics of the HTCC. To optimize the light collection light produced at scattering angles less than about 20 degree is reflected toward large angles in the same Torus sector, while light produced at scattering angle greater than 20 degree is reflected toward the opposite Torus sector. The expected response in terms of the number of collected photoelectrons has been simulated using the measured properties of the mirror system in the CLAS Cerenkov counter, and photomultipliers with known photocathode sensitivities and quartz windows [1]. Fig 4.21 shows the projected distribution of the average numbers of photoelectrons (N_{pe}) across the $\phi - \theta$ plane. In the polar angle range from 6 to 35 degrees the N$_{pe}$ is between 8 and 12, slightly dependent on the polar angle. N$_{pe}$ is independent of the azimuthal angle ϕ. Influence of the magnetic field of the solenoid on the particle trajectories is neglected as for the high momentum electrons (1 GeV/c) the solenoid field in first approximation will only produce a change in azimuthal angle. The main effect is a smearing of the photon distribution in the detector plane.

Most photons will directly hit the photocathode area in the 5" photomultiplier tubes, those outside are collected in Winston cone mirrors around the PMTs. The PMTs are located in the fringe field of the Torus magnet and will be magnetically isolated with a multi-layer magnetic shield. Such magnetic shields has been used successfully in the CLAS Cerenkov detector [224].

4.4.3 Forward Tracking Chambers

The forward tracking chambers measure charged tracks which have polar angles between 5° and 40°. In order to use the missing mass technique effectively, the forward chambers must have excellent momentum resolution. The design we present here should allow momentum determination of $\delta p/p = \sqrt{(0.1\% * p)^2 + (0.2\%/\beta)^2}$. The spatial resolution portion of $0.1\% * p$ is a factor of three better than the performance of the current CLAS tracking system. The chambers' intrinsic resolution is expected to decrease from the present 330 μm to 200 μm, due to smaller cell size. We also expect to gain another factor of 1.5 by more carefully controlling our knowledge of the B field and the chamber positions.

The forward tracking system consists of three sets of drift chambers: region 1, located immediately before the Torus magnet; region 2, located between the Torus coils, and region 3, just behind the Torus coils. This arrangement is similar to the one currently used in CLAS, and optimizes the momentum resolution. The cell structure will be very similar to the current design, and will consist of a hexagonal cell geometry. Because the polar angular coverage will be half that of the current chambers, the cell size and hence the time window and the spatial resolution are expected to be roughly half that of the present chambers.

---

[1] The characteristics of the Burle 8854 photomultiplier have been used

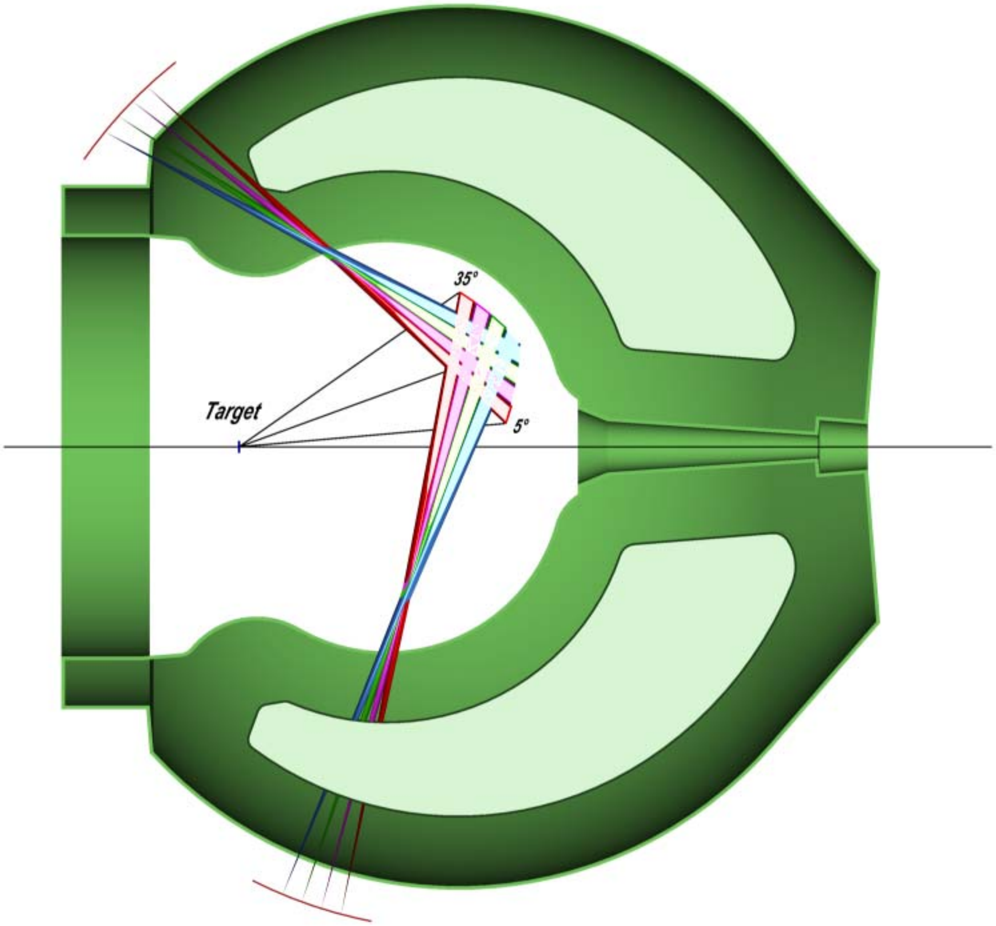

Figure 4.20: Optics of the High Threshold Cerenkov Detector. Cerenkov photons are generated in the gas volume beginning after the microstrip detector and the mirror system. The mirror system consists of 4 small angle segments which reflect the light toward the outside region of the torus magnet in the same sector. The 4 large angle mirrors reflect the light toward the PMTs located in the opposite sector. In order to avoid light obstruction due to the beam pipe the mirrors are tilted by about $\pm 15^o$ left and right of the beam pipe.

This design will provide precise measurements of the particle trajectory (100 μm accuracy per 12-layer chamber). They are also much less sensitive to background rates than the current chambers; by keeping the channel count constant but making the cell size twice as small and reducing the sensitive time by a factor of two, we reduce the phase space volume (volume × drift-time) by a factor of eight compared to the present chambers for isolated hit backgrounds from X-rays (a factor of four for track backgrounds). The background rates for the R1 chambers will be reduced by an additional factor of two by using a special, high drift-velocity gas mixture such as $He - CF_4$.

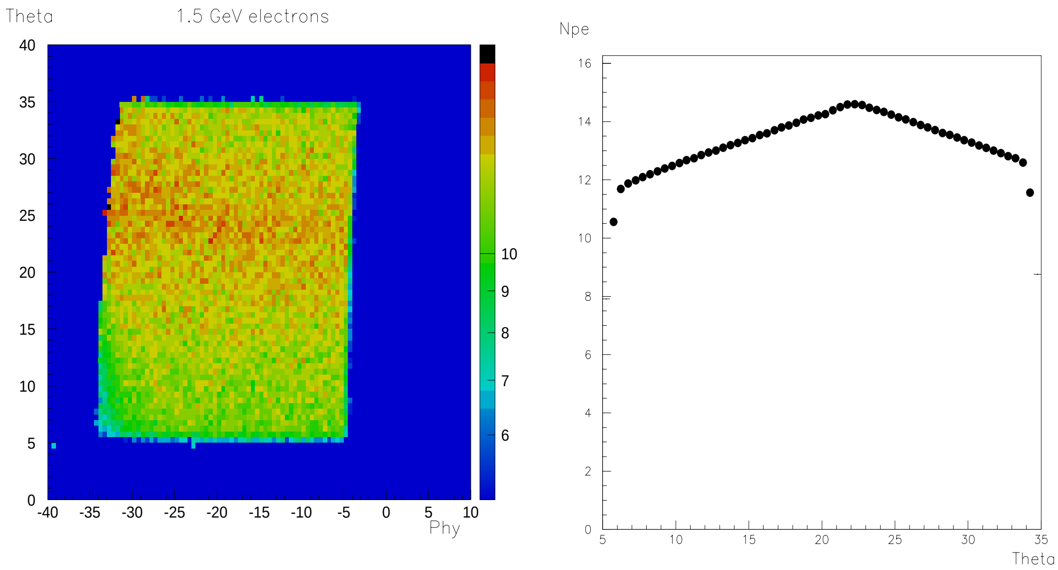

Figure 4.21: Left: Distribution of the number of photoelectrons N_{pe} for the HTCC in the $\phi-\theta$ plane. The simulation was done for electrons of 1.5 GeV/c momentum. The solenoidal field was included in the simulation at full strength of 5 Tesla central field. The phi motion of the electrons in the solenoid field leads to a slight broadening of the photon distribution at the Winston cones and PMTs. Right: Average N_{pe} versus the polar angle (projection of the graph on the left onto the θ axis). The θ-dependence in N_{pe} is due to the different radiator gas length for different polar angles.

4.4.4 Low Threshold Cerenkov Counter

The Cerenkov counter installed in the existing CLAS detector will be re-used to provide electron/pion separation for momenta up to 2.7 GeV/c and to identify π^+ and π^- for momenta greater than 3 GeV/c. The radiator gas will be C_4F_{10} as in the current system. In CLAS the Cerenkov counter is exclusively used for electron/π^- separation. The mirror system in the CLAS Cerenkov counter was designed to be most efficient for inbending particles, while for outbending trajectories less than full efficiency for detection is obtained. At the higher energies after the upgrade CLAS^{++} will be used to identify pions both inbending and outbending. In order to achieve full detection efficiency the optical system needs to be re-adjusted and likely the ellipical mirrors need to be replaced. Simulations are currently underway to determine the optimal optics for use with CLAS^{++}.

4.4.5 Outer TOF System

The outer TOF system has the geometry of the existing CLAS detector [225, 226], but the detectors will be upgraded for improved timing resolution. The design goal is to achieve timing resolution of σ =50 ps. This timing resolution allows separation of pions from kaons up to 3 GeV/c and pions from protons up to 6 GeV/c (Fig. 4.22). This assumes a "4σ" difference in time between the two particles and allows identification of a signal in the present of other particles with ten times higher rates.

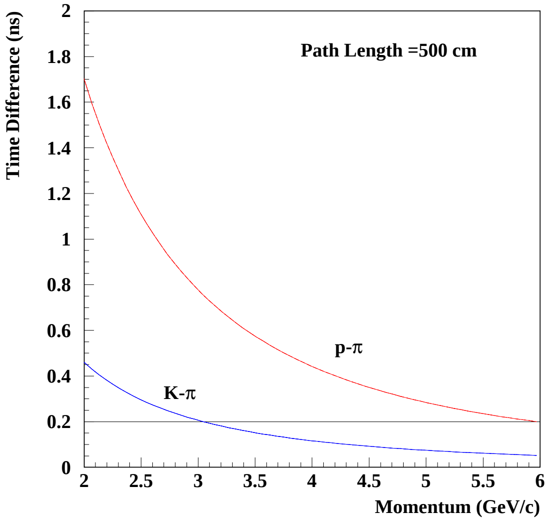

Figure 4.22: Time differences between protons and pions, and between kaons and pions over the 500 cm path length expected for the outer TOF system.

The resolution of the counters in the present CLAS TOF system can be summarized as follows: The attenuation length of the forward-angle counters (15-cm wide) can be approximated by λ = 134 cm + 0.36$\cdot L$, where L is the length of the counter in cm. The large-angle scintillators (22-cm wide) have an approximate attenuation length of 430 cm. The time resolution of each counter has been measured with cosmic-rays; it can then be parametrized with the following formula:

$$\sigma_{TOF}(ns) \quad = \quad \sqrt{\sigma_0^2 + \frac{\sigma_1^2 + (\sigma_P \cdot L/2)^2}{N_{pe} \cdot \exp(-L/2\lambda)}} \qquad (4.1)$$

where σ_0=0.062 ns represents the intrinsic resolution of the electronic measuring systems and other processes which are independent of light level, $\sigma_1 = 2.1$ ns is the combined single-photoelectron response of the scintillator and PMT, and $\sigma_P = 0.0118$ ns/cm corresponds to path length variations in the light collection. Path length variations in the scintillator scale with the distance from the source to the PMT, which we take to be half the length of the counter ($L/2$). The statistical behavior of the last two terms is indicated by scaling the single-photoelectron responses by $\sqrt{N_{pe}}$, where $N_{pe} = 1043$ is the average number of photoelectrons seen by the PMT of a counter with an infinitely long attenuation length. For scintillators which are several meters in length, the dominant contribution comes from transit time variations of photon paths in the scintillator.

Prototypes have achieved the desired resolution for counters 200 cm in length. Two examples are shown in Fig. 4.23 proving that a single plane of scintillators can achieve a resolution of 70 ps. The combined resolution of two measurements achieves the resolution of 50 ps. The prototypes used fast scintillator and XP2020 PMTS.

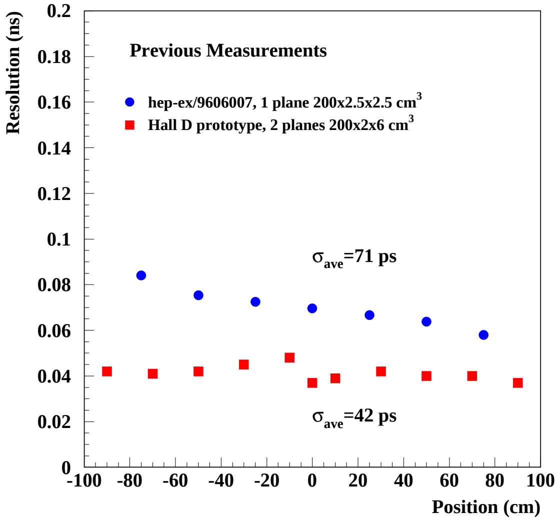

Figure 4.23: Previous measurements from two prototypes, 200 cm in length. The resolution of 50 ps is achieved using two scintillator planes which determine times with resolution of 70 ps.

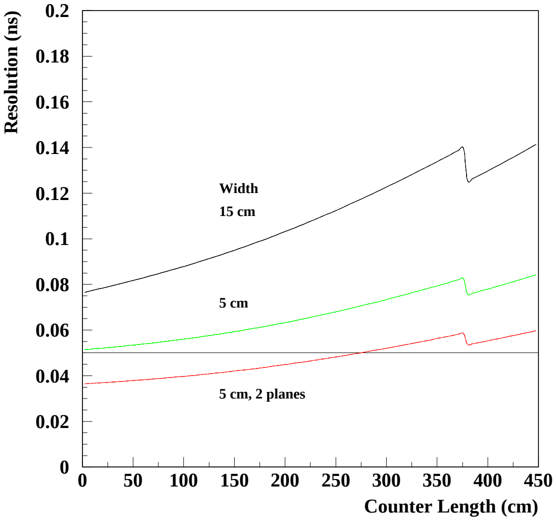

Figure 4.24: Expected resolution for the existing detectors (15 cm wide) with an intrinsic electronic resolution of σ_0= 40 ps. Also shown are preditions for counters 5 cm in width and for two planes of 5 cm wide counters.

Electronics

As a guide to necessary improvements in the time resolution of the system, we scale the parameterization of the CLAS system to narrow counters. The intrinsic resolution of the electronics system (σ_0 in Eq. 4.1) must be reduced and we have measured it to be as small as 14 ps in various setups [227]. There are many contributions to this term, and each electronic compoment will have to be selected carefully to insure that it mets our specifications. In order to achieve the rate capability at a luminosity of $10^{35} cm^{-2} s^{-1}$ (see Section on Central TOF system), a pipeline TDC will be used to readout these detectors. The Jefferson Lab Fast Electronics group is developing such a TDC based on the COMPASS F1 chip which satisfies our requirements. Therefore, we assume that σ_0= 40 ps determined by the resolution of the TDC, which is 40 ps

PMT (2")	Rise Time (ns)
XP2262B	2.0
XP2020	1.5
XP2020/UR	1.4
R2083	0.7

Table 4.4: Rise time for various PMTs. The exiting CLAS detector uses XP2262 PMTs.

Scintillator	Bulk λ (cm)	τ (ns)
BC-408	380	2.1
BC-404	160	1.8
BC-418	100	1.4

Table 4.5: Properties of several scintillators. The existing CLAS detector utilizes BC-408 scintillator.

for the COMPASS F1 chip. The predicted resolution from Eq. 4.1 is 65 ps, assuming that the width of the counters is reduced to 5 cm, and is consistent with prototyping measurements of Fig. 4.23. The predictions are shown in Fig. 4.24.

Photomultiplier Tubes

The prototypes that have achieved the desired resolution have used XP2020 PMTs, which have faster rise times than our current CLAS detector. While detailed prototyping efforts should be performed to optimize the choice of components, we expect that a faster PMT will be required. In Table 4.4 we give the rise time of various common tubes. The XP2020 PMTs have 25% faster rise time than the XP2262 tubes used in the current detector which is achieved with improved transit time spread across the photocathode. Faster PMTs are available, but in practice should be matched to the decay times of the scintillator material for improved performance of the overall system.

Scintillator

We use this parameterization to study the possible improvements in resolution based on a tradeoff between the decay time of the scintillator (σ_1 in Eq. 4.1) and the number of photoelectrons arriving at the PMT which depends on the attenuation length λ. The bulk attenuation length and the scintillator decay times for three typical scintillators are listed in Table 4.5. In Fig. 4.25 we plot the expected resolution as a function of counter length for the three scintillators listed in Table 4.5. For the figure we have used bulk attenuation lengths for BC-404 and BC-418, while we have used the measured values for BC-408. We have also plotted the resolution for BC-418 for half the bulk attenuation length. The plot indicates that, if the actual attenuation lengths approach the bulk attenuation of the material, the decay time dominates the performance for counters less than 200 cm in length. This is an option that should be explored experimentally for the shortest counters. Otherwise, we see that the existing material BC-408 is a good choice for scintillation material.

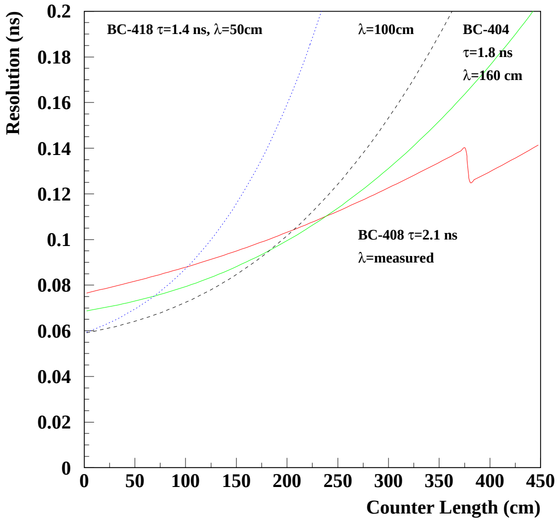

Figure 4.25: Resolution for various scintillators showing the tradeoff between attenuation length and scintillator decay time.

4.4.6 Inner Calorimeter

In the present CLAS system, neutral particles heading for the coils are not detected. Like for charged particles one would like to determine the directions of all photons. This requires to cover the inside of the torus coils with photon detectors. Ideally, the detector should also give some information on charged particles, like energy deposition, range, etc.

The detector is very compact since there is little space available in the angular range between 5° and 40° to complement the forward calorimeters. There is also a significant magnetic field in the region of the Torus coils that must be accomodated in the calorimeter design. A promising solution is to install short radiation length crystals. The currently most likely candidate is the scintillator crystal lead tungstate ($PbWO_4$). To avoid problems with the magnetic field interfering with photomultiplier readout, the crystal light can be collected with avalanche photodiodes (APD). The signal will be further amplified in low noise preamplifiers and in post amplifiers, before digitization.

This technique is currently planned for use in large detectors at CERN (e.g. CMS). Our collaborators from ITEP have carried out measurements in a test beam at ITEP [228], demonstrating the viability of such a calorimeter for use in the planned DVCS experiment in Hall B. The DVCS experiment has requirements very similar to the requirements for the CLAS upgrade. In particular the experiment will use a superconducting solenoid for shielding the detectors from the Möller electron background.

A conceptual design of a $PbWO_4$ calorimeter for the Torus coil region is shown in Fig. 4.26

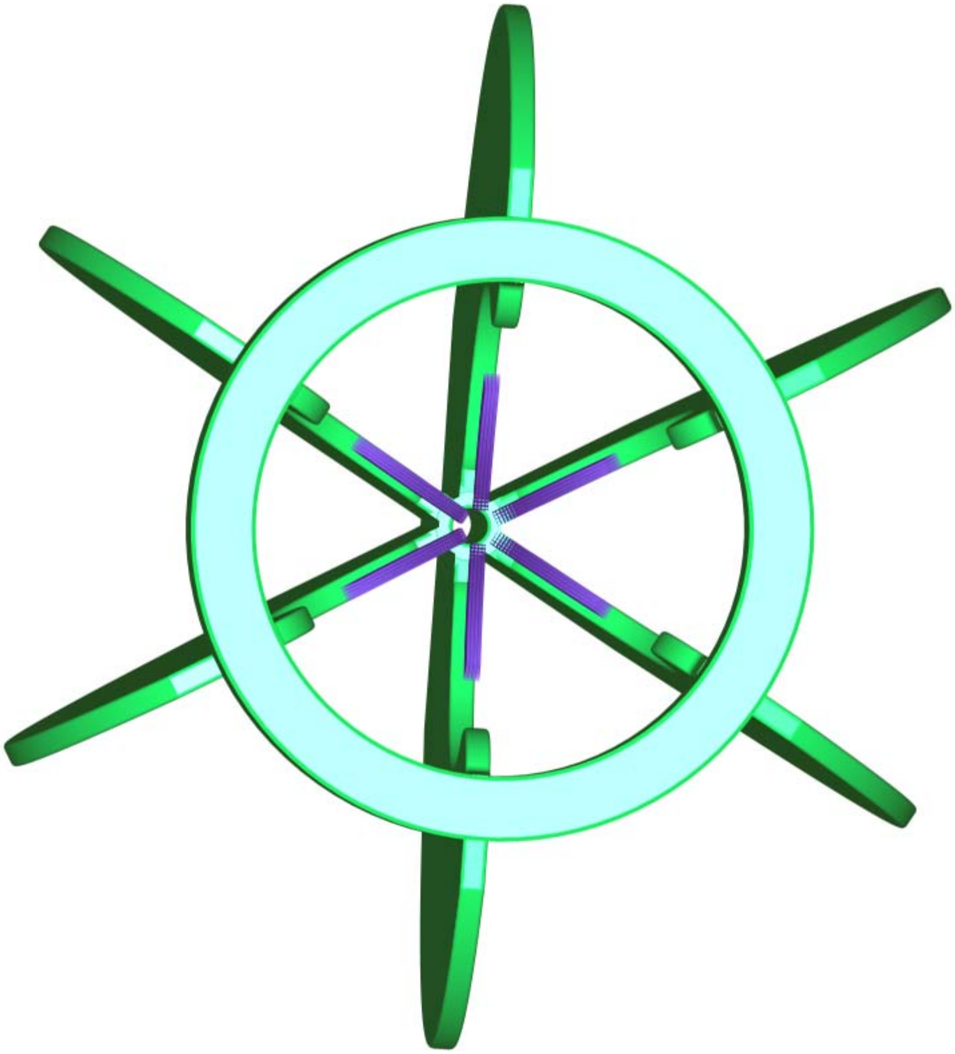

Figure 4.26: Arrangement of the Inner Calorimeter covering the regions of the torus magnet coils. The calorimeter consists of lead-tungstate crystals. The light is collected in Avalanche Photodiodes which are insensitive to magnetic fields. The APD signal is then amplified in low noise preamplifiers.

4.4.7 Forward Angle Calorimeter

The CLAS forward electromagnetic calorimeter (FEC) will be reused in CLAS++ without any modifications. In conjunction with the two threshold Cherenkov detectors the FEC provides electron identification up to the highest particle momenta, and efficient pion rejection with a rejection factor of > 2000 at an electron detection efficency of >99%. Above the pion threshold of the HTCC the FEC will continue to provide pion rejection, however with reduced rejection power (> 100 at > 95% electron detection efficiency) [229].

4.4.8 Pre-shower calorimeter

A major part of the physics program will require reliable detection of π^0s through their two-photon decays, in a wide range of momentum and angles. Forward-going photons in CLAS are detected in the forward electromagnetic calorimeter (FEC) [230]. FEC is a lead-scintillator sandwich with three stereo readout planes oriented at 120^o one each other. The transverse size of the read out module in a plane is bout $10cm$. The energy of a photons is reconstructed using the fraction of the shower energy deposited in the scintillators. For the FEC this is about 30% of the total energy deposited in the calorimeter. The production angles of the photons are determined via the hit position on the FEC, reconstructed from three stereo readouts. There are six calorimeter modules, one per CLAS sector. In Figure 4.27 reconstructed hits from two photons of a π^0 decay are shown using CLAS event display. In this example two hits are separated in two of the three stereo readout planes (named V and W views), but they are merged in the third one (U-view).

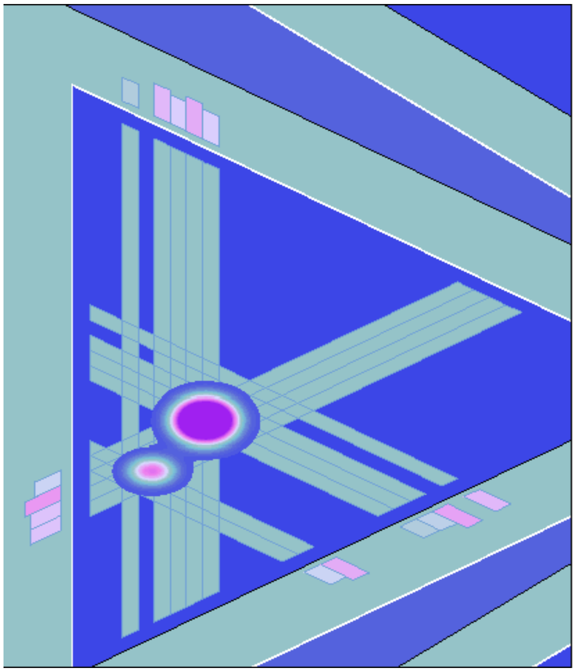

Figure 4.27: Reconstruction of two photons from π^0 decay in the FEC. Two peaks are seen on two of the views (called V and W views). Only one peak is reconstructed in the third view (called U-view).

With 12 GeV beams π^0s will be produced with momenta up to 9 GeV/c. With increase of the pion energy the spatial distance between two photons at the calorimeter will decrease, Figure 4.28, and at pion momenta above 4 GeV/c the distance between two hits will be too small to allow unambiguous reconstruction as two separate hits. Most of high energy pions will be reconstructed as a single hit and can be misidentified as a single high energy photon. In Figure 4.29 π^0 detection efficiency of as a single hit (triangles) or as two hits (squares) in the forward calorimeter is shown as a function of

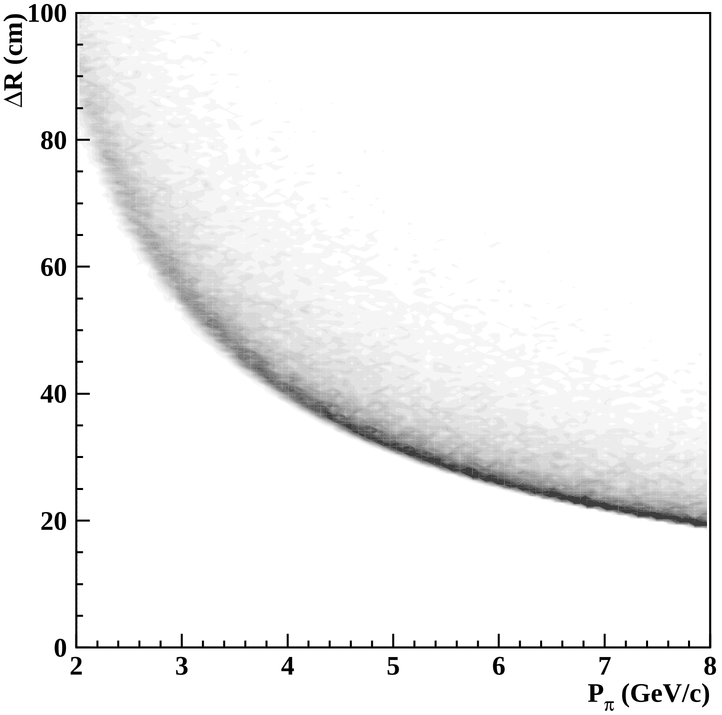

Figure 4.28: Distance between hit positions of the two photons from π^0 decay at the FEC plane as a function of the pion momentum. At a pion momentum of 8 GeV/c the minimum distance between the two photons is 20 cm which does not allow a reconstruction of the two photons in the existing CLAS FEC.

pion momentum. Open symbols represent GEANT simulations with existing geometry. As one can see with increase of pion momentum the efficiency for reconstruction of two hits rapidly decreases, and two photons are mostly reconstructed as a single hit.

To resolve two photons from high energy pions finer transverse granularity of the readout plane is needed. This can be done with a finer segmented pre-shower located in front of each FEC module. The pre-shower will be used for a more precise determination of the hit position. Most of the shower energy will still be absorbed and reconstructed in the FEC. In Figure 4.29 full symbols are simulations with higher transverse segmentation of the calorimeter. Having two hits spaced more than 3 readout segments in a view will allow to separate 2 photons from π^0 decay with momentum up to 9 GeV/c.

The conceptual design for the pre-shower is similar to the existing FEC of CLAS. It is based on a lead-scintillator sandwich arrangement with the shape of an approximately equilateral triangle. Three stereo readout planes are oriented parallel to the sides of the triangle. There are 9 layers of scintillators, 3 alternating layers in each view. Each layer will consist of 3 cm wide and 0.5 cm thick scintillator strips. 2 mm thick lead sheets are interleaved between two scintillator layers. Light produced in the scintillator will be transported to the photo detector via four 1 mm radius wave-shifting (WS) fibers embedded in the half-circular equally spaced grooves on

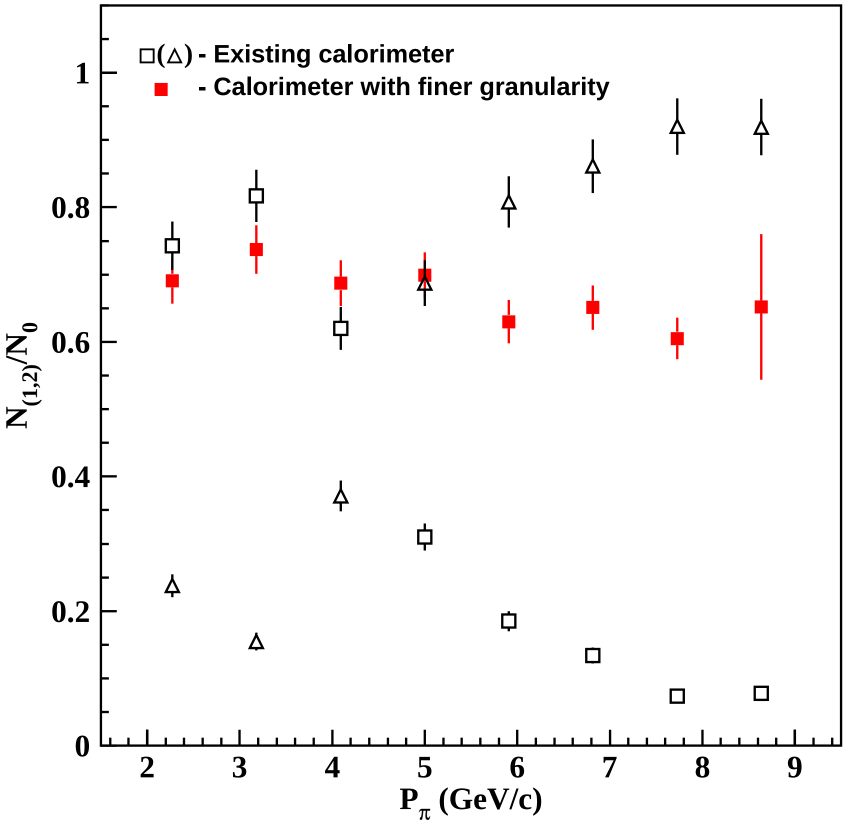

Figure 4.29: π^0s reconstruction efficiency from the reaction $ep \rightarrow ep\pi^0$ with beam energy of 11.5 GeV. Simulations are done with the CLAS FEC only. Open squares symbols indicate events when two hits are reconstructed, the invariant mass of the two photons is near the π^0 mass, and the energy sum is about the energy of the pion. Open triangles show the freqency of single hit reconstruction with the energy corresponding to the π^0 energy. For momenta of 4 GeV/c and higher most of the π^0 events are misidentified as single photons. The full red squares show the results of a simulation when the preshower detector is used in the reconstruction. Pions are reconstructed over the full momentum range in this case.

the surface of the scintillator [231], as seen in Figure 4.30. Photomultiplier tubes with $\sim 1''$ green sensitive photocathode will be used for light detection. Corresponding strips from 3 layers of the same view will be read out with a single PMT. From studies using a prototype model, described in [231], we expect about 15 photoelectrons for 1 MeV energy deposition in the scintillator. With a sampling ratio of 0.3 this corresponds to 5 photoelectrons per 1 MeV deposited in the full calorimeter.

Simulations of exclusive, $ep \rightarrow ep\pi^0$, and semi-inclusive, $ep \rightarrow e\pi^0$, reactions showed that pions with momenta $> 4\ GeV$ are produced at angles $\theta < 25°$. Therefore, the pre-shower must provide coverage for straight tracks up to 25°. This corresponds to about half the size of the existing FEC. This implies that the height of the triangle, corresponding to the active area of pre-shower detector must be about 180 cm. The 64 scintillator strips in a layer with 3cm width cover the desired area. As described above, corresponding scintillator strips of the layers of a view are read out with a single PMT via four green WS fibers per strip, 12 fibers for each PMT.

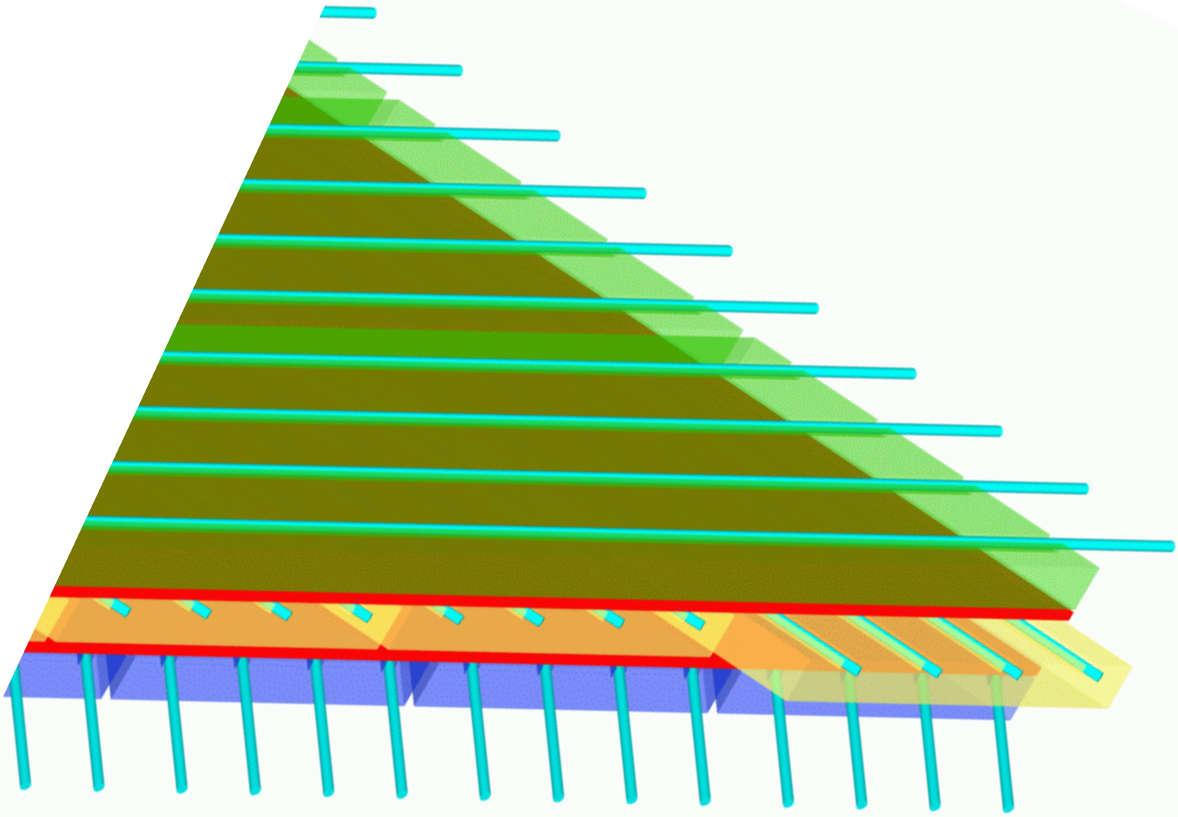

Figure 4.30: 3-d view of a corner of the pre-shower module. Three layers are shown only. Wavelength-shifting fibers are used to read out the light generated in the plastic scintillators. The scintillators and embedded fibers provide stereo information due to a geometry which is similar to the geometry of the CLAS FEC.

There will be 192 readout channels in each sector, making a total of 1152 channels for the entire system. Each read out channel will be furnished with trigger electronics, ADCs and TDCs.

Chapter 5

Other Equipment Components in Hall B

5.1 Polarized Target Operation in CLAS^{++}

A significant portion of the physics program for CLAS^{++} requires use of a dynamically polarized solid state target for use as a polarized hydrogen or deuterium (neutron) target. A large program has already been carried out successfully with CLAS to measure inclusive polarized structure functions $g_1(x, Q^2)$ on the proton[232] or deuterium[233] and to study polarization observables in exclusive pion production from polarized protons and neutrons [234]. For these experiments the target was polarized parallel or anti-parallel to the electron beam direction. This configuration can be achieved in CLAS^{++} using two different options. These are briefly described below.

5.1.1 Polarized Target in Solenoid Magnet

Part of the program for CLAS^{++} is an extension of this program to higher energies. It will require use of a target polarized parallel or anti-parallel to the beam line. In CLAS^{++} this can be accomplished by adding some correction coils to the superconducting solenoid to improve the field uniformity around the target. The correction coils are needed since the solenoid magnet alone may not produce a sufficiently uniform magnetic field in a large enough volume around the target to achieve highly polarized protons or deuterons (neutrons). With this option, the complete central detector could be used for polarized target experiments, allowing nearly full coverage for particle detection. This arrangement will allow measurement of multi-hadron final states in addition to the scattered electron. The target cryostat will have to be re-designed to allow for its operation in a warm bore magnetic field environment.

5.1.2 Polarized Target with Helmholtz Coil Arrangement.

A second option is, to remove the entire central detector including the solenoid magnet with its iron flux return, and replace it with the existing polarized target magnet. This option will not require any changes on the CLAS polarized target, and will be adequate, and highly efficient for inclusive measurements. However, it would impose limitations on the kinematics accessible in hard exclusive processes. For example, the DVCS process is of highest interest at small momentum transfer t to the recoil proton. The Helmholtz coil would limit proton detection to angles $\leq 45^\circ$, while the minimum t is achieved at angles $60^\circ - 70^\circ$. Such limitations would significantly reduce the physics impact of these measurements.

5.1.3 Transversely Polarized Target.

The Helmholtz magnet has been used inside CLAS with a cryostat inserted from the upstream end of CLAS. This made it very difficult to achieve a configuration where the Helmholtz field is oriented transverse to the beamline. At the higher energies there is a significant interest in semi-inclusive/exclusive processes involving transversely polarized targets. In the CLAS^{++} configuration, and if the central detector is removed, the polarized target cryostat can be inserted from the top in between the torus coils which are no longer instrumented with tracking chambers. This provides a straight forward way of rotating the magnet by 90° to provide a transverse (to the beamline) polarization. As the magnetic field will deflect the incident beam vertically a magnetic chicane will be needed to compensate for that deflection. The chicane is to be inserted into the beamline upstream of CLAS^{++}. The Helmholtz coil geometry will restrict the acceptance for particle detection to the forward region.

The target polarization is usually required to be transverse not to the beamline but to the virtual photon direction. This may be accommodated in certain kinematics by rotating the field direction by a smaller than 90° angle. In any case, the kinematics accessible for a dynamically polarized solid state target with transverse field orientation and operating in an electron beam will always be more limited than for a longitudinally polarized target.

5.2 Beam Line

5.2.1 Introduction

There are no major changes in the beamline necessary for the main 12 GeV operation. The bulk of the beamline equipment will operate as designed or better with an electron beam of higher energy and current. The items that should work without major upgrades include the three nA RF beam position and current monitors, beam profile harps, beam charge asymmetry monitors, beam halo monitors, beam viewers and beam raster magnets. One beamline element that is not-upgradeable to 12GeV running is the tagger magnet. New beamline elements or existing equipment that needs modification for the upgrade are described in the following sections.

5.2.2 Faraday Cup

The Faraday cup (FC) currently installed in the Hall B beamline contains no provision for water cooling. With the increase in beam energy by a factor of 2, and with the increase in luminosity by a factor 10, which will mostly come from an increase in beam current, the total power absorbed in the FC could increase by a factor of 20. This will either require the implementation of some cooling capability into the Faraday cup, or limit the duration during which the FC can be exposed to the beam. Another, though less desirable, possibility could be to limit use of the Faraday cup to short periods of time, e.g. for calibrating the upstream beam current monitors, and to move the FC out of the beam after the calibration is completed. This in turn would require installation of a low power beam dump located downstream of the FC that would dump the electron beam during routine operation.

5.2.3 Møller Polarimeter

The Hall-B Møller polarimeter consists of a magnetized permadur target followed by two magnetic quadrupole magnets that deflect the electrons into scintillating fiber bundles. The maximum beam energy of the present polarimeter is given by the maximum field of the quadrupole magnets. This maximum is $\sim$ 8.5GeV. In order to achieve operations with an 12 GeV beam energy the polarimeter will need to be reconfigured. A combination of increasing the distance separating the two magnets and relocating the detector bundles further from the magnets should be sufficient for 11 GeV operation. The determination of the optimum configuration for operation with any beam energy between 3 and 11 GeV is ongoing.

5.2.4 Magnetic Chicane

Additional modifications will be needed when operating a polarized target in CLAS^{++} where the magnetic field is oriented transverse to the beam line. To compensate for the beam deflection of about 3.2° (at 12 GeV) in the polarized target field, a beam chicane will be needed. This chicane will be inserted into the beam line upstream of CLAS^{++}. The chicane needs to compensate for the 2 Tm integrated transverse magnetic field of the polarized target [1].

---

[1] The chicane is not part of the equipment complement for the upgrade, however it is part of a proposal currently under development for an experiment at 6 GeV, and may therefore exist before the energy upgrade

5.2.5 Beam raster magnets

The currently installed beam raster system, which is used in conjunction with the polarized target is dimensioned sufficiently high to allow full rastering over a polarized target with the currently used dimensions of 1.5 cm diameter. The power supplies will be replaced with more powerful supplies.

5.3 Radial TPC Low Energy Particle Tracking Detector

Low momentum particles lose energy rapidly as they pass through any material, and therefore leave short tracks or no tracks at all in solid detector components. In a detector based on gas ionization, however, ionization trails of significant length are readily achieved as the particles pass entirely through, or gradually slow down and stop, in the detection medium. Multiple measurements along the track provide a wealth of information about the particle that created it. Therefore, a promising spectator or low energy recoil detector would be a gas chamber with appropriate geometry and minimum material content. It would provide position and timing information sufficient to identify particles and connect them to an outgoing electron sensed in CLAS. Associated information about the particle's energy loss rate (dE/dx) as it precipitated the ion trail would provide additional information for PID.

A gas chamber configuration that provides all of these needs is a Radial Time Projection Chamber (RTPC). A diagram of the proposed detector for the BoNuS experiment on CLAS is shown in Figure 5.1. (BoNuS studies neutron structure using a tagging of a very low energy backward going spectator protons). In outline, it consists of a pair of concentric cylinders with the annular space between the cylinders containing a sensitive gas. The cylinder axis would be placed along the beam line and target. Charged particles produced at sufficient angle pass through the gas and leave a trail of electron-ion pairs. An electric field between the cylinders forces the electrons to drift towards the outer cylinder where appropriate electrodes cause avalanche multiplication. The resulting signal is collected on the outer surface by either individual pads or a stereo arrangement of conductive strips. The locations of the pads (strips) provides position information (ϕ-z) for the collected drift electrons, and the times of their arrivals provide a measure of the radius (r) at which they were produced. A string of such measurements constitutes multiple position measurements along the particle's track. By recording the amount of charge produced along the track one can estimate dE/dx and thereby constrain the mass of the particle that produced it.

As shown in Figure 5.1, the sensitive volume of the BoNuS RTPC will be an annulus with inner radius $\simeq$ 4 cm and outer radius $\simeq$ 6 cm. The 20 cm length (shown in the figure) will extend beyond the target in order to provide coverage from

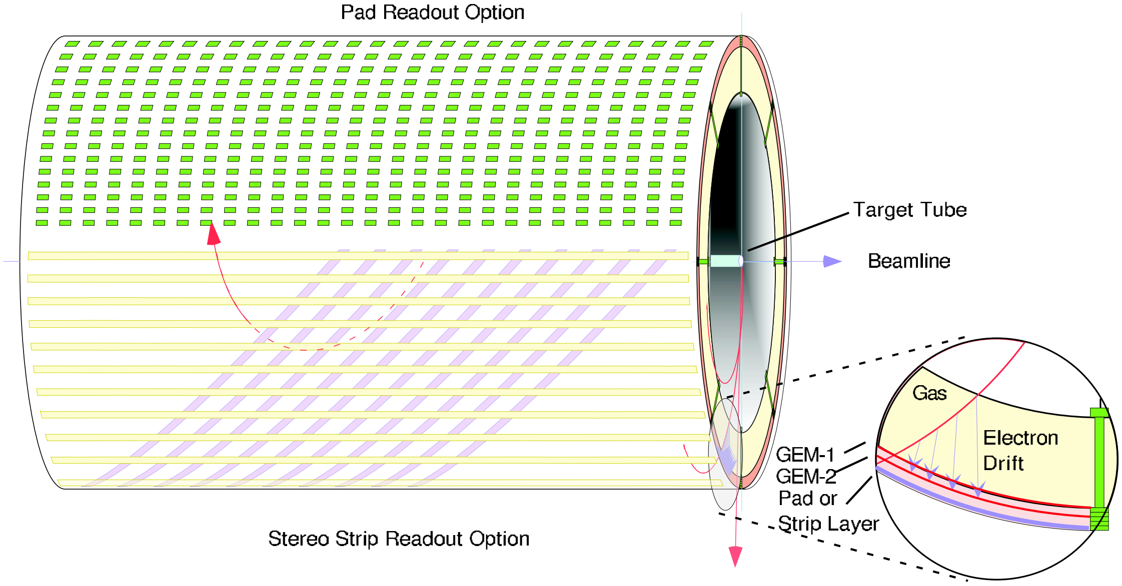

Figure 5.1: Sketch of the Radial Time Projection Chamber for BoNuS. In this figure the upper portion shows pad readout while the lower portion shows readout by two planes of strip electrodes providing stereo coordinate measurements.

90° to 160° for the entire target. The 4 cm space between the target vessel and the inner cylinder will be filled with helium to minimize the scattering and energy loss of particles before they enter the detector. This space also serves as a dead zone in which Møller electrons can be curled up without affecting any detector elements.

The inner cylinder of the RTPC, which serves both as a gas barrier and as the first drift electrode, will be thin gold-plated kapton. Outside $\simeq 2$ cm of sensitive gas will be the first of two Gas Electron Multipliers (GEM). Another $\simeq 0.2$ cm out will be the second GEM followed by the readout pads or strips $\simeq 0.2$ cm later. While each of these four cylindrical electrode assemblies will be largely self-supporting, they will be constrained by precisely machined endcaps and, periodically in azimuth, by radial frames. The frames will deaden a small and quantifiable part of the chamber volume.

GEMs were chosen as the readout sensors because they are mechanically simple and lend themselves naturally to a curved geometry. A GEM is fabricated by chemically etching closely spaced tiny holes through a kapton sheet clad on both surfaces with a thin layer of copper. A modest voltage (few hundred volts) between the two conductive layers produces a large electric field in the holes. Ionization electrons which enter the holes on the negative-biased side of the GEM initiate a gas avalanche within the holes resulting in a large number of electrons being emitted on the positive side. These secondary electrons can be directed onto a pickup electrode a short distance away, or into another GEM for further amplification. The pickup electrodes collect the resulting charge cloud. Electronics connected to these electrodes sense the charge and record its magnitude and time of arrival.

The electronics used to read out the RTPC must provide both charge and time information. This problem has been solved for the STAR FTPCs and the main STAR TPC by a system of charge pre-amplifiers whose output is fed to a switched capacitor array (SCA). The SCA is clocked at 5 MHz, causing the charge collected in each ~200 ns interval to be transported in a bucket-brigade fashion through the chain of capacitors. Upon receipt of a trigger signal, charge stored in the appropriate capacitors is digitized and the results are passed to the data acquisition system. Readout of this system takes about 10 milliseconds. An upgrade is currently planned for the main TPC which will use flash ADCs and digital storage to significantly reduce the readout time. A very similar (or identical) readout system could be applied to the BoNuS RTPC. Discussions about this possibility are currently ongoing with members of the STAR collaboration.

5.4 Small Angle Electron Detection

Part of the physics program anticipated for 12 GeV requires the detection of scattered electrons in the range of 0.5° to 1.2° . The detection system is currently being designed for use at 6 GeV, and should be available before the upgrade. The hardware envisioned for 6 GeV is described in the following sections, this hardware should work without any modifications at the upgraded energies. In fact the backgrounds should be lower at higher energies.

The most obvious location for this detector system is at the apex of the forward carriage, 7m downstream of the CLAS target. The CLAS bore limits the θ angular coverage to a maximum of 1.2°, a particle with $\theta = 1.2°$ is 15cm off the axis radially 7m from the target. The minimum θ of the angular range must be large enough that the electron is sufficiently removed from the scattered beam. A minimum θ of 0.5° results in an offset of 6cm from the scattered beam. Any detector must not disturb the scattered electron beam so that it impinges on the Faraday Cup.

5.4.1 Beampipe

A beam pipe that allows electrons with an angular range, $0° < \theta < 1.2°$, to be transported 7m from the target without any material obstructions must be designed. A thin Aluminum window just upstream of the low Q^2 tagging system with outer radius of $\sim$ 20cm and an inner radius of $\sim$ 4cm will allow the small angle electrons to enter the tagging system. The vacuum pipe will step down to 4cm diameter at this point and continue to the Faraday Cup. This transition will have to be carefully designed to minimize backgrounds in the detector.

5.4.2 The θ and ϕ Detector

The θ and ϕ of the electron will be measured with a detector just downstream of the thin Aluminum window. The electron rate for all ϕ is $\sim$ 1MHz at $\theta = 0.5^\circ$ and $\sim$ 10kHz for $\theta = 1.2^\circ$ at $10^{33}\text{cm}^{-2}\text{sec}^{-1}$. Two detectors that provide a high rate capability and the required position resolution; they are scintillating fiber array or wire chamber.

A scintillating fiber array using 64 2mmx2mm fibers and multi-anode PMT's have been successfully used to measure the photon beam profile with individual fibers operating at 1Mhz of rate. A simple XYU array of fibers would provide a resolution of 600μm in X and Y, or a resolution 850μm radially (121μradians). The ϕ resolution does not benefit from the 7m lever arm, but $\tan\phi$ will have resolution of 3.3% for $\phi = 45^\circ$ and $r = 6$cm. A more sophisticated geometry for the fibers which is designed to measure θ and ϕ (rather than x and y) might improve the resolution or reduce the channel count. 6 fiber arrays (XYU planes) (540 channels, 34 multi-anode PMT's) would be needed to for complete ϕ and θ coverage. The rate will be highest for those fibers at small θ and would be $\sim$ 1Mhz.

Another possibility would be to use a wire chamber design similar to that proposed by the CKM experiment at Fermilab. By using a 800μm wire pitch and low gain, the chambers can operate at 0.61Mhz. With a finer segmentation than 2mmx2mm fiber detectors, the rate per channel will be smaller. Approximately 1350 channels are needed.

5.4.3 Energy Measurement

To measure the energy or momentum of the electron there are two options. The first option uses a toriod magnetic field to bend the electrons away from the beam and onto a focal plane. A second option being pursued is to use a calorimeter of PbWO4 crystals to measure the electrons energy.

The energy of the electron is to be measured directly via a calorimeter directly downstream of the ϕ and θ detector. A calorimeter consisting of PbWO_4 crystals is placed directly downstream of the ϕ and θ detector would provide a energy measurement. The Mainz group has achieved $\frac{\sigma_E}{E}(\%) = \frac{1.54}{\sqrt{E}} + 0.3$. Using an 11GeV primary beam energy, a tagged 1GeV e^- in the calorimeter would measure ν with 0.2% error. A total of 150 2cmx2cm crystals would be needed. If the rate per crystal is determined by simulation or beam tests to be too high smaller crystals may be used (1cmx1cm).

Chapter 6

Computing

6.1 Data Acquisition System and Trigger

The primary feature driving the redesign of the CLAS^{++} Data Acquisition (DAQ) and triggering system is the higher data rates associated with the approximate factor of 10 increase in instantaneous luminosity that will be delivered to the experiments at Hall B.

6.1.1 DAQ and trigger upgrade motivation

A fast and flexible DAQ is the cornerstone of a modern nuclear or high energy physics experiment. Similarly, DAQ performance highly depends on the quality of the triggering system. The JLAB 12GeV upgrade poses unique challenges to both the trigger and data acquisition systems for the CLAS^{++} detector.

Taking into account that the current DAQ system is operating at the limits of its capabilities, fulfilling the requirements of the CLAS^{++} DAQ without a major upgrade of the existing system will be a difficult job. During the years of the CLAS detector operation, the DAQ system was upgraded and optimized both in hardware and software to meet increasing requirements of the ongoing CLAS experiments. As a result, system performance exceeded the initial design criteria by almost factor of 3 and demonstrated that the present system performance is solely limited by the front-end digitization hardware.

Three main factors prevent further improvements of the existing system. First, the slow digitization sequence in the CLAS high precision TDCs (Lecroy 1872/75. 10000ns+2500ns/hit conversion time), second , the slow converting CLAS ADCs with 12000 ns per module conversion time and third, data rate limitations ($<$ 23Mbyte/s). The data rate problems can be solved by utilizing permanent storage units with fast access times, and by using different storage management software. Also, higher level software triggers (level3) can be implemented to reduce the data rate to disk. In order to reduce front-end dead time limitations, the high resolution TDCs and ADCs must be replaced.

6.1.2 Design criteria for the system

The CLAS^{++} DAQ must be able to handle level1 trigger rates up to 20kHz at 10kByte/event event size with less then 15% dead time. High data transfer rates over the network will be handled by using gigabyte Ethernet. The proposed DAQ system must assemble the event data from many front-end buffers to the Event Recorder (ER). The system must provide sufficient computing resources for executing physics algorithms which can substantially reduce the expected input rates. It must also provide continuous monitoring of the detector so that malfunctions may be readily identified and corrective measures taken. These functions will be performed by using a high performance readout network to connect the sub-detector readout units (ROC) via multiple event builders (EB) to the event filtering units (EFU, possibly implemented in computer farms). The flow of event data will be controlled by the triggering and timing system (TTS).

6.1.3 System upgrade

CLAS^{++} DAQ system design requirements are based on the rate estimates of the 12GeV leading physics programs. Current system will be upgraded to meet the mentioned design requirements and to minimize the efforts, which will be invested to satisfy increased requirements of 12GeV future physics programs. Following upgrade strategy will be used to achieve desired goal.

- Utilizing pipelined digitization hardware for the CLAS^{++} new detector components.

- Replace the CLAS existing detector components: ADCs and high resolution TDCs with the equivalent pipelined digitization hardware, ready to function in the free-running DAQ mode.

- Keep existing low resolution TDC (TDC1877/1877S) in the system.

Mentioned hardware upgrades, with conjunction of the fast and optimized readout system, will guarantee fulfillment of the CLAS^{++} DAQ design requirements. Using pipelined digitization hardware components in the system will provide most of the benefits, typical for the free-running DAQ systems. Gradual replacement of the remaining hardware (low resolution DC TDCs) with the pipelined equivalent will help us eventually implement full operational free-running DAQ system for future CLAS experiments.

6.1.4 Overview of the proposal

The system including free-running, pipelined DAQ front-end components is an ideal solution, which satisfies all CLAS^{++} data production requirements, and gives us flexibility for future improvements. Proposed system has the following benefits. First, pulse shapes are easily captured and stored for immediate or delayed analyses. Second, the system will have an enhanced ability to delay signals while accurately preserving time information between different events. A digital delay line, for example, is just a FIFO memory which can easily be 10s of microseconds long, with perfect signal fidelity. This property of the DAQ system will be extremely profitable for the CLAS^{++} new detector components, saving time, space, and money by eliminating signal delay cables. Finally, data processing is extremely flexible. This means that signal processing algorithms (level1, level2) in either firmware or software are easily modified so that different, triggering algorithms can be added without any hardware reconfiguration. However, before complete replacement of the low resolution TDC's, flexibility of the low level triggering system will be somewhat limited. The speed requirements of the low level triggering system will be defined by the TDC1877 multi-event buffer memory depth.

Proposed system will open areas of new capabilities for CLAS^{++}, for example:

- Pulse specific corrections and shape analyses to provide particle identification.
- Inner tracking chamber transient signal analyses. Analyses of the induced charged signals can provide interaction location information.
- Hierarchies of processing complexity, which readily support simple-fast (level1) versus complex-slow (level3) decision making on an event by event basis.
- Complex coincidence criteria, which will support capturing and/or processing data either immediately or after delay.
- Digital communication, which will enhance operating convenience by allowing remote operation, digital hardware calibration, and restoration of previous setup data from files or databases.

Figure 6.1 shows possible data flow diagram of the CLAS^{++} DAQ system. Here is a possible scenario of implementing higher level triggering algorithms, which demonstrates flexibility of the proposed system. In order to optimize the data flow, the event filtering computer farm performs event selection in two stages. First, a level2 filtering decision is made on a subset of the data from a programmable set of the detector components. This will help us to avoid system bandwidth saturation by reading out large volumes of tracking data at high level1 rates. The remainder of the full event data are only transferred to the filtering farm on a level2 accept, and a final level3 algorithm is then applied to the complete event. This activity is controlled by the Filtering Supervisor (FS) system.

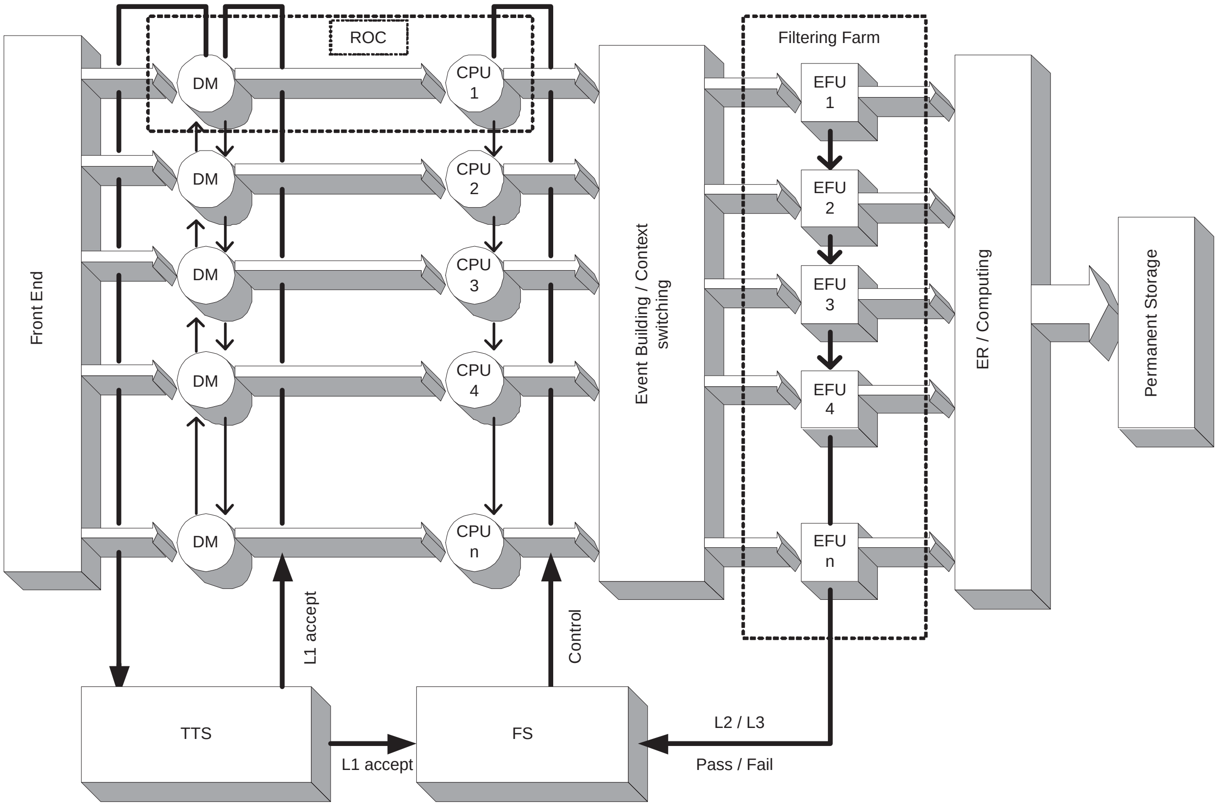

Figure 6.1: CLAS^{++} DAQ bloc diagram. DM - Digitization Module, TTS - Triggering and Timing System, FS - Filtering Supervisor, EFU - Event Filtering Unit, ER - Event Recorder.

The FADC data can be used to form the level 1 trigger by utilizing a tree of digital adders to sum information from various channels in the detector system (Figure 6.2).

If we assume a reasonable time window of 100ns for FADCs with 8bit sampling depth and 250MHz sampling frequency, we would expect 25bytes/FADC channel to get energy and timing information. Taking into account approximately 5300 FADC channels, and assuming 2% occupancy, the data volume from all FADCs will be 2.6kBytes (no headers included). However, using the FADC built-in computational resources (digital signal processors or DSP) one can perform FADC data reduction in real-time. Currently we are studying a FADC prototype developed by the Hall-D collaboration to determine time, energy and spatial resolutions possible to get using that particular module. For the pulses, corresponding to the very small energy depositions in the calorimeter, FADC sampling depth and sampling frequency will be simulated to determine the optimum FADC design. We hope that at the time of the CLAS^{++} DAQ commissioning there will be FADC with higher sampling depth and frequencies in the market within current estimated price range. Otherwise conventional fast ADCs will be used (currently available 6000nsec conversion time in the same price range), with the conventional triggering system. This backup plan will satisfy CLAS^{++} DAQ design requirements, however it will complicate further

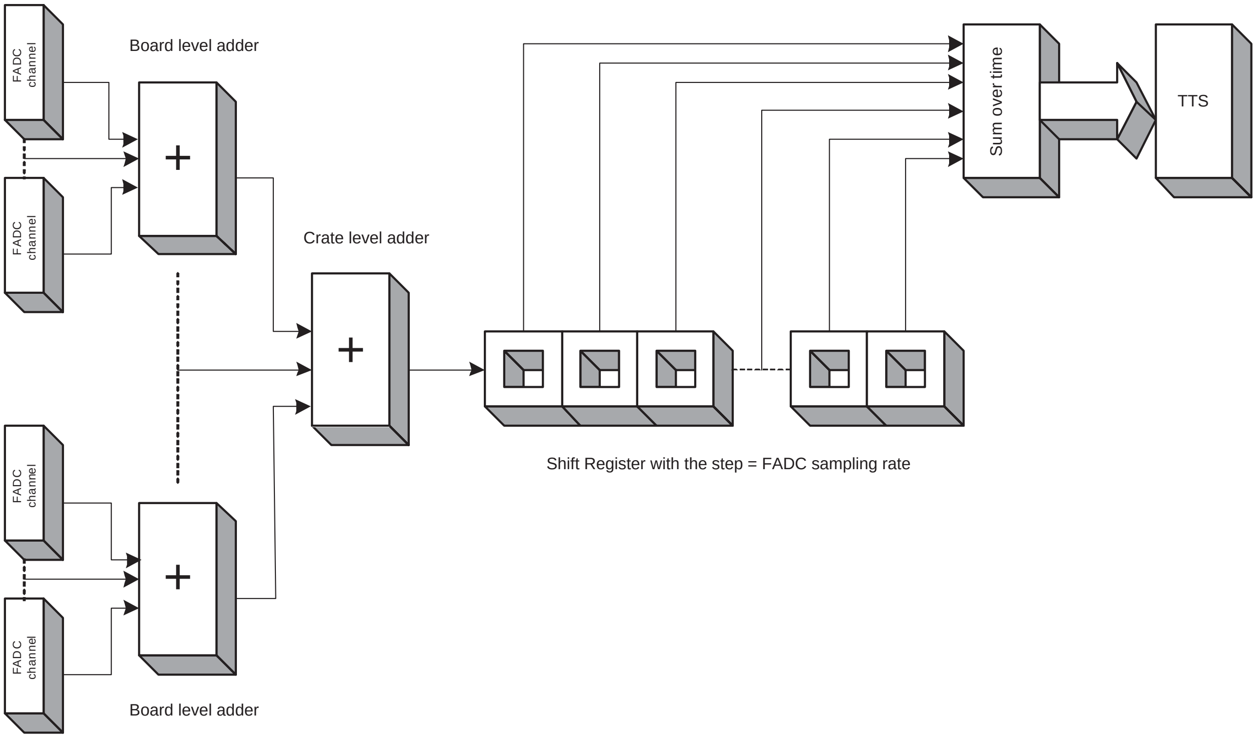

Figure 6.2: Level1 triggering system based on flash ADCs.

improvements of the entire system.

For precise time measurements we will use multi-hit TDCs. Currently, a high resolution multi-hit TDC based on the F1 ASIC, which was developed at Jefferson Lab for Hall-D collaboration, is at the test stage. This TDC design can provide up to 60ps of resolution and will sustain high rates.

The manufacturer of the digitization hardware has not been finally determined. However, we prefer digitization hardware developed in-house for Hall-D over the commercially available alternatives due to channel and maintenance cost considerations.

6.1.5 Level1 triggering and timing system

The TTS is responsible for selecting physics events and for suppressing background as efficiently as possible. It will adopt a real-time, parallel, pipelined architecture for the trigger electronics. High speed triggering algorithms will be designed and implemented in Field Programmable Gate Arrays (FPGA). This approach will help us to minimize the trigger latency and shrink DPRAM depth of the digitization modules. After getting a trigger decision, the TTS will initiate detector readout by sending an L1Accept signal to the ROCs. The TTS will also be responsible for injecting calibration pulses as well as SYNC pulses used to resynchronize the entire DAQ system. It is obvious that we will need a series of trigger simulations to help define trigger algorithms and understand the real requirements of level1.

6.1.6 Higher level triggering systems

Level2 and Level3 filtering processes are performed by the computer farm processors. Currently, one full event analysis using RECSIS, with momentum resolution of less then 1%, requires 40miliseconds on a 500MHz Pentium III processor (21SPECint). It is clear that at the trigger level we do not need high resolution momentum reconstruction. Based on a recent development of the fast reconstruction program, we are quite confident that we will be able to analyze the events at level3 with less then 5% momentum resolution, spending 3-4 milliseconds on a 21SPECint processor. Therefore, filtering 50KHz events at level3 will need 4200 SPECints processing power. This can be achieved with a filtering farm, composed of 42 computers each with 200 SPECints of processing power (50% cpu utilization is estimated, due to I/O overhead, brakes, etc.).

The FS will be designed to maintain coherency between the two filtering stages. It will be important for error detection too. Several recovery protocols will be defined to restore and maintain system synchronization and data flow. The Level3 pass will finally send events for recording, and monitoring.

6.1.7 Control and monitoring

The control and monitoring system must be able to deal with network distributed hardware components and their heterogeneous software environments. This system must have the ability to efficiently retrieve, organize, and manage information from widely dispersed sources within as well as from outside the CLAS^{++} control environment. Feedback systems between the DAQ, trigger and slow control systems will be of paramount importance.

Statistical information about data taking, as well as detector performance will be accumulated and visually presented. On-line databases will store run conditions, configuration parameters and calibration constants for later processing and evaluation. Data integrity will be checked continuously. Physics performance histograms will be accumulated and presented. The system will detect, record, and analyze error conditions. Serious conditions will generate informative alarms for operators.

In order to achieve scalability and robustness, the control and monitoring system will be designed under a single framework. This will allow interconnection and interoperation with multiple legacy systems (EPICS, Smart Sockets, etc.). The dynamic and distributed nature of both data and applications for the CLAS^{++} DAQ will require that software not merely respond to requests for information but intelligently anticipate, adapt, cooperate, and actively seek ways to optimized the performance of the entire system. Thus the control system will be designed using software agents. A very basic definition of an agent is atomic entities that communicate to implement the functionality of the control system with the following properties: autonomy, reactivity, social ability, proactivity, temporal continuity, goal orientedness, mobility, collaboration and adaptivity.

To achieve these goals using a traditional client-server approach will be difficult. The agent paradigm is different then the client-server approach, since agents can interact on a peer-to-peer level, collaborating, and cooperating to achieve their goals.

Agents engineering aspects will be addressed by adopting the domain independent software standard formulated by FIPA (Foundation for Intelligent Physical Agents). Currently, a control software framework based on agent technology is under development by the JLAB Data Acquisition group.

6.2 Event Reconstruction and Offline Computing

The expected on-line data rate of 100 to 200 MByte/s cannot efficiently be handled when using the same procedures adopted by CLAS in the past: an efficient online event reduction is required to keep the data transfer rates to the Jefferson Lab tape silo within the bandwidth limits. Furthermore, the on-line event reduction and event processing will allow for a comparatively fast access to processed data for further analysis. We consider establishing a "grid-based" cluster of analysis and simulation centers to optimize the data processing.

6.2.1 Data Reduction and On-line Event Reconstruction

Major parts of data reduction will have to be performed on-line. The first stage of data reduction (noise reduction) will be performed at the crate level, the second stage in form of fast event filtering and tagging of events (Level 3) which will remove data which are not of interest for further analysis.

A fast on-line reconstruction will provide sufficient information on data quality and first-pass analyses of basic reactions. Depending on the available CPU power it is possible to perform a full event reconstruction of all events: using an on-line farm in the Hall-B Counting House and/or part of the JLab CUE farms which requires either a second output stream or large pre-silo stage disks. Taking into consideration the current achievements (7-10 ms/event) and the projected increase of CPU speed over the next 6 years, a full event reconstruction can be performed within 3-4 ms despite the more complex detector setup of CLAS^{++}. The output will be written to disk in form of data summary files which contain all information required to perform a first-pass event analysis.

The (quasi-) on-line event reconstruction requires zero order calibration constants which have to come from analyses of previous run periods (and commissioning data) as well as the analysis of data taken during the first days in the specific run period. Additionally, small subsets of data will be selected for further analysis to perform a quasi-online calibration of all detector components. This continuous calibration process will provide a quick response to any changes in crucial detector parameters. In parallel, these subsets will be transferred to university-based analysis centers which will be responsible for a refinement of the on-line calibration.

The data summary files as well as the data subsets to be used for calibration purposes will be stored for several days on large RAID arrays to allow for fast access. We expect that the Jlab Computer Center will provide the necessary infrastructure of fast network connections as well as short- and long-term storage media.

6.2.2 Offline Data Analysis

Since the first-pass reconstruction is performed (quasi-) on-line, it is convenient to distribute the data summary files to university-based analysis centers for further analysis: refinement of detector calibrations and quality controls, preliminary physics analyses. The results will be used as input for a final (second-pass) reconstruction process which can most efficiently be performed at Jefferson Lab. This strategy enables collaborators in their home institutions to contribute effectively to the analysis process. It requires to create appropriate software that minimizes the efforts to complete these – mostly labor intensive – tasks. A grid-based computing environment including IT services customized for scientific computing will be developed in close collaboration with the Hall-D efforts and groups in the high-energy physics community.

6.2.3 Event Simulation

For most experiments to be performed in Hall B, the quality of the results will be limited by systematic uncertainties rather than statistical errors. Therefore it is crucial to understand the acceptance and efficiency of the detector very well. Extensive Monte Carlo simulations play a key role to this end. They will be distributed over several university-based simulation centers extending the use of these institutions in the current CLAS projects. An effective infrastructure has to be developed to manage and coordinate the simulation centers (remote submission, job tracking, communicating of results, simulation database).

Storage and accessibility of simulated data will be an important issue since we expect that at least four times more simulated than real data will be required to ensure high precision of the results. With respect to the pressure on the Jlab tape silo it may be more convenient to add appropriate storage media to the simulation centers.

The design and construction of the new detector parts will be accompanied by the development of corresponding simulation software which will have to be continuously adjusted to an optimal description of the real detector in later years.

6.2.4 Software Development

The development of simulation, reconstruction, and analysis software requires a group of experienced programmers. To optimize the process, parts of the CLAS software as well as techniques and experiences of high-energy physics and other nuclear physics communities will be adapted to the needs of CLAS^{++}. It will be essential to integrate the on-line and offline software efforts as the calibration and event reconstruction will run quasi-online which requires speed-optimized, multi-threaded code.

University-based groups will be involved in the development and maintenance of software, especially those groups who take over the responsibilities to create an analysis or simulation center. The software efforts will be coordinated by a small group of physicists/programmers who are familiar with modern programming techniques and tools as well as the physics program of CLAS^{++}.

Chapter 7

CLAS^{++} - Expected Performance

To fully understand the expected performance of a complex detector such as CLAS++ complete GEANT simulations of the detector system will be needed. This requires more detailed knowledge of the detector components that are used for tracking and particle identification which can currently only be estimated. In addition full charged particle tracking and photon reconstruction in the calorimeters will be needed. Such software requires a significant development effort and manpower which is currently not available. However, certain features of the event reconstruction can be reasonably well estimated using simple approximations.

The following tables 7.1, 7.2, and 7.3 summarize the expected operating conditions of CLAS^{++}.

7.1 Missing mass resolution for exclusive processes

The thrust of the physics program with CLAS^{++} remains in the measurement of exclusive processes with full kinematic coverage. With CLAS the missing mass techniques was used to identify undetected particles, usually a π^0, η, γ, or a neutron. Good missing mass resolution remains important for CLAS^{++} where the undetected

Table 7.1: CLAS^{++} Forward detector - Expected properties

Particle type	polar angle(°)	phi range (°)	$\delta p/p$	δT(ps)
Electron	8 - 40	0 - 270	$\sqrt{(0.1\%p)^2 + (0.2\%/\beta)^2}$	60
Hadrons (inbend.)	8 - 40	0 - 270	same	60
(outbend.)	5 - 35	0 - 270	same	60
Photons	5 - 40	360	$9\%/\sqrt{E(GeV}$	150
Neutrons	5 - 40	0 - 270	-	300

Table 7.2: CLAS^{++} - Central detector properties

Particle type	polar angle (°)	phi range (°)	$\delta p/p$ (%)	δT (ps)
Charged hadrons	40 - 135	360	2.2% at 90°, p= 1 GeV/c	60
Photons	40 - 135	360	$8\%/\sqrt{E(GeV)}$	1 nsec

Table 7.3: CLAS^{++} Luminosity and Particle identification

Operating Luminosity	H_2	$10^{35} cm^{-2} s^{-1}$
	^3He	$1.5 \times 10^{35} cm^{-2} s^{-1}$
	^2H, ^4He, ^{12}C, ^{16}O	$2 \times 10^{35} cm^{-2} s^{-1}$
	polarized NH_3, ND_3	$2 \times 10^{35} cm^{-2} s^{-1}$
pion rejection factor	$>> 1000$	$p < 2.7 GeV/c$
	≈ 1000	$p > 3 GeV/c$
	≈ 100	$p > 5 GeV/c$
π/K separation	Forward detector	$p < 3 GeV/c$
	Central detector	$p < 0.6 GeV/c$
K/p separation	Forward detector	$p < 4.5 GeV/c$
	Central detector	$p < 1.2 GeV/c$

particle may reside on a much larger background. In addition to good missing mass resolution the detector has to provide much better hermeticity to directly detect photons and charged tracks also in regions which are not sensitive in CLAS.

Figure 7.1 shows simulated mass resolution for the reaction $ep \rightarrow e\pi^+ X$ with X = neutron in the final state. The drift chamber resolution is assumed to be significantly better than what has been achieved with CLAS. This will be achieved by using a different gas mixture and smaller drift cell, resulting in improved position resolution.

7.2 Effect of the solenoid field on the Moller electrons

The most severe background in any large acceptance detector using an external electron beam on a fixed target is due to scattering of the beam electrons from the atomic electrons of the target material. Moller electron rates are several orders of magnitude greater in magnitude than hadronic production rates. Most crucial is the shielding of the innermost tracking devices such as drift chambers or silicon microstrip detectors. Passive shielding is excluded as it is not very efficient in shielding electrons with typical Moller electron energies (1 MeV to 100 MeV). Moreover, passive shielding

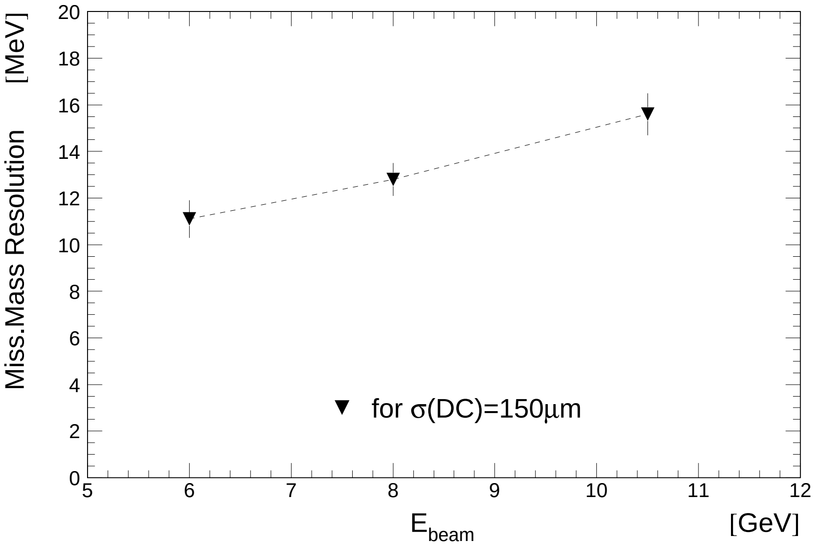

Figure 7.1: Projected missing mass resolution for $ep \rightarrow e\pi^+X$ for different beam energies. Eventa were generated in a range $2.0 < W < 3.0$ GeV, and $2.5 < Q^2 < 7.5$ GeV^2 assuming asymptotic scaling behavior. A drift chamber resolution of 150 μm is assumed for the tracking.

would also adversely affect angle and momentum resolution of charged tracks. For the existing CLAS detector this problem has been addressed by inserting a small version of a toroidal magnet ("Mini-torus'). Although this provides satisfactory shielding in CLAS, it requires the presence of magnetic coils in the active detector volume and produces blind areas in the detector. For CLAS^{++} this is avoided by using a solenoidal magnet as a shield. This provides a very effective suppression of Moller electrons interacting with the sensitive detectors. The solenoidal field was shown to be significantly more efficient in background suppression compared to the mini-torus. This is largely due to the strong longitudinal field component in the solenoid magnet. The Moller electrons are absorbed on the inside of the lead shielding pipe rather than on the outside.

The shielding effect for Moller electrons is depicted in Fig. 7.2 where the Moller electron trajectories are shown if the solenoid field is turned off, and under the influence of the solenoidal field with 5 Tesla central strength. The magnetic field squeezes most of the Moller electrons, which are emitted at angles up to about 70^o into a small cone around the beamline where they can be absorbed into a heavy metal shielding pipe. In order to allow particle detection down to small angles a strong magnetic field, and an extended fringe field is required. While the magnetic field eliminates practically all the Moller background, the background due to photons remains. As is clearly visible in Fig. 7.2 only a small fraction of photons are produced in the target. Most photons are produced in secondary interactions of the Moller electrons at the entrance to the downstream lead shielding pipe.

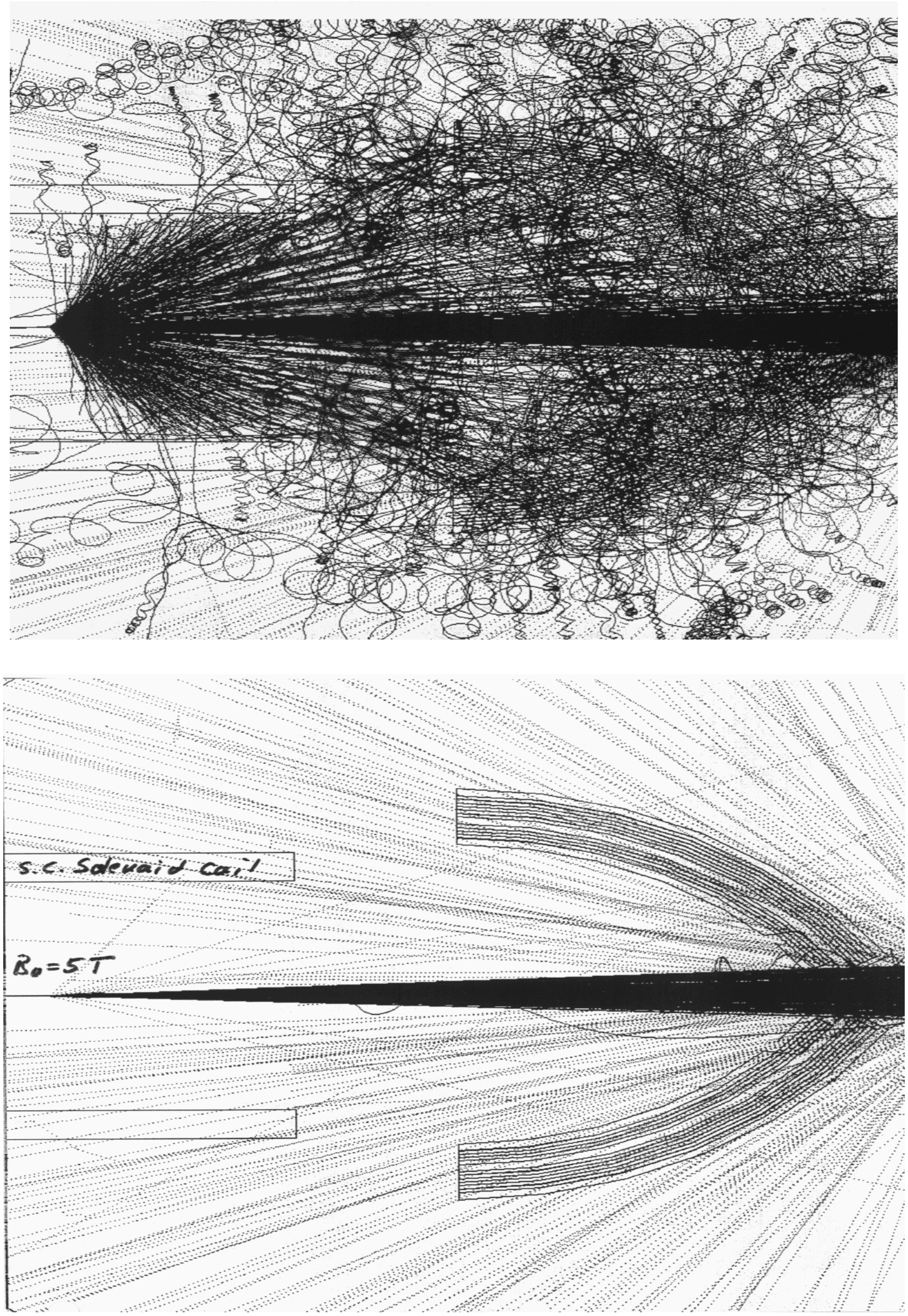

Figure 7.2: Trajectories of Moller electrons at a luminosity $10^{35} cm^{-2} s^{-1}$ within a time window of 250 nsec. Top: Solenoid field turned off. Bottom: 5 Tesla solenoid field is turned on. The straight dotted lines indicate photons. Note that the source of most photons is at a location downstream of the tracking chamber and coincides with the position of the entrance to the Möller shielding pipe.

7.3 Identification of Single Photon Production from $ep \rightarrow ep\gamma X$ Final State

This section serves as an illustrative example of how the large acceptance of CLA^{++} can be used to eliminate background events and isolate the reaction of interest.

In the DVCS experiment reaction $ep \rightarrow ep\gamma X$ will be used to identify a single photon production process. The main background to single photon production will be from π^0 production, when one of the photons from pion decay will not be detected in the CLAS^{++} calorimeter system. Using cuts on missing energy and on the azimuth angle of the proton and the photon in the system of virtual photon (co-planarity requirements) one can reduce the number of π^0 events in the final selection. To estimates the rejection efficiency for pion events and the detection efficiency for single photon events reactions $ep \rightarrow ep\gamma$ and $ep \rightarrow ep\pi^0$ were simulated with proper Q^2 and t distributions in the deep inelastic scattering region. To simulate detector response a fiducial function corresponding to the design geometry of CLAS^{++} detector system is used. All efficiencies are assumed to be 1. The parameterization of detector resolution for each component is included.

In Figure 7.3 distribution of final state electrons and protons that pass geometrical fiducial cuts of CLAS^{++} are plotted. Full 2π acceptance for protons is assumed in the central detector. In the forward region acceptance holes are due to CLAS torus coils. In both reactions distribution of scattered electrons and recoil protons are the same at a given Q^2 and t.

The angular and momentum distribution of photons from reaction $ep \rightarrow ep\gamma$ and $ep \rightarrow ep\pi^0$, when only one photon was in the fiducial region of the detector is shown in Figure 7.4. Since CLAS^{++} will have calorimeter coverage in the dead regions of the torus coils, losses are minimal in the forward region. Gaps are introduced to account for edge effects in the calorimeter. As in the case of protons, full 2π acceptance is assumed in the central detector.

In order to separate $ep \rightarrow ep\gamma$ and $ep \rightarrow ep\pi^0$, the missing energy of the $ep\gamma$ system is analyzed for both reactions together with the $p\gamma$ azimuthal angle, $\phi^*_{p\gamma}$ in the system of coordinates where "Z" axis is in the direction of the virtual photon. In Figure 7.5a,b distribution of $\phi^*_{p\gamma}$ vs missing energy is presented for both reactions. For both, $ep \rightarrow ep\gamma$ and $ep \rightarrow ep\pi^0$, the $\phi^*_{p\gamma}$ distribution is centered around 180^o, while distribution on missing energy has long tail for $ep \rightarrow ep\pi^0$ events. Using cut on E_{miss} one can effectively eliminate events from pion production. In Figure 7.5c $\phi^*_{p\gamma}$ after cut on missing energy, $E_{miss} < 0.8$ GeV is shown. Although the distribution is symmetric around 180^o for pion events (dashed histogram), it is much wider than the distribution for single photon events. Additional cuts can be applied on $\phi^*_{p\gamma}$ to reduce $ep \rightarrow ep\pi^0$ event in the $ep \rightarrow ep\gamma X$ sample. The effect of E_{miss} and $\phi^*_{p\gamma}$ cuts is demonstrated in Figure 7.5d. Vertical axis is the efficiency of reconstruction of $ep \rightarrow ep\gamma$ events with given cuts. The horizontal axis shows the fraction of$ep \rightarrow ep\pi^0$ misidentified as $ep \rightarrow ep\gamma$. Efficiencies are normalized to the

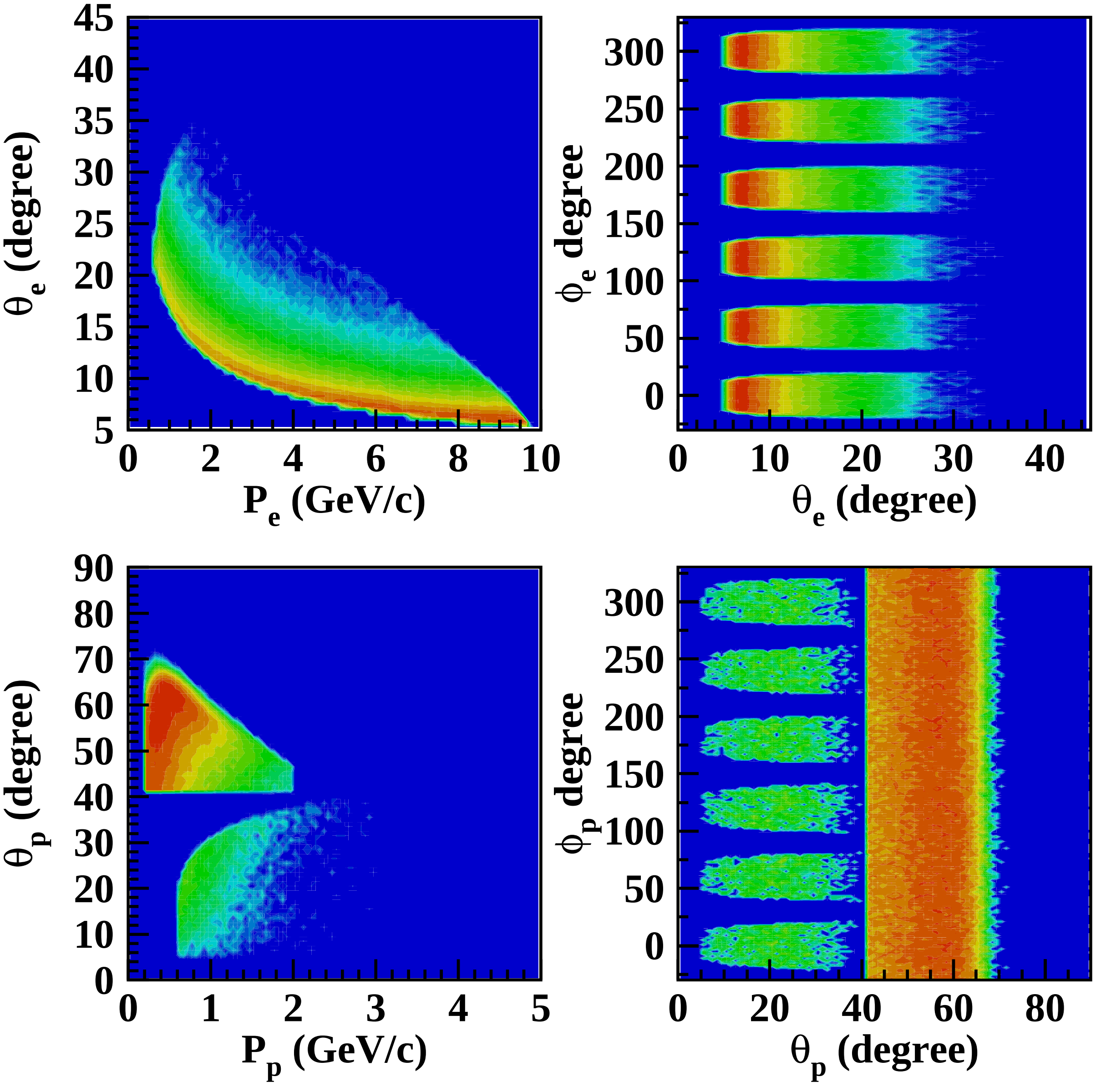

Figure 7.3: Angular and momentum spectra of electrons and protons from deep inelastic scattering processes at small t after CLAS^{++} fiducial cuts.

efficiency for the detection of the ep pair. Already at high missing energy cuts, the loss of $ep \rightarrow ep\gamma$ events is minimal, and the rejection factor for π^0 events is more than factor of 10.

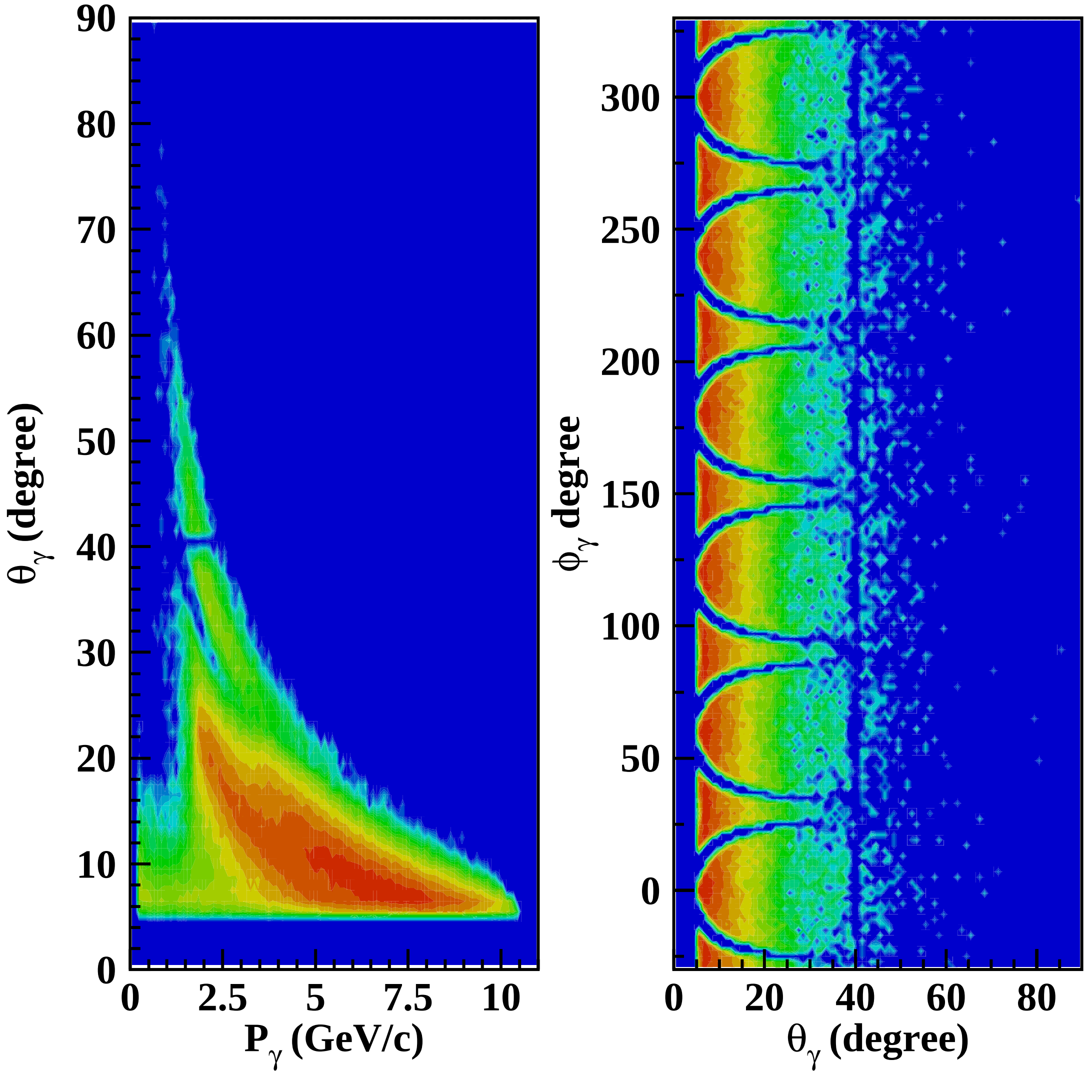

Figure 7.4: Angular and momentum distributions of photons, produced by $ep \rightarrow ep\gamma$ and $ep \rightarrow ep\pi^0$ reaction, after CLAS^{++} fiducial cuts.

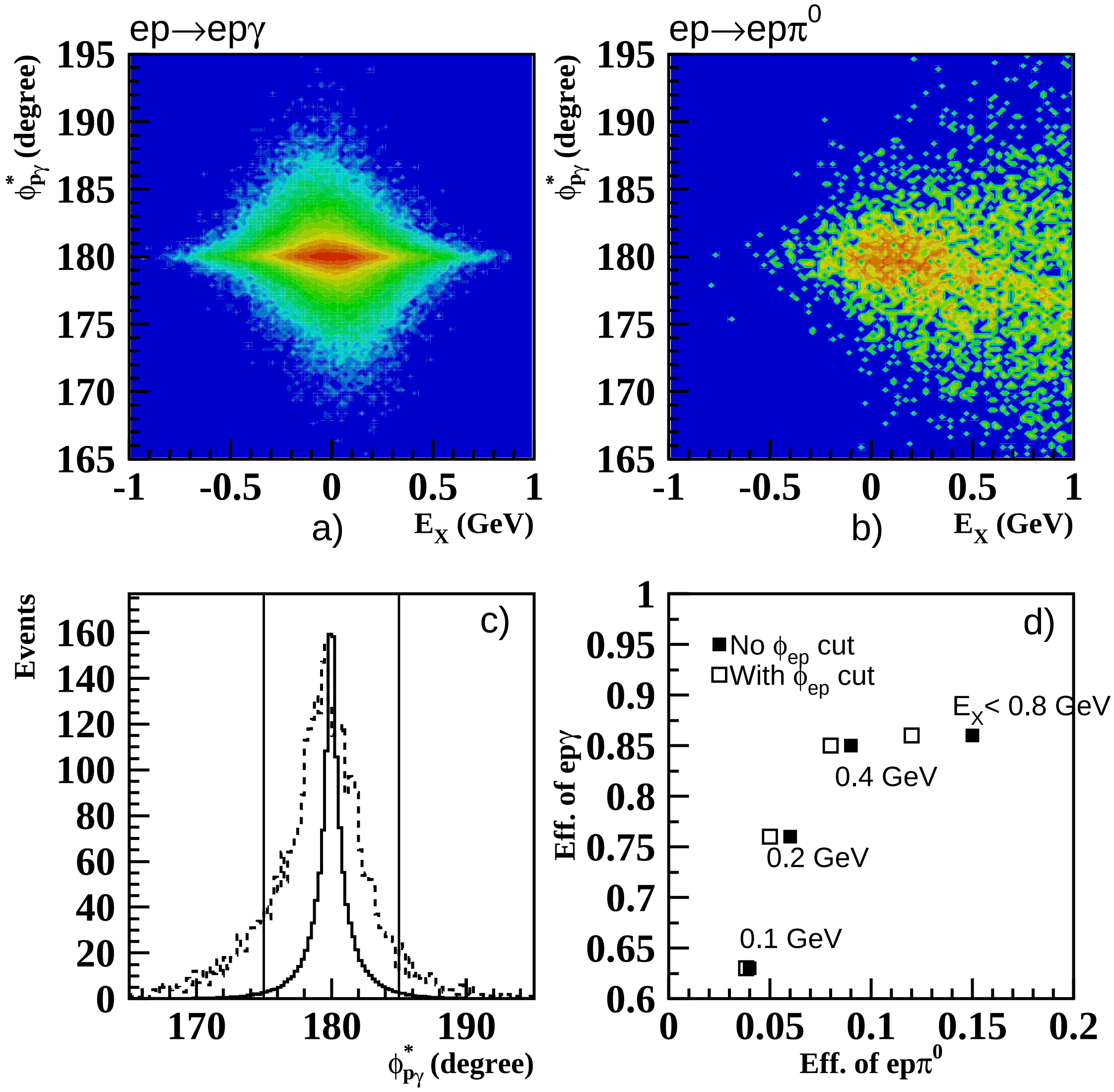

Figure 7.5: Identification of the $ep \rightarrow ep\gamma$ reaction using cuts on missing energy and (γp) azimuthal angle, $\phi^*_{p\gamma}$. a) - $\phi^*_{p\gamma}$ vs missing energy of ($ep\gamma$ system for events from reaction $ep \rightarrow ep\gamma$, b) - the same distribution for events from $ep \rightarrow ep\pi^0$ when one of photons is not detected, c) - $\phi^*_{p\gamma}$ distribution for events $E_{miss} < 0.8$ GeV, dashed histogram is for $ep \rightarrow ep\pi^0$ events and full line histogram is for $ep \rightarrow ep\gamma$ events. On plot d) the efficiency of reconstruction of $ep \rightarrow ep\gamma$ events (Y-axis) vs the efficiency of reconstruction of $ep \rightarrow ep\pi^0$ events as $ep \rightarrow ep\gamma$ (X-axis) is plotted for different missing energy cuts. Open symbols are efficiencies after selecting events in $\phi^*_{p\gamma} = 180^o \pm 5^o$ interval.

Bibliography

[1] R.W. Mcallister and R. Hofstadter, Phys.Rev. **102** (1956) 851.

[2] E.D. Bloom et al., Phys.Rev.Lett. **23** (1969) 930.

[3] M. Breidenbach et al., Phys.Rev.Lett. **23** (1969) 935.

[4] M. Gell-Mann, Phys. Lett. **8** (1964) 214.

[5] G. Zweig, CERN-TH-412 (1964) 412.

[6] B. Fillipone and X. Ji, Advances in Nuclear Physics **20** (2001) 1.

[7] D. Mueller et al., Fortschr. Phys. **42** (1994) 101.

[8] X. Ji, Phys.Rev.Lett. **78** (1997) 610,.

[9] X. Ji, Phys.Rev. D **55** (1997) 7114,.

[10] A.V. Radyushkin, Phys. Lett. B **380** (1997) 417.

[11] M. Burkardt, hep-ph/0206269 .

[12] A. Belitsky and D. Mueller, hep-ph/0206306 .

[13] S. Stepanyan et al., Phys.Rev.Lett., **87** (2001) 182002.

[14] M. Diehl et al., Eur. Phys. J **C8** (1999) 409.

[15] H.W. Huang and P. Kroll, Eur. Phys. J **C17** (2000) 423.

[16] CLAS Collaboration (H. Avakian et al.), in preparation .

[17] D. Soper, Phys. Rev. Lett. **43** (1979) 1847.

[18] D.Sivers, Phys.Rev. D **43** (1991) 261.

[19] J. Collins, Nucl. Phys. B **396** (1993) 161.

[20] P.J. Mulders and R.D. Tangerman, Nucl. Phys. B **461** (1996) 197.

[21] A. Kotzinian, Nucl. Phys. B **441** (1995) 234.

[22] M. Anselmino and F. Murgia, Phys. Lett. B **442** (1998) 470.

[23] A. Belitsky et al., hep-ph/0208038 .

[24] X. Ji et al., hep-ph/0210430. .

[25] S. Brodsky et al., Phys. Lett. **530** (2002) 99.

[26] J. Collins, Phys. Lett. B **536** (2002) 43.

[27] M. Diehl, hep-ph/0205208. .

[28] X. Ji and F. Yuan, hep-ph/0206057. .

[29] J. Ralston and D. Soper, Nucl. Phys. B **152** (1979) 109.

[30] R.L.Jaffe and X.Ji Nucl. Phys., Nucl. Phys. B **375** (1992) 527.

[31] A. Airapetian et al., Eur. Phys. J. C **20** (2001) 479.

[32] Paul van der Nat, Hadronization at 12 gev, Master's thesis, Vrije Universiteit, Amsterdam/Nikhef, 2002.

[33] JLab Experiment E94-017, W. Brooks and M. Vineyard, spokespersons (1994).

[34] L.C. Smith et al. K. Joo, Phys.Rev.Lett. **88** (2002) 122001.

[35] V.V. Frolov et al., Phys.Rev.Lett. **82** (1999) 45.

[36] J.C. Collins et al., Phys. Rev. D **56** (1997) 2982.

[37] K. Goeke et al., Prog.Part.Nucl.Phys. **47** (2001) 401.

[38] A. Belitsky et al., Nucl.Phys., **B629** (2002) 323.

[39] A. Radyushkin, Phys. Rev. D **59** (1999) 014030.

[40] M. Polyakov and C. Weiss, Phys. Rev. D **60** (1999) 114017.

[41] M. Pemttinen et al., Phys. Lett. B, **491** (2000) 96.

[42] A. Belitsky and D. Mueller, Nucl. Phys. B **589** (2000) 611.

[43] A. Airapetian et al., Phys.Rev.Lett., **87** (2001) 182001.

[44] C. Adloff et al., Phys.Lett.B **517** (2001) 47.

[45] M. Guidal and M. Vanderhaeghen, "Computer Code for DVCS and BH Calculations" Private communications..

[46] M. Vanderhaeghen, P.A.M. Guichon, and M. Guidal, Phys. Rev. D **60** (1999) 094017.

[47] M. Vanderhaeghen, P.A.M. Guichon, and M. Guidal, Phys. Rev. Lett. **80** (1998) 5064.

[48] M. Guidal and M. Vanderhaeghen, hep-ph/0208275 (2002). .

[49] A. Belitsky and D. Mueller, hep-ph/0210313 (2002).

[50] M. Diehl et al., Phys. Lett. **B411** (1997) 193.

[51] F. Ellinghaus (HERMES Collaboration), hep-ex/0207092 (2002).

[52] E.R. Berger, M. Diehl and B. Pire **DESY-01-119 hep-ph/0110062** (2001).

[53] L. Frankfurt et al., Phys. Rev. Lett., **84** (2000) 2589.

[54] M. Eides et al., Phys.Rev.D **59** (1999) 114025.

[55] A. Airapetian et al., HERMES Collaboration, submitted to Eur.Phys.J., **C17** (2000) 389.

[56] "CLAS experiment E1-6", November 2001 to January 2002. .

[57] C.J. Bebek et al., Phys. Rev. D **13** (1978) 1693.

[58] L. Frankfurt et al., Phys. Rev. D **60** (1999) 014010.

[59] L. Mankiewicz et al., Eur. Phys. J. C **5** (1998) 119.

[60] A. Garcia and P. Kielanowsk, Berlin, Germany: Springer Verlag . (*Lecture Notes In Physics, 222*). (1985) 173.

[61] E.D. Bloom and F.J. Gilman, Phys. Rev. Lett. **16** (1970) 1140.

[62] R. P. Feynman, *Photon Hadron Interactions* (Benjamin Reading, Massachusetts, 1972)..

[63] F. E. Close, Phys. Lett. **43** (1973) 422.

[64] R. D. Carlitz, Phys. Lett. B **58** (1975) 345.

[65] F. E. Close, *An Introduction to Quarks and Partons* (Academic Press 1979.

[66] F. E. Close and A. W. Thomas, Phys. Lett. B **212** (1988) 227..

[67] N. Isgur, Phys. Rev. D **59** (1999) 03413..

[68] A. D. Martin et al., Eur. Phys. J. C **12** (1998) 375.

[69] G. R. Farrar and D. R. Jackson, Phys. Rev. Lett. **35** (1975) 1416.

[70] S. Kuhlmann al., Phys. Lett. B **476** (2000) 291.

[71] L. W. Whitlow *et al.*, Phys. Lett. B **282** (1991) 475.

[72] W. Melnitchouk and A. W. Thomas, Phys. Lett. B **377** (1996) 11.

[73] L. L. Frankfurt and M. I. Strikman, Nucl. Phys. **B250** (1988) 1585.

[74] I. Niculescu et al., Phys. Rev. Lett. **85** (2000) 1182,.

[75] M. E. Christy et al., E94-110 Collaboration in preparation..

[76] A. de Rújula, Ann. Phys. **103** (1975) 315.

[77] W. Melnitchouk N. Isgur, S. Jeschonnek and J. W. Van Orden, Phys. Rev. D **65** (2001) 054005.

[78] F. E. Close and N. Isgur, Phys. Lett. B **509** (2001) 81.

[79] Jefferson Lab Letter of Intent LOI-02-105, S. Kuhn contact person. .

[80] L. L Frankfurt and M. I. Strikman, Phys. Rep. **76** (1981) 217.

[81] S. Simula, Phys. Lett. B **387** (1996) 245.

[82] W. Melnitchouk et al., Z. Phys. A **359** (1997) 99.

[83] W. Melnitchouk et al., Phys. Lett. B **335** (1994) 1183.

[84] S. A. Kulagin et al., Phys. Rev. C **50** (1995) 1154.

[85] S. Dieterich et al., Phys. Lett. B **500** (2002) 47.

[86] W. Melnitchouk et al., Eur. Phys. J. A **14** (2002).

[87] L. L. Frankfurt et al., Z. Phys. A **352** (1996) 97.

[88] M. I. Strikman et al., (1996).

[89] M. R. Adams et al., Phys. Rev. Lett. **74** (1995) 5198.

[90] V. D. Burkert and B. L. Ioffe, Phys. Lett. B **296** (1992) 223.

[91] X. Ji and P. Unrau, Phys. Rev. D **52** (1997) 72.

[92] J. Edelmann et al., Nucl. Phys. **A665** (2000) 125.

[93] L. Mankiewicz E. Stein, P. Gornicki and A. Schafer, Phys. Lett. B **353** (1995) 107.

[94] H. Burkhardt and W. N. Cottingham, Ann. Phys. **56** (1970) 453.

[95] O. V. Teryaev A. V. Efremov and E. Leader, Phys. Rev. D **55** (1997) 4307.

[96] J. Levelt and P. J. Mulders, Phys. Lett. B **338** (1994) 357.

[97] A. Bacchetta et.al, Phys. Rev. D **65** (2002) 094021.

[98] L. Frankfurt et al., Phys. Rev. D **60** (1999).

[99] A. Belitsky and D. Muller, Phys. Lett. B **513** (2001) 349.

[100] HERMES Collaboration (K. Ackerstaff et al.), Phys. Lett. B **464** (1999) 123.

[101] D. Boer and P. Mulders, Phys. Rev. D **57** (1998) 5780.

[102] S. Brodsky et.al, Phys. Rev. D **65** (2002) 114025.

[103] L. Trentadue and G. Veneziano, Phys. Lett. B **323** (1994) 201.

[104] K.Heller et al., 'Proceedings of Spin 96' Amsterdam (1996) 23.

[105] Fermilab E704 collaboration (A. Bravar et al.), Phys. Rev. Lett. **77** (1996) 2626.

[106] HERMES collaboration (A. Airapetyan et al.), Phys. Rev. Lett. **84** (2000) 4047.

[107] HERMES collaboration (A. Airapetyan et al.), Phys. Rev. D **64** (2001) 097101.

[108] A. Bravar, Nucl. Phys. (Proc. Suppl.) B **79** (1999) 521.

[109] S. Brodsky et.al, Nucl. Phys. B **642** (2002) 344.

[110] X. Ji, Phys. Rev. Lett. **78** (1997) 610.

[111] A.V. Radyushkin, Phys. Lett. B **380** (1997) 417.

[112] A. Efremov et al. Proceedings of QCD'N02 Ferrara 2002, hep-ph/0206267. .

[113] A.M. Kotzinian and P.J. Mulders, Phys. Rev. D **54** (1996) 1229.

[114] K. Goeke A. Efremov and P. Schweitzer, Phys. Lett. B **552** (2001) 37.

[115] A. M. Kotzinian et al., Nucl. Phys. A **666** (2000) 290.

[116] H. Avakian, Proceedings of DIS-2000 Liverpool University 2000. .

[117] E. Christova et al., hep-ph/9907265 .

[118] V. V. Khoze A. Brandenburg and D. Muller, Phys. Lett. B **347** (1995) 413.

[119] C. E. Carlson A. Afanasev and C. Wahlquist, Phys. Lett. B **398** (1998) 393.

[120] P. Hoyer S. J. Brodsky, M. Diehl and S. Peigne, Phys. Lett. **449** (1999) 306.

[121] C. E. Carlson A. Afanasev and C. Wahlquist, Phys. Rev. D **62** (2000) 074011.

[122] R. Jaffe, Proceedings of QCD-N'02, Ferrara 2002 .

[123] M. Diehl and R. Jakob, private communication .

[124] B. Kopeliovich, J. Nemchik and E. Predazzi, hep-ph/9511214 (1995).

[125] B. Kopeliovich, J. Nemchik and E. Predazzi, hep-ph/9607036 (1996).

[126] E. Wang and X.-N. Wang, Phys. Rev. Lett. **89** (2002) 162301.

[127] B.Z. Kopeliovich and B.G. Zakharov, Phys. Rev. D **44** (1991) 3466.

[128] L. D. Landau and I. Y. Pomeranchuk, Dokl. Akad. Nauk SSSR **92:535** (1953) 735.

[129] A.B. Migdal, Phys. Rev. **103** (1956) 1181.

[130] L. Anthony et al., Phys. Rev. D **56** (1997) 1373.

[131] A. Bialas and T. Chmaj, Phys. Lett. **133B** (1983) 241.

[132] Jefferson Lab Proposal number E02-104, W. Brooks, spokesperson (2002).

[133] J.W. Cronin et al., Phys. Rev. D **11** (1975) 3105.

[134] B. Z. Kopeliovich et al., Phys. Rev. Lett. **88** (2002) 232303.

[135] J. Rathsman G. Ingleman, A. Edin, LEPTO **6.5.1**.

[136] R. Baier, D. Schiff and B. G. Zakharov, Annu. Rev. Nucl. Part. Sci. **50** (2000) 37.

[137] X.-N. Wang et al., Phys. Rev. **D51** (1995) 3436.

[138] X. Guo and J.-W. Qiu, Phys. Rev. D **61** (2000) 096003.

[139] V. Muccifora, hep-ex/0106088 (2001).

[140] S.J. Brodsky and G.P. Lepage, Phys.Rev. D **50** (1980).

[141] L. Frankfurt et al., Ann.Rev.Nucl.Part.Sci. **45** (1994) 501.

[142] P. Jain et al., Phys. Rep. **271** (1995) 133.

[143] et al. R. L. Anderson, Phys. Rev. **D4** (1971) 3245.

[144] L. Frankfurt et al., Nucl.Phys. A **622** (1997) 511.

[145] L. Frankfurt et al., Eur. Phys. J. A **2** (1998) 301.

[146] F. Klein, L. Kramer and S. Stepanyan (2002) "Coherent.

[147] A.S. Carroll et al., Phys. Rev. Lett. **61** (1988) 1698.

[148] J.P. Ralston and B. Pire, Phys. Rev. Lett. **61** (1988) 1823.

[149] N.C.R. Makins et al., Phys. Rev. Lett. **72** (1995) 87.

[150] T.G. O'Neill et al., Phys. Lett. **B351** (1995) 87.

[151] E.M. Aitala et al., Phys. Rev. Lett. **86** (2001) 4773.

[152] M.R. Adams et al., Phys. Rev. Lett. **74** (1995) 1525.

[153] B. Kopeliovich and J. Nemchik, Phys. Lett. **B368** (1996) 187.

[154] P.V.R. Murthy et al., Nucl. Phys. **B92** (1975) 269.

[155] A. Gsponer et al., Phys. Rev. Lett. **42** (1979) 9.

[156] B. Kopeliovich et al., Phys. Lett. **B324** (1994) 469.

[157] K. Ackerstaff et al., Phys. Rev. Lett. **82** (1999) 3025.

[158] K. Hafidi et al., CLAS proposal E02-110 (2002).

[159] B. Kopeliovich et al., Phys. Rev. C. **65** (2002) 035201.

[160] D.G. Cassel et al., Phys. Rev. D. **24** (1981) 2787.

[161] E.J. Moniz et al., Phys. Rev. Lett. **26** (1971) 445.

[162] C.E. Carlson and K.E. Lassila, Phys. Rev. C **51** (1995) 364.

[163] C.E. Carlson et al., Phys. Rev. **D63** (2001) 117301.

[164] R. Hofstadter and R.W. McAllister, Phys. Rev. **98** (1955) 183.

[165] G.P. Lepage and S.J. Brodsky, Phys. Rev. D **22** (1980) 2157.

[166] M.K. Jones et al., Phys. Rev. Lett. **84** (2002) 1398.

[167] The Lattice Hadron Physics Collaboration, “Nuclear Theory with Lattice QCD: A Proposal to use Lattice QCD to Understand the Structure and Interactions of Hadrons” (2000) submitted to the U. S. Dept. of Energy.

[168] S. Platchkov et al., Nucl. Phys. **A510** (1990) 740.

[169] N. Isgur, G. Karl and D.W.L. Sprung, Phys. Rev. D **23** (1981) 163.

[170] A.W. Thomas, Adv. Nucl. Phys. **13** (1984) 1.

[171] P. E. Bosted, Phys. Rev. C **51** (1995) 409.

[172] X. Ji, J. Phys. G **24** (1998) 1181.

[173] A.V. Radyushkin, Phys. Rev. D **56** (1997) 5524.

[174] I. Niculescu et al., Phys. Rev. Lett. **85** (2000) 1182,.

[175] A. de Rújula, H. Georgi and H.D. Politzer, Ann. Phys. **103** (1975) 315.

[176] X. Ji and P. Unrau, Phys. Rev. D **52** (1995) 72.

[177] X. Ji and W. Melnitchouk, Phys. Rev. D **56** (1997) 1.

[178] S.D. Drell and T.-M. Yan, Phys. Rev. Lett. **24** (1970) 181.

[179] G.B. West, Phys. Rev. Lett. **24** (1970) 1206.

[180] W. Melnitchouk, Phys. Rev. Lett. **86** (2001) 35.

[181] C.E. Carlson and N.C. Mukhopadhyay, Phys. Rev. D **58** (1998) 094029.

[182] P. Stoler, Phys. Rep. **226** (1993) 103.

[183] V.D. Burkert and B.L Ioffe, Phys. Lett. **B296** (1992) 223.

[184] S. Rock et al., Phys. Rev. Lett. **49** (1982) 1139.

[185] V.D. Burkert, Presentation at BARYONS2002 conference, http://www.jlab.org/baryons2002/program.html#mon1 (2002).

[186] M. Ripani, in *Proceedings of the Workshop on The Physics of Excited Nucleons NSTAR2001*, edited by D.Drechsel and L.Tiator, page 429, World Scientific, 2001.

[187] M. Ripani et al., Nucl. Phys. **A672** (2000) 220.

[188] V. Mokeev et al., Phys. of Atom. Nucl. **64** (2001) 1292.

[189] E.M. Salesky D.M. Manley, Phys. Rev. D **43** (1992) 4002.

[190] T.P.Vrana el al, Phys. Rep. **328** (2000) 181.

[191] K. Joo et al. (The CLAS Collaboration), Phys. Rev. Lett. **88** (2002) 122001.

[192] R. Thompson et al. (The CLAS Collaboration), Phys. Rev. Lett. **86** (2001) 1702.

[193] V. Mokeev et al., ibid 181.

[194] V.D. Burkert, Czech. Journ. of Phys. **46** (1996) 627.

[195] N. Isgur, JLAB-THY-00-20 (2000).

[196] N. Isgur et al., Phys. Rev. D **64** (2001) 054005.

[197] N. Isgur et al., Phys. Lett. **B509** (2001) 81.

[198] ABBHHM Collaboration, Phys. Rev. **175** (1968) 1669.

[199] P. Page, in *Proceedings of NSTAR2000: Excited Nucleons and Hadronic Structure*, edited by J. Kelly V. Burkert, L. Elouadrhiri and R. Minehart, World Scientific, 2000.

[200] R. Koniuk and N. Isgur, Phys. Rev. D **21** (1980) 1868.

[201] M.M. Giannini, Rep. Prog. Phys. **54** (1990) 453.

[202] S. Capstick and W. Roberts, Phys. Rev. D **49** (1994) 4570.

[203] F. Stancu and P. Stassart, Phys. Rev. D **47** (1993) 2140.

[204] K.F. Liu and C.W. Wong, Phys. Rev. D **28** (1983) 170.

[205] I. Aznauryan, arXiv:nucl-th/0206033 (2002).

[206] N. Dombey, Rev.of Mod. Phys. **41** (1969) 236.

[207] I. Akushevich et al., RADGEN 1.0 (2000).

[208] N. Isgur and J. Paton, Phys. Rev. D **31** (1985) 2910.

[209] N. Isgur et al., Phys. Rev. Lett. **54** (1985) 869.

[210] S.U. Chung, BNL-QGS-93-05 (1995).

[211] S.U. Chung and T.L. Trueman, Phys. Rev. D **11** (1975) 633.

[212] G.S. Adams et al., PAC19/E01-017 (2001).

[213] T. Barnes, N. Black and P.R. Page, Nucl-th/0208072 (2002).

[214] I. Aznauryan, Z. Phys. C **68** (1995) 459.

[215] Y. Eisenberg et al., Phys. Rev. Lett. **23** (1972) 1322.

[216] C. Fabjan, in *Techniques and Concepts in High Energy Physics III*, edited by T. Ferbel, Plenum Pub., 1985.

[217] R. Wigmans, *Calorimetry*, Oxford Science Pub., 2000.

[218] M. Antonelli et al., Nucl. Instr. and Meth. **A409** (1996) 558.

[219] D.W. Hertzog, Nucl. Instr. and Meth. **A294** (1990) 446.

[220] E.S. Smith, CLAS-NOTE 2002-004 (1991).

[221] STAR TOF Group, in *IV Workshop on Resistive Plate Chambers and Related Detectors*, 2001.

[222] Z. Li, Brokhaven National Laboratory, private communications (2002).

[223] P. Bertin, Clermond-Ferrand, private communications (2002).

[224] G. Adams et al., Nucl. Instr. and Meth. A **465** (2001) 414.

[225] G. Adams et al., submitted to Nucl. Instr. and Meth. (2003).

[226] E.S. Smith et al., Nucl. Instr. and Meth. **A432** (1999) 265.

[227] E.S. Smith and R. Jacobs, CLAS-NOTE 91-003 (1991).

[228] V. Koubarovski et al., CLAS-NOTE 2001-011 (2001).

[229] CEBAF Conceptual Design Report (1990).

[230] M. Amarian et al., Nucl. Instr. and Meth. **A460** (2001) 239.

[231] S. Majewski et al., CLAS-NOTE 2002-01 (2002).

[232] V. Burkert et al., Jefferson Lab Proposal E-91-023 (1991).

[233] G. Dodge et al., Jefferson Lab Proposal E-93-009 (1993).

[234] R. DeVita (The CLAS Collaboration), Phys. Rev. Lett. **88** (2002) 082001.